A study of CP violation in $B^{\mp} \to Dh^{\mp}$ ($h = K, \pi$) with the modes $D \to K^{\mp}\pi^{\pm}\pi^{0}$, $D \to \pi^{+}\pi^{-}\pi^{0}$ and $D \to K^{+}K^{-}\pi^{0}$

Nazim Hussain

University College, University of Oxford

A thesis submitted in fulfilment of the requirements for the degree of Doctor of Philosophy at the University of Oxford

Trinity Term, 2015

A study of CP violation in $B^{\mp} \to Dh^{\mp}$ $(h = K, \pi)$ with the modes $D \to K^{\mp}\pi^{\pm}\pi^{0}$, $D \to \pi^{+}\pi^{-}\pi^{0}$ and $D \to K^{+}K^{-}\pi^{0}$

Nazim Hussain
University College, University of Oxford

A thesis submitted in fulfilment of the requirements for the degree of Doctor of Philosophy at the University of Oxford

Trinity Term, 2015

Abstract

One of the objectives of the LHCb experiment at CERN is a precision determination of the angle γ from the CKM Unitarity Triangle, a CP-violating parameter of the Standard Model. Sensitivity to γ can be obtained by exploiting the interference effects in $B^{\mp} \to Dh^{\mp}$ $(h = K, \pi)$ decays, which can lead to measurable charge asymmetries.

This thesis presents an analysis of the decays $B^{\mp} \to DK^{\mp}$ and $B^{\mp} \to D\pi^{\mp}$ where the D meson is reconstructed in the three-body final states of $K^{\mp}\pi^{\pm}\pi^{0}$, $\pi^{+}\pi^{-}\pi^{0}$ and $K^{+}K^{-}\pi^{0}$. The analysis is performed using 3.0 fb^{-1} of pp collision data collected by LHCb in 2011 and 2012. It represents the first time that these particular decay modes are studied at the LHCb experiment.

Several CP observables are measured using a simultaneous fit to the invariant $B^{\mp}$ mass distributions of the decay channels of interest. A first observation is obtained of the decays $B^{\mp} \to [\pi^{\mp}K^{\pm}\pi^{0}]_{D}\pi^{\mp}$ and $B^{\mp} \to [K^{+}K^{-}\pi^{0}]_{D}\pi^{\mp}$ at 5.3σ and greater than 10σ significance levels, respectively. In addition, first evidence of the decay $B^{\mp} \to [K^{+}K^{-}\pi^{0}]_{D}K^{\mp}$ is obtained at a significance of 4.5σ. The results are interpreted in the context of γ and related parameters.

For those who dare to dream.

Acknowledgements

It is often said that “It takes a city to raise a child.” By that measure, it is not preposterous to claim that the creation of a doctoral thesis requires the support from a small settlement’s worth of people.

Firstly, I extend my deepest thanks to my supervisor, Guy Wilkinson. Over the past four years, I have been consistently amazed by his understanding of flavour physics and his uncanny ability to glance at an incorrect plot and immediately recognise the underlying problem. His critical eye and attention to detail have served to improve my research beyond measure. Under his tutelage, I have become a better student, a better writer and, dare I say, a better scientist.

I am thoroughly indebted to Malcolm John for his wealth of ideas, patience and code. There are too many instances to count where his support allowed me to overcome an obstacle that seemed hopeless at the time. This thesis would not have been possible without his expertise.

The LHCb group at Oxford has benefited from the incredible talents of its postdoctoral researchers. Sneha Malde, Denis Derkach, Paolo Gandini and Chris Thomas have all helped to improve this thesis in a variety of ways, and for that I am grateful. Special thanks are in order to Andrew Powell who patiently took me under his wing during my first LHCb analysis, giving me the skills and confidence required to undertake a second analysis, the one discussed in this thesis.

Oxford’s particle physics subdepartment has a set of world-class administrators. In particular, I offer my thanks to Kim Proudfoot and Sue Geddes for their unfailing dedication to the subdepartment’s students. Their efforts have helped me out of an inordinate amount of sticky situations.

My fellow D. Phil candidates in physics have greatly contributed to maintaining my sanity over the past few years. A big thanks to Kate Pachal and Mireia Crispín Ortuzar for our two years of real estate adventures in multiple countries. I could not have asked for a pair of more intelligent, cultured or compassionate flatmates. I thank my fellow LHCb students, Scott Stevenson, Donal Hill and Faye Cheung for enduring my office anecdotes. Moreover, I am in their debt for the myriad of useful physics discussions we have had over the years. I am grateful to Krish Majumdar for allowing me to wax poetic on matters of inconsequence. For Neven Blaskovic Kraljevic, Amy Cottle, James Henderson, Craig Sawyer, Abe Jacobs, Shaun Gupta and Stephen Dann, I thank them for our always enlightening lunchtime conversation.

Many thanks are owed to Daniel Hugo Cámpora Pérez for his hospitality, humour, and many late nights discussing niche technological interests. My time at CERN would not have been nearly as enjoyable without his presence.

My affiliation to University College at Oxford has given me the opportunity to befriend

some remarkable individuals over the course of my studies. I thank Rebecca Merkley and Andreas Tischbirek for keeping me laughing. Evan Wilson and Erin Meyer Wilson have my gratitude for their continual interest in my well-being. Rebecca Elvin and Emily Kiss are owed thanks for allowing me to monopolise their living room on more occasions than I deserve. David Quick, I thank, for being a legend. For Matt Garraghan, Helena Mills, Tess Sheppard, Harriet Rawson, Neil Dewar and Sarah Dixon-Clarke, I am grateful for our many pub discussions.

I thank the late Theresa Schlagheck for her friendship.

I extend my gratitude to Mike Wood, Chris Govias, Leah Bevington and Amar Dattani for their enthusiasm and for dragging me away from Oxford every now and then.

Finally, I thank Azeem, Ameer and my parents for putting up with my shenanigans for longer than I can remember.

In nature's infinite book of secrecy
A little I can read.

— William Shakespeare
Anthony & Cleopatra, I.ii (1606-7)

Contents

List of Figures

List of Tables

Preface

In the Standard Model of particle physics, the complex phase of the CKM Matrix is the origin of *CP*-violating phenomena. The unitarity constraints of this matrix can be geometrically represented as a Unitarity Triangle in the complex plane. Of the three angles in this triangle, only one, γ, can be measured directly in tree-level processes. Since loop-level processes are expected to have sensitivity to New Physics contributions, a tree-level measurement of γ constitutes a benchmark to which indirect, loop-level measurements can be compared and any observed deviations may be indicative of New Physics. Experimentally, the uncertainty on direct measurements of γ must be reduced in order to make such comparisons meaningful.

The LHCb detector, one of the four major LHC experiments at CERN, is a single-arm, forward spectrometer. It is optimised for the study of *CP* violation through the decay of beauty and charm hadrons produced from the LHC's proton-proton collisions.

This thesis presents a study of *CP* violation in the decays $B^{\mp} \to DK^{\mp}$ and $B^{\mp} \to D\pi^{\mp}$, where the D meson decays to the three-body final states $K^{\mp}\pi^{\pm}\pi^{0}$, $\pi^{+}\pi^{-}\pi^{0}$ and $K^{+}K^{-}\pi^{0}$. In these decays, the final particle states are accessible both by D^0 and $\overline{D}^0$ meson decays, leading to interference. The resulting ratio of branching fractions and charge asymmetries are *CP* observables related to γ and can be used to perform a measurement of this quantity.

The analysis uses a total of 3.0 fb^{-1} of data collected by the LHCb detector in 2011 and 2012. The *CP* observables are measured via a simultaneous fit to the $B^{\mp}$ invariant mass distributions of the decay modes of interest. Using these observables, a χ^2 minimisation fit is performed to extract measurements of γ; the *CP*-conserving strong-phase difference, δ_B; and the absolute ratio of the amplitudes of colour suppressed to colour favoured $B^{\mp} \to DK^{\mp}$ decays, r_B. This analysis is the first time these particular decay modes have been studied at LHCb and represents the first time that the decays $B^{\mp} \to [\pi^{+}\pi^{-}\pi^{0}]_{D}\pi^{\mp}$, $B^{\mp} \to [K^{+}K^{-}\pi^{0}]_{D}\pi^{\mp}$ and $B^{\mp} \to [K^{+}K^{-}\pi^{0}]_{D}K^{\mp}$ have been studied at any experiment. In particular, for LHCb, this is the first b-physics measurement to use π^{0} meson decays. The results of the analysis have been published in Physical Review D **91**, 112014 (2015).

Chapter 1 of this thesis presents the formalism of *CP* violation, the Unitarity Triangle and the angle γ. In addition, an introduction is provided to the measured observables. The Chapter discusses the current experimental status of the relevant measurements and concludes with a presentation of the external inputs measured at CLEO-c that are required for this analysis. Chapter 2 discusses the LHC and the LHCb experiment, with particular emphasis on the detector subsystems relevant to this study.

The original research performed by the author in this analysis is primarily documented in Chapters 3 to 7. In Chapter 3, there is a discussion of the primary selection mechanism used in this analysis, the Boosted Decision Tree, as well as requirements placed on reconstructed mesons. Chapter 4 continues the selection discussion by presenting the modelling of background contributions. In this Chapter, Section 4.2 describes the partially reconstructed low-mass backgrounds. This study was performed entirely by Paolo Gandini and this analysis is able to benefit from its results. In Chapter 5, the simultaneous fit to data is presented along with the systematic uncertainties of the analysis. The results from this fit are discussed in Chapter 6 along with the measurement of the parameters r_B, δ_B and γ. In this Chapter, the study regarding the use of the external inputs at LHCb, detailed in Section 6.4, was performed by Christopher Thomas. The conclusions of his study are exploited in this analysis. Finally, Chapter 7 summarises the results and presents a future outlook for these measurements for the LHC Run II and the LHCb upgrade.

Chapter 1

Introduction

Particle physics is described by a theory known as the Standard Model (SM). Developed in the 1960s and the 1970s, the SM has been remarkably accurate in describing the vast majority of experimentally observed particle interactions.

This Chapter describes the fundamentals of the SM and the role of charge-parity (CP) violation within the model. It then elaborates on the phenomenon of quark flavour mixing and how this is described by the Cabibbo-Kobayashi-Maskawa (CKM) matrix. From this, it introduces the parameter γ and explains its importance in CP violation studies. Afterwards, it then describes the Gronau-London-Wyler (GLW) and Atwood-Dunietz-Soni (ADS) methods of measuring γ using $B^{\mp} \to DK^{\mp}$ decays and the physical observables that are critical to this analysis. Finally, it concludes with some of the prior measurements that have either directly contributed to this analysis, or have been performed on similar or related decays.

1.1 The Standard Model

The Standard Model of particle physics describes all of the elementary particles and their interactions [1,2]. Although there are indications that the SM is not the complete description of particle physics in our universe, many theorists believe that it is most likely a subset of a larger, broader theory, rather than being wrong altogether [3].

The SM is a relativistic quantum field theory [4] in which there are 12 spin-1/2 fermions found in three generations, illustrated in Table 1.1. The fermions are grouped as *quarks* and *leptons*. Each of these fermions are fundamental matter particles and they possess a corresponding antifermion, an antimatter particle. For electrically charged fermions, their corresponding antifermions are of opposite charge. In the SM, these quarks and leptons may interact via three forces: the electromagnetic force, the strong force and the weak force. These forces are mediated by a series of fundamental bosons that are illustrated in Table 1.2. The charged leptons interact via the electromagnetic interaction and the weak interactions, while the neutrinos only interact via the weak interaction. Quarks, however, can couple to all three of the forces.

Table 1.1: Standard Model quarks and leptons.

	Flavour	Charge (units of e)
Quarks	*First Generation:*	
	up (u)	+2/3
	down (d)	-1/3
	Second Generation:	
	charm (c)	+2/3
	strange (s)	-1/3
	Third Generation:	
	top (t)	+2/3
	bottom (b)	-1/3
Leptons	*First Generation:*	
	electron (e)	-1
	electron neutrino (ν_e)	0
	Second Generation:	
	muon (μ)	-1
	muon neutrino (ν_μ)	0
	Third Generation:	
	tau (τ)	-1
	tau neutrino (ν_τ)	0

Table 1.2: Standard Model force carriers.

Name	Force	Charge (units of e)
photon (γ)	Electromagnetic	0
Z^0	Weak	0
$W^\pm$	Weak	±1
gluon (g)	Strong	0

In nature, due to the phenomenon of colour confinement, bare quarks are not observed [5]. Instead, they are always found in bound subatomic objects known as *hadrons*; traditionally, a hadron is a composite particle made up of two or three quarks[1] (known as *mesons* and *baryons*, respectively). Hadrons have varying lifetimes, at the end of which they may decay into combinations of lighter particles. In this thesis, we are primarily concerned with B^+ and B^- hadrons, mesons composed of $u\bar{b}$ and $\bar{u}b$ quark pairings, respectively.

The concept of symmetry plays an important role in the SM and in physics in general. In order for the laws of physics to make reliable predictions about nature, these laws must be invariant (or symmetric) under certain transformations. In the formalism of group theory, the symmetry of the SM is expressed as [3]

$$\mathrm{SU}(3)_C \times \mathrm{SU}(2)_L \times \mathrm{U}(1)_Y.$$

In this expression, the first term represents the strong interaction while the second and third terms relate to the unified electromagnetic and weak forces (the *electroweak* interaction). The C is representative of the colour charge, the L represents left-handed particles and the Y is the weak hypercharge. At low energies, the symmetry of the electroweak portion is spontaneously broken by the Higgs mechanism [9, 10], giving rise to the masses of the $W^\pm$ and Z bosons while the photon remains massless. The Higgs mechanism predicts a scalar field, the *Higgs field*, the quantum of which is the *Higgs boson*. The interaction of the SM fermions with this Higgs field leads to their acquisition of mass without breaking gauge invariance and ultimately, the phenomenon of quark flavour mixing. This latter phenomenon is important to the decay of $B^\pm$ hadrons.

In particle physics, a major concept is that of the violation of theorised symmetries. The product of two particular symmetries, *charge* (C) and *parity* (P), known as CP symmetry, was once thought to be a fundamental symmetry of the universe [1]. However, it is now known that CP symmetry can be violated and, in fact, the decays of B hadrons, according to the SM, are particularly sensitive to this phenomenon.

One of the big unanswered questions in modern physics is that of the matter-antimatter asymmetry. It is still unknown why our universe possesses an overwhelming abundance of

---

[1] In recent years, experimental evidence has been obtained of bound states with more than three quarks. In 2007, the Belle Collaboration reported observation of a tetraquark state [6] that was later confirmed and characterised by LHCb [7]. In 2015, LHCb reported the first observation of a pentaquark state [8].

matter over antimatter. In the SM, *CP* violation can lead to processes that ultimately yield an imbalance between matter and antimatter, however none of the observed processes is sufficient in explaining the imbalance present in the universe. Thus, further study of *CP* violating processes is essential as it may yield some important insight into unravelling the matter-antimatter asymmetry mystery.

1.2 C and P Transformations

The physics conservation laws (such as conservation of energy, angular momentum and charge), which are fundamental to our understanding of nature, are all related to symmetries. In the SM, there are two discrete transformations that are of particular interest to this thesis: charge conjugation, C and parity, P [3]. We define the operators of these transformations, $\mathcal{C}$ and $\mathcal{P}$, respectively, using the framework of a relativistic quantum field theory:

- **Charge Conjugation ($\mathcal{C}$)**

  Transforms the sign of all additive quantum numbers to the opposite sign while leaving all other particle properties intact.

- **Parity ($\mathcal{P}$)**

  Under the parity operator, spatial axes are reversed, *i.e.*, $(t, \vec{x}) \rightarrow (t, -\vec{x})$. Therefore, momenta have their directions inverted but spins remain unchanged.

It must be noted that neither of these transformations are actual symmetries of the SM. Individually, C and P symmetries can be violated and indeed, such violations have been experimentally observed [3]. For example, under the $\mathcal{C}$ operator, after transformation, the resulting particle should retain the same spin as the original. So, if C symmetry were to hold, a left-handed neutrino under $\mathcal{C}$ transformation would become a left-handed antineutrino. However, experimentally, there is no evidence for the existence of left-handed antineutrinos [2], thus neutrinos must violate C symmetry. Similarly, P symmetry was famously found to be violated in weak interactions in 1957 [11].

Historically, it was thought that the simultaneous application of the C and P transformations, a *CP* symmetry, was an exact symmetry of nature. However, experimentally, *CP* violation was first found in the neutral kaon system in 1964 [12] and has since been unambiguously observed in several mesonic systems including the neutral B^0 [13] and B_s^0 [14], as well as the charged $B^\pm$ [15] sectors.

1.3 *CP* Violation in Meson Decay

There are three major mechanisms through which *CP* violation in mesons may manifest itself:

- *CP* violation in neutral meson mixing;
- *CP* violation in meson decay;
- *CP* violation in the interference between decay and mixing.

In this thesis, we are primarily interested in the phenomenon of *CP* violation in meson decay, and thus this section shall describe this mechanism in greater detail. Throughout this section, the term *meson* is used (as this thesis mainly discusses *CP* violation in mesonic systems), but the description and arguments apply equally to baryons.

Let us start by defining a generic meson M (with corresponding antiparticle $\overline{M}$), which can be charged or neutral, that decays into a final state f (with *CP* conjugate state of $\overline{f}$). Let us further define A_f as the amplitude of the decay $M \to f$. Depending on what our initial and final states are, we may define a set of amplitudes

$$A_f = \langle f|\,\mathcal{H}\,|M\rangle\,, \quad \overline{A}_f = \langle f|\,\mathcal{H}\,|\overline{M}\rangle\,, \tag{1.1}$$

$$A_{\overline{f}} = \langle \overline{f}|\,\mathcal{H}\,|M\rangle\,, \quad \overline{A}_{\overline{f}} = \langle \overline{f}|\,\mathcal{H}\,|\overline{M}\rangle\,, \tag{1.2}$$

where $\mathcal{H}$ is the Hamiltonian of the time-dependent Schrodinger equation. *CP* violation in meson decay occurs when the rate of $M \to f$ differs from that of its *CP* conjugate process $\overline{M} \to \overline{f}$, expressly when $|A_f| \neq |\overline{A}_{\overline{f}}|$. This mechanism is known as *direct CP violation.*

For the decay $M \to f$, the amplitude A_f is formed from the different distinct decay paths that the process may take. If we say that the amplitude for one such path is A_i, the total amplitude A_f is given by

$$A_f = \sum_{i}^{n} A_i. \tag{1.3}$$

For each of these component amplitudes, there may be two additional phase components: a *CP*-violating (weak) phase, ϕ_i, and a *CP*-conserving (strong) phase, δ_i. If we incorporate these phases into Equation 1.3, we obtain:

$$A_f = \sum_{i}^{n} |A_i| e^{i(\delta_i + \phi_i)}. \tag{1.4}$$

Similarly, the expression for $\overline{A}_{\overline{f}}$ is given by

$$\overline{A}_{\overline{f}} = \sum_{i}^{n} |A_i| e^{i(\delta_i - \phi_i)}, \tag{1.5}$$

the chief difference being the sign of the *CP* violating phase component. Combining Equations 1.4 and 1.5, we see that

$$|A_f|^2 - |\overline{A}_{\overline{f}}|^2 = -2 \sum_{i,j} A_i A_j \sin\left(\phi_i - \phi_j\right) \sin\left(\delta_i - \delta_j\right). \tag{1.6}$$

Given that *CP* violation occurs when $|A_f| \neq |\overline{A}_{\overline{f}}|$, *CP* violation also implies a non-zero weak phase difference and a non-zero strong phase difference. *CP* violation in meson decay requires two different decay pathways from the final to initial states; the interference between these decays is the manifestation of *CP* violation and may lead to measurable particle/antiparticle asymmetries.

Direct *CP* violation can occur for both charged and neutral hadrons. It is the type of *CP* violation responsible for the various charge asymmetries and *CP* observables reported in this thesis.

1.4 *CP* Violation in the Standard Model

Although *CP* violation's experimental discovery in 1964 [12] may have been surprising to the physics community, it is now well-established as part of the Standard Model. Quark flavour mixing in the weak interactions, originated by Cabibbo in 1963 [16] and expanded to three generations of quarks by Kobayashi and Maskawa in 1973 [17], is the origin of *CP* violation in the SM. These flavour-changing weak decays are described by a quark mixing matrix and this matrix incorporates *CP* violation through the presence of a complex phase factor. Let us explore more formally this mixing matrix and the parameterisation of *CP* violation in the SM.

1.4.1 Flavour Mixing and the CKM Matrix

The SM, as a quantum field theory, can be described using the formalism of a Lagrangian density [3]. For the quark fields in the SM, under the simplifying assumption that only the first generation of quarks is present, their Lagrangian mass terms are given by [4]

$$\mathcal{L}_q = -\lambda_d \overline{Q}_L \cdot \phi d_R - \lambda_u \epsilon^{ab} \overline{Q}_{La} \phi_b^\dagger u_R + \text{h.c.} \tag{1.7}$$

where λ_d and λ_u are the Yukawa couplings, ϕ is the Higgs field [9], ϵ^{ab} is the 2×2 antisymmetric tensor, Q_L are left-handed $SU_L(2)$ quark doublets, and d_R and u_R are right-handed quark singlets for down quarks and up quarks, respectively. If we make the substitution that ϕ acquires a vacuum expectation value of the form

$$\langle\phi\rangle = \frac{1}{\sqrt{2}} \begin{pmatrix} 0 \\ v \end{pmatrix}, \tag{1.8}$$

our expression now becomes

$$\mathcal{L}_q = -\frac{1}{\sqrt{2}} \lambda_d v \overline{d}_L d_R - \frac{1}{\sqrt{2}} \lambda_u v \overline{u}_L u_R + \text{h.c.} + \dots\ , \tag{1.9}$$

which are standard mass terms for down and up quarks. From this expression, we can further isolate the masses

$$m_d = \frac{1}{\sqrt{2}} \lambda_d v, \quad m_u = \frac{1}{\sqrt{2}} \lambda_u v. \tag{1.10}$$

When additional quark generations are introduced, the Yukawa couplings, λ, are 3×3 matrices. In a purely general form, these are non-diagonal matrices, meaning that there is possible mixing between quark flavours.

Rather than work in this flavour basis, we can make a transformation to a basis that diagonalises the Higgs couplings. This is a sensible approach, for this basis is a physical one that diagonalises the mass matrix [4]. Let us now include all three generations of quarks and define

$$u_L^i = (u_L, c_L, t_L)\,, \quad d_L^i = (d_L, s_L, b_L) \tag{1.11}$$

as the up and down-type quarks, respectively, in the flavour basis and $u_L'^i$ and $d_L'^i$ as the family of quarks in the new basis. The two bases are related by the unitary transformations

$$u_L^i = U_u^{ij} u_L'^j \text{ and } d_L^i = U_d^{ij} d_L'^j. \tag{1.12}$$

In this new basis, the W boson current (weak current) can be written as

$$J_W^{\mu+} = \frac{1}{\sqrt{2}} \overline{u}_L^i \gamma^\mu d_L^i = \frac{1}{\sqrt{2}} \overline{u}_L'^i \gamma^\mu \left(U_u^\dagger U_d\right)_{ij} d_L'^i \tag{1.13}$$

where γ^μ are the Dirac matrices. As a further simplification, we may write

$$J_W^{\mu+} = \frac{1}{\sqrt{2}} \overline{u}_L'^i \gamma^\mu V_{ij} d_L'^j \tag{1.14}$$

where V_{ij} is defined as

$$V_{CKM} \equiv V_{ij} = U_u^\dagger U_d = \begin{pmatrix} V_{ud} & V_{us} & V_{ub} \\ V_{cd} & V_{cs} & V_{cb} \\ V_{td} & V_{ts} & V_{tb} \end{pmatrix}. \tag{1.15}$$

This matrix is known as the Cabibbo-Kobayashi-Maskawa (CKM) matrix and is used to describe quark mixing. Since U_u and U_d are unitary matrices, by construction, the CKM matrix is also unitary. Each element, V_{ij}, specifies the coupling of a quark of flavour i to a quark of flavour j. For example, V_{tb} represents the coupling of a bottom quark to a top quark in the weak decay of $t \to b + W^+$. One can consider that the square modulus of each element of the CKM matrix, $|V_{ij}|^2$, represents the probability of a quark decaying from one flavour to another, as specified by the lower indices. A V_{ij} value closer to unity indicates a highly probable decay, while a value approaching zero indicates a rarer decay process.

Experimentally, the diagonal elements of V_{CKM} are found to have values that are approximately equal to one, while the off-diagonal elements have values closer to zero [2]. Thus, decays involving a coupling along the diagonal of the matrix are said to be *Cabibbo favoured* while those involving off-diagonal elements are termed *Cabibbo suppressed.*

1.4.1.1 Parameterisations of the CKM Matrix

Although a number of different parameterisations of the CKM Matrix are possible, a standard choice is the so-called Chau-Keung parameterisation [18]. In this form, V_{CKM} is described exactly through the use of three Euler angles $(\theta_{12}, \theta_{23}, \theta_{13})$ and a complex phase δ. This phase is responsible for all *CP*-violating phenomena in quark flavour-changing processes in the SM [2]. Explicitly, in the Chau-Keung parameterisation, the elements of the CKM matrix are:

$$V_{CKM} = \begin{pmatrix} c_{12}c_{13} & s_{12}c_{13} & s_{13}e^{-i\delta} \\ -s_{12}c_{23} - c_{12}s_{23}s_{13}e^{i\delta} & c_{12}c_{23} - s_{12}s_{23}s_{13}e^{i\delta} & s_{23}c_{13} \\ s_{12}s_{23} - c_{12}c_{23}s_{13}e^{i\delta} & -c_{12}s_{23} - s_{12}c_{23}s_{13}e^{i\delta} & c_{23}c_{13} \end{pmatrix}, \tag{1.16}$$

where $c_{ij} = \cos\theta_{ij}$ and $s_{ij} = \sin\theta_{ij}$.

A useful alternative parameterisation is the Wolfenstein parameterisation [19]. Experimentally, it is known that $s_{13} \ll s_{23} \ll s_{12} \ll 1$ and that the diagonal elements of the matrix have values approximate to unity while the off-diagonal elements have values approaching zero. Taking these factors into consideration, it is convenient to use a parameterisation where all of the elements are expressed as an expansion of the power series of the parameter $\lambda = s_{12}$. If we make the following substitutions (approximate experimental values provided as a reference [2]),

$$s_{12} = \frac{|V_{us}|}{\sqrt{|V_{ud}|^2 + |V_{us}|^2}} = \lambda \approx 0.225, \tag{1.17}$$

$$s_{23} = A\lambda^2 = \lambda \left|\frac{V_{cb}}{V_{us}}\right| \approx 0.0412, \tag{1.18}$$

$$\left|s_{13}e^{-i\delta}\right| = |V_{ub}| = A\lambda^3 \left|\rho - i\eta\right| \approx 0.0036, \tag{1.19}$$

we obtain a matrix of the form:

$$V_{CKM} = \begin{pmatrix} 1-\lambda^2/2 & \lambda & A\lambda^3(\rho - i\eta) \\ -\lambda & 1-\lambda^2/2 & A\lambda^2 \\ A\lambda^3(1-\rho-i\eta) & -A\lambda^2 & 1 \end{pmatrix} + \mathcal{O}(\lambda^4). \tag{1.20}$$

In this parameterisation, λ, A, ρ and η are all real numbers and the CKM matrix is unitary to all orders of λ. Furthermore, it is particularly convenient to use the Wolfenstein parameterisation as every element of V_{CKM} can be estimated via its leading term in λ.

1.4.2 Unitarity Triangles and the Angle γ

Since the CKM matrix is unitary,

$$V^{\dagger}_{CKM}V_{CKM} = V_{CKM}V^{\dagger}_{CKM} = I. \tag{1.21}$$

This further implies the following restrictions on the elements of the matrix

$$\sum_j V^*_{ji}V_{jk} = \sum_j V_{ij}V^*_{kj} = \delta_{ik}. \tag{1.22}$$

Consequently, we have a total of 9 independent equations; three in which the right-hand side is unity and six in which it is zero. The equations pertaining to the non-diagonal elements of δ_{ik} are:

$$V_{cd}V_{ud}^{*} + V_{cs}V_{us}^{*} + V_{cb}V_{ub}^{*} = 0 \tag{1.23}$$

$$V_{cd}V_{td}^{*} + V_{cs}V_{ts}^{*} + V_{cb}V_{tb}^{*} = 0 \tag{1.24}$$

$$V_{ud}V_{td}^{*} + V_{us}V_{ts}^{*} + V_{ub}V_{tb}^{*} = 0 \tag{1.25}$$

$$V_{us}^{*}V_{ud} + V_{cs}^{*}V_{cd} + V_{ts}^{*}V_{td} = 0 \tag{1.26}$$

$$V_{ub}^{*}V_{us} + V_{cb}^{*}V_{cs} + V_{tb}^{*}V_{ts} = 0 \tag{1.27}$$

$$V_{ub}^{*}V_{ud} + V_{cb}^{*}V_{cd} + V_{tb}^{*}V_{td} = 0. \tag{1.28}$$

These six relationships can each be represented geometrically as triangles in the complex plane, where one of the terms of the equation is chosen as the length of the base of the triangle (normalised to unity) and the other two sides have lengths representative of the ratio of another term versus the base term. For example, Equation 1.28 can be drawn as the triangle seen in Figure 1.1; similar triangles can be drawn for the other five equations. Such triangles are known as *unitarity triangles*, though the most commonly studied one is presented in Figure 1.1. This triangle is the most interesting to probe experimentally because all of the terms of Equation 1.28 are of the same order ($\mathcal{O}(\lambda^3)$) and thus all of the sides of the triangle have lengths of the same order[2].

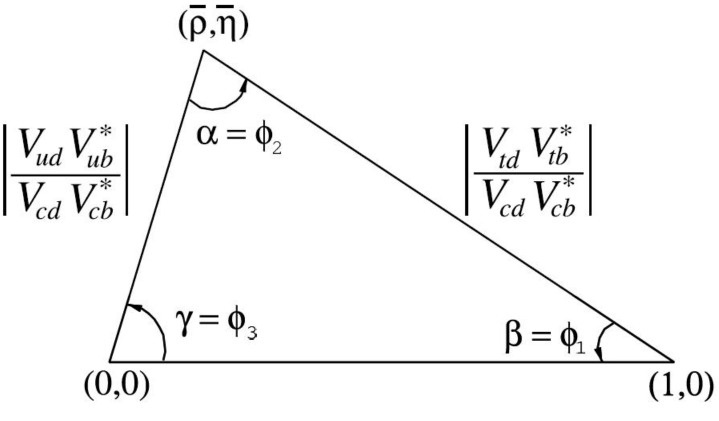

Figure 1.1: One of the six possible CKM triangles. Each of the equations with a right-hand side that equals 0 from expression 1.22 can be drawn as a similar unitarity triangle [2].

---

[2] All of the terms of Equation 1.25 are also of order $\mathcal{O}(\lambda^3)$ and thus could also be used for the construction of an experimentally interesting triangle. However, by convention, the triangle depicted in Figure 1.1 is the one commonly studied.

The unitarity triangle describes the relationship between different elements of the CKM matrix, and these elements include *CP*-violating phases. As such, in the limit that there is no *CP* violation, all six unitarity triangles are simply straight lines on the real axis. Therefore, the area of the triangles is a measure of the *CP* violation as described by the SM.

The triangle depicted in Figure 1.1 is generally referred to as *The Unitarity Triangle* (UT). In this shape, the sides have been normalised such that $V_{cd}V_{cb}^*$ is a real number and $|V_{cd}V_{cb}^*| = 1$. This quantity is taken as the base of the triangle on the real axis. Hence, by construction, the UT has vertices at $(0,0)$ and $(1,0)$ with an apex at $(\bar{\rho},\bar{\eta})$ where

$$\bar{\rho} = \rho\left(1 - \frac{\lambda^2}{2}\right), \qquad \bar{\eta} = \eta\left(1 - \frac{\lambda^2}{2}\right). \tag{1.29}$$

The internal angles of the triangle, α, β and γ (also known as ϕ_2, ϕ_1 and ϕ_3, respectively) are defined as

$$\alpha = \phi_2 \equiv \arg\left(-\frac{V_{td}V_{tb}^*}{V_{ud}V_{ub}^*}\right), \qquad \beta = \phi_1 \equiv \arg\left(-\frac{V_{cd}V_{cb}^*}{V_{td}V_{tb}^*}\right), \tag{1.30}$$

$$\gamma = \phi_3 \equiv \arg\left(-\frac{V_{ud}V_{ub}^*}{V_{cd}V_{cb}^*}\right). \tag{1.31}$$

Each of the angles in the UT can be measured either via ‘direct’ methods where a physical observable can be expressed in relation to the angle or via ‘indirect’ methods where a physical observable relates to other angles or sides of the triangle and can be used to infer the value of the angle of interest. For example, measuring α and β and invoking that the sum of angles in a triangle is 180°, would constitute an indirect measurement of γ. The UT, with the measurement uncertainties on its angles, is graphically presented in Figure 1.2. We note immediately that the angle with the largest uncertainty is γ. A summary of the measurement of the CKM triangle angles is provided in Table 1.3.

Table 1.3: Direct and indirect measurements of the UT angles [21].

Parameter	Direct Measurements	Indirect Measurements
$\alpha[^\circ]$	$87.7^{+3.5}_{-3.3}$	$91.5^{+4.2}_{-1.3}$
$\beta[^\circ]$	$21.50^{+0.75}_{-0.74}$	$25.22^{+0.78}_{-1.79}$
$\gamma[^\circ]$	$73.2^{+6.3}_{-7.0}$	$66.9^{+1.0}_{-3.7}$

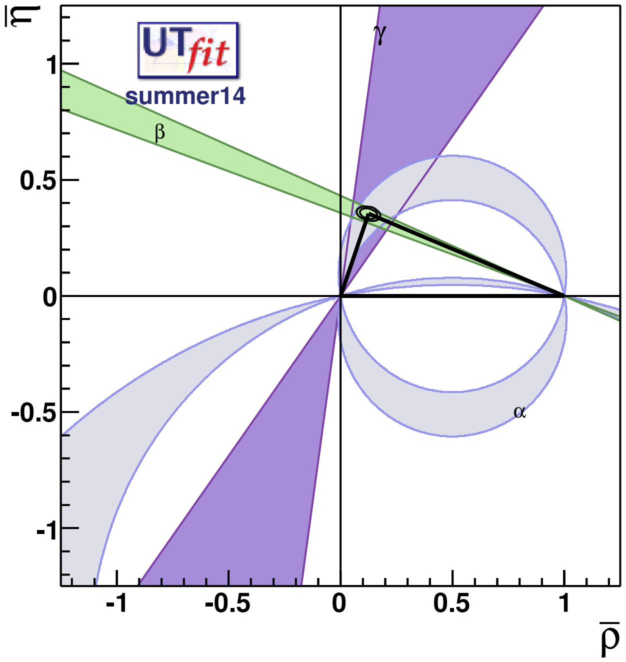

Figure 1.2: The CKM triangle, with the bands in grey, green and purple representing the uncertainties on the angles α, β and γ, respectively. The uncertainties are obtained from a fit performed to combined experimental results from direct measurements [20].

Up to $\mathcal{O}(\lambda^3)$ in the Wolfenstein parameterisation, the only elements in the CKM matrix with complex phases are V_{ub} and V_{td}. If we divide each element of the matrix by its modulus, we get

$$\begin{pmatrix} 1 & 1 & e^{-i\gamma} \\ 1 & 1 & 1 \\ e^{-i\beta} & 1 & 1 \end{pmatrix}. \tag{1.32}$$

This result relates the complex phases of the CKM matrix to the angles of the UT.

1.4.2.1 Motivation for a Precision Measurement of γ

Since γ is effectively the weak phase of V_{ub}, this implies that it can be measured in tree-level processes. In fact, γ is the only angle of the UT that can be measured at tree level and thus constitutes an SM benchmark. While loop-level processes may have sensitivity to New Physics (NP) beyond the SM, tree-level processes are expected to be unaltered by these NP contributions. Indirect measurements of γ, generally obtained by measuring other parameters of the UT, have loop-level contributions. Consequently, a comparison between direct and indirect γ measurements, and the observation of any differences, should be a powerful probe for NP. However, in order for such comparisons to be meaningful, the uncertainty on direct, tree-level measurements must be reduced. Currently, of the three CKM angles, with respect to direct measurements, γ has the largest uncertainties. Direct measurements of γ have approximately 7° of uncertainty compared to 4° from indirect methods.

1.5 Tree Level Determination of γ Using $B^{\mp} \to DK^{\mp}$ Decays

At tree level, γ can be measured through the study of decays of the form $B^{\mp} \to DK^{\mp}$ (here and henceforth D represents a D^0 or a $\overline{D}^0$ meson). Such measurements exploit the interference between $b \to c(\overline{u}s)$ and $b \to u(\overline{c}s)$ transitions. Figure 1.3 demonstrates the decay of $B^- \to D^0K^-$ and $B^- \to \overline{D}^0K^-$. The amplitudes of these two diagrams are different in magnitude given that the former is colour favoured and the latter is colour suppressed and due to different levels of CKM suppression as a result of the involved decay vertices.

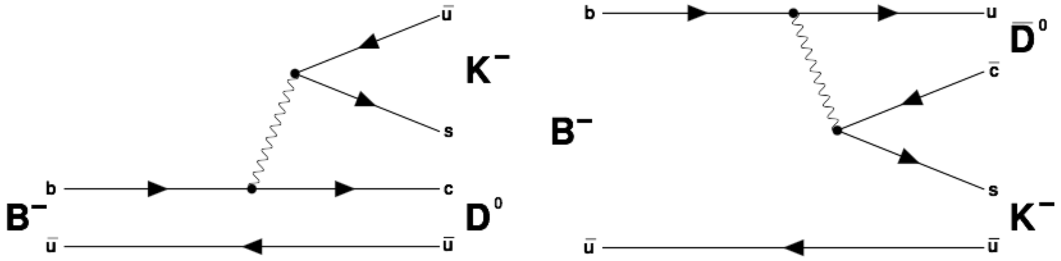

Figure 1.3: Feynman diagrams for $B^- \to D^0K^-$ and $B^- \to \overline{D}^0K^-$. The former is colour favoured while the latter is colour suppressed [22].

Of particular interest, the colour-suppressed decay involves the vertex V_{ub}, which is sensitive to γ and by extension, *CP* violation. When the $B^- \to D^0K^-$ and $B^- \to \overline{D}^0K^-$ decays have a D^0 and $\overline{D}^0$ that decay to a common final state f_D, interference occurs. We can express the ratio of the amplitudes of such decays (and their charge conjugates) in Equation 1.33, where we have normalised according to the favoured modes:

$$\frac{A(B^- \to \overline{D}^0K^-)}{A(B^- \to D^0K^-)} = r_B e^{i(\delta_B - \gamma)}, \qquad \frac{A(B^+ \to D^0K^+)}{A(B^+ \to \overline{D}^0K^+)} = r_B e^{i(\delta_B + \gamma)}. \tag{1.33}$$

These equations are functions of three parameters: γ, δ_B and r_B. The angle γ is a *CP*-violating weak phase angle from the CKM triangle, δ_B is the *CP*-conserving strong phase difference and r_B is the absolute ratio of the amplitudes. Alternatively, if we define the amplitude of the colour favoured decay as A_{fav} and that of the colour suppressed decay as A_{sup},

$$r_B = \left|\frac{A_{\text{sup}}}{A_{\text{fav}}}\right| \propto \left|\frac{\epsilon_{\text{colour}} V_{cs} V_{ub}^*}{V_{us} V_{cb}^*}\right|, \tag{1.34}$$

where V_{ij} are CKM matrix elements and ϵ_{colour} is a naive colour suppression factor.

In this argument, we neglect *CP* violation in the D system, which is compatible with existing measurements [23]. For simplicity, we also neglect D^0–$\overline{D}^0$ mixing, although this may be included, as explained in Reference [24]. Using these simplifying assumptions, we may write the ratio of the amplitudes of the complete decay chain $B^- \to [f_D]_D K^-$ to the favoured amplitude as

$$\frac{A(B^- \to [f_D]_D K^-)}{A(B^- \to D^0 K^-)} = A_D + r_B e^{i(\delta_B - \gamma)} \bar{A}_D, \tag{1.35}$$

where A_D and $\bar{A}_D$ represent the D^0 and $\overline{D}^0$ decay amplitudes, respectively. The normalisation to the favoured decay modes leads to the right hand side terms of Equation 1.35 being either factors of A_D or $\bar{A}_D$. As a result, the first term represents contributions from the colour favoured decay, whereas the second term represents contributions from the colour suppressed decay. Similarly, we may write for the complete B^+ decay chain,

$$\frac{A(B^+ \to [f_D]_D K^+)}{A(B^+ \to \overline{D}^0 K^+)} = \bar{A}_D + r_B e^{i(\delta_B + \gamma)} A_D. \tag{1.36}$$

Since equations 1.35 and 1.36 are different, we expect directly observable *CP* violation in the $B^\mp \to DK^\mp$ system. However, given that r_B is a small number due to colour suppression ($r_B \approx 0.1$ [25]), the overall effects of the interference are expected to be small. In addition, $B^\mp \to D\pi^\mp$ decays also exhibit sensitivity to γ. The same arguments as those stated for $B^\mp \to DK^\mp$ apply, however the r_B and δ_B parameters are replaced by r_B^π and δ_B^π, respectively, where the superscript designates the bachelor particle in the $B^\mp$ decay is not a kaon. However, since r_B^π is expected to be very small ($r_B^\pi \approx 0.01$ [23]), the interference effects will be small compared to $B^\mp \to DK^\mp$ decays and thus sensitivity to γ is much reduced.

1.5.1 GLW and ADS Methods

The original proposition to measure γ using $B^\mp \to DK^\mp$ decays was made by Gronau, London and Wyler (GLW) [26, 27] in the early 1990s. At the most basic level, the strategy involves a simple counting and comparison exercise between different charged decay modes. The GLW method consists of studying $B^\mp \to DK^\mp$ decays where f_D is a *CP* eigenstate such as $D \to K^+K^-$ or $D \to \pi^+\pi^-$. Alternatively, Atwood, Dunietz and Soni (ADS) proposed the study of $B^\mp \to DK^\mp$ systems where the D decay mode f_D is a non self-conjugate final state such as $D \to K^+\pi^-$ [28, 29]. A graphical representation of these two classes of decays is presented in Figure 1.4 [30].

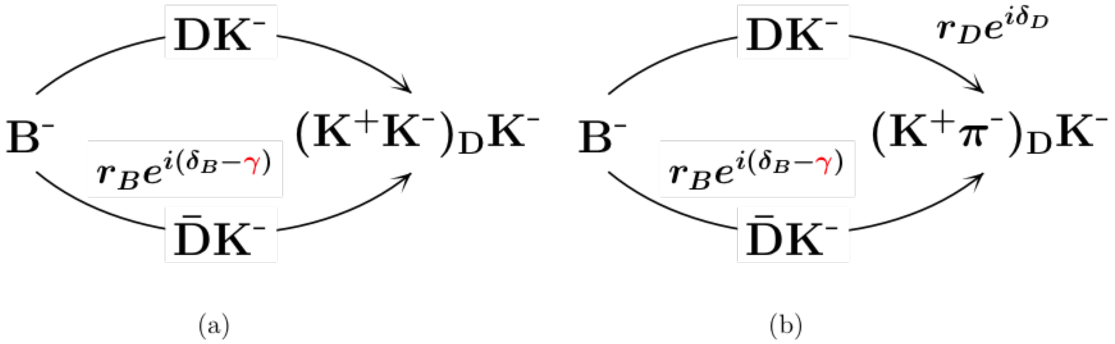

(a) (b)

Figure 1.4: The interfering decay paths of $B^- \to DK^-$ and $B^- \to \overline{D}K^-$. In (a), the GLW method is presented. The f_D *CP* eigenstate is equally accessible from D^0 or $\overline{D}^0$ decays. In (b), the ADS method is presented. Here, f_D is a non self-conjugate final state and the D^0 decay has an additional suppression factor relative to the $\overline{D}^0$ decay [30].

Because the D final states in GLW decays are *CP* eigenstates, which we can label as f_{GLW}, Equations 1.35 and 1.36 can be factorised such that

$$A(B^- \to [f_{\text{GLW}}]_D K^-) \;\propto\; 1 + r_B e^{i(\delta_B - \gamma)} \tag{1.37}$$

$$A(B^+ \to [f_{\text{GLW}}]_D K^+) \;\propto\; r_B e^{i(\delta_B + \gamma)} + 1. \tag{1.38}$$

Equtions 1.37 and 1.38 assume that there is no CP violation in the D decays. Furthermore, these expressions also assume that $A(B^- \to D^0 K^-)$ and $A(B^+ \to \overline{D}^0 K^+)$, the denominators of Equations 1.35 and 1.36, are equal. Under these assumptions, the GLW partial widths can be expressed as

$$\Gamma(B^- \to [f_{\mathrm{GLW}}]_D K^-) \propto \left|A(B^- \to [f_{\mathrm{GLW}}]_D K^-)\right|^2 \propto 1 + (r_B)^2 + 2r_B \cos(\delta_B - \gamma) \tag{1.39}$$

$$\Gamma(B^+ \to [f_{\mathrm{GLW}}]_D K^+) \propto \left|A(B^+ \to [f_{\mathrm{GLW}}]_D K^+)\right|^2 \propto 1 + (r_B)^2 + 2r_B \cos(\delta_B + \gamma). \tag{1.40}$$

There are also D final states, such as $D \to K^+K^-\pi^0$ and $D \to \pi^+\pi^-\pi^0$, where the D decays to a self-conjugate final state of three or more hadrons, that approximate *CP* eigenstates [31]. Due to the presence of resonances in the multi-body decay space, these decay modes are not true *CP* eigenstates, but rather diluted versions (with reduced γ sensitivity). This dilution can be parameterised by the factor F_+ [31], the *CP*-even fraction, ranging from 0 to 1, a measure of how *CP*-even the system is. We may refer to such approximate *CP* eigenstate decay modes as quasi-GLW (qGLW). For D final states f_{qGLW}, Equations 1.39 and 1.40 become

$$\Gamma(B^- \to [f_{\mathrm{qGLW}}]_D K^-) \quad \propto \quad 1 + (r_B)^2 + 2\left(2F_+^{\mathrm{qGLW}} - 1\right) r_B \cos(\delta_B - \gamma) \tag{1.41}$$

$$\Gamma(B^+ \to [f_{\mathrm{qGLW}}]_D K^+) \quad \propto \quad 1 + (r_B)^2 + 2\left(2F_+^{\mathrm{qGLW}} - 1\right) r_B \cos(\delta_B + \gamma). \tag{1.42}$$

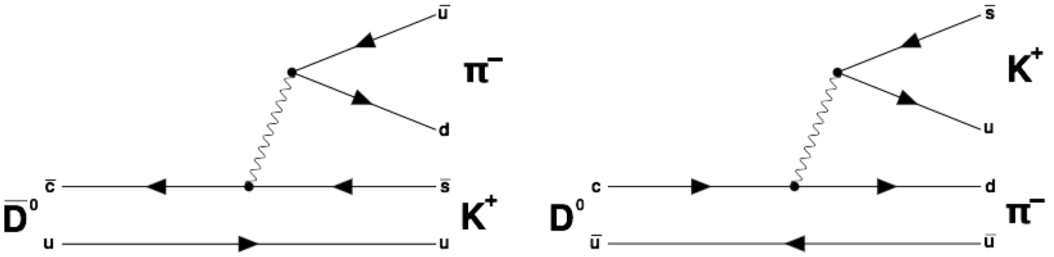

Figure 1.5: Feynman diagrams for $\overline{D}^0 \to K^+\pi^-$ and $D^0 \to K^+\pi^-$. While the $\overline{D}^0$ decay is Cabibbo favoured, the D^0 decay is doubly Cabibbo suppressed [22].

In the case of the ADS decays, although the D^0 and $\overline{D}^0$ decay to the same final states, they proceed via two very different amplitudes. As seen in Figure 1.5, for the example where $D \to K^+\pi^-$, the $\overline{D}^0$ decay is Cabibbo favoured (CF), while the D^0 decay is doubly Cabibbo suppressed (DCS) due to the presence of both V_{cd} and V_{us} vertices. We can express the ratio of the amplitudes of the D decays for a final state $K^+\pi^-$, normalised to the amplitude of the favoured decay, as

$$\frac{A(D^0 \to K^+\pi^-)}{A(\overline{D}^0 \to K^+\pi^-)} = r_D^{K\pi} e^{-i\delta_D^{K\pi}}, \tag{1.43}$$

where r_D is the magnitude of the D amplitude ratio and δ_D is the strong phase, both of which are dependent on the particular D final state ($K^\pm\pi^\mp$ in this example). We note that although $D^0 \to K^+\pi^-$ is a DCS decay, $D^0 \to K^-\pi^+$, the charge conjugate of the $\overline{D}^0$ decay in Figure 1.5, is CF. When examined in the larger context of $B^- \to DK^-$ decays, for ADS modes, cases where the kaon from the D decay is of opposite charge to the bachelor of the $B^\mp$ decay are suppressed, whereas decays where the kaon from the D has the same charge as the bachelor from the $B^\mp$ are favoured. The amplitudes of the various ADS $B^\mp$ decays in this example are thus:

$$\begin{aligned}
A(B^- \to [\pi^-K^+]_D K^-) &\propto r_D^{K\pi} e^{-i\delta_D^{K\pi}} + r_B e^{i(\delta_B-\gamma)} && (1.44)\\
A(B^+ \to [\pi^+K^-]_D K^+) &\propto r_D^{K\pi} e^{-i\delta_D^{K\pi}} + r_B e^{i(\delta_B+\gamma)} && (1.45)\\
A(B^- \to [K^-\pi^+]_D K^-) &\propto 1 + r_B r_D^{K\pi} e^{i(\delta_B-\gamma)} e^{-i\delta_D^{K\pi}} && (1.46)\\
A(B^+ \to [K^+\pi^-]_D K^+) &\propto 1 + r_B r_D^{K\pi} e^{i(\delta_B+\gamma)} e^{-i\delta_D^{K\pi}}. && (1.47)
\end{aligned}$$

Here, we have used the nomenclature where a leading pion in the D decay description of an ADS decay indicates a suppressed mode. The partial widths of the suppressed decays are:

$$\begin{aligned}
\Gamma(B^- \to [\pi^-K^+]_D K^-) &\propto (r_B)^2 + (r_D^{K\pi})^2 + 2r_B r_D^{K\pi}\cos(\delta_B + \delta_D^{K\pi} - \gamma) && (1.48)\\
\Gamma(B^+ \to [\pi^+K^-]_D K^+) &\propto (r_B)^2 + (r_D^{K\pi})^2 + 2r_B r_D^{K\pi}\cos(\delta_B + \delta_D^{K\pi} + \gamma) && (1.49)
\end{aligned}$$

and those of the favoured modes are:

$$\begin{aligned}
\Gamma(B^- \to [K^-\pi^+]_D K^-) &\propto 1 + (r_B r_D^{K\pi})^2 + 2r_B r_D^{K\pi}\cos(\delta_B - \delta_D^{K\pi} - \gamma) && (1.50)\\
\Gamma(B^+ \to [K^+\pi^-]_D K^+) &\propto 1 + (r_B r_D^{K\pi})^2 + 2r_B r_D^{K\pi}\cos(\delta_B - \delta_D^{K\pi} + \gamma). && (1.51)
\end{aligned}$$

In ADS decays, r_D, the ratio of DCS to CF amplitudes, is approximately 0.06 [23] and therefore of similar magnitude to r_B. Thus, in Equations 1.48 and 1.49, the interference term with γ is at leading order in the expression. This is in contrast to the GLW decays of Equations 1.39 and 1.40 where the interference term is of order $r_B r_D$, but the leading order of the equation is unity.

The ADS example provided was for a two-body D final state. However, for ADS decays where the D decays to three or more hadrons, such as $D \to K^\pm\pi^\mp\pi^0$, there are also the presence of resonances in the decay space. Similar to the quasi-GLW modes, these resonances have the net effect of diluting the sensitivity to γ. This dilution is represented by the coherence factor, κ_D, which ranges in value from 0 to 1. For a generic ADS decay with D final state f_{ADS}, the rate expressions are:

$$\Gamma(B^- \to [f_{\text{ADS sup}}]_D K^-) \propto (r_B)^2 + (r_D^{\text{ADS}})^2 + 2\kappa_D^{\text{ADS}} r_B r_D^{\text{ADS}} \cos(\delta_B + \delta_D^{\text{ADS}} - \gamma) \tag{1.52}$$

$$\Gamma(B^+ \to [f_{\text{ADS sup}}]_D K^+) \propto (r_B)^2 + (r_D^{\text{ADS}})^2 + 2\kappa_D^{\text{ADS}} r_B r_D^{\text{ADS}} \cos(\delta_B + \delta_D^{\text{ADS}} + \gamma) \tag{1.53}$$

$$\Gamma(B^- \to [f_{\text{ADS fav}}]_D K^-) \propto 1 + (r_B r_D^{\text{ADS}})^2 + 2\kappa_D^{\text{ADS}} r_B r_D^{\text{ADS}} \cos(\delta_B - \delta_D^{\text{ADS}} - \gamma) \tag{1.54}$$

$$\Gamma(B^+ \to [f_{\text{ADS fav}}]_D K^+) \propto 1 + (r_B r_D^{\text{ADS}})^2 + 2\kappa_D^{\text{ADS}} r_B r_D^{\text{ADS}} \cos(\delta_B - \delta_D^{\text{ADS}} + \gamma), \tag{1.55}$$

where δ_D^{ADS} is a mean strong-phase difference integrated over the phase space of the D decay.

1.5.2 Physical Observables

In this thesis, we are concerned with the $B^\mp \to DK^\mp$ and $B^\mp \to D\pi^\mp$ favoured and suppressed ADS decays where the D meson decays to $K^\pm\pi^\mp\pi^0$ (abbreviated as $K\pi\pi^0$). Furthermore, we are also interested in the $B^\mp \to DK^\mp$ and $B^\mp \to D\pi^\mp$ quasi-GLW decays where the D decays to $\pi^+\pi^-\pi^0$ and $K^+K^-\pi^0$ (abbreviated as $\pi\pi\pi^0$ and $KK\pi^0$, respectively). The variable h can be used to represent either a kaon or a pion, so we may write $B^\mp \to Dh^\mp$ to represent both $B^\mp \to DK^\mp$ and $B^\mp \to D\pi^\mp$. Explicitly, the decays of interest in this thesis are:

- The favoured ADS decays $B^\mp \to [K^\mp\pi^\pm\pi^0]_D K^\mp$ and $B^\mp \to [K^\mp\pi^\pm\pi^0]_D \pi^\mp$
- The suppressed ADS decays $B^\mp \to [\pi^\mp K^\pm\pi^0]_D K^\mp$ and $B^\mp \to [\pi^\mp K^\pm\pi^0]_D \pi^\mp$

- The quasi-GLW decays $B^{\mp} \to [\pi^+\pi^-\pi^0]_D K^{\mp}$ and $B^{\mp} \to [\pi^+\pi^-\pi^0]_D \pi^{\mp}$
- The quasi-GLW decays $B^{\mp} \to [K^+K^-\pi^0]_D K^{\mp}$ and $B^{\mp} \to [K^+K^-\pi^0]_D \pi^{\mp}$.

Collectively, in an abbreviated fashion, these decays may be referred to as $B^{\mp} \to [h'^{\pm}h''^{\mp}\pi^0]_D h^{\mp}$.

For the $B^{\mp} \to DK^{\mp}$ modes, the partial width expressions from Section 1.5.1 for the decays of interest are:

$$\Gamma(B^{\mp} \to [K^{\mp}\pi^{\pm}\pi^0]_D K^{\mp}) \propto 1 + (r_B r_D^{K\pi\pi^0})^2 + 2\kappa_D^{K\pi\pi^0} r_B r_D^{K\pi\pi^0} \cos(\delta_B - \delta_D^{K\pi\pi^0} \mp \gamma) \quad (1.56)$$

$$\Gamma(B^{\mp} \to [\pi^{\mp}K^{\pm}\pi^0]_D K^{\mp}) \propto (r_B)^2 + (r_D^{K\pi\pi^0})^2 + 2\kappa_D^{K\pi\pi^0} r_B r_D^{K\pi\pi^0} \cos(\delta_B + \delta_D^{K\pi\pi^0} \mp \gamma) \quad (1.57)$$

$$\Gamma(B^{\mp} \to [\pi^+\pi^-\pi^0]_D K^{\mp}) \propto 1 + (r_B)^2 + 2\left(2F_+^{\pi\pi\pi^0} - 1\right) r_B \cos(\delta_B \mp \gamma) \quad (1.58)$$

$$\Gamma(B^{\mp} \to [K^+K^-\pi^0]_D K^{\mp}) \propto 1 + (r_B)^2 + 2\left(2F_+^{KK\pi^0} - 1\right) r_B \cos(\delta_B \mp \gamma). \quad (1.59)$$

The expressions for the $B^{\mp} \to D\pi^{\mp}$ decays are identical, except r_B and δ_B are replaced by r_B^{π} and δ_B^{π}, respectively. These partial width expressions can be used to construct *CP*-related physical observables that are functions of r_B, δ_B and γ.

For the $K\pi\pi^0$ modes, an important quantity is the ratio between the suppressed and favoured decays. This observable, $R_{\mathrm{ADS}}^{K\pi\pi^0}$, is defined separately for the $B^{\mp} \to DK^{\mp}$ and $B^{\mp} \to D\pi^{\mp}$ decays:

$$R_{\mathrm{ADS}(K)}^{K\pi\pi^0} \equiv \frac{\Gamma(B^- \to [\pi^-K^+\pi^0]_D K^-) + \Gamma(B^+ \to [\pi^+K^-\pi^0]_D K^+)}{\Gamma(B^- \to [K^-\pi^+\pi^0]_D K^-) + \Gamma(B^+ \to [K^+\pi^-\pi^0]_D K^+)} \quad (1.60)$$

$$R_{\mathrm{ADS}(\pi)}^{K\pi\pi^0} \equiv \frac{\Gamma(B^- \to [\pi^-K^+\pi^0]_D \pi^-) + \Gamma(B^+ \to [\pi^+K^-\pi^0]_D \pi^+)}{\Gamma(B^- \to [K^-\pi^+\pi^0]_D \pi^-) + \Gamma(B^+ \to [K^+\pi^-\pi^0]_D \pi^+)}. \quad (1.61)$$

Both of these expressions have a dependence on γ as can be seen in the expressions below:

$$R_{\mathrm{ADS}(K)}^{K\pi\pi^0} = \frac{(r_B)^2 + (r_D^{K\pi\pi^0})^2 + 2\kappa_D^{K\pi\pi^0} r_B r_D^{K\pi\pi^0} \cos(\delta_B + \delta_D^{K\pi\pi^0}) \cos\gamma}{1 + (r_B r_D^{K\pi\pi^0})^2 + 2\kappa_D^{K\pi\pi^0} r_B r_D^{K\pi\pi^0} \cos(\delta_B - \delta_D^{K\pi\pi^0}) \cos\gamma}, \quad (1.62)$$

$$R_{\mathrm{ADS}(\pi)}^{K\pi\pi^0} = \frac{(r_B^{\pi})^2 + (r_D^{K\pi\pi^0})^2 + 2\kappa_D^{K\pi\pi^0} r_B^{\pi} r_D^{K\pi\pi^0} \cos(\delta_B^{\pi} + \delta_D^{K\pi\pi^0}) \cos\gamma}{1 + (r_B^{\pi} r_D^{K\pi\pi^0})^2 + 2\kappa_D^{K\pi\pi^0} r_B^{\pi} r_D^{K\pi\pi^0} \cos(\delta_B^{\pi} - \delta_D^{K\pi\pi^0}) \cos\gamma}. \quad (1.63)$$

Another observable of interest in the $K\pi\pi^0$ modes is $A_{\mathrm{ADS}}^{K\pi\pi^0}$, a measure of charge asymmetry that quantifies the amount of *CP* violation in the suppressed modes. For $B^{\mp} \to DK^{\mp}$

and $B^{\mp} \to D\pi^{\mp}$ decays, these observables are:

$$A^{K\pi\pi^0}_{\mathrm{ADS}(K)} \equiv \frac{\Gamma(B^- \to [\pi^- K^+ \pi^0]_D K^-) - \Gamma(B^+ \to [\pi^+ K^- \pi^0]_D K^+)}{\Gamma(B^- \to [\pi^- K^+ \pi^0]_D K^-) + \Gamma(B^+ \to [\pi^+ K^- \pi^0]_D K^+)} \tag{1.64}$$

$$A^{K\pi\pi^0}_{\mathrm{ADS}(\pi)} \equiv \frac{\Gamma(B^- \to [\pi^- K^+ \pi^0]_D \pi^-) - \Gamma(B^+ \to [\pi^+ K^- \pi^0]_D \pi^+)}{\Gamma(B^- \to [\pi^- K^+ \pi^0]_D \pi^-) + \Gamma(B^+ \to [\pi^+ K^- \pi^0]_D \pi^+)}. \tag{1.65}$$

Explicitly, the $A^{K\pi\pi^0}_{\mathrm{ADS}}$ dependence on γ can be expressed as

$$A^{K\pi\pi^0}_{\mathrm{ADS}(K)} = \frac{2\kappa_D^{K\pi\pi^0} r_B r_D^{K\pi\pi^0} \sin(\delta_B + \delta_D^{K\pi\pi^0}) \sin\gamma}{(r_B)^2 + (r_D^{K\pi\pi^0})^2 + 2\kappa_D^{K\pi\pi^0} r_B r_D^{K\pi\pi^0} \cos(\delta_B + \delta_D^{K\pi\pi^0}) \cos\gamma}, \tag{1.66}$$

$$A^{K\pi\pi^0}_{\mathrm{ADS}(\pi)} = \frac{2\kappa_D^{K\pi\pi^0} r_B^\pi r_D^{K\pi\pi^0} \sin(\delta_B^\pi + \delta_D^{K\pi\pi^0}) \sin\gamma}{(r_B^\pi)^2 + (r_D^{K\pi\pi^0})^2 + 2\kappa_D^{K\pi\pi^0} r_B^\pi r_D^{K\pi\pi^0} \cos(\delta_B^\pi + \delta_D^{K\pi\pi^0}) \cos\gamma}. \tag{1.67}$$

Since r_B and r_D are much smaller than 1, the denominators in Equations 1.62 and 1.63 can be approximated as unity. Under this approximation, we can write the $A^{K\pi\pi^0}_{\mathrm{ADS}}$ expressions as

$$A^{K\pi\pi^0}_{\mathrm{ADS}(K)} \approx \frac{2\kappa_D^{K\pi\pi^0} r_B r_D \sin(\delta_B + \delta_D) \sin\gamma}{R^{K\pi\pi^0}_{\mathrm{ADS}(K)}}, \tag{1.68}$$

$$A^{K\pi\pi^0}_{\mathrm{ADS}(\pi)} \approx \frac{2\kappa_D^{K\pi\pi^0} r_B^\pi r_D \sin(\delta_B^\pi + \delta_D) \sin\gamma}{R^{K\pi\pi^0}_{\mathrm{ADS}(\pi)}}. \tag{1.69}$$

Henceforth, it will be assumed that the terms A_{ADS} and R_{ADS} refer to the observables specific to the suppressed $K\pi\pi^0$ modes, unless explicitly stated otherwise.

For the favoured $B^{\mp} \to [K^{\mp}\pi^{\pm}\pi^0]_D K^{\mp}$ decay, a similar asymmetry is defined as

$$A^{K\pi\pi^0}_{K} \equiv \frac{\Gamma(B^- \to [K^- \pi^+ \pi^0]_D K^-) - \Gamma(B^+ \to [K^+ \pi^- \pi^0]_D K^+)}{\Gamma(B^- \to [K^- \pi^+ \pi^0]_D K^-) + \Gamma(B^+ \to [K^+ \pi^- \pi^0]_D K^+)}, \tag{1.70}$$

though this asymmetry is expected to be small. Furthermore, analogous asymmetries are also defined for the $B^{\mp} \to DK^{\mp}$ and $B^{\mp} \to D\pi^{\mp}$ quasi-GLW decays:

$$A^{KK\pi^0}_{\mathrm{qGLW}(K)} \equiv \frac{\Gamma(B^- \to [K^+ K^- \pi^0]_D K^-) - \Gamma(B^+ \to [K^+ K^- \pi^0]_D K^+)}{\Gamma(B^- \to [K^+ K^- \pi^0]_D K^-) + \Gamma(B^+ \to [K^+ K^- \pi^0]_D K^+)}, \tag{1.71}$$

$$A^{KK\pi^0}_{\mathrm{qGLW}(\pi)} \equiv \frac{\Gamma(B^- \to [K^+ K^- \pi^0]_D \pi^-) - \Gamma(B^+ \to [K^+ K^- \pi^0]_D \pi^+)}{\Gamma(B^- \to [K^+ K^- \pi^0]_D \pi^-) + \Gamma(B^+ \to [K^+ K^- \pi^0]_D \pi^+)}, \tag{1.72}$$

$$A^{\pi\pi\pi^0}_{\mathrm{qGLW}(K)} \equiv \frac{\Gamma(B^- \to [\pi^+\pi^-\pi^0]_D K^-) - \Gamma(B^+ \to [\pi^+\pi^-\pi^0]_D K^+)}{\Gamma(B^- \to [\pi^+\pi^-\pi^0]_D K^-) + \Gamma(B^+ \to [\pi^+\pi^-\pi^0]_D K^+)}, \tag{1.73}$$

$$A^{\pi\pi\pi^0}_{\mathrm{qGLW}(\pi)} \equiv \frac{\Gamma(B^- \to [\pi^+\pi^-\pi^0]_D \pi^-) - \Gamma(B^+ \to [\pi^+\pi^-\pi^0]_D \pi^+)}{\Gamma(B^- \to [\pi^+\pi^-\pi^0]_D \pi^-) + \Gamma(B^+ \to [\pi^+\pi^-\pi^0]_D \pi^+)}. \tag{1.74}$$

In terms of the parameters r_B, δ_B and γ, Equations 1.70 to 1.74 can be rewritten as

$$A^{K\pi\pi^0}_{K} = \frac{2\kappa_D^{K\pi\pi^0} r_B r_D^{K\pi\pi^0} \sin(\delta_B - \delta_D^{K\pi\pi^0}) \sin\gamma}{1 + (r_B r_D^{K\pi\pi^0})^2 + 2\kappa_D^{K\pi\pi^0} r_B r_D^{K\pi\pi^0} \cos(\delta_B - \delta_D^{K\pi\pi^0}) \cos\gamma}. \tag{1.75}$$

$$A^{KK\pi^0}_{\mathrm{qGLW}(K)} = \frac{2\left(2F_+^{KK\pi^0} - 1\right) r_B \sin\delta_B \sin\gamma}{1 + (r_B)^2 + 2\left(2F_+^{KK\pi^0} - 1\right) r_B \cos\delta_B \cos\gamma}, \tag{1.76}$$

$$A^{KK\pi^0}_{\mathrm{qGLW}(\pi)} = \frac{2\left(2F_+^{KK\pi^0} - 1\right) r_B^\pi \sin\delta_B^\pi \sin\gamma}{1 + (r_B^\pi)^2 + 2\left(2F_+^{KK\pi^0} - 1\right) r_B^\pi \cos\delta_B^\pi \cos\gamma}, \tag{1.77}$$

$$A^{\pi\pi\pi^0}_{\mathrm{qGLW}(K)} = \frac{2\left(2F_+^{\pi\pi\pi^0} - 1\right) r_B \sin\delta_B \sin\gamma}{1 + (r_B)^2 + 2\left(2F_+^{\pi\pi\pi^0} - 1\right) r_B \cos\delta_B \cos\gamma}, \tag{1.78}$$

$$A^{\pi\pi\pi^0}_{\mathrm{qGLW}(\pi)} = \frac{2\left(2F_+^{\pi\pi\pi^0} - 1\right) r_B^\pi \sin\delta_B^\pi \sin\gamma}{1 + (r_B^\pi)^2 + 2\left(2F_+^{\pi\pi\pi^0} - 1\right) r_B^\pi \cos\delta_B^\pi \cos\gamma}. \tag{1.79}$$

An important quantity in this thesis is the ratio of the relative branching fractions of $B^\mp \to DK^\mp$ to $B^\mp \to D\pi^\mp$ decays. For the $K\pi\pi^0$ modes, this is defined as

$$R^{K\pi\pi^0}_{K/\pi} \equiv \frac{\Gamma(B^- \to [K^-\pi^+\pi^0]_D K^-) + \Gamma(B^+ \to [K^+\pi^-\pi^0]_D K^+)}{\Gamma(B^- \to [K^-\pi^+\pi^0]_D \pi^-) + \Gamma(B^+ \to [K^+\pi^-\pi^0]_D \pi^+)}. \tag{1.80}$$

For the quasi-GLW modes, the analogous expressions are:

$$R^{KK\pi^0}_{K/\pi} \equiv \frac{\Gamma(B^- \to [K^+K^-\pi^0]_D K^-) + \Gamma(B^+ \to [K^+K^-\pi^0]_D K^+)}{\Gamma(B^- \to [K^+K^-\pi^0]_D \pi^-) + \Gamma(B^+ \to [K^+K^-\pi^0]_D \pi^+)} \tag{1.81}$$

$$R^{\pi\pi\pi^0}_{K/\pi} \equiv \frac{\Gamma(B^- \to [\pi^+\pi^-\pi^0]_D K^-) + \Gamma(B^+ \to [\pi^+\pi^-\pi^0]_D K^+)}{\Gamma(B^- \to [\pi^+\pi^-\pi^0]_D \pi^-) + \Gamma(B^+ \to [\pi^+\pi^-\pi^0]_D \pi^+)}. \tag{1.82}$$

Furthermore, for the quasi-GLW modes, another quantity of interest is R_{qGLW}, where

$$R^{KK\pi^0}_{\mathrm{qGLW}} \equiv \frac{\Gamma(B^- \to [K^+K^-\pi^0]_D K^-) + \Gamma(B^+ \to [K^+K^-\pi^0]_D K^+)}{\Gamma(B^- \to D^0 K^-) + \Gamma(B^+ \to \overline{D}^0 K^+)} \tag{1.83}$$

$$R^{\pi\pi\pi^0}_{\text{qGLW}} \equiv \frac{\Gamma(B^- \to [\pi^+\pi^-\pi^0]_D K^-) + \Gamma(B^+ \to [\pi^+\pi^-\pi^0]_D K^+)}{\Gamma(B^- \to D^0 K^-) + \Gamma(B^+ \to \bar{D}^0 K^+)}. \tag{1.84}$$

In practice, this quantity is obtained by measuring the ratio of ratios

$$R^{KK\pi^0}_{\text{qGLW}} \approx \frac{R^{KK\pi^0}_{K/\pi}}{R^{K\pi\pi^0}_{K/\pi}}, \tag{1.85}$$

$$R^{\pi\pi\pi^0}_{\text{qGLW}} \approx \frac{R^{\pi\pi\pi^0}_{K/\pi}}{R^{K\pi\pi^0}_{K/\pi}}. \tag{1.86}$$

In terms of γ, the R_{qGLW} quantities are

$$R^{KK\pi^0}_{\text{qGLW}} \approx 1 + (r_B)^2 + 2\left(2F_+^{KK\pi^0} - 1\right) r_B \cos\delta_B \cos\gamma \tag{1.87}$$

$$R^{\pi\pi\pi^0}_{\text{qGLW}} \approx 1 + (r_B)^2 + 2\left(2F_+^{\pi\pi\pi^0} - 1\right) r_B \cos\delta_B \cos\gamma. \tag{1.88}$$

In summary, therefore, measurements are made of $R^{K\pi\pi^0}_{\text{ADS}(K)}$, $R^{K\pi\pi^0}_{\text{ADS}(\pi)}$, $A^{K\pi\pi^0}_{\text{ADS}(K)}$, $A^{K\pi\pi^0}_{\text{ADS}(\pi)}$, $A^{K\pi\pi^0}_{K}$, $A^{KK\pi^0}_{\text{qGLW}(K)}$, $A^{KK\pi^0}_{\text{qGLW}(\pi)}$, $A^{\pi\pi\pi^0}_{\text{qGLW}(K)}$, $A^{\pi\pi\pi^0}_{\text{qGLW}(\pi)}$, $R^{KK\pi^0}_{\text{qGLW}}$ and $R^{\pi\pi\pi^0}_{\text{qGLW}}$. These observables are then used to extract information related to the parameters r_B, δ_B and γ.

1.6 B^+/B^- Production Asymmetry

An important quantity in *CP* violation measurements using charged B hadrons is the charge production asymmetry, A_{Prod}, the different rate with which B^- and B^+ mesons are produced from the initial collisions of the particle collider. A_{Prod} depends on the initial state and the acceptance of the measurement and thus is not a universal quantity. Given that the measurement of *CP* asymmetry in this analysis consists largely of counting exercises for B^+ and B^- candidates, it is important to understand if there is an inherent charge asymmetry in candidate production. In fact, since the quark content of B^+ is $(\bar{b}u)$ and that of B^- is $(b\bar{u})$ and the LHC is a *pp* collider, there is the expectation of a slight excess of B^+ events due to the u being one of the proton's constituent quarks.

The production asymmetry is defined as

$$A_{\text{Prod}} \equiv \frac{\sigma(B^-) - \sigma(B^+)}{\sigma(B^-) + \sigma(B^+)} \tag{1.89}$$

where σ represents the production cross-section within the acceptance of the detector. Any observed experimental charge asymmetry can be expressed as

$$A_{\text{Obs}} = A_{\text{Prod}} + A_{\text{Phys}} + A_{\text{Inst}} \tag{1.90}$$

where A_{Phys} are asymmetries due to *CP* violation and A_{Inst} are asymmetries due to detector instrumentation. In this thesis, A_{Prod} is measured using the favoured decay $B^{\mp} \to [K^{\mp}\pi^{\pm}\pi^0]_D\pi^{\mp}$ where high statistics are expected, but *CP* violation is minimal. Under the assumption that there is no measurable *CP* violation in this mode, and using the pion and kaon detection asymmetry values previously measured at LHCb [32, 33], we can determine A_{Prod} by studying the differences in yields between B^+ and B^- candidates in this decay mode.

The $B^{\mp}$ production asymmetry at LHCb has been previously measured using $B^{\mp} \to J/\psi K^{\mp}$ decays and was determined to be $(-0.3 \pm 0.9)\%$, a value compatible with zero [34].

1.7 Current Experimental Status

The decays of interest listed in Section 1.5.2 have never before been studied by the LHCb collaboration. However, the $K\pi\pi^0$ modes have been studied by BaBar and Belle [35, 36] and the $B^{\mp} \to [\pi^+\pi^-\pi^0]_D K^{\mp}$ asymmetries were previously studied at BaBar [37]. The $B^{\mp} \to [\pi^+\pi^-\pi^0]_D\pi^{\mp}$ decay and both of the $KK\pi^0$ decays have never been studied previously.

Many decay channels are sensitive to the measurement of γ. As a result, LHCb has studied several of these modes and combined their results in order to obtain the world's most precise measurements of γ, r_B and δ_B from a single experiment [38]. Let us briefly summarise this γ combination measurement in addition to the $K\pi\pi^0$ and $\pi\pi\pi^0$ analyses of Belle and BaBar.

1.7.1 LHCb γ Combination

One of the advantages of studying a variety of modes with the common parameters γ, r_B and δ_B is that a measurement of these parameters which is more precise than any of the individual modes, can be made through their combination. Such a γ combination (as it is often called), at LHCb, was initially performed in 2013 [39] and further updated in 2014 with additional decay modes and data [38]. This latest LHCb γ combination uses the following decay modes

- $B^{\mp} \to Dh^{\mp}$, $D \to h'^{\pm}h''^{\mp}$
- $B^{\mp} \to Dh^{\mp}$, $D \to K^{\pm}\pi^{\mp}\pi^{+}\pi^{-}$
- $B^0_s \to D^{\mp}_s K^{\pm}$
- $B^{\mp} \to DK^{\mp}$, $D \to K^0_{\mathrm{S}}h^{\pm}h^{\mp}$
- $B^{\mp} \to DK^{\mp}$, $D \to K^0_{\mathrm{S}}K^{\pm}\pi^{\mp}$
- $B^0 \to DK^{*0}$, $D \to h^{\pm}h'^{\mp}$

where the first three were performed using 1 fb^{-1} of data and the latter three with 3 fb^{-1} of LHCb data.

The combination is calculated for the $B \to DK$-like modes using a frequentist approach. The combination takes into consideration potential *CP* violation in the D^0 system (at first order) in addition to the effects of D^0–$\overline{D}^0$ mixing. Confidence level (CL) scans for the parameters of interest of r_B, δ_B and γ are presented in Figure 1.6. At the 68% CL, using the measurements of the $B \to DK$-like modes alone, it is determined that $r_B = 0.0914^{+0.0083}_{-0.0088}$, $\delta_B = (126.8^{+9.9}_{-11.5})^{\circ}$ and $\gamma = (72.9^{+9.2}_{-9.9})^{\circ}$. These measurement are of greater precision than the legacy measurements made by the BaBar and Belle collaborations [40, 41].

1.7.2 $K\pi\pi^0$ Analysis at BaBar

The BaBar experiment has performed a search for the suppressed $B^{\mp} \to [\pi^{\mp}K^{\pm}\pi^0]_D K^{\mp}$ decay [35]. This was done using 431 fb^{-1} of e^+e^- collisions from the PEP-II collider at SLAC at the $\Upsilon(4S)$ resonance.

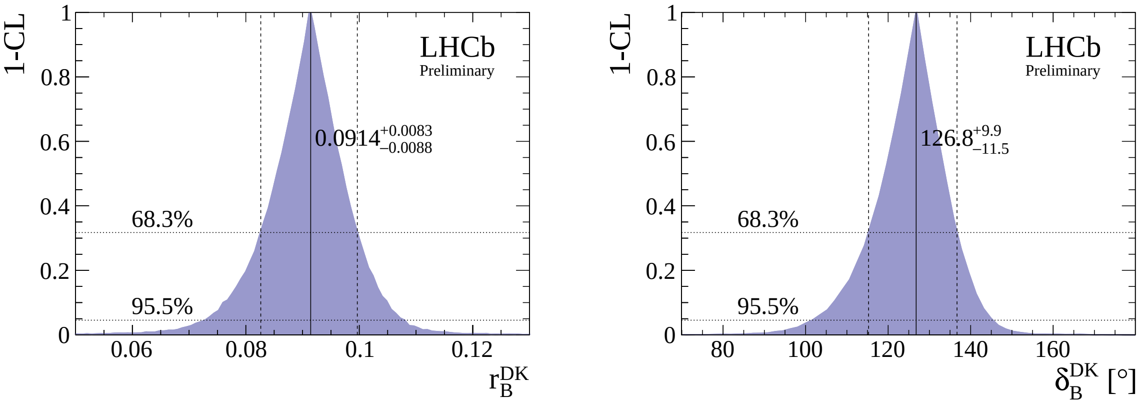

(a) CL scan for r_B (b) CL scan for δ_B

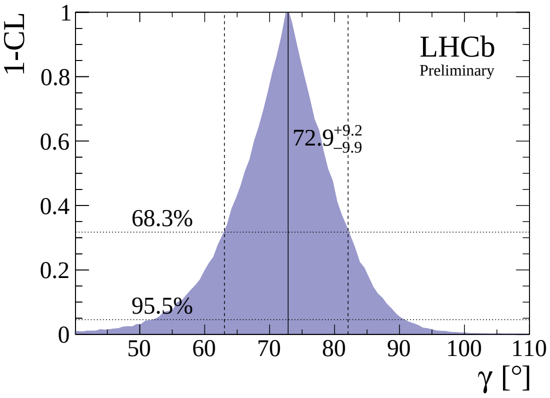

(c) CL scan for γ

Figure 1.6: r_B, δ_B and γ, as measured from the LHCb γ combination, using a variety of $B \to DK$-like decays [38].

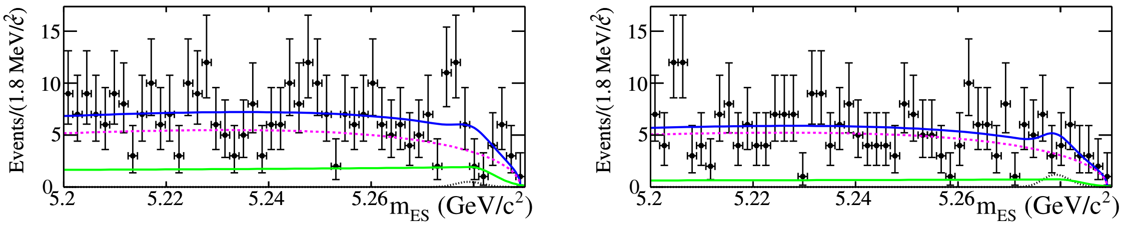

(a) B^+ candidates (b) B^- candidates

Figure 1.7: Mass distributions for the $B^{\mp} \to [\pi^{\mp}K^{\pm}\pi^0]_D K^{\mp}$ decays from BaBar. The magenta and green curves are background contributions, while the signal is the dotted black peak near 5.28 GeV/c^2 [35].

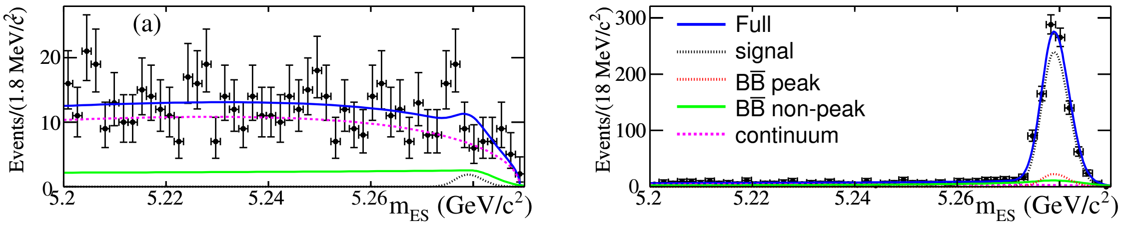

(a) $B^{\mp} \to [\pi^{\mp}K^{\pm}\pi^{0}]_{D}K^{\mp}$ (b) $B^{\mp} \to [K^{\mp}\pi^{\pm}\pi^{0}]_{D}K^{\mp}$

Figure 1.8: Mass distributions of the $B^{\mp} \to [K\pi\pi^{0}]_{D}K^{\mp}$ data, from BaBar, summed by charge. The suppressed decays are in Figure 1.8(a) and the favoured decays are shown in Figure 1.8(b) [35].

Figure 1.7 shows the mass distributions for the B^{+} and B^{-} candidates after the full event selection has been applied. The summed-by-charge $B^{\mp} \to DK^{\mp}$ distributions for the favoured and suppressed ADS $K\pi\pi^{0}$ decays are presented in Figure 1.8. Fits to these sets of distributions were used to calculate CP observables, including $R_{\mathrm{ADS}(K)}$. The analysis determined a value for the latter of

$$R_{\mathrm{ADS}(K)} = 0.0091^{+0.0082}_{-0.0076}(\mathrm{stat})^{+0.0014}_{-0.0037}(\mathrm{syst}) \tag{1.91}$$

and a limit of $r_{B} < 0.13$ was set at the 90% probability level.

1.7.3 $K\pi\pi^{0}$ Analysis at Belle

The Belle experiment performed a search for the suppressed $K\pi\pi^{0}$ ADS modes in both the $B^{\mp} \to D\pi^{\mp}$ and $B^{\mp} \to DK^{\mp}$ channels [36]. This analysis was performed using a sample of 772×10^{6} $B\overline{B}$ pairs from $e^{+}e^{-}$ collisions at the $\Upsilon(4S)$ resonance.

From this study, first evidence of the suppressed ADS modes $B^{\mp} \to [\pi^{\mp}K^{\pm}\pi^{0}]_{D}\pi^{\mp}$ and $B^{\mp} \to [\pi^{\mp}K^{\pm}\pi^{0}]_{D}K^{\mp}$ was obtained at the 3.3σ and 3.2σ levels, respectively. In Figure 1.9, we present the mass distributions, split by charge, of the $B^{\mp}$ candidates for these two decay modes.

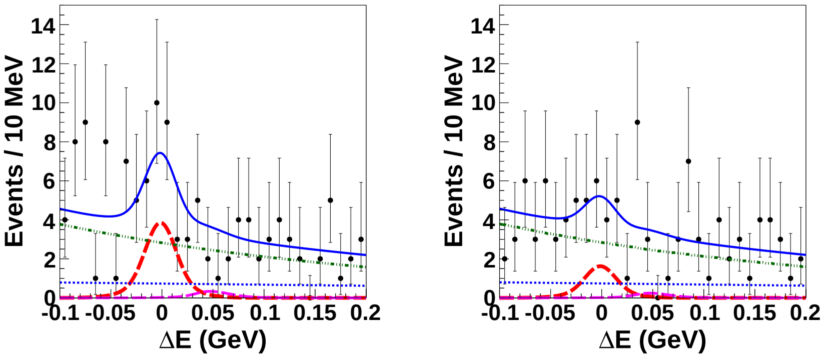

(a) $B^- \to [\pi^- K^+ \pi^0]_D K^-$ (b) $B^+ \to [\pi^+ K^- \pi^0]_D K^+$

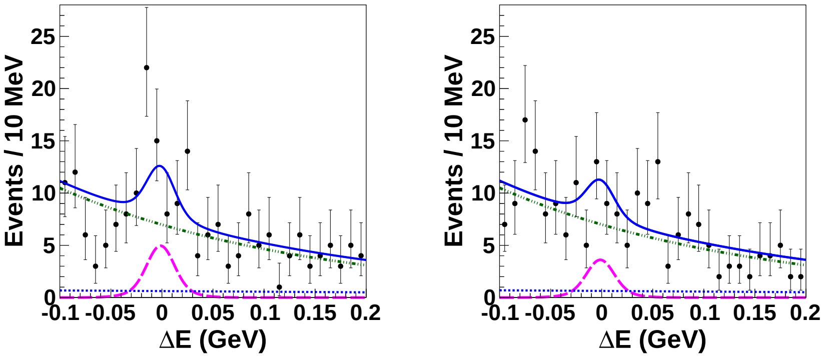

(c) $B^- \to [\pi^- K^+ \pi^0]_D \pi^-$ (d) $B^+ \to [\pi^+ K^- \pi^0]_D \pi^+$

Figure 1.9: $B^\mp$ candidates from Belle, separated by charge, for the suppressed ADS decays of $B^\mp \to [\pi^\mp K^\pm \pi^0]_D K^\mp$ and $B^\mp \to [\pi^\mp K^\pm \pi^0]_D \pi^\mp$. DK events are illustrated in red, $D\pi$ events in magenta, while $B\overline{B}$ backgrounds ($B^\mp \to D^* h^\mp$, $B^\mp \to D\rho^\mp$ and combinatoric backgrounds) are modelled in green and $e^+e^- \to q\overline{q}$ backgrounds in blue. The units on the x-axis are such that the nominal $B^\mp$ mass corresponds to $\Delta E = 0$ [36].

From the $B^\mp \to [\pi^\mp K^\pm \pi^0]_D \pi^\mp$ decay, the following CP observables were measured:

$$A_{\mathrm{ADS}(\pi)} = 0.16 \pm 0.27(\mathrm{stat})^{+0.03}_{-0.04}(\mathrm{syst}), \tag{1.92}$$

$$R_{\mathrm{ADS}(\pi)} = 0.00189 \pm 0.00054(\mathrm{stat})^{+0.00022}_{-0.00025}(\mathrm{syst}). \tag{1.93}$$

Comparably, from the $B^\mp \to [\pi^\mp K^\pm \pi^0]_D K^\mp$ decay, the CP observables were measured to be

$$A_{\mathrm{ADS}(K)} = 0.41 \pm 0.30(\mathrm{stat}) \pm 0.05(\mathrm{syst}), \tag{1.94}$$

$$R_{\mathrm{ADS}(K)} = 0.0198 \pm 0.0062(\mathrm{stat}) \pm 0.0024(\mathrm{syst}). \tag{1.95}$$

In all cases, the measured CP asymmetries were seen to be relatively small and compatible with zero.

1.7.4 $\pi\pi\pi^0$ Analysis at BaBar

The BaBar collaboration performed a study of *CP* violation in $B^{\mp} \to [\pi^+\pi^-\pi^0]_D K^{\mp}$ decays [37] using a total of 324×10^6 $e^+e^- \to B\overline{B}$ events collected from the PEP-II collider. In this analysis, the extraction of *CP* observables was performed primarily through a study of D decay Dalitz distributions [42, 43]. Limits, at the 1σ level, were set on the parameters γ and r_B at $-30° < \gamma < 76°$ and $0.06 < r_B < 0.78$, respectively. However, an inclusive study was performed and the *CP* asymmetry was measured to be

$$A^{\pi\pi\pi^0}_{\mathrm{qGLW}(K)} = -0.02 \pm 0.15(\mathrm{stat}) \pm 0.03(\mathrm{syst}), \tag{1.96}$$

a value compatible with zero.

1.8 External Inputs

In order to extract the parameters γ, r_B and δ_B from the *CP* observables specified in Section 1.5.2, it is necessary to make use of external measurements of D decay parameters. These include branching fractions [2], in addition to the coherence factor $\kappa_D^{K\pi\pi^0}$, the average strong-phase difference $\delta_D^{K\pi\pi^0}$ and the *CP*-even fractions $F_+^{\pi\pi\pi^0}$ and $F_+^{KK\pi^0}$. Much work has been done using the data from the CLEO-c experiment to measure these parameters [31, 44, 45] and ultimately those results are used as inputs in this analysis.

1.8.1 $K\pi\pi^0$ Coherence Factor and Average Strong-Phase Difference

The coherence factor, $\kappa_D^{K\pi\pi^0}$ and the average strong-phase difference, $\delta_D^{K\pi\pi^0}$, have been measured by the CLEO-c experiment in 2009 [46]. A later update, based on the same dataset but including new analysis techniques, was released in 2014 [44]. Both measurements were performed by studying the decays of coherently produced $D\bar{D}$ pairs at the $\psi(3770)$ resonance from 818 pb^{-1} of e^+e^- collision data.

The measured values, including statistical and systematic uncertainties are presented in Table 1.4. The coherence factor, which can range from 0 to 1, was found to be relatively high, and thus the channel offers a greater sensitivity to γ than decay modes where the coherence factor is closer to zero.

Table 1.4: Coherence factor and average strong-phase difference for $K\pi\pi^0$, as measured with CLEO-c data. The uncertainties listed include both statistical and systematic contributions [44].

Paramaeter	Value
$\kappa_D^{K\pi\pi^0}$	0.82 ± 0.07
$\delta_D^{K\pi\pi^0}$	$\left(164^{+20}_{-14}\right)^\circ$

Scans of the $\left(\kappa_D^{K\pi\pi^0}, \delta_D^{K\pi\pi^0}\right)$ parameter space were performed, where κ and δ were fixed, but the other experimental parameters were allowed to vary, while minimising the χ^2 at each point. This was done in order to determine the one, two and three standard deviation confidence intervals of the two observables. These scans are presented in Figure 1.10.

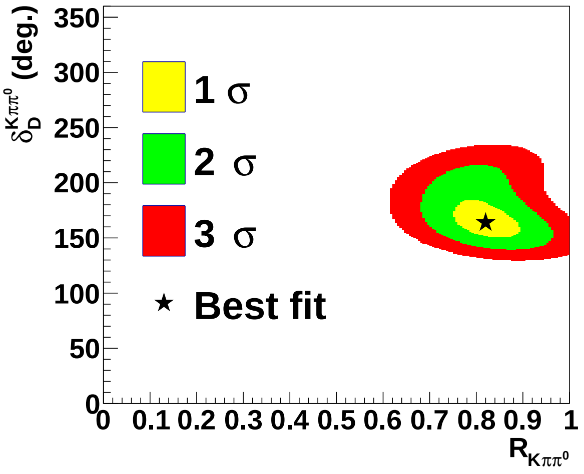

Figure 1.10: One, two and three sigma contours of the coherence factor and average strong-phase difference for $K\pi\pi^0$. The x-axis represents the coherence factor [44].

1.8.2 *CP*-Even Fraction of $\pi\pi\pi^0$ and $KK\pi^0$

The *CP*-even fractions of the decays $D \to \pi^+\pi^-\pi^0$ and $D \to K^+K^-\pi^0$ have been measured using 818 pb^{-1} of e^+e^- collision data at $\sqrt{s} = 3.77$ GeV collected at the $\psi(3770)$ resonance with the CLEO-c detector. The measurement of both F_+ values was originally presented as a dedicated analysis [31], however a new analysis technique developed for the measurement of $F_+^{\pi\pi\pi\pi}$ was then applied to $F_+^{\pi\pi\pi^0}$ and $F_+^{KK\pi^0}$ in order to reduce their uncertainties [45].

The latest measurements of the *CP*-even fractions of interest are presented in Table 1.5. Similar to the coherence factors, these F_+ factors range from 0 to 1, where 0 represents a fully *CP*-odd signal eigenstate while 1 represents a fully *CP*-even one.

Table 1.5: F_+ factors measured using CLEO-c data. The uncertainties listed include both statistical and systematic contributions [45].

Parameter	Value
$F_+^{\pi\pi\pi^0}$	0.973 ± 0.017
$F_+^{KK\pi^0}$	0.732 ± 0.055

Interestingly, the $\pi\pi\pi^0$ final state is almost a pure *CP* eigenstate as it has an F_+ value of almost unity. This indicates higher sensitivity to γ than modes with a lower F_+ value.

Chapter 2

The LHC and LHCb

The data analysed in this thesis originate from particle collisions at the Large Hadron Collider (LHC) that are recorded by the Large Hadron Collider beauty (LHCb) experiment. This Chapter briefly presents the LHC and then describes the different components of the LHCb detector, including its common software framework.

2.1 The LHC

The LHC [47] at CERN (European Organisation for Nuclear Research[3]) is currently the world's most powerful particle accelerator. Located roughly 100 m underground beneath the French/Swiss countryside and situated in a circular tunnel with a 27 km circumference, the LHC is also the world's largest particle accelerator. In the most common form of operation, the LHC is a proton-proton collider where separate beams of particles circulate in the accelerator in opposite directions. At four interaction points, the locations of the four major LHC experiments, the beams are crossed and focused to allow for collisions. Figure 2.1 presents a diagram of the accelerator tunnel and the caverns of the four major experiments on the accelerator ring.

In order to guide the protons through the curved sections of the collider, the LHC uses a series of 1232 superconducting dipole magnets. The superconducting wires are cooled to a

---

[3] The acronym is based on the organisation's original French name, *Conseil européen pour la recherche nucléaire*.

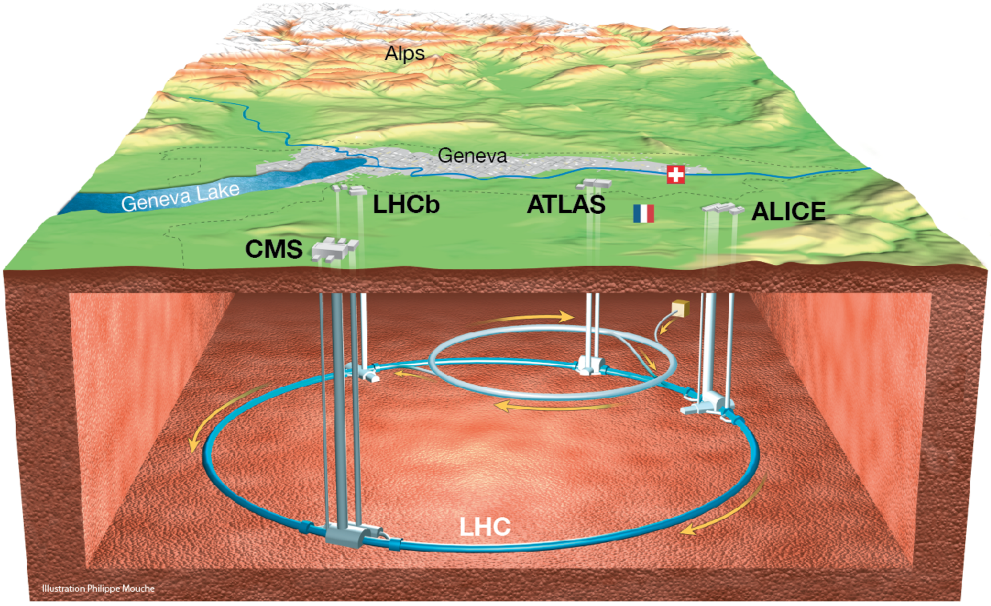

Figure 2.1: Illustration of the LHC tunnel underneath France and Switzerland. The relative positions of the four major experiments, including LHCb, are indicated [48].

temperature of 1.9 K using superfluid helium allowing them to produce a magnetic field of 8.3 T when a current of 11 850 A is run through the wires. In each of the dipole magnets there are two pipes for the beams to circulate in. Both of these pipes are cooled by the same cryogenic system, but are subject to a magnetic flux circulating in the opposite direction from each other. A cross-sectional illustration of an LHC dipole is presented in Figure 2.2.

Before injection into the LHC, the protons are accelerated by a series of smaller accelerator systems. Initially, hydrogen atoms are stripped of their electrons and are accelerated by CERN's Linac 2 to an energy of 50 MeV. They are then injected into the Proton Synchrotron Booster where they are accelerated to 1.4 GeV and then injected into the Proton Synchrotron. In this ring with a circumference of 628 m, the protons are accelerated to 26 GeV. Finally, the protons are injected into the Super Proton Synchrotron, the second-largest of the CERN accelerators with a circumference of 6.9 km, which accelerates the protons to 450 GeV and injects them into the LHC, where they are ramped to their collision energy. Although the LHC is designed to operate at a collision centre-of-mass energy ($\sqrt{s}$) of 14 TeV, the data collected during its Run I period and used in this analysis (as discussed in Section 3.3), were delivered at $\sqrt{s} = 7$ TeV and $\sqrt{s} = 8$ TeV.

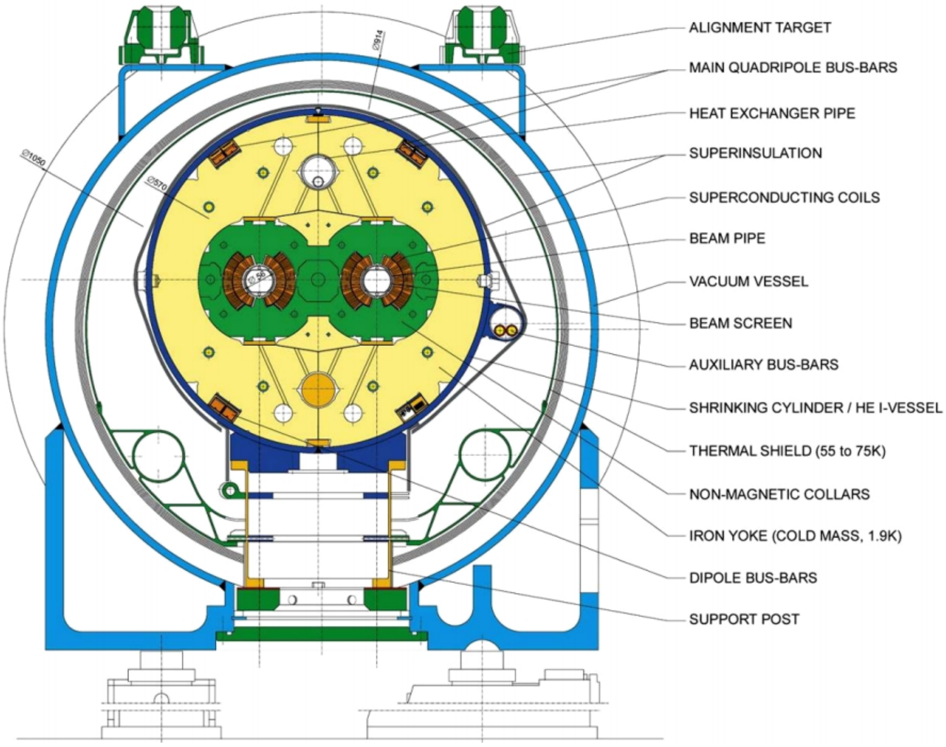

Figure 2.2: A cross-sectional view of one of the LHC superconducting dipole magnets [47].

The LHC is designed to operate at a luminosity of 10^{34} cm^{-2}s^{-1}. In 2012, a peak luminosity of 7.7×10^{33} cm^{-2}s^{-1} was achieved at the ATLAS and CMS interaction points [49]. This luminosity is obtained through the collision of proton bunches; each bunch carries approximately 1.6×10^{11} protons with collisions occurring every 50 ns. LHCb, however, does not use all of the available LHC luminosity as part of its data collection activities. For this experiment, the practice of luminosity levelling is performed to reduce the luminosity to 4×10^{32} cm^{-2}s^{-1} before delivering it to the detector. Such a reduction is performed in order to reduce pile-up, which is beneficial for flavour physics studies, as well as preventing premature deterioration of detector components. Lower luminosity is achieved through separating the beams in the interaction region before collision. As the beam currents decrease over the course of a LHC fill, the beams are brought closer together so as to maintain a consistent luminosity to the detector [50].

2.2 LHCb

The LHCb detector is a dedicated experiment at CERN that has been optimised for the study of *CP* violation and the decay of beauty and charm hadrons. The detector is a single-arm, forward spectrometer. This geometry is chosen because at the collision energies, both the b and $\bar{b}$-hadrons are predominantly produced in either the forward or backward region.

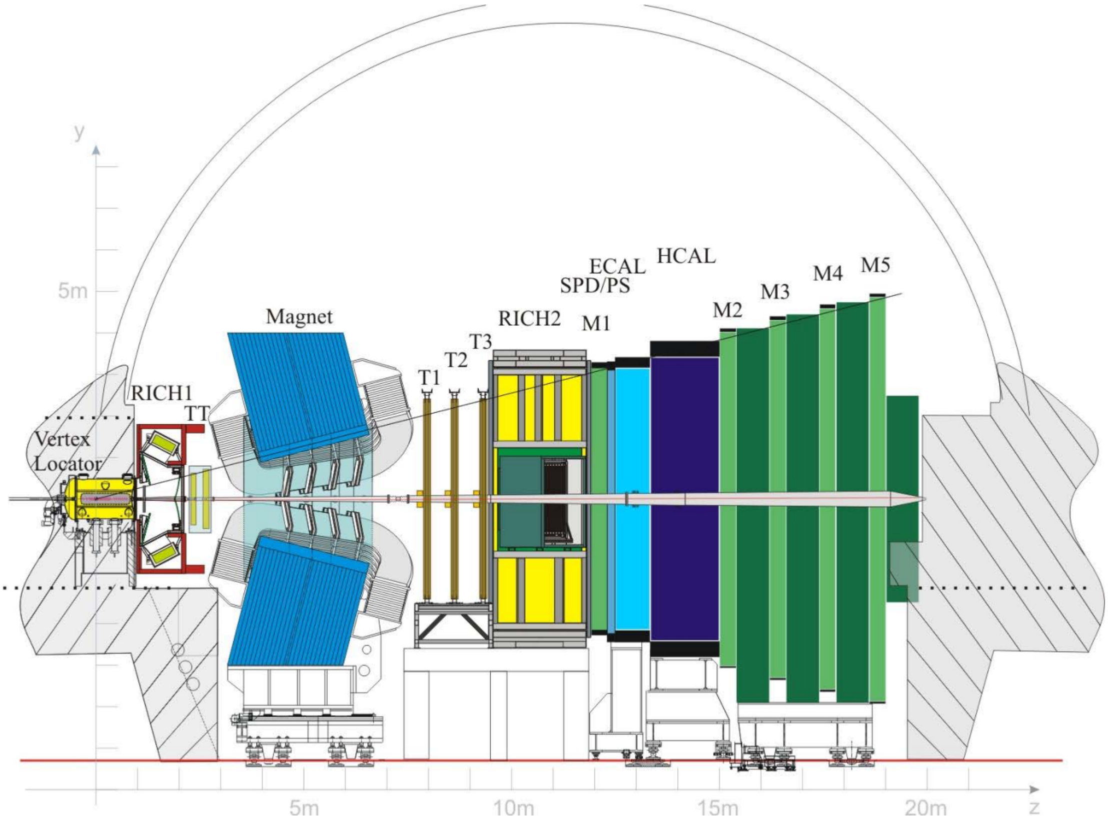

Figure 2.3: A cross-sectional schematic of the LHCb detector. The beampipe is present along the centre of the diagram and the detector subsystems are labelled accordingly [51].

A 19 m long vacuum chamber, the beampipe, is the interface between the LHC and the detector. The beampipe begins downstream of the collision interaction point and traverses most of the length of the detector. The beampipe is separated into four sections; the three closest to the interaction point are made of beryllium while the fourth is made of stainless steel [52]. This choice is made because beryllium has a low interaction length and hence minimises multiple coulomb scattering of charged particles [52]. When discussing LHCb, a right-handed coordinate system is adopted where z is the direction along the beampipe, y is vertically upwards and x points towards the centre of the accelerator ring.

LHCb is composed of several subdetectors, as seen in Figure 2.3. In this diagram, the locations of the VErtex LOcator (VELO), the Ring Imaging CHerenkov detectors (RICH1, RICH2), the Tracker Turicensis (TT), the magnet, the tracking stations (T1–T3), the Scintillator Pad Detector (SPD), the Preshower (PS), Electromagnetic Calorimeter (ECAL), Hadronic Calorimeter (HCAL) and the muon stations (M1–M5) are presented. From this diagram, the geometry of the detector is evident. The forward spectrometer design allows for most subdetectors to have coverage in the region of $2 < \eta < 5$, where η is pseudorapidity. This quantity is defined as

$$\eta \equiv -\ln\left[\tan\frac{\theta}{2}\right] \tag{2.1}$$

where θ is the angle between the particle's momentum vector and the beam axis. In general, most of the detector subsystems are assembled in two halves, the left and right sides of the detector, where left and right are defined in relation to the beam axis. This allows for the components to be moved horizontally for maintenance purposes or to access the beampipe.

LHCb has performed efficiently during LHC Run I. As seen in Figure 2.4, over 90% of the delivered luminosity by the collider was recorded. Let us now discuss the relevant subdetectors that make such data collection possible.

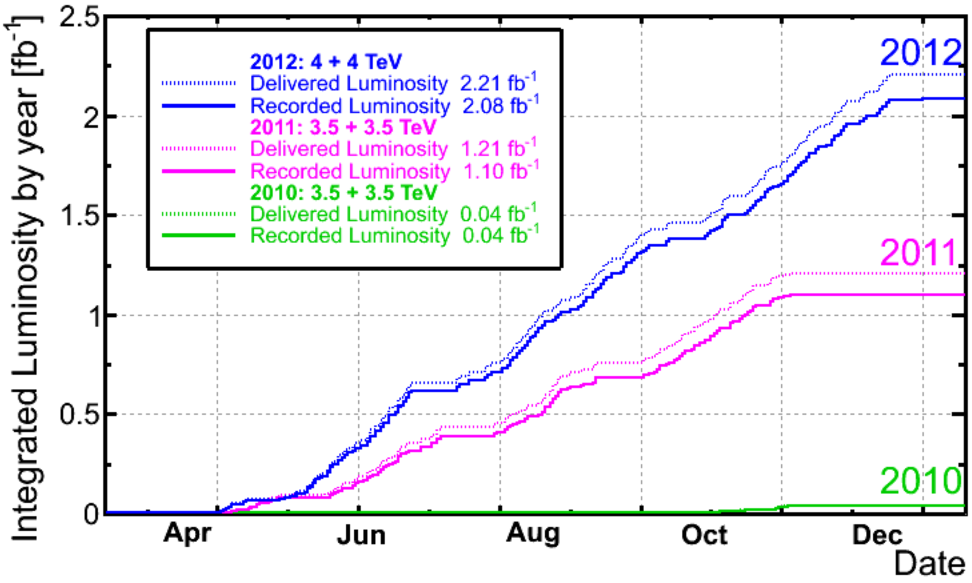

Figure 2.4: The total delivered and collected integrated luminosity by LHCb, separated by year [53].

2.2.1 VELO

The identification of particle vertices is critical to many LHCb analyses. The VELO performs precision position measurements of particle tracks near the interaction point, allowing for the identification of primary and secondary vertices. Displaced secondary vertices are a feature of the decay of b-hadrons and c-hadrons and are useful in their identification. Furthermore, for many measurements, one needs to know the separation between primary and secondary vertices so as to determine the b- or c-hadron's lifetime.

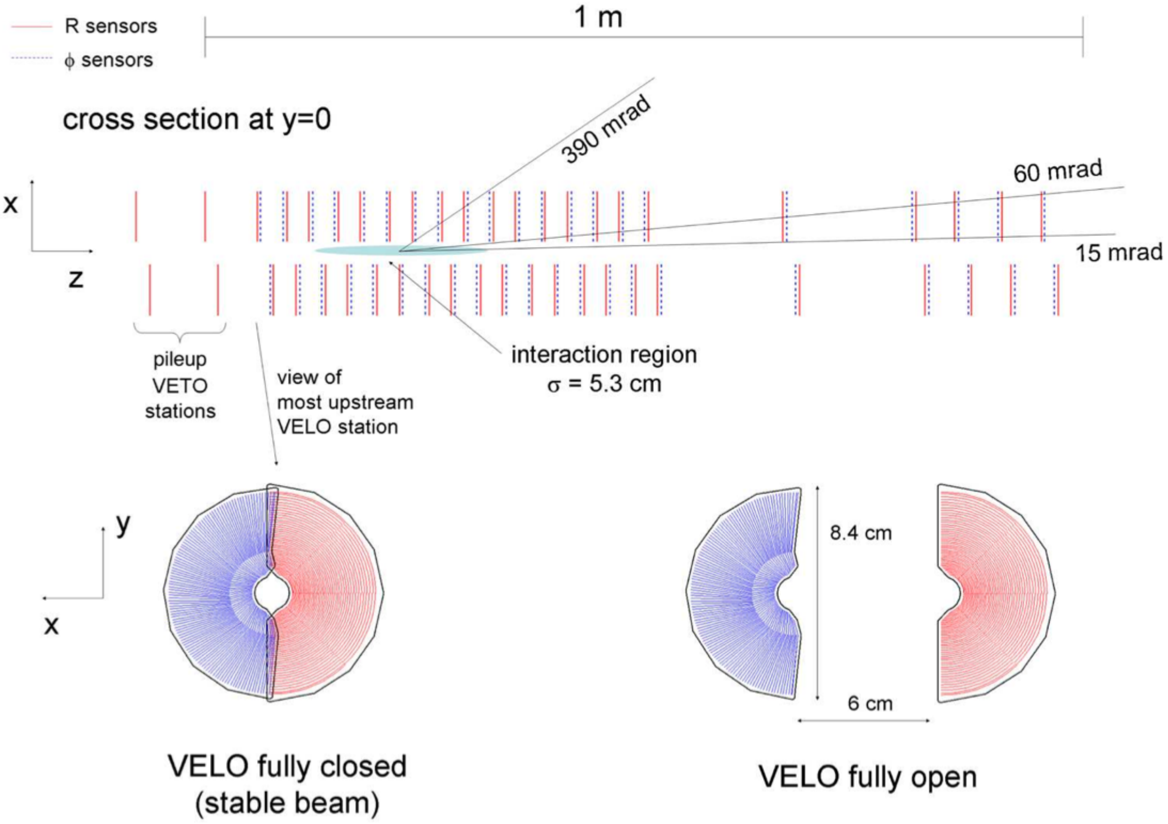

Figure 2.5: The LHCb VELO. The sensors optimised for r information are in red, while those optimised for ϕ information are in blue. The positions of the 21 stations are indicated. The bottom of the figure demonstrates two VELO sensors in the closed, stable beam, position and in the open position [52].

The VELO is composed of a series of semi-circular silicon microstrip modules. These sensors are 300 μm thick [54] and are positioned, in pairs, in 21 stations perpendicular to the beamline. As depicted in Figure 2.5, the VELO is located about the interaction region and the entire system is under vacuum. This is a separate, secondary vacuum system from the primary beam vacuum, and the two are separated using an RF-box. Specifically, the surfaces near the beam and parallel to the sensors are made of a thin-walled corrugated aluminium sheet that provides shielding against RF pickup from the LHC beams [55]. The VELO subdetector provides coverage in the region $1.6 < \eta < 4.9$ [52]. With regards to particle position, a cylindrical coordinate system is adopted where r and ϕ information is provided by the surface of the modules and the z information is provided by the known position of the stations. As a result, some sensors have the silicon applied in a semi-circular pattern to be more sensitive to r information, while others adopt a radial pattern to extract ϕ information.

The VELO, in the $r\phi$ plane, has a resolution of order 10 μm [56]. Figure 2.6 presents the vertex resolution in the x, y and z planes and how they vary as a function of the number of tracks that make up the vertex. Such precision is attainable because the VELO, under data taking conditions, is in close physical proximity to the beam axis, at a distance of 8 mm. This distance is smaller than the aperture required by the LHC during beam injection, so to prevent damage to the VELO, the sensors physically move. During beam injection, the sensors are separated in an open position and when stable accelerator beam is achieved, the two sensors are moved closer to the beam line.

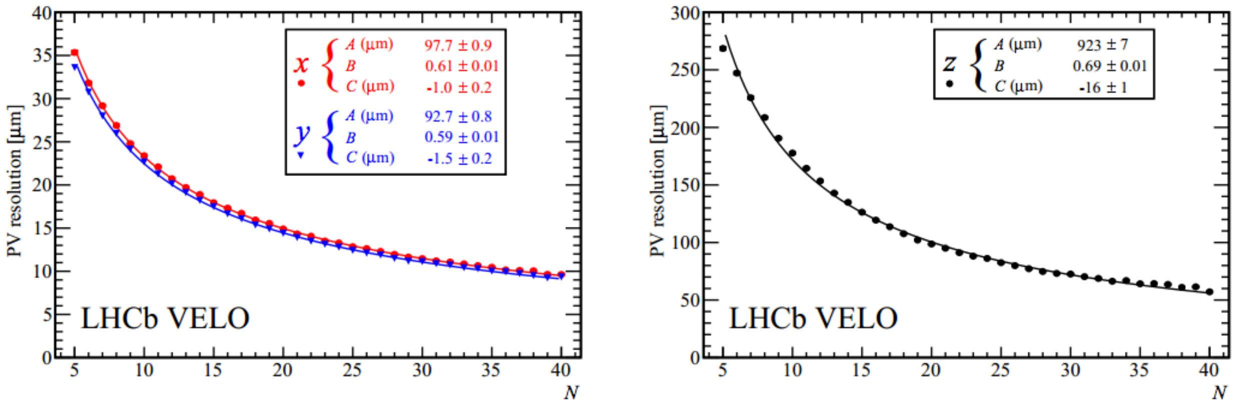

Figure 2.6: Primary vertex resolution as a function of track multiplicity. The red, blue and black lines represent resolution in the x, y and z planes, respectively, as measured in data [55].

For decays involving long-lived particles, impact parameter (IP), discussed more thoroughly in Section 3.2.1, is a variable of particular importance. It is defined as the distance between a track and the primary vertex at the track's closest approach to the primary vertex.

Generally speaking, tracks from the decay of longer-lived particles have larger IP than those produced promptly at the primary vertex. Figure 2.7 presents the IP resolution as measured in data, as a function of particle momentum. The coarsest resolutions are of approximately 90 μm for particles with momentum less than 10 GeV/c, however this resolution becomes approximately 20 μm as the momentum approaches 60 GeV/c.

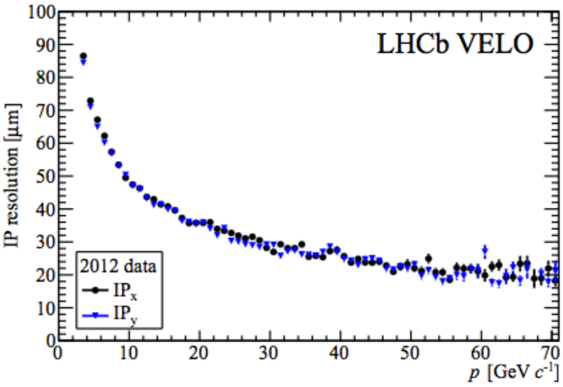

Figure 2.7: Impact parameter resolution in the x and y planes, measured as function of momentum [55].

2.2.2 Magnet

The LHCb dipole is a warm magnet weighing approximately 1600 tonnes [57]. The magnet has an iron yoke within which two sets of Al-99.7 saddle-shaped coils are mounted. There is a top coil and a bottom coil, installed mirror-symmetrically to each other. The purpose of the magnet is to provide an intense magnetic field to assist in the momentum measurement of charged particles. Under the presence of a magnetic field, positively and negatively charged particles will move in opposite directions and the magnitude of their curvature is indicative of their momentum. The magnet provides a field integral of 4 Tm. The orientation of the magnetic field is vertical and can be changed so that its vector is either in the positive or negative y direction.

In terms of positioning, the magnet is installed downstream from the VELO and before the tracking stations. This location is chosen so that the tracks in the VELO are not curved so as to facilitate straight fitting for vertex determination. Furthermore, due to the magnet's location, the charged tracks entering the tracking stations exhibit greater separation than before the magnet, allowing for less uncertainty during the reconstruction process.

2.2.3 Tracking System

In addition to the tracking information provided by the VELO, LHCb has a dedicated tracking system composed of the TT before the magnet and the tracking stations T1, T2 and T3 located downstream of the magnet. Each tracking station is composed of an Inner Tracker (IT) and an Outer Tracker (OT). A diagram of the Tracking System is presented in Figure 2.8.

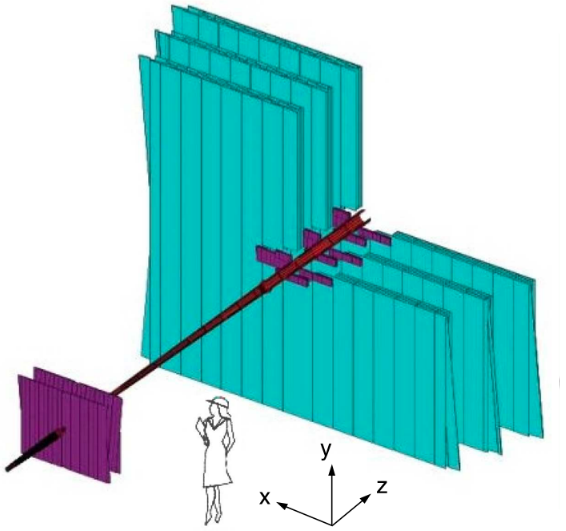

Figure 2.8: The LHCb tracking system. The rectangular plates in violet in the foreground are the TT, while the turquoise plates further downstream are the OT. The devices illustrated in violet on the OT detectors are the IT modules [52].

2.2.3.1 Tracking Turicensis

The TT is composed of silicon microstrips and is situated immediately upstream of the dipole magnet. It has an active detection area of 8.4 m^2 and covers the full LHCb acceptance region. The TT is arranged in 4 layers distributed over two physical detectors. Layers 1 and 2 are on the first detector and layers 3 and 4 are on the second, physically located 27 cm downstream along the beam axis from the first detector. Layers 1 and 4 have vertical readout strips, while those on layers 2 and 3 and rotated by -5° and 5°, respectively. This layout is chosen so that transverse momentum (p_{T}) measurements can be made.

The tracking resolution of the TT is approximately 50 μm [56]. Its primary purpose is to reconstruct the trajectories of low momentum particles; its location before the magnet is crucial to this task as these particles are bent out of the acceptance region after passing through the magnetic field. In addition, it is also used for the reconstruction of long lived particles such as the K^0_{S} that decay outside of the VELO. It is also used by the HLT1 trigger (as discussed in Section 2.2.7.2) to assign transverse momentum information [58].

2.2.3.2 Inner Tracker

The IT, like the TT, is a silicon microstrip detector. Its modules are small and cross-like in geometry with dimensions of roughly 130 cm × 40 cm [58]. They are mounted on the T1, T2 and T3 tracking stations, nearest to the beampipe, as this is the region with the greatest particle flux. Similar to the TT, the IT has a tracking resolution of approximately 50 μm [56].

2.2.3.3 Outer Tracker

The outer tracker is a straw tube detector physically located on the three tracking stations. In Figure 2.8, the OT is represented by the three large turquoise plates; they occupy much of the physical area of the tracking stations. The OT is composed of modules that have two staggered layers of drift tubes, with each tube possessing a diameter of 4.9 mm. These tubes contain a mixture of 70% argon and 30% carbon dioxide gas. On each of the tracking stations, the modules are arranged so as to form four layers with a similar layout to that of the TT described in Section 2.2.3.1, where the middle two layers are rotated by ±5°. The track resolution of the OT is 205 μm [56].

2.2.3.4 Performance

At LHCb, the tracking efficiency is defined as the probability that the trajectory of a charged particle that passes through the full tracking system is reconstructed. Figure 2.9 presents the tracking efficiency, as measured in data, as a function of momentum, η, track multiplicity and the number of primary vertices in the event. Excellent performance is observed, as an efficiency greater than 90% is noted in all cases.

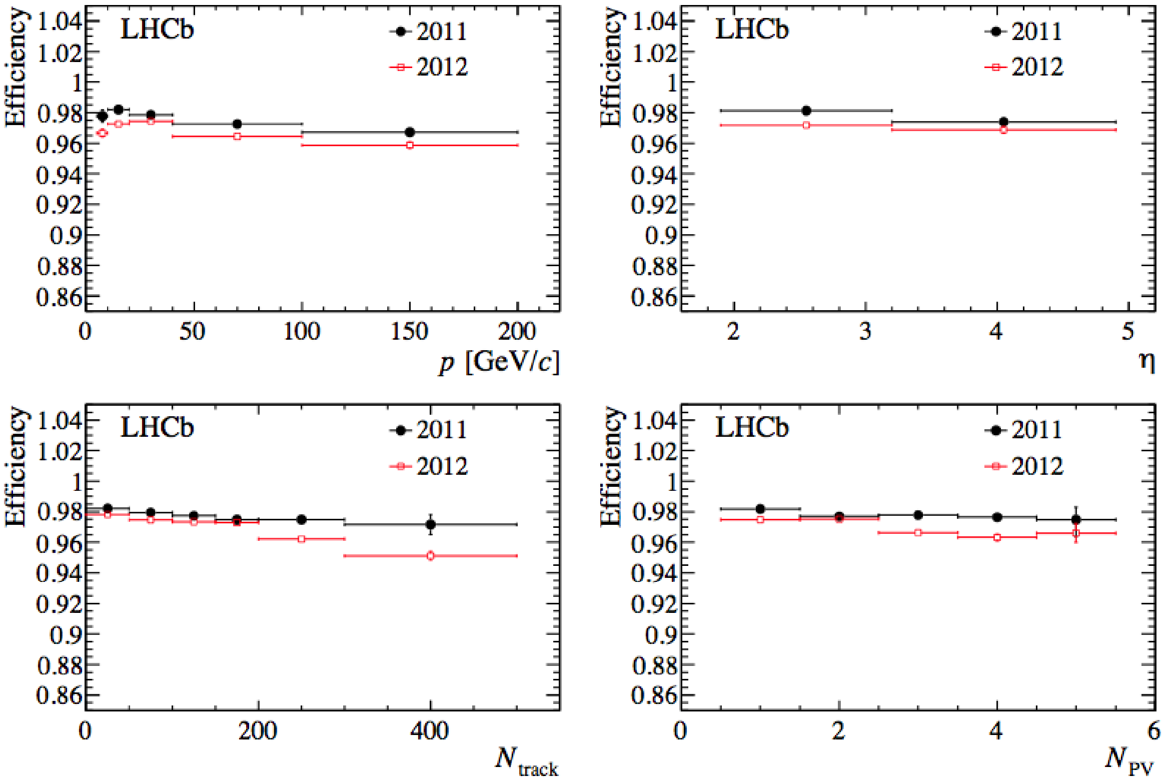

Figure 2.9: Tracking efficiency, as measured in data. It is presented as a function of p, η, the number of tracks and the number of reconstructed primary vertices in the event. 2012 data shows slightly reduced efficiency compared to 2011 due to higher vertex multiplicity resulting from the increased center-of-mass energy for the proton-proton collisions [56].

The momentum resolution of the tracker is measured through the study of $J/\psi \to \mu^+\mu^-$ decays. As seen in Figure 2.10, the momentum resolution, expressed as $\delta p/p$, is approximately 5 per mille for candidates with a momentum less than 20 GeV/c. This value rises to 8.5 per mille for candidates with a momentum of approximately 100 GeV/c.

The tracking detectors are also used in measuring the invariant mass of decaying hadrons. To quantify their mass resolution, similar to the momentum resolution, comparisons to dimuon systems are used. In particular, the measured mass is compared to decays of J/ψ, $\psi(2S)$, $\Upsilon(1S)$, $\Upsilon(2S)$, $\Upsilon(3S)$ and Z. The results are presented in Figure 2.11, where it is seen that the relative resolution, σ_m/m, is approximately 5 per mille up to 10 000 MeV/c^2. Mass resolution does, however, have a dependence on the number of tracks in the decay.

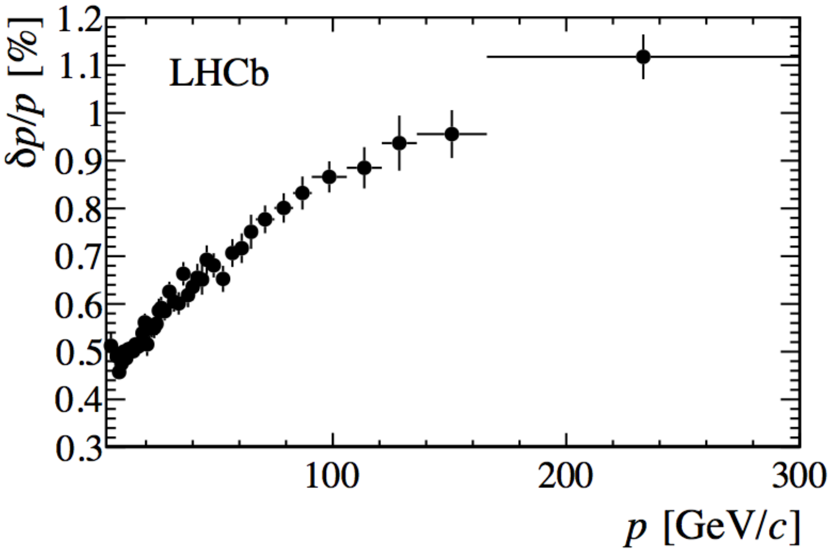

Figure 2.10: Tracking system momentum resolution, as measured in $J/\psi \to \mu^+\mu^-$ decays in data [56].

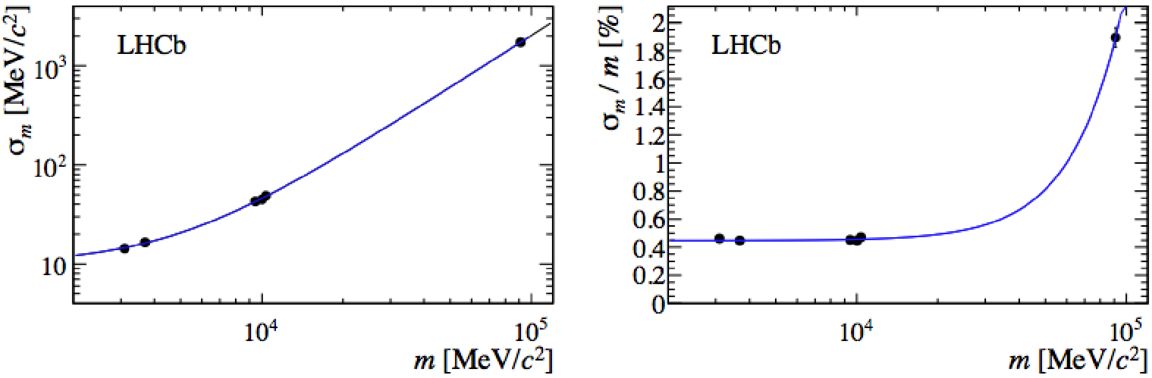

Figure 2.11: Absolute and relative mass resolution from the tracking system, as measured in dimuon resonances, as a function of mass. The curve in blue is an empirical power-law fit [56].

2.2.4 RICH

Many physics analyses at LHCb rely upon the ability to distinguish between charged kaons and pions. This is achieved through two Ring Imaging Cherenkov detectors. These detectors function on the principle that when a charged particle travels through a dielectric medium with a velocity greater than the speed of light in that medium, a cone of Cherenkov radiation is emitted [59]. The aperture angle of the cone, θ_c, can be expressed as

$$\cos\theta_c = \frac{1}{n\beta}, \tag{2.2}$$

where n is the index of refraction of the medium and β is the ratio v/c with v being the particle's velocity. Since β is related to momentum, if θ_c and the momentum of the particle are both measured, the particle's mass (and hence identity) can be ascertained.

LHCb has two RICH systems, RICH1 and RICH2, that are designed to operate in different momentum regimes. RICH1, illustrated in Figure 2.12(a), is situated upstream of the TT and magnet and is designed to identify particles in the low momentum region of 2–40 GeV/c with an angular acceptance of 25–300 mrad [60]. Two media are used in RICH1, aerogel and C_4F_{10} gas, and the ensuing Cherenkov radiation cones are deflected outside the geometric acceptance region of the detector using a series of spherical and flat mirrors. These mirrors focus the Cherenkov light cones onto an array of Hybrid Photon Detectors (HPD), where these cones are seen as ring patterns in the array of HPDs. The aperture angle of the cone can be calculated from the size of the ring. An example of such rings, as seen in RICH1, is depicted in Figure 2.13.

RICH2 is located after the tracking stations and is illustrated in Figure 2.12(b). This sub detector is designed to work in the momentum regime of approximately 15–100 GeV/c in the angular range of 15–120 mrad. Its medium is CF_4 gas and it operates in much the same way as RICH1, where mirrors reflect the Cherenkov radiation onto HPD arrays where the reconstructed rings are used to identify the particle tracks.

The Cherenkov angular resolution, one of the primary measures of RICH performance, is dependent on the medium. This angular resolution, $\Delta\theta_c$, is measured to be 1.618±0.002 mrad

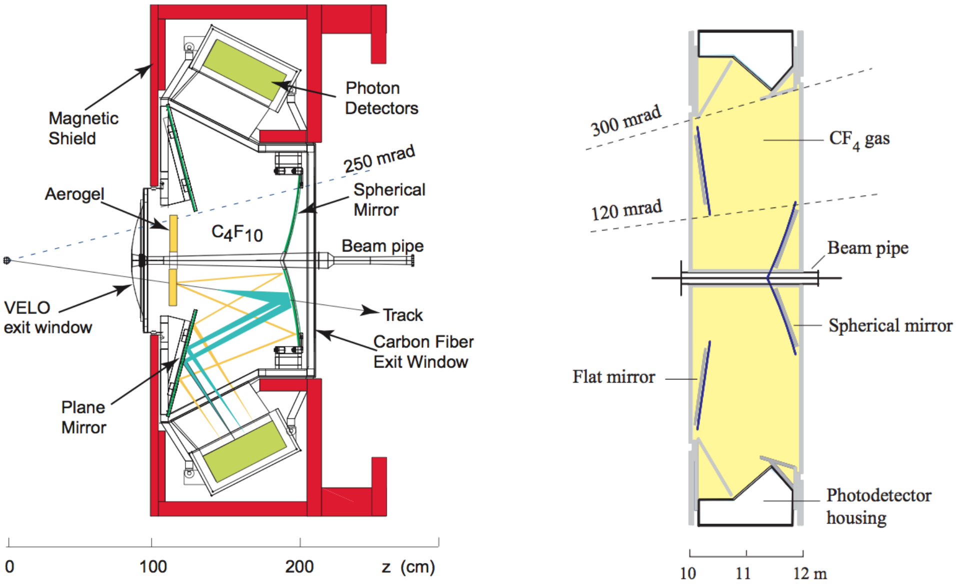

(a) RICH1 (b) RICH2

Figure 2.12: A schematic view of RICH1 and RICH2 in the $y - z$ plane. In Figure 2.12(a), the Cherenkov light cone and its focussing are illustrated in blue [52].

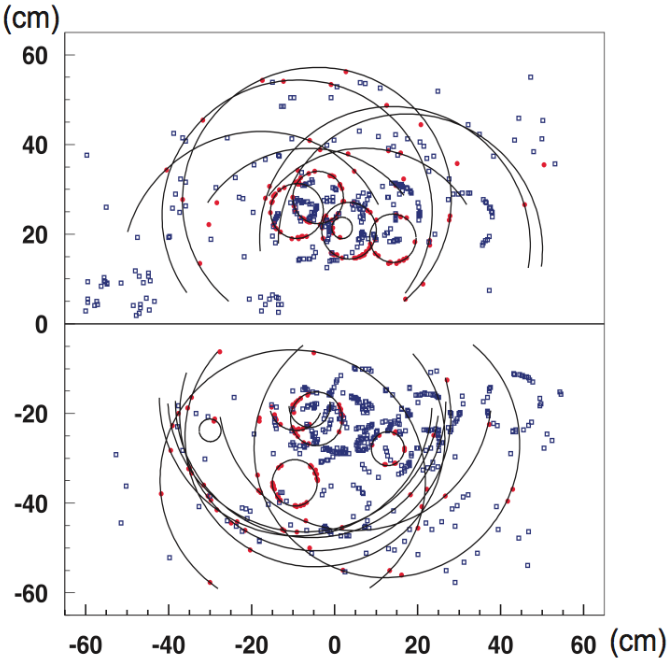

Figure 2.13: Display of a typical LHCb event in RICH1. Cherenkov light cones are fitted and reconstructed as rings [52].

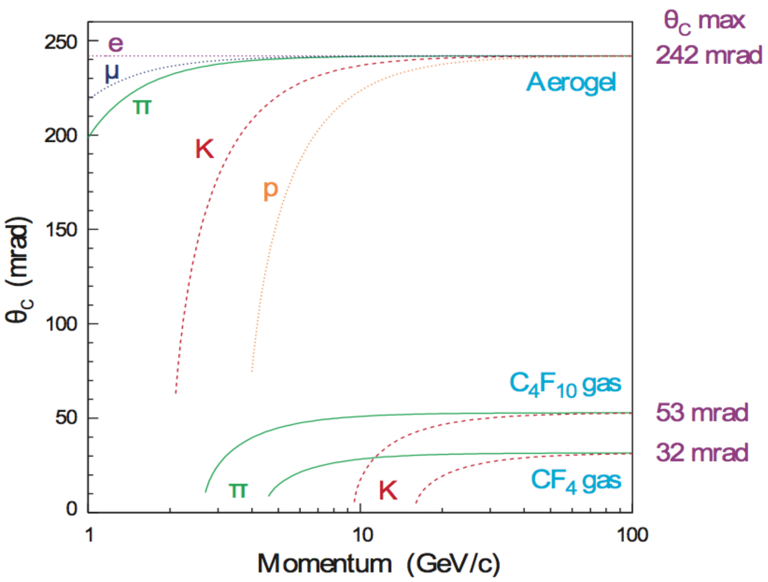

Figure 2.14: Cherenkov angle as a function of momentum for a variety of particles for the three RICH radiators [52].

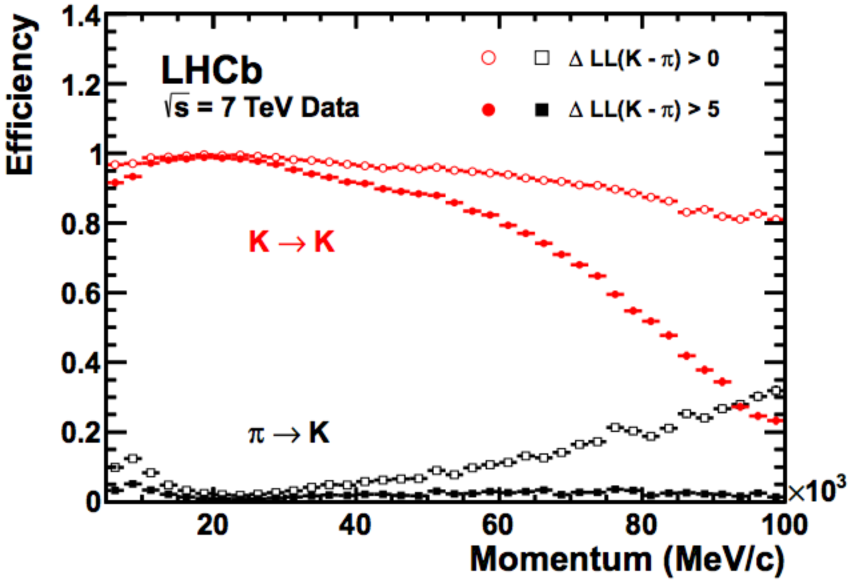

Figure 2.15: Kaon identification efficiency and pion misidentification efficiency as a function of momentum. Two different $\mathrm{DLL}_{K\pi}$ requirements are presented [60].

for C_4F_{10} and 0.68 ± 0.02 mrad for CF_4. Aerogel has a non-symmetric angular resolution, but the standard deviation is estimated at 5.6 mrad [56].

The three different media are chosen for use in the RICH because they each have different indices of refraction. This leads to different momentum thresholds for the particles of interest to produce Cherenkov radiation. These different thresholds are illustrated in Figure 2.14, reflecting the momentum regions of sensitivity for RICH 1 and RICH2.

In more practical terms, RICH performance can be quantified with respect to $\mathrm{DLL}_{K\pi}$, a particle identification variable used in analyses to distinguish between kaons and pions (see Section 3.2.9). The efficiency of correctly identifying a charged kaon as such and that of misidentifying a charged pion as a kaon is presented in Figure 2.15. As illustrated, RICH performance deteriorates with increasing momentum because the Cherenkov rings saturate in angle. Based on the performance of the radiators, the optimum momentum range for the distinguishing of pions and kaons is 5–100 GeV/c with a p_{T} range of 0.5–10 GeV/c.

2.2.5 Calorimetry

The calorimeter system at LHCb provides a measurement of energy and position for photons, electrons and hadrons. Although the detector subsystems discussed up to this point are only sensitive to charged particles, the calorimeters can detect neutral particles and in particular play an important role for analyses involving electrons, π^0 mesons and photons. Furthermore, this ability to detect electromagnetic particles is exploited by the LHCb Level-0 trigger system in its decisions regarding which pp collision events to keep (the trigger is more thoroughly discussed in Section 2.2.7.1). There are four main components to the calorimetry system: the SPD, the PS, the ECAL and the HCAL. They are all located downstream of RICH2, after M1, the first muon station.

2.2.5.1 SPD and PS

The SPD is an array of 15 mm thick scintillator pads. Given that particle density is expected to be higher in the region immediately surrounding the beampipe, the SPD is segmented into three different regions, as illustrated in Figure 2.16(a), where the tiles have different dimensions. These calorimeter tiles correspond to *cells* within the detector. In the inner section, the cells are approximately 4×4 cm in size, 6×6 cm in the middle section and 12×12 cm in the outer section [52]. As particles traverse the tiles, the generated scintillation light is transmitted to a series of photo multiplier tubes via wavelength-shifting (WLS) fibres in the tile. However, only charged particles deposit their energy in the SPD [61], allowing it to distinguish between electrons and photons that are deposited further downstream.

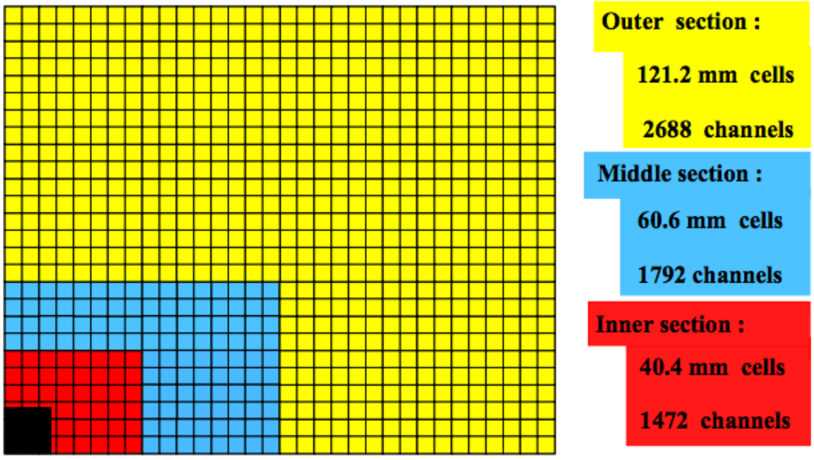

(a) Lateral segmentation of SPD, PS and ECAL. The dimensions listed are the tile sizes for the ECAL.

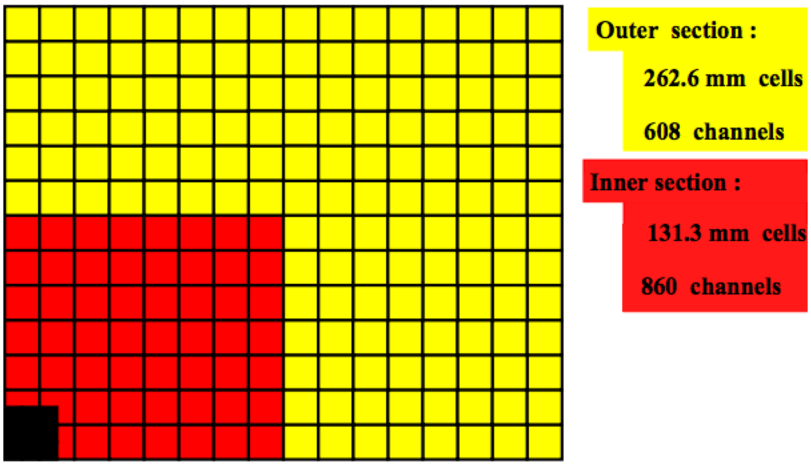

(b) Lateral segmentation of the HCAL.

Figure 2.16: Segmentation in the LHCb calorimetry system. The black section represents the non-instrumented region where the beampipe is present [61].

Downstream of the SPD lies the PS, another array of scintillator pads that is identical to the SPD. However, between the SPD and the PS is a 15 mm lead converter, corresponding to approximately 2.5 X_0, where X_0 is a radiation length. Electrons will shower in this converter, with the effects of the shower being detected by the PS and continuing further downstream to the ECAL. This process allows data from the ECAL and PS to be used to distinguish between electron candidates and charged pion candidates.

2.2.5.2 ECAL

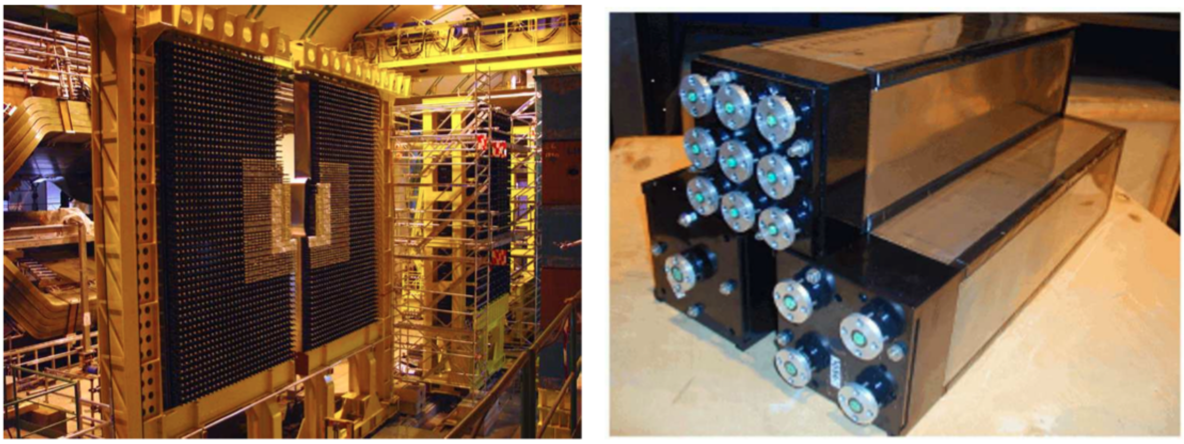

Figure 2.17: The electromagnetic calorimeter. The image on the left clearly shows the three different sections and the image on the right shows the three different types of modules [52].

The electromagnetic calorimeter is situated immediately downstream from the PS. It is a sampling calorimeter consisting of a *shashlik* layout where alternating layers of absorber and scintillator material are penetrated by a WLS running perpendicular to the face of the layers. Specifically, the ECAL is made of a series of modules, each containing 66 layers. These layers are composed of a 2 mm thick lead tile, a 120 μm white reflecting paper and 4 mm thick tile of scintillator [52]. This overall depth of these modules (and, consequently, the ECAL itself) is approximately 25 X_0; as a result, all showers from high energy photons are contained within the subdetector. The absorber material is sufficient to stop electrons and photons within the ECAL. Furthermore, like the SPD and PS, the ECAL is segmented into three different sections with different values of calorimeter cell density, as illustrated in Figure 2.16(a). In practice, this is achieved by using different quantities of WLS traversing the calorimeter modules, leading to three different types of modules, as depicted in Figure 2.17.

The energy resolution of the ECAL is

$$\frac{\sigma_E}{E} = \frac{a}{\sqrt{E}} \oplus b \tag{2.3}$$

where a varies between $8.5\% < a < 9.5\%$, b is approximately 0.8% and E is measured in GeV [52]. The exact resolution value is dependent on the type of ECAL module.

2.2.5.3 HCAL

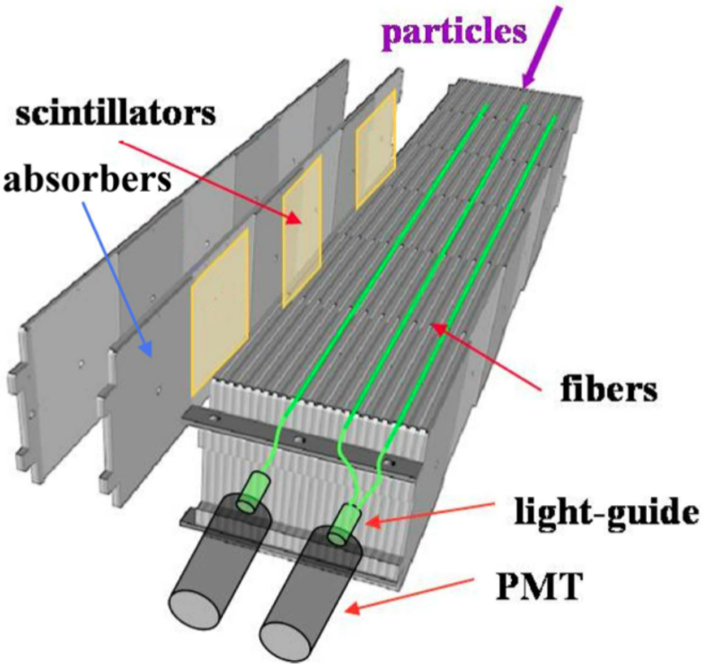

Figure 2.18: A schematic of a hadronic calorimeter module [52].

The hadronic calorimeter is a sampling calorimeter that uses scintillating tiles and an iron absorber. Unlike the ECAL, the plates of scintillator and absorber are oriented such that the faces with the greatest surface area lie parallel to the direction of the beam, as is illustrated in Figure 2.18. In the x-direction, the scintillator plates are separated from each other by 1 cm of iron, while the total length of the module corresponds to 5.6 interaction lengths [61]. The scintillation light is carried from the scintillating tiles to the photomultipliers via WLS, like the other subdetectors in the calorimetry system. However, instead of three areas of lateral segmentation, the HCAL only has two, where the outer cells are four times the area of the inner cells. Like the ECAL, cell density is varied by the amount of WLS fibres in the modules.

The energy resolution of the HCAL is

$$\frac{\sigma_E}{E} = \frac{(69 \pm 5)\%}{\sqrt{E}} \oplus (9 \pm 2)\% \tag{2.4}$$

where E is measured in GeV [52].

2.2.6 Muon System

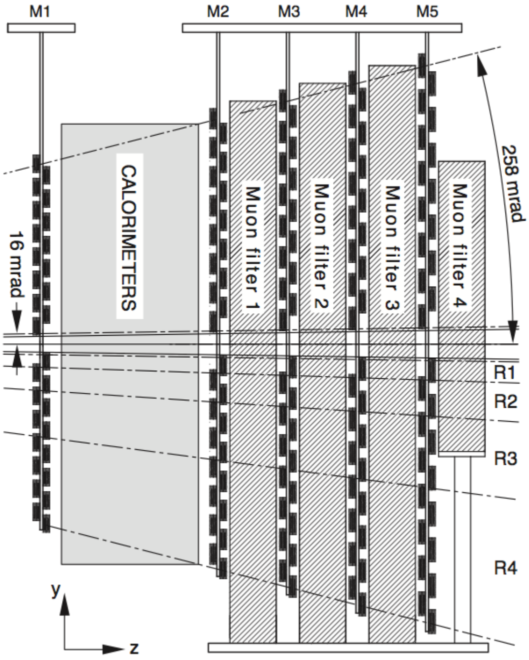

Figure 2.19: Side view of the muon stations and the lead absorbers. R1 is closest to the beampipe while R4 is furthest away [52].

The detection of muons at LHCb is performed by the five muon stations, M1 to M5, in which there are a total of 1380 chambers. The placement of M1 is directly upstream of the SPD, while M2 to M5 are situated downstream of the HCAL. The latter are separated by iron plates, 80 cm in thickness, which are used to stop hadrons from entering the chambers while allowing muons to penetrate. The muon stations are separated into four regions, R1 to R4, as depicted in Figure 2.19. These regions, have linear dimensions that scale as 1:2:4:8, which allows for roughly the same quantity of particle flux in each of the regions, per station.

In addition to determining the trajectory and momentum of muons, the muon system also plays a vital role in the LHCb Level-0 trigger (further discussed in Section 2.2.7.1).

M1, located closest to the interaction point, is composed of triple-GEM (Gas Electron Multiplier) detectors, so chosen because of their radiation hardness properties [52]. The gas used is a mixture of $C_2H_2F_4$, C_4H_{10} and SF_6 [62]. The other muon stations are Multi-Wire Proportional Chambers. These chambers allow for the measurement of muon p_{T} and the trajectory of the different stations that have been hit by a muon allows for tracking to be performed.

2.2.7 Trigger

Proton bunch crossings that contain at least one inelastic pp collision occur at a rate of approximately 11 MHz at LHCb. The role of the trigger system is to reduce this value to a rate of 5 kHz [63] so that these events can be written to storage. Effectively, the trigger decides which collision events are most relevant to the physics research objectives of LHCb and stores them for future analysis. A two-stage approach is used in the trigger system: there is a Level-0 (L0) trigger implemented in hardware which reduces the event rate to 1 MHz, followed by a High Level Trigger (HLT) implemented in software that further reduces the rate to 5 kHz. Groupings of trigger selections are referred to as trigger *lines*.

2.2.7.1 L0

In general, the decay of B mesons tend to produce particles with high transverse momenta (p_{T} up to approximately 5 GeV/c) and transverse energy (E_{T}), relative to the background of low-energy QCD processes. The L0 trigger, therefore, exploits this signature in its decision process. However, the buffer time of the hardware read-out chips of the trigger is only 4 μs, meaning that decisions must be made within this time period. In order to decide whether the event is kept or not, the trigger reconstructs the highest E_{T} hadron, electron and photon deposits in the calorimeters and the two highest p_{T} muons in the muon stations. Specifically, the L0 trigger relies on two independent systems: the L0 calorimeter trigger and the L0 muon trigger.

The L0 calorimeter trigger creates 2×2 clusters of calorimeter cells and chooses those with the highest E_{T}. Depending on whether energy is deposited in the SPD, PS, the ECAL or the HCAL, the clusters are identified either as photon-based (`L0Photon`), electron-based (`L0Electron`) or hadron-based (`L0Hadron`). The measured E_{T} is compared to a fixed threshold and events containing at least one candidate above the threshold are kept by the L0 calorimeter trigger [64].

The L0 muon trigger reconstructs muon tracks by searching for hits in the muon chambers compatible with a straight line through the chambers and that point towards the interaction point in the yz plane. Two values are calculated: the candidate with the highest p_{T} (`L0Muon`) and the product of the p_{T} of the candidates with the highest and second-highest transverse momentum (`L0DiMuon`) [64]. Both of these values are compared to their respective thresholds and if either pass, the event is kept by the L0 muon trigger.

Collectively, all of the L0 calorimeter and muon triggers are grouped under the `L0Global` trigger. Effectively, any event kept by any L0 trigger is kept by the `L0Global` trigger.

The L0 decision process also includes a pile-up system that is not used for selecting physics events. This system is used exclusively for measuring pile-up for the purposes of luminosity levelling. A schematic of the inputs into the L0 decision process is provided in Figure 2.20.

2.2.7.2 HLT

The HLT is written in C++ and installed on a farm of 2000 multiprocessor nodes. Approximately 29000 logical cores are available to simultaneously process the data from the L0 trigger, with a processing time limited to roughly 30 ms per event.

There are two stages to the HLT. The first, the HLT1, executes a partial reconstruction of events and performs an inclusive selection of signal candidates, reducing the event rate to 80 kHz [63]. The second, the HLT2, undertakes a complete event reconstruction and then implements a set of inclusive and exclusive selections, further reducing the event rate to 5 kHz.

The HLT1 performs a partial reconstruction by reconstructing tracks in the VELO,

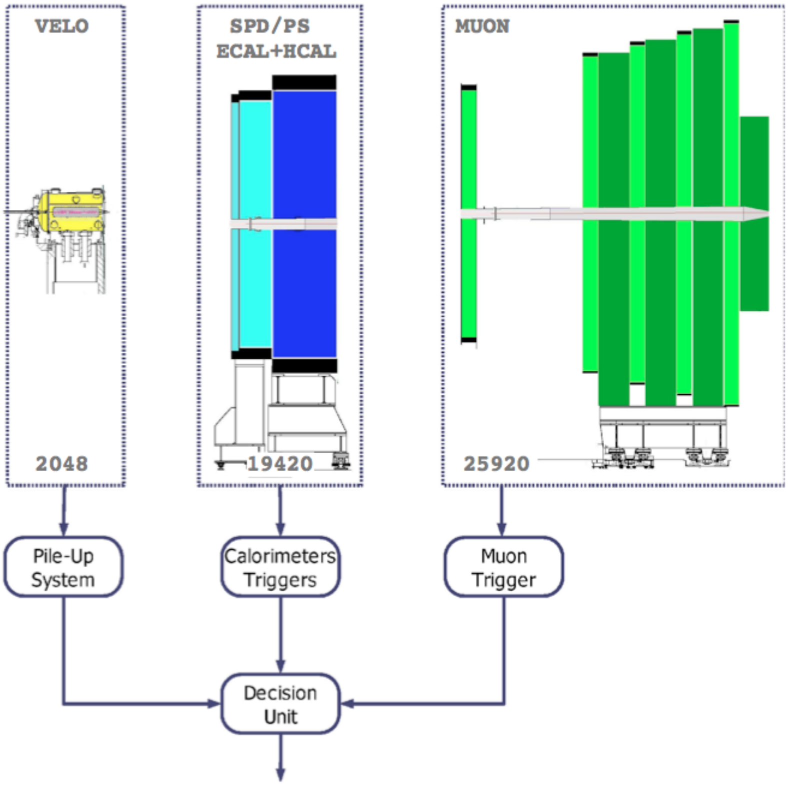

Figure 2.20: A schematic of the L0 decision process. The numbers indicate the quantity of logical channels that are used for each of the trigger components. The pile-up system is used exclusively for luminosity levelling and does not play a role in selecting physics events [52].

matching them to tracks in the muon stations and extrapolating their trajectory through the tracking stations. The `HLT1TrackAllL0Decision` trigger lines, developed specifically for the identification of b- and c-hadrons, select tracks with a $p_{\mathrm{T}} > 1.6\ \mathrm{GeV}/c$ and displacement from the primary vertex. If the track can be matched to activity in the muon chambers and has a $p_{\mathrm{T}} > 1\ \mathrm{GeV}/c$ and is not from a primary vertex, it is selected. If it has a $p_{\mathrm{T}} > 4.8\ \mathrm{GeV}/c$, it is selected regardless of vertex considerations. Dimuon candidates are selected if the sum of the muon masses is greater than $2.5\ \mathrm{GeV}/c^2$, or based on the distance between their primary and secondary vertices without any mass considerations [63].

The HLT2 performs a full event reconstruction for all HLT1 selected tracks with $p_{\mathrm{T}} > 300\ \mathrm{MeV}/c$. Several selections are applied, some pertaining to events with a muon or with c-hadrons. However, for decays involving b-hadrons, the most relevant selection are the topological `HLT2Topo(N)BodyBDTDecision` trigger lines which use two-, three- and four-prong vertices [65]. These trigger lines rely upon the use of a Boosted Decision Tree multivariate classifier [66], for which one of the input variables is the *corrected mass*, defined as

$$m_{\mathrm{corr}} \equiv \sqrt{m^2 + |p_{\mathrm{T}}{}^{\mathrm{miss}}|^2} + p_{\mathrm{T}}{}^{\mathrm{miss}}, \tag{2.5}$$

where $p_{\mathrm{T}}{}^{\mathrm{miss}}$ represents the missing momentum in the transverse direction. The use of such a variable allows for the selection of events containing b-hadrons, even in the case where not all of the final state particles are reconstructed [63]. Events that pass the HLT2 selection are written to tape storage, where each event is about 60 kB in size [67]. Of the total bandwidth of the HLT2, roughly 20% is allocated to muonic selections while approximately 40% each are dedicated to the charm streams and the topological b-quark triggers [63].

2.2.8 Stripping

Before data are analysed at LHCb, an effective offline trigger, the *Stripping*, is applied to reconstructed events that pass the HLT2 requirements. Analogous to the trigger lines, stripping lines are a series of selection criteria that are made to identify certain candidates of importance for physics analyses. As such, stripping lines are generally designed with the objective of isolating specific decays or specific collections of decays of interests for analysts or for the purposes of calibration. This selection process has the effect of separating the datasets into smaller, more manageable samples, each one relevant for a specific set of analyses. Stripping is a computationally intensive exercise as it must be run over all of the collected data from HLT2 for several hundred different stripping lines. The processing of each event per stripping line can take up to 0.5 ms. The particular stripping lines of use in this analysis are more thoroughly discussed in Section 3.5.

2.2.9 Software Framework

The LHCb software framework is based on GAUDI [68]. It is an Object Oriented Framework used for simulation and reconstruction. Since the framework is common to simulated Monte Carlo (MC) events and collision data reconstruction, both MC and data are processed through the same software environment.

2.2.9.1 Simulation

The simulation of LHCb events is achieved using the GAUSS software [69]. This application performs both event generation and detector simulation tasks. Primary interactions of pp collisions are generated using a LHCb-tuned version of PYTHIA 8 [70, 71] with CTEQ6L parton distribution functions [72] and the decays of the produced particles are performed by EVTGEN [73]. The interaction of these particles with the detector is then modelled using GEANT4 [74, 75].

The output from GAUSS is then used as an input to the BOOLE software [76] where simulation of the LHCb subdetectors is performed. BOOLE simulates the energy deposited in the active material of the LHCb detector. In addition, BOOLE also simulates the L0 hardware trigger. The output from BOOLE is the same format as the raw LHCb data files, and can thus be reconstructed using the same software process.

2.2.9.2 Reconstruction

The HLT1 and HLT2 trigger systems are run by the Moore package [77] in both the LHCb online system and offline for MC events. The trigger settings are defined by a Trigger Configuration Key (TCK), and the simulated data must be run over using the same TCK to ensure accurate emulation of the trigger performance in the online system.

The Brunel software package [78] is used to read raw detector hits and reconstruct them into physics objects such as charged tracks, calorimeter clusters and Cherenkov rings. The software accesses the LHCb condition database in order to retrieve the detector conditions at the time that the event was recorded. These physical objects are saved for data analysis.

The final stage of reconstruction is performed by the DaVinci package [79]. From the physics objects, it creates composed objects such as decay chains and particles and performs the selection of candidates. When analysing MC data, DaVinci is able to access MC Truth information and metadata related to the simulation process. This MC specific information reveals what a given particle and its decay products are at the generator level, regardless of how they may be ultimately reconstructed. Although DaVinci can output to a variety of file formats, it is commonly used to produce Ntuples suitable for further analysis.

Chapter 3

Candidate Selection

This Chapter describes the procedures used to reconstruct and select candidate decays from LHCb that are ultimately fitted to extract *CP* observables. The candidates are characterised as having two displaced vertices corresponding to the $B^{\mp}$ and the D mesons. Specific particle properties are then discussed as these characteristics are used in the training of a Boosted Decision Tree (BDT) for suppression of backgrounds and enhanced signal isolation. This BDT requires training inputs from both a data sample and simulated events from Monte Carlo, so some discussion is made regarding these samples. The optimisation of the BDT is then described. The Chapter ends with a discussion of several constraints that are placed on the particle masses and the efficiencies of several selection requirements.

3.1 Particle Reconstruction

The reconstruction of particles from LHCb data varies somewhat depending on the nature of the particle in question. In this analysis, we are concerned with decays of the form $B^{\mp} \to [h'^{\pm}h''^{\mp}\pi^0]_D h^{\mp}$, where h, h', h'' may each be a charged pion or kaon, and thus reconstruct a charged $B^{\mp}$ that decays into a four-body final state, including a π^0 meson. A total of 16 different potential final state combinations are possible and all of these are studied simultaneously in this analysis. The h particle that originates from the $B^{\mp}$ decay is referred to as the *bachelor* particle whereas the D decay products are termed *daughter* particles.

The primary vertex (PV) of the pp collision occurs in the LHCb VELO. Given the relatively long lifetime of the b quark [2], the $B^{\mp}$ candidate is identified by a vertex from the PV that is displaced in space. A D candidate in combination with another charged track is used to reconstruct the $B^{\mp}$ particle.

D candidates are identified as secondary displaced vertices. They are reconstructed as having two charged h daughters and a π^0. The charged kaons and pions of the event are identified as such through their interaction with the RICH system. However, the π^0 does not leave a track in the detector as it is uncharged. As such, it must be reconstructed through other means as discussed in Section 3.1.1.

Related to reconstruction is the concept of refitted decay trees. Traditionally, a decay tree is fit by starting with the fitting of the most downstream vertex in the decay and building the tree by propagating this information upstream. Such a method, however, does not permit the downstream reconstruction to take advantage of the known constraints (such as mass) from the upstream vertices. In this analysis, the `DecayTreeFitter` algorithm [80] is used where a decay chain is parameterised in terms of vertex positions, momenta and decay times and all of these parameters are fitted simultaneously using a least squares fit while taking into account relevant constraints. Specifically, the algorithm is run with 4-momentum conservation at vertices, mother-daughter distance, lifetime constraints, origin vertex constraints and mass constraints. Ultimately, in this analysis, the decision to use `DecayTreeFitter` is due to improved precision on the invariant mass of the $B^{\mp}$ candidate.

3.1.1 π^0 Reconstruction

Overwhelmingly, π^0 mesons decay to a pair of photons [2]. These photons deposit their energy in the electromagnetic calorimeter system of the detector and allow for a measure of the original particle's momentum. For a high momentum π^0 candidate ($p_{\mathrm{T}} > 2$ GeV/c), the two photons may emerge with a shallow angle between their momentum vectors, while this angle will be larger for a slower moving neutral pion. Depending on the angle between the momentum vectors and the cell density in a particular region of the calorimeter, the two photons may either leave separate energy deposits in the calorimeter (known as *resolved* π^0 candidates) or a single deposit (known as *merged* π^0 candidates).

This analysis uses exclusively resolved π^0 candidates as they have a 33% finer mass resolution compared to their merged counterparts [56].

3.2 Particle Characteristics

Various properties of the reconstructed particles are exploited in this analysis. Some of them, such as invariant mass and momentum, are standard quantities that require no additional introduction. In this section, we present explanations from some characteristics that may be less obvious or are unique to LHCb.

3.2.1 Impact Parameter χ^2

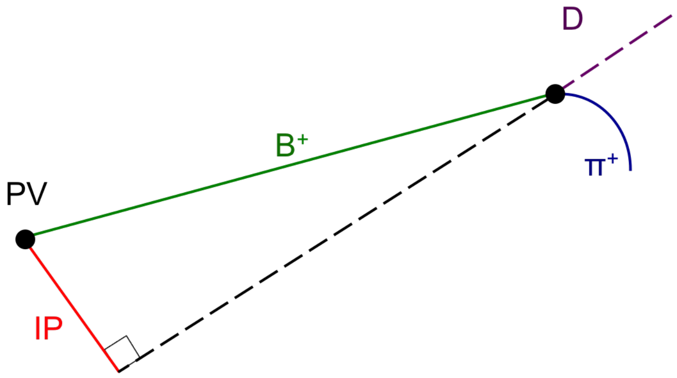

Figure 3.1: A schematic description of impact parameter for the D meson. The dashed black line is an extrapolation of the D meson track.

For a particular track, the impact parameter (IP) is defined as its distance from the primary vertex at the point of closest approach to the primary vertex [56]. A schematic is presented in Figure 3.1. As discussed in Section 3.2.2, a fitting procedure is performed on vertices and assigned a χ^2 value based on the tracks that make up the vertex. The IP χ^2 (χ^2_{IP}) is defined as the difference between the χ^2 of the PV reconstructed with and without the track of interest. Cases where the IP and the χ^2_{IP} are small offer a greater likelihood that the particle in question is associated to the primary vertex. For instance, a χ^2_{IP} requirement can be used to select $B^{\mp}$ candidates that originate from the PV.

3.2.2 Vertex χ^2

Identifying the location of particle vertices in space plays an important role in the reconstruction of the $B^{\mp}$ and D candidates. The particle tracks that appear to originate from a vertex may relate to the decay products of the vertex, or they may be due to spectator tracks unrelated to the vertex. There is also the possibility that intersections of random tracks may lead to the appearance of a false vertex. Vertex χ^2, χ^2_{vtx}, is a quantitative measure of the quality of a particle vertex. When determining the tracks corresponding to a vertex, the vertexing algorithm begins with a base track and selects the partner tracks that lie close to it. Close proximity is defined as the partner having a distance of closest approach (see Section 3.2.3) to the base track of less than 1 mm. From this grouping of tracks, for each pair of tracks, the point of closest approach (POCA) is calculated. The tracks contributing the largest POCA are de-selected from the vertex construction if their POCA is greater than 5 mm [81].

The position of the reconstructed vertex is determined by a least squares method that minimises the χ^2 per degree of freedom. This χ^2 number is a weighted sum involving the χ^2_{IP} of the tracks relevant to the vertex [81]. Depending on the value of χ^2_{IP}, a weight, W_T, is assigned using the Tukey biweight method [82]. Formally, the χ^2_{vtx} is given by

$$\chi^2_{\text{vtx}} = \sum_{i=1}^{n_{\text{tracks}}} \chi^2_{\text{IP},i} \cdot W_{T,i}, \tag{3.1}$$

where i represents the different tracks contributing to the vertex. Generally speaking, the lower the value of this χ^2 per degree of freedom, the better the quality of the vertex, and thus the greater confidence that the vertex belongs to the desired particle.

3.2.3 Distance of Closest Approach

The distance of closest approach (DOCA) is a measure of the closest distance between a parent particle and its decay products. For the case of the D meson in this analysis, the DOCA is measured for each of its daughters including the π^0, while for the $B^{\mp}$ candidate, it is calculated for the D and the bachelor. When discussing DOCA, it is common to consider the *maximum* DOCA; the largest DOCA of the associated decay products.

3.2.4 Director Angle

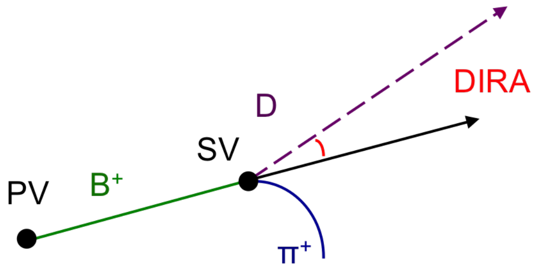

Figure 3.2: A schematic description of DIRA for the D meson. SV represents the secondary vertex and the trajectory of the B^+ meson in the diagram is assumed to be identical to the direction vector between the PV and SV.

The director angle (DIRA) is defined as the angle between the momentum vector of a given particle and the direction vector between the primary and secondary vertices. A schematic is provided in Figure 3.2. This quantity is commonly calculated for particles with displaced vertices, such as $B^{\mp}$ and D candidates.

3.2.5 p_{T} Asymmetry

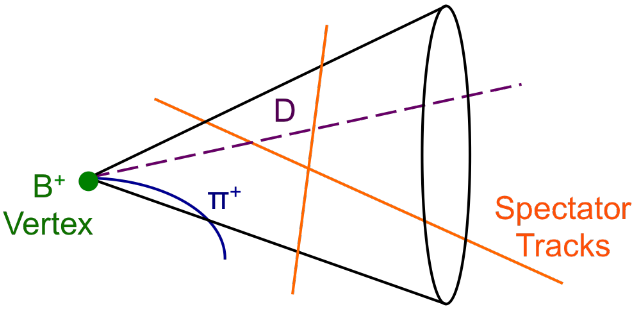

Figure 3.3: A schematic representation of the cone construction used in the calculation of $\mathrm{A}_{p_{\mathrm{T}}}$.

The p_{T} asymmetry, $\mathrm{A}_{p_{\mathrm{T}}}$, is an isolation variable that considers the p_{T} imbalance about the charged B candidate. This variable is constructed by building a cone around the candidate and counting the charged tracks in this cone that do not contribute to the candidate's reconstruction. For example, in $B^+ \rightarrow D\pi^+$ decays, the tracks of the D and π^+ candidates relate to the B candidate while spectator tracks from the event do not. An illustration of such a cone is provided in Figure 3.3. The $\mathrm{A}_{p_\mathrm{T}}$ quantity is defined as

$$\mathrm{A}_{p_\mathrm{T}} = \frac{p_T(B) - \sum_n p_t}{p_T(B) + \sum_n p_t}, \tag{3.2}$$

where the sum is performed over the n tracks not related to the $B^{\mp}$ candidate.

Under idealised circumstances where no spectator tracks are present in the cone, $\mathrm{A}_{p_\mathrm{T}}$ has a value of unity. However, in any case where spectator tracks are present, this value will be less than one. In general, an $\mathrm{A}_{p_\mathrm{T}}$ value closer to unity is preferred as it represents a greater probability that B candidate vertex is properly reconstructed; fewer spectator tracks imply a smaller likelihood of the B vertex of being misreconstructed.

Based on previous studies [83], the cone is defined to have a circle of radius 1.5 units in the plane of pseudorapidity and azimuthal angle (measured in radians).

3.2.6 Flight Distance χ^2

The flight distance (FD) of a particle is the spatial distance traversed before it decays. Experimentally, a measurement of flight distance is performed in relation to the two vertices that mark the ends of the track of the particle in question. However, as discussed in Section 3.2.2, there is uncertainty as to the position of vertices or whether they are actually genuine vertices at all. As a result a measurement of FD has an accompanying uncertainty, σ_FD. Flight distance χ^2, χ^2_FD, quantifies the quality of the flight distance measurement. It is expressed as [84]

$$\chi^2_\mathrm{FD} = \frac{\mathrm{FD}^2}{\sigma^2_\mathrm{FD}}. \tag{3.3}$$

3.2.7 D Flight Distance z-Significance

Since D mesons are not experimentally observed in this analysis and are instead, reconstructed from their final-state decay products, it is important to be able to distinguish between $B^{\mp}$ decays with a D meson and those that do not have a D but have a final state with the same daughters of the D decay. In order to suppress such events, one can study the D flight distance z-significance, FD_D. This quantity is defined as

$$\mathrm{FD}_D \equiv \frac{z_D^{\mathrm{vtx}} - z_B^{\mathrm{vtx}}}{\sqrt{\sigma_{z_D}^2 + \sigma_{z_B}^2}}, \tag{3.4}$$

where $z_{D/B}^{\mathrm{vtx}}$ refers to the z-position of the D or $B^{\mp}$ vertex and $\sigma_{z_{D/B}}$ is the uncertainty on this position measurement. Effectively, FD_D quantifies the separation between the B and D vertices and thus the greater its value, the greater the probability that a true D is present in the event and not a misidentified D due to a poorly reconstructed vertex. An illustration of D flight distance is provided in Figure 3.4.

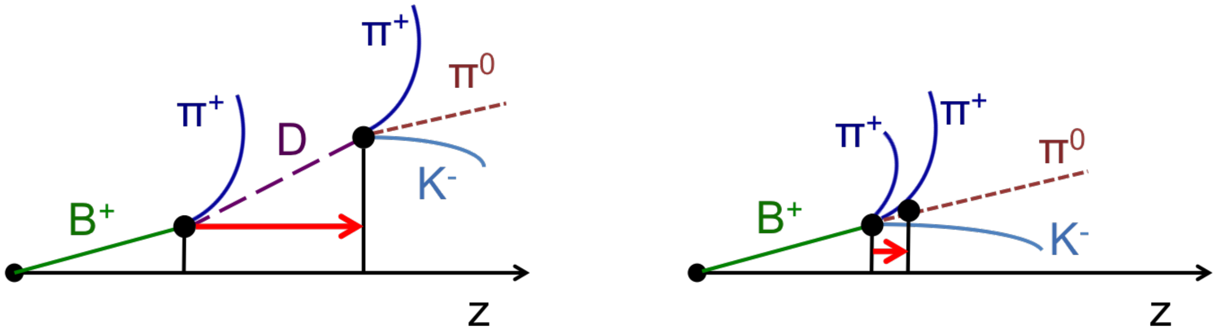

Figure 3.4: A schematic of D flight distance in the z plane, represented by the red arrow. On the left, the flight distance is measured correctly between the B^+ and D vertices. On the right, a D vertex is mistakenly reconstructed leading to a shorter measured D flight distance.

3.2.8 Photon Confidence Level

Since photons from decayed π^0 candidates are only detected by the electromagnetic calorimeter, it is possible to mistakenly attribute an energy deposit in the calorimeter to a photon and thus incorrectly identify a photon. In order to quantify the probability that an identified photon is indeed the particle in question, a photon hypothesis likelihood is used. This hypothesis is computed using signal and background probability density functions of several variables, notably the PS energy deposits, a χ^2 estimator between the energy cluster and a track of a charged particle and the ratio between the energy of the central cell of the ECAL cluster and the total ECAL energy [56]. The difference in log-likelihood between the photon and background hypotheses is calculated and generally yields a distribution with values from

-5 to 5. These values are then transformed with a hyperbolic tangent function so as to give a distribution between 0 and 1. This quantity is termed *photon CL*, with 1 corresponding to a greater confidence that the signal originates from a genuine photon.

3.2.9 Particle Identification

Particle identification (PID) information is obtained from LHCb's RICH, muon and calorimeter systems. The information from these subsystems is combined in order to create a powerful set of separation variables. A logarithm of likelihoods, $\ln \mathcal{L}_x$, is calculated for five separate mass hypotheses where $x \in \{e, \mu, \pi, p, K\}$. A difference of these log likelihoods (DLL), with respect to the pion hypothesis, can then be constructed where $\mathrm{DLL}_{x\pi} \equiv \ln \mathcal{L}_x - \ln \mathcal{L}_\pi$. In this analysis, we are particularly interested in distinguishing kaons from pions, so a $\mathrm{DLL}_{K\pi}$ is commonly used, abbreviated as PIDK. In general, PIDK values range from -100 to 100, with the vast majority of entries of order unity. Most genuine kaon candidates will have positive PIDK values, whereas most pions will have negative values, however misidentifications are common in the vicinity of PIDK = 0. Section 3.9 discusses bachelor PID requirements in further detail. Unless otherwise stated, PID requirements in this thesis will refer to PIDK.

3.3 Data and MC Events

The data used in this thesis were collected by LHCb, corresponding to a total integrated luminosity of 3 fb^{-1}. Of these, 1 fb^{-1} was collected in 2011 in pp collisions at $\sqrt{s} = 7$ TeV and 2 fb^{-1} were collected in 2012 at $\sqrt{s} = 8$ TeV. In order to compensate for potential material differences and detection inefficiencies in the left and right portions of the detector, the LHCb magnet polarity is switched several times during data taking. The two states are referred to as *MagUp* and *MagDown*. Table 3.1 lists the different amounts of data collected per year, as split by magnet polarity.

The MC used in this analysis was simulated using the software described in Section 2.2.9.1. Approximately two million events each of the decay modes $B^\mp \to [K^\mp\pi^\pm\pi^0]_D\pi^\mp$, $B^\mp \to [K^\mp\pi^\pm\pi^0]_D K^\mp$, $B^\mp \to [\pi^+\pi^-\pi^0]_D\pi^\mp$, $B^\mp \to [\pi^+\pi^-\pi^0]_D K^\mp$, $B^\mp \to [K^+K^-\pi^0]_D\pi^\mp$ and

Table 3.1: Integrated luminosities of data collected for different years and magnet polarities.

Year	Magnet Polarity	Integrated Luminosity (pb^{-1})
2011	MagUp	434 ± 15
2011	MagDown	584 ± 20
2012	MagUp	1006 ± 51
2012	MagDown	1026 ± 51

$B^{\mp} \to [K^+K^-\pi^0]_D K^{\mp}$ were generated. These events are generated without any generator filters and include both MagUp and MagDown contributions and correspond to the number of events prior to the consideration of geometric detector acceptance, trigger or selection effects.

Both the data and MC undergo the same reconstruction procedure described in Section 3.1.

3.4 Trigger Requirements

In this analysis, we do not use all of the LHCb events that are written to storage. Instead, in order to reduce the data volume and focus on those events most relevant for the analysis, only events that follow a specific trigger chain are used.

Section 2.2.7.1 has previously discussed the L0 triggers at LHCb. In this analysis, at the L0 level, the `L0Hadron` and `L0Global` triggers are the most relevant. However, these triggers are further qualified by the use of Trigger on Signal (TOS) and Trigger Independent of Signal (TIS) classifications. An event where the signal candidate is sufficient for the trigger is TOS, while an event that is not triggered by the signal candidate is relegated as TIS. Here, 'signal' refers to the decay products of the final $B^{\mp}$ candidate. TOS and TIS are mutually exclusive classifications; if an event is classified as TOS because it is triggered by a signal candidate, it cannot also be classified as TIS.

At the L0 level, there is a requirement that the event is either classified as TOS from the hadron calorimeter trigger or as TIS (`L0HadronTOS || L0GlobalTIS`). This selection is specifically chosen so as to eliminate TOS events from the muon system because none of the final states of interest include a muon. As a result, decays of the form $B^{\mp} \to J/\psi K^{\mp}$ are excluded by this requirement.

All events that pass the L0 requirements are then subject to the HLT1 requirement, `HLT1TrackAllL0_TOS`. This selection implies that the signal candidates pass the single track trigger. Specifically, this trigger selects the decays of long-lived particles, generally hadrons with a b or c quark, and thus is of interest for our $B^{\mp}$ signal decays. The `HLT1TrackAllL0_TOS` requirement attempts to select hadron candidates with vertices significantly displaced from the PV. This is achieved by requiring at least 10 VELO hits per track, a track $\chi^2_{\mathrm{IP}} > 16$, a track $p_{\mathrm{T}} > 1.7\ \mathrm{GeV}/c$ and a track $p > 10\ \mathrm{GeV}/c$, among other criteria [64].

Finally, the events that pass the HLT1 trigger are subject to the HLT2 requirements. The `HLT2Topo2BodyBDTDecision_TOS` trigger and its 3- and 4-body equivalents are used as they involve signal events with a D decaying to 2, 3 or 4 daughters. Given that all the decays of interest in this analysis involve a multi-body D decay, this is a beneficial choice of HLT2 trigger.

3.5 Stripping

After track reconstruction, the B candidates are built and filtered according to some loose selection criteria. This stripping selection has the main purpose of reducing sample sizes so as to decrease CPU time during analysis as well as providing the analyst with more manageable file sizes.

In this thesis, all samples come from the `Beauty2Charm` algorithms run with the `Bhadron` stripping stream [85], which specialises in inclusive decays of the form $B \to DX$ (where X represents a generic single or multi-body final state). In particular, all decay modes are taken from the `B2D0PiD2Pi0HHResolved` and `B2D0KD2Pi0HHResolved` stripping lines which have loose selection criteria on $B^{\mp} \to Dh^{\mp}$ events where the D decays to a three-body final state composed of two charged h candidates and a resolved π^0.

The general strategy of the stripping lines is to select events with the appropriate topological triggers as a base and then perform background rejection by placing loose cuts on the B and D candidates. These cuts include requiring B and D vertices to have a χ^2 less than 10 and for the B to have a proper lifetime of greater than 0.2 ps. In addition, the B candidate must lie in the range of 4500–7000 MeV/c^2. All D candidates, on the other hand, must lie in a mass window of ±250 MeV/c^2 about the nominal D mass. For the photons from the π^0 decays, both must have a photon CL of greater than 0.25.

Figure 3.5 shows the mass distributions for the D and π^0 candidates, in data, from the decay $B^\mp \to [K^\mp\pi^\pm\pi^0]_D\pi^\mp$ after the stripping selection. Peaks can be identified in each distribution, though the high level of backgrounds mean that more advanced selection methods are required for the final analysis. The B mass distribution for the same decay mode after the stripping selection is presented in Figure 3.10(a). For reference, in the B mass range of 5000-7000 MeV/c^2, for $B^\mp \to [K^\mp\pi^\pm\pi^0]_D\pi^\mp$ decays, after the stripping selection, a total of 6.7×10^7 events remain.

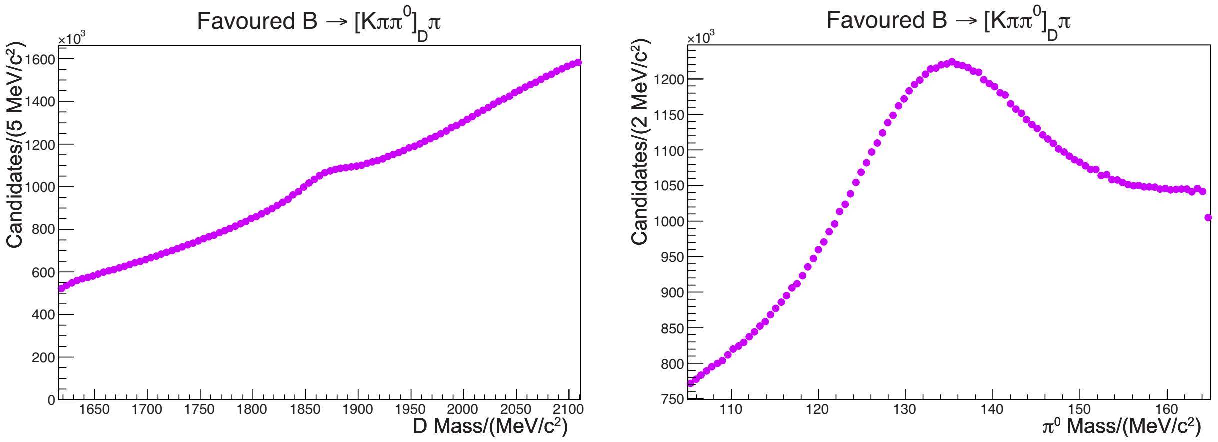

(a) D mass distribution for $B^\mp \to [K^\mp\pi^\pm\pi^0]_D\pi^\mp$

(b) π^0 mass distribution for $B^\mp \to [K^\mp\pi^\pm\pi^0]_D\pi^\mp$

Figure 3.5: The D and π^0 mass distributions direct from the stripping selection for $B^\mp \to [K^\mp\pi^\pm\pi^0]_D\pi^\mp$ decays.

3.6 Boosted Decision Tree Selection

For $B^\mp \to Dh^\mp$ decays, the relevant branching fractions are [2]

$$\mathcal{B}(B^- \to D^0\pi^-) = (4.81 \pm 0.15) \times 10^{-3}$$

$$\mathcal{B}(B^- \to D^0K^-) = (3.70 \pm 0.17) \times 10^{-4}.$$

The branching fractions of the D decays relevant to this analysis are

$$\begin{aligned}
\mathcal{B}(D^0 \to K^-\pi^+\pi^0) &= 0.139 \pm 0.005 \\
\mathcal{B}(D^0 \to K^+\pi^-\pi^0) &= (3.04 \pm 0.17) \times 10^{-4} \\
\mathcal{B}(D^0 \to \pi^+\pi^-\pi^0) &= (1.43 \pm 0.06) \times 10^{-2} \\
\mathcal{B}(D^0 \to K^+K^-\pi^0) &= (3.29 \pm 0.14) \times 10^{-3}.
\end{aligned}$$

Consequently, a suppressed decay of the form $B^\mp \to [\pi^\mp K^\pm \pi^0]_D K^\mp$ has a branching fraction of order 10^{-7}. To observe such a rare process is a challenging endeavour and one which requires significant background suppression.

In order to separate signal from backgrounds, a common selection procedure at LHCb is the use of a multivariate analysis (MVA). A particular MVA classifier, the Boosted Decision Tree (BDT) [86,87] has been demonstrated to be very effective for the purposes of background suppression while maintaining a high level of signal efficiency in studies of $B^\mp \to Dh^\mp$ decays [83,88,89]. BDTs (and MVA methods in general) can exploit the correlations between input variables and allow for a signal efficiency that can be higher than simply applying cuts to kinematic variables. In fact, in highly correlated systems, it may not be obvious which variables will lead to an effective suppression of backgrounds. A BDT helps by providing a single response variable, incorporating information from several input variables, which can be used instead.

3.6.1 BDT Overview

In decision-tree learning, a series of binary decisions are used as a predictive model. These decision nodes are used to categorise an event as either signal or background. Each node uses a signal discriminating variable (input variable) in its decision. As more nodes are added, a tree-like structure forms, as seen in Figure 3.6, where the *leaf* nodes at the end of the tree have mainly signal-like or background-like events [90]. This is a machine learning process in which starting signal and background samples are used to train the classifier. The training process is what defines the cut criteria for each decision node.

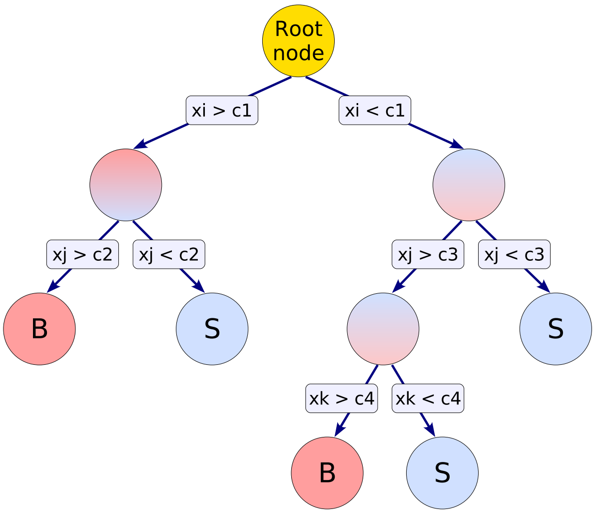

Figure 3.6: A schematic representation of a decision tree. Binary decisions using the discriminating variables x_i are applied to the data. After a series of these decisions, the leaf nodes at the bottom of the tree have events that mainly signal-like (S) or background-like (B) [90].

A boosted decision tree generally uses some form of weighting in the decision process so as to extract greater overall discrimination power by exploiting variables that may not be very good signal/background discriminators on their own. An application of boosting is taking training signal events that end up in a background leaf and giving them a larger weight than events that end up in the correct leaf node. This leads to a reweighted training sample from which a new decision tree can be developed. In principle, this boosting can be performed multiple times leading to a set of decision trees. The average of the individual decision trees is used to make a single classifier which is less susceptible to fluctuations in the original training samples and can offer enhanced discrimination performance compared to a single tree [90].

In this thesis, we use the BDT implementation from the Toolkit for Multivariate Data Analysis with ROOT (TMVA [90]) with the *GradientBoost* algorithm [91]. This provides a response variable that ranges from -1 to 1, with -1 corresponding to a purely background-like event and 1 being a purely signal-like event.

3.6.2 Signal and Background Training Samples

Combinatorial background, in this thesis, is formed from the random combinations of charged tracks and a neutral π^0 that have the same final state particles as our decay channels of interest, but are not related to our signal decays. These events are independent of the physics topology of the signal modes and consequently are distributed across all of the B mass region of interest to this analysis. This combinatorial background is the primary background that we attempt to suppress through the use of a BDT.

The signal candidates used to train the BDT come from simulated data (MC). The sample is made up of reconstructed $B^{\mp} \to [K^{\mp}\pi^{\pm}\pi^0]_D K^{\mp}$ and $B^{\mp} \to [K^{\mp}\pi^{\pm}\pi^0]_D \pi^{\mp}$ candidates that pass the stripping selection, the trigger selection and satisfy MC truth requirements that the individual candidate particles are indeed what they are reconstructed as. A total of 9299 candidates are present in the signal sample.

The background training sample is supplied from data. In the mass regime significantly greater than the nominal $B^{\mp}$ mass, the only background contribution is combinatorial in nature. Thus, the background training sample consists of wrongly reconstructed $B^{\mp} \to [K^{\mp}\pi^{\pm}\pi^0]_D K^{\mp}$ and $B^{\mp} \to [K^{\mp}\pi^{\pm}\pi^0]_D \pi^{\mp}$ candidates that pass the stripping and trigger selections and lie in the upper B invariant mass sideband of 5900 MeV/c^2 and greater. These events also include the additional constraint that when their vertices are refitted using `DecayTreeFitter`, a D and a π^0 candidate are successfully reconstructed. Over 7 million events are found in this background sample.

3.6.3 Input Variables

Both the signal and background training samples use the same set of variables for the BDT training. The following properties of the B, D, D daughters and bachelor are used (in some instances where the distribution has long tails or a wide range, the logarithm of the variable is used):

- p and p_{T} of the bachelor, D and D daughters;
- DOCA and DIRA for B and D;

- flight distance χ^2 for B and D;
- lifetime with respect to the primary vertex for B and D;
- vertex quality (χ^2 per degree of freedom) of the B and D;
- primary vertex χ^2_{IP} for the B, D and charged D daughters;
- photon CL for π^0 decays;
- B p_{T} asymmetry.

The TMVA package, after performing the training, ranks the variables in terms of discrimination power. These results are presented in Table 3.2 alongside the variable importance, as reported by TMVA. This value is the weighting, as attributed by the boosting process. We note that the most powerful variable is the B p_{T} asymmetry variable and that the properties of the π^0 are also rather important as they appear twice in the top five ranked variables. For completeness, signal and background distributions of the training input variables are presented in Appendix A.

The Receiver Operating Characteristic (ROC) curve for the training process is presented in Figure 3.7, which is a plot of background rejection versus signal efficiency. We see that the BDT is rather performant. Even while suppressing more than 90% of the background, it is able to maintain a signal efficiency of greater than 90%.

After the BDT training is completed, TMVA uses a portion of the unused signal and background training events to test the classifier for potential overtraining. The phenomenon of overtraining can occur when statistical fluctuations in the training samples are interpreted by the BDT as genuine features of the variable distributions. Overtraining can be observed by comparing the distribution of the BDT response variable from the events used in the training to that of a test sample of similar training events. A common strategy is to split the original training samples in two and use half for the actual training and the other half for overtraining testing. Figure 3.8 shows the overtraining checks for the BDT, with backgrounds in red and signal in blue. Given that there are no significant and consistent deviations between the test samples and training samples, we conclude that no overtraining

Table 3.2: Ranked BDT input variables. The use of $\pi^\pm$ and $K^\pm$ refers to the charged D daughters.

Rank	Variable	Variable Importance
1	B p_T asymmetry	1.292e-01
2	π^0 p_T	1.119e-01
3	$\log(1-B$ DIRA)	1.115e-01
4	log(Bachelor Min χ^2_IP)	1.073e-01
5	π^0 p	5.800e-02
6	Bachelor p	4.099e-02
7	$\log(B\ \chi^2_\mathrm{FD})$	3.856e-02
8	$\log(D$ Min $\chi^2_\mathrm{IP})$	3.758e-02
9	D p	3.449e-02
10	D p_T	3.225e-02
11	Bachelor p_T	2.710e-02
12	$\log(1-D$ DIRA)	2.663e-02
13	$\log(\pi^\pm$ Min $\chi^2_\mathrm{IP})$	2.622e-02
14	$\log(K^\pm$ Min $\chi^2_\mathrm{IP})$	2.440e-02
15	$K^\pm$ p_T	2.433e-02
16	$\log(D\ \chi^2_\mathrm{FD})$	1.760e-02
17	D τ	1.752e-02
18	Photon CL 1	1.711e-02
19	B vertex χ^2	1.708e-02
20	Photon CL 2	1.631e-02
21	$K^\pm$ p	1.629e-02
22	B τ	1.513e-02
23	$\pi^\pm$ p	1.502e-02
24	D Max DOCA	1.310e-02
25	D vertex χ^2	9.585e-03
26	B Min χ^2_IP	7.962e-03
27	$\pi^\pm$ p_T	6.802e-03
28	B Max DOCA	0.000e+00

is present. The x-axis of the overtraining plot shows the BDT response variable ranging from -1 to 1. Based on the distribution of signal and background from these plots, we can also infer that a loose BDT cut, closer to -1 than to 1, will be needed in order to maximise the presence of signal events. This is only an indication, however; a more rigorous procedure is required to select the optimum value of the cut for use in the analysis.

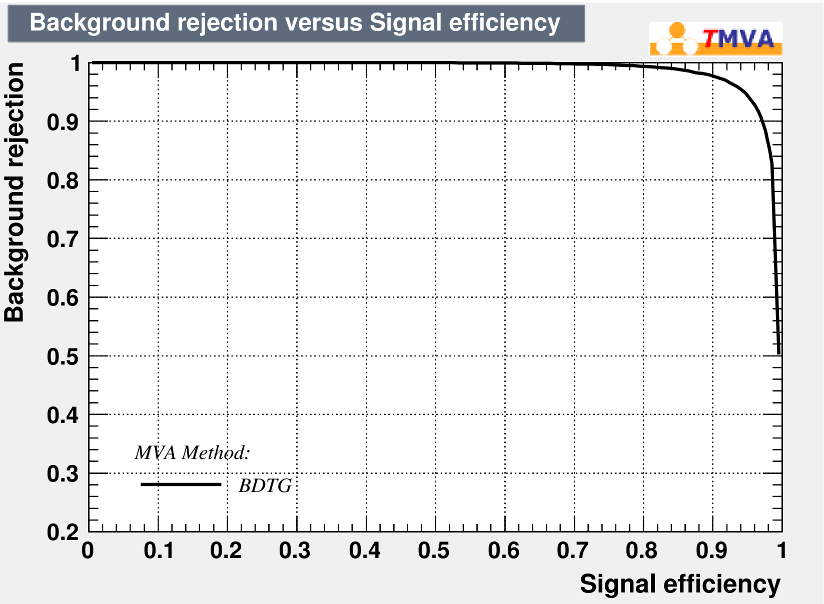

Figure 3.7: ROC curve for the BDT. In the legend, BDTG refers to the fact that a gradient boosted BDT is used.

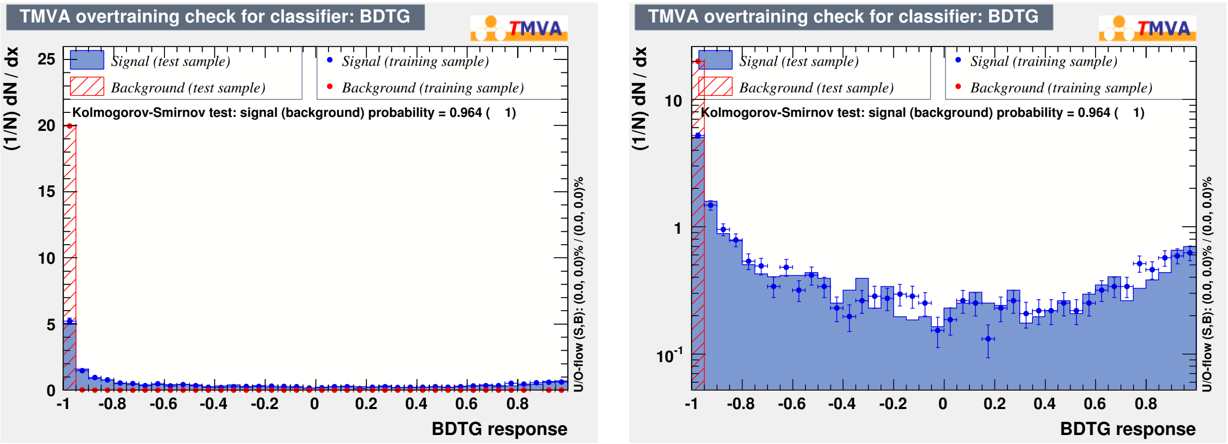

(a) Linear y-axis of the plot

(b) Log y-axis to show structure

Figure 3.8: Overtraining plot for the BDT. No significant deviations from the training and test samples are noted.

3.6.4 Choice of Working Point

Since the suppressed decay $B^{\mp} \to [\pi^{\mp}K^{\pm}\pi^{0}]_{D}K^{\mp}$ has not yet been observed and is central to the ADS analysis, the BDT response value working point is chosen with the intention of maximising the significance of this particular decay. This optimisation is calculated by performing a simultaneous fit to the $B^{\mp}$ mass distributions of the four $B^{\mp} \to [K\pi\pi^{0}]_{D}h^{\mp}$ modes of interest, but keeping the signal yields of the suppressed $B^{\mp} \to [\pi^{\mp}K^{\pm}\pi^{0}]_{D}K^{\mp}$ and $B^{\mp} \to [\pi^{\mp}K^{\pm}\pi^{0}]_{D}\pi^{\mp}$ modes blinded.

From this fit, we are able to make an estimate of the suppressed $B^{\mp} \to [\pi^{\mp}K^{\pm}\pi^{0}]_{D}K^{\mp}$ signal yields by examining the favoured $B^{\mp} \to [K^{\mp}\pi^{\pm}\pi^{0}]_{D}\pi^{\mp}$ yields. This is done by multiplying the yield of the latter by an $R_{K/\pi}$ of 7.74% (as measured in [83]) and an estimated $R_{\mathrm{ADS}(K)}$ value of 0.013 [4]. Effectively, this procedure uses the observed yield in a favoured mode to calculate the expected yield in a suppressed mode by assuming their relative branching fractions. We take this result as S, the estimated number of signal events. Although the signal yields are blinded for the suppressed modes, the background yields are not. The number of background events, B, is thus taken directly from the fit results for the $B^{\mp} \to [\pi^{\mp}K^{\pm}\pi^{0}]_{D}K^{\mp}$ mode. A figure of merit of $S/\sqrt{S+B}$, the statistical significance of the expected signal yields, is calculated for differing values of BDT response and is presented in Figure 3.9.

The exercise is only performed up to a BDT response value of -0.2 because beyond this point the background levels become too low to be accurately modelled. According to Figure 3.9, the highest point of significance is at a BDT response value of -0.5. However, if we consider the uncertainties on the data points, we see that a response value of -0.8 is the loosest cut that still agrees with the point of highest significance. Ultimately, this is the value chosen for use in the analysis as it allows one to maximise the signal yield in addition to maintaining the significance of the suppressed decay mode.

The effect of the BDT in eliminating backgrounds is readily apparent if we compare the B mass distribution for $B^{\mp} \to [K^{\mp}\pi^{\pm}\pi^{0}]_{D}\pi^{\mp}$ immediately after the stripping selection to

---

[4] In Reference [88], $R^{K\pi\pi\pi}_{\mathrm{ADS}(K)}$ was measured with a central value of 0.015; $R^{K\pi\pi^{0}}_{\mathrm{ADS(K)}}$ should be somewhat similar. In this analysis, we make the conscious choice of using a conservative lower value in our yield estimates.

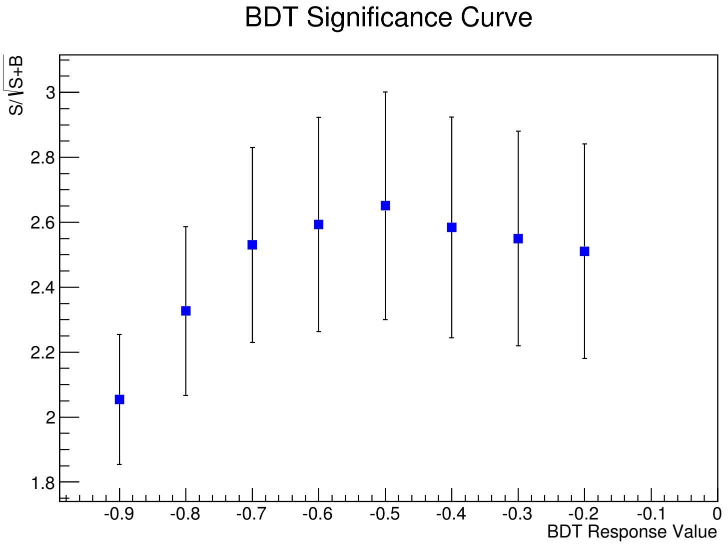

Figure 3.9: Significance plot for a variety of BDT response values

the distribution after the stripping and the application of the BDT cut. Such a comparison is presented in Figure 3.10. Directly after the stripping selection, a slight peak can be seen at the nominal B mass. However, when a BDT cut of -0.8 is applied to this distribution, the result is seen in Figure 3.10(b); a much more pronounced signal peak is now visible. As a comparison to the value quoted in Section 3.5, after the BDT cut, in the B mass range of 5000-7000 MeV/c^2, 1.2×10^6 $B^{\mp} \rightarrow [K^{\mp}\pi^{\pm}\pi^0]_D\pi^{\mp}$ events remain, a reduction by an order of magnitude.

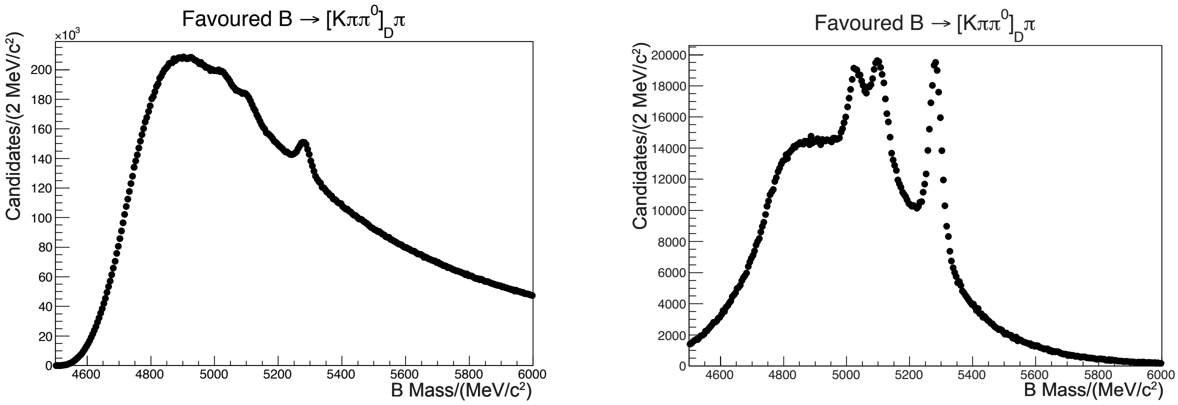

(a) Direct from the stripping.

(b) After a BDT cut of -0.8.

Figure 3.10: A comparison between the B mass distributions for $B^{\mp} \rightarrow [K^{\mp}\pi^{\pm}\pi^0]_D\pi^{\mp}$ decays in the case with only the stripping selection applied and with the additional constraint of a BDT >-0.8 cut. The double-peaking structure to the left of the signal peak in Figure 3.10(b) is a background discussed in Section 4.2.

3.6.5 BDT Usage for $\pi\pi\pi^0$ and $KK\pi^0$ Modes

Up until now, we have only discussed the BDT as applied to the favoured and suppressed $K\pi\pi^0$ modes. For the $\pi\pi\pi^0$ and $KK\pi^0$ sets of decays, the same BDT and the same BDT response variable cut are used. This decision is taken because there are inadequate MC statistics available for these modes to train the BDT as thoroughly as was the case for $K\pi\pi^0$ decays. Although the branching fractions for the $K\pi\pi^0$ decays are not the same as those for the $\pi\pi\pi^0$ and $KK\pi^0$ modes, and the working point may be non-optimal for these modes. However, its use can be justified.

Figure 3.11 presents the corresponding significance plots where $B^{\mp} \rightarrow [\pi^+\pi^-\pi^0]_D\pi^{\mp}$ is used to estimate the significance of $B^{\mp} \rightarrow [\pi^+\pi^-\pi^0]_D K^{\mp}$ and $B^{\mp} \rightarrow [K^+K^-\pi^0]_D\pi^{\mp}$ is used to estimate $B^{\mp} \rightarrow [K^+K^-\pi^0]_D K^{\mp}$ significance. In both cases, a BDT cut of -0.8 is consistent with the point of highest significance.

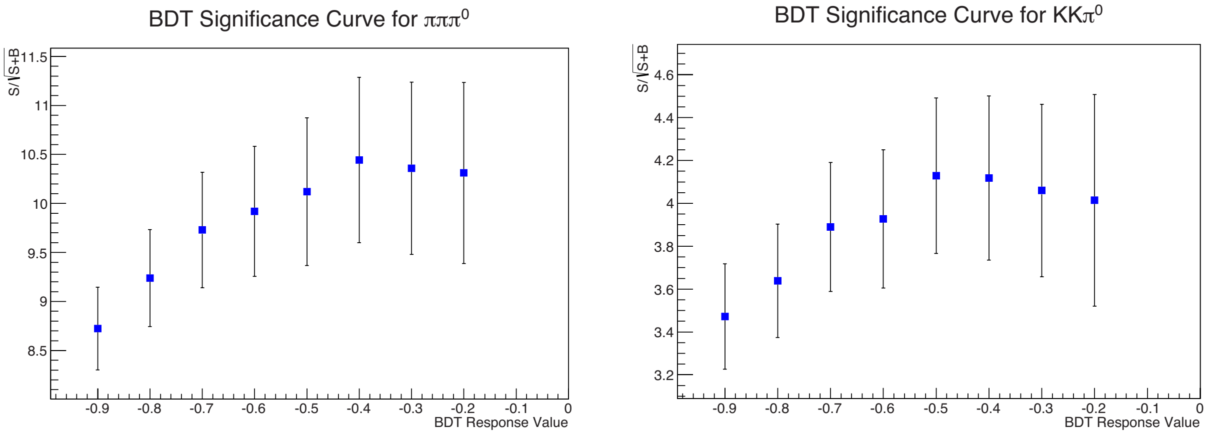

(a) $\pi\pi\pi^0$ significance curve (b) $KK\pi^0$ significance curve

Figure 3.11: BDT significance curves for $\pi\pi\pi^0$ and $KK\pi^0$ modes.

In order to adapt the BDT from the $K\pi\pi^0$ modes to the $\pi\pi\pi^0$ and $KK\pi^0$ modes, it is assumed that the BDT weights assigned to the input variables can be interchanged between the modes. In particular, it is assumed that the charged kaon and pion from the D in the $K\pi\pi^0$ decays behave similarly to the charged D-daughters in the $KK\pi^0$ and $\pi\pi\pi^0$ decays. There are a total of four variables from the BDT training that fall under this category, namely the momentum and transverse momentum of the charged kaon and pion. For the sake of simplifying the discussion, let us classify the kaon as the first D daughter and the charged pion as the second.

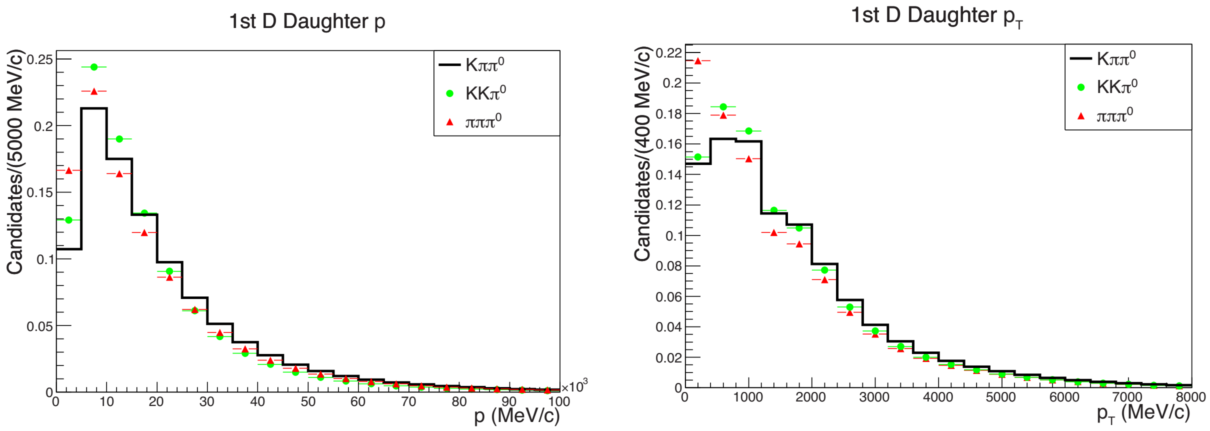

(a) First D daughter momentum (b) First D daughter transverse momentum

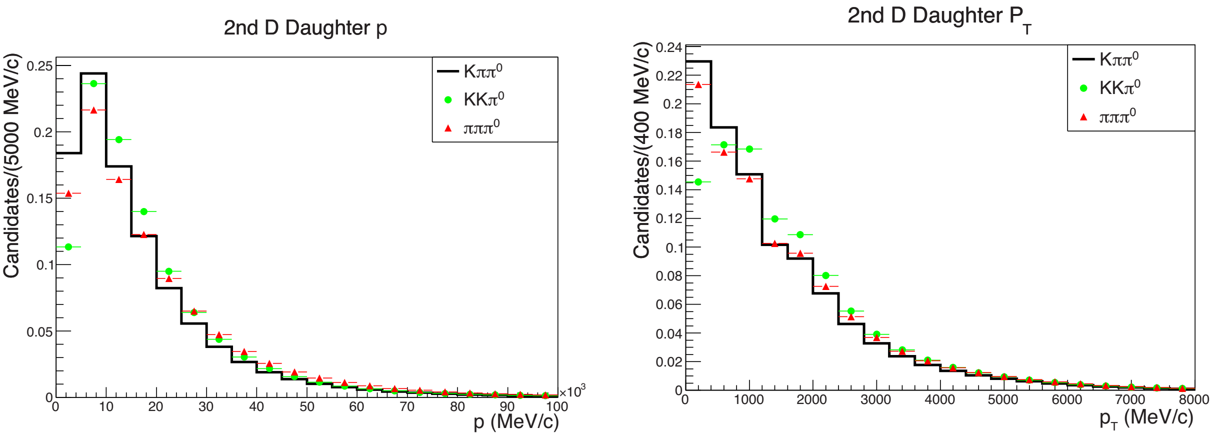

(c) Second D daughter momentum (d) Second D daughter transverse momentum

Figure 3.12: Distributions for the four variables relating to the charged D daughters used in the BDT. Each plot shows the normalised distributions from the $B^{\mp} \to D\pi^{\mp}$ data, direct from the stripping, for three different D decay channels: favoured $K\pi\pi^0$, $KK\pi^0$ and $\pi\pi\pi^0$.

Figure 3.12 shows the distribution of these four variables, in data, for $B^{\mp} \to [K^{\mp}\pi^{\pm}\pi^0]_D\pi^{\mp}$, $B^{\mp} \to [\pi^+\pi^-\pi^0]_D\pi^{\mp}$ and $B^{\mp} \to [K^+K^-\pi^0]_D\pi^{\mp}$. In order to compare the different distributions, they have been normalised, so the units on the y-axis are arbitrary. From these distributions, we notice that despite some relative differences in the low momentum regions, the same general shape is present for all of the decay modes. Given that we do not see large fluctuations in distribution shape across momentum space, although non-optimal, we expect the $K\pi\pi^0$ trained BDT to be able to reduce the backgrounds of the $KK\pi^0$ and $\pi\pi\pi^0$ decay modes in an effective manner. Furthermore, examination of the rank of the training variables in Table 3.2 reveals that the four D daughter variables all lie within the bottom half of the rankings, with variable importance at least an order of magnitude less than the highest ranking variables. Thus, these differences in momentum distribution should not have a significant effect when the BDT is used to select decay modes other than $K\pi\pi^0$.

3.7 Requirements and Fit Constraints on the Reconstructed Meson Masses

Based on the resolution of the π^0 and D candidates, it is necessary to determine the size of the mass windows to be used in the final selection. However, the resolution of the B and D mass distributions can be affected by the choice of vertex fitter constraints, if any, that are applied to these mass variables. In the case of $B^{\mp} \to DK^{\mp}$ and $B^{\mp} \to D\pi^{\mp}$ decays, given that these decays involve a D meson, it may be of value to consider the use of a `DecayTreeFitter` constraint to the nominal D mass. Indeed, such a constraint was used with positive effects in the study of $B^{\mp} \to [K^{\pm}\pi^{\mp}\pi^{+}\pi^{-}]_D h^{\mp}$ and $B^{\mp} \to [h'^{\pm}h''^{\mp}]_D h^{\mp}$ decays [83,88]. The presence of a π^0 meson in the decay modes of interest of this analysis may also suggest that a π^0 mass constraint should be used as well. In order to examine the effect of these mass constraints, a study is performed using $B^{\mp} \to [K^{\mp}\pi^{\pm}\pi^{0}]_D \pi^{\mp}$ truth-matched MC.

3.7.1 Cruijff Probability Density Function

Named after legendary Dutch footballer Johan Cruijff, the Cruijff PDF [92] was developed for use in B physics analyses at the BaBar collaboration. In its most general form, the Cruijff PDF is a bifurcated Gaussian with asymmetric tails. This makes it a rather versatile shape that is particularly useful for describing Gaussian-like decays, but with the added benefit of tails that are more flexible than those of a standard Gaussian. The Cruijff PDF can be expressed as

$$f(x) \propto \exp\left(\frac{-(x-\mu)^2}{2\sigma_{L,R}^2 + (x-\mu)^2\alpha_{L,R}}\right). \tag{3.5}$$

In this expression, μ represents the mean, $\sigma_{L,R}$ the width and parameters α_L and α_R are used to describe the tails. In the region $(x < \mu)$, σ_L and α_L are used, while in the region

($x > \mu$), σ_R and α_R are used. In this thesis, unless otherwise stated, the Cruijff that is used has a single width parameter, where $\sigma_L = \sigma_R = \sigma$.

3.7.2 π^0 Mass

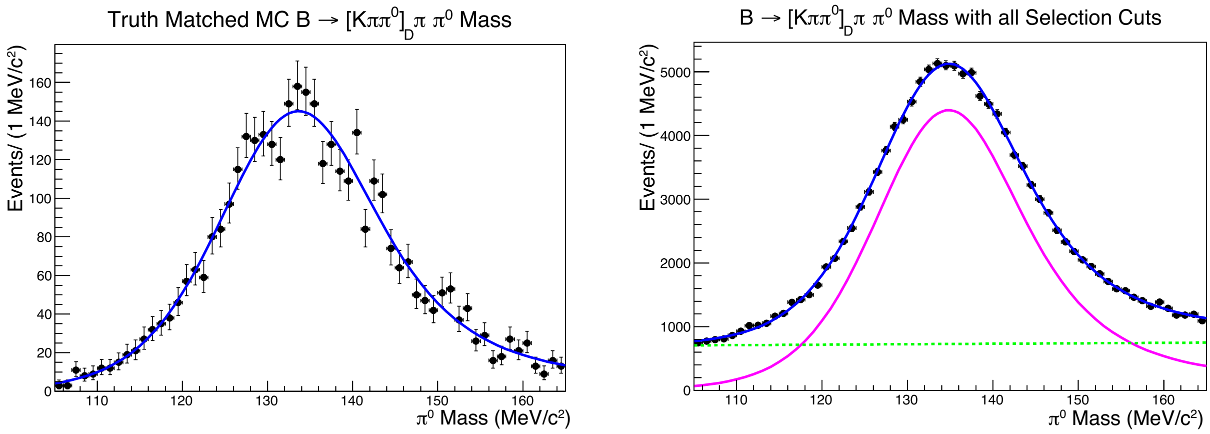

(a) MC π^0 mass distribution for $B^\mp \to [K^\mp\pi^\pm\pi^0]_D\pi^\mp$. The width is measured at 9.0 ± 0.4 MeV/c^2.

(b) Data π^0 mass distribution for $B^\mp \to [K^\mp\pi^\pm\pi^0]_D\pi^\mp$. The width is measured at 8.6 ± 0.1 MeV/c^2.

Figure 3.13: The mass distributions for the π^0 candidates as seen in MC and data. In (b), the signal is modelled in magenta and backgrounds in green. In both cases, the signal is modelled using the Cruijff function.

The mass distributions of the π^0 from $B^\mp \to [K^\mp\pi^\pm\pi^0]_D\pi^\mp$ decays in MC and data are presented in Figure 3.13. Both distributions have widths that are compatible. Based on this study, in order to obtain a cleaner signal, a mass window of ± 20 MeV/c^2 about the nominal π^0 mass of 135 MeV/c^2 [2] is used in the full selection. This window corresponds to roughly $\pm 2\sigma$.

3.7.3 D Mass Distributions

Depending on the width of the D mass distribution, it may be beneficial to place an experimental cut surrounding the nominal D mass for background suppression. Events with a D candidate are the ones of interest, but events where the D candidate mass is far from the nominal D mass may indicate a poorly reconstructed D from a source of background.

In the study of decays $B^\mp \to [h'^\pm h''^\mp]_D h^\mp$, a D mass window of ± 25 MeV/c^2 was applied as part of the event selection. This mass window is a sensible selection, given that it corresponds to approximately 3.5 times the resolution of the D mass distribution [22]. As a comparison, the D mass distribution in truth-matched MC for $B^{\mp} \to [K^{\pm}\pi^{\mp}]_D\pi^{\mp}$ is presented in Figure 3.14(a) and the MC D distribution for $B^{\mp} \to [K^{\mp}\pi^{\pm}\pi^0]_D\pi^{\mp}$ is presented in Figure 3.14(b).

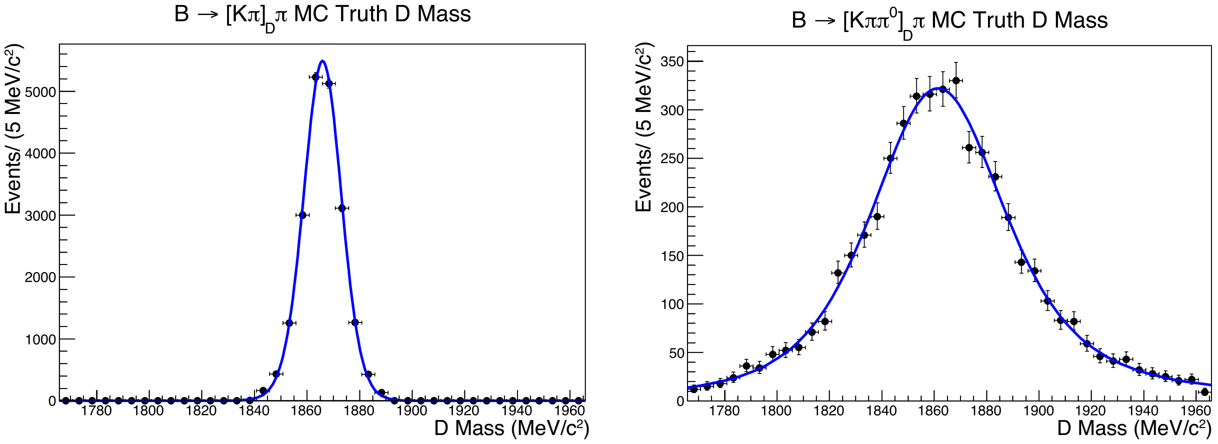

(a) MC D mass distribution for $B^{\mp} \to [K^{\pm}\pi^{\mp}]_D\pi^{\mp}$ with a width of 7 MeV/c^2.

(b) MC D mass distribution for $B^{\mp} \to [K^{\mp}\pi^{\pm}\pi^0]_D\pi^{\mp}$ with a width of 24 MeV/c^2.

Figure 3.14: In MC, we readily notice that the width of the D mass distribution for the $K\pi\pi^0$ mode is larger than that of the corresponding $K\pi$ mode. Both distributions are fitted with a Cruijff function.

While the distribution on the left has a width of 7 MeV/c^2, the $K\pi\pi^0$ decay has a width of 24 MeV/c^2. This difference can be attributed to the presence of a π^0 daughter, a particle with a wide mass resolution. Consequently, due to the larger D mass width present, a selection cut of ±50 MeV/c^2 about the nominal D mass of 1865 MeV/c^2 [2] is chosen.

3.7.4 B Mass Distributions

The B mass distribution from MC is fitted using a Cruijff with all parameters floating. Fits are performed using combinations of `DecayTreeFitter` mass constraints for the D and π^0; a fit with no `DecayTreeFitter` constraint is termed as "raw". Graphically, these fits are presented in Figure 3.14 and their widths are collated in Table 3.3.

We note that the least wide distribution occurs when only the D mass constraint is used. Surprisingly, using both the D and the π^0 mass constraints leads to a worse resolution. This result, however, has been attributed to a limitation of `DecayTreeFitter` when using two

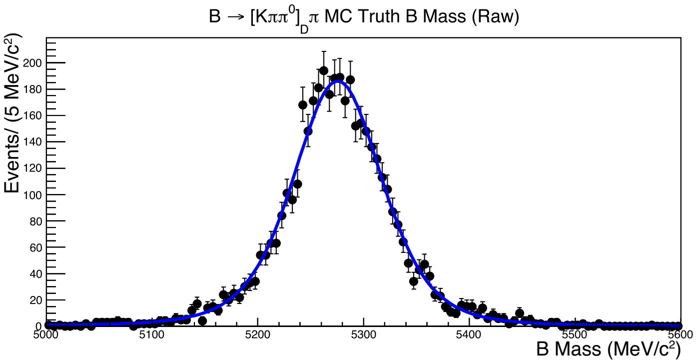

(a) MC B mass peak with no mass constraints. The distribution has a width of 37.0 ± 1.1 MeV/c^2.

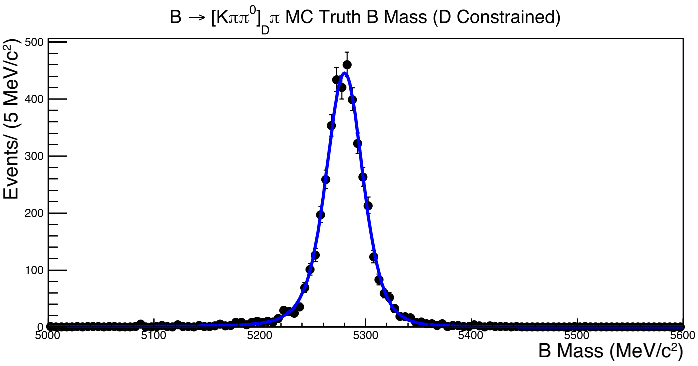

(b) MC B mass peak with D mass constraint. The distribution has a width of 15.2 ± 0.3 MeV/c^2.

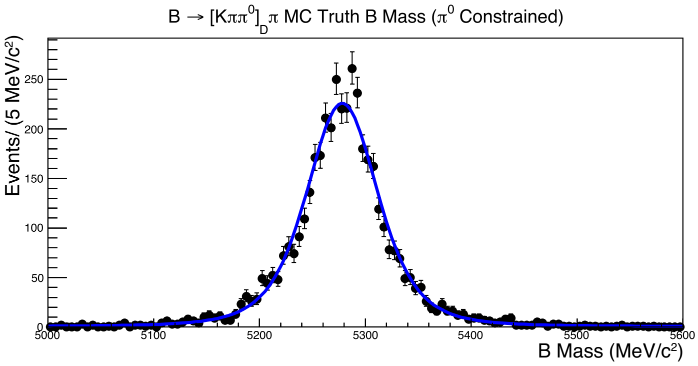

(c) MC B mass peak with π^0 mass constraint. The distribution has a width of 29.6 ± 0.8 MeV/c^2.

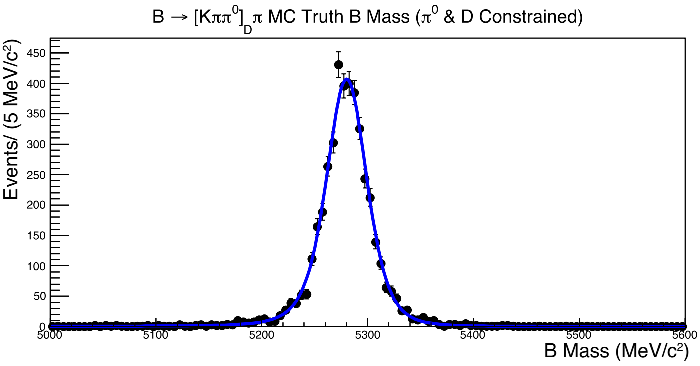

(d) MC B mass peak with D and π^0 mass constraint. The distribution has a width of 16.6 ± 0.3 MeV/c^2.

Figure 3.14: B mass distribution for $B^{\mp} \rightarrow [K^{\mp}\pi^{\pm}\pi^0]_D\pi^{\mp}$ MC with and without `DecayTreeFitter` π^0 and D mass constraints.

Table 3.3: B mass distribution widths from MC

Constraint Type	Sigma (MeV/c^2)
No mass constraints	37.0 ± 1.1
π^0 mass constraint	29.6 ± 0.8
D mass constraint	15.2 ± 0.3
D and π^0 mass constraint	16.6 ± 0.3

mass constraints for particles that are correlated and have wide mass distributions. The decision is thus made to use the `DecayTreeFitter` version of the $B^{\mp}$ mass with only a D mass constraint applied.

3.7.5 B Mass Widths in $B^{\mp} \to DK^{\mp}$ Versus $B^{\mp} \to D\pi^{\mp}$

MC can also be used to study differences in width between the $B^{\mp} \to DK^{\mp}$ and $B^{\mp} \to D\pi^{\mp}$ decay modes. In Figure 3.15, a simultaneous fit is performed to the B mass distribution of $B^{\mp} \to [K^{\mp}\pi^{\pm}\pi^0]_D\pi^{\mp}$ and $B^{\mp} \to [K^{\mp}\pi^{\pm}\pi^0]_D K^{\mp}$ in truth-matched MC. As seen in the plots, the $B^{\mp} \to DK^{\mp}$ distribution is marginally narrower than its $B^{\mp} \to D\pi^{\mp}$ counterpart. Such behaviour is expected as kaons, on average, have less momentum than pions which leads to less uncertainty in 4-momentum calculations and thus mass measurements. The ratio between the two sigmas is measured to be 0.95 ± 0.02. In the full fits to data, we can use this ratio to constrain the width of the $B^{\mp} \to DK^{\mp}$ signal peaks with respect to the $B^{\mp} \to D\pi^{\mp}$ signal distributions where we expect a statistically greater abundance of events.

3.8 Acceptance, Stripping, Selection and Trigger Efficiencies

In this Chapter, we have discussed a variety of selection cuts. These cuts each have efficiencies attributed to them that together make up the total efficiency of candidate observation. These efficiencies may also vary between modes that have a kaon bachelor and those with a bachelor pion. As such the ratio of efficiencies between $B^{\mp} \to DK^{\mp}$ and $B^{\mp} \to D\pi^{\mp}$ modes is an important value to be considered, especially when measuring any experimental observables

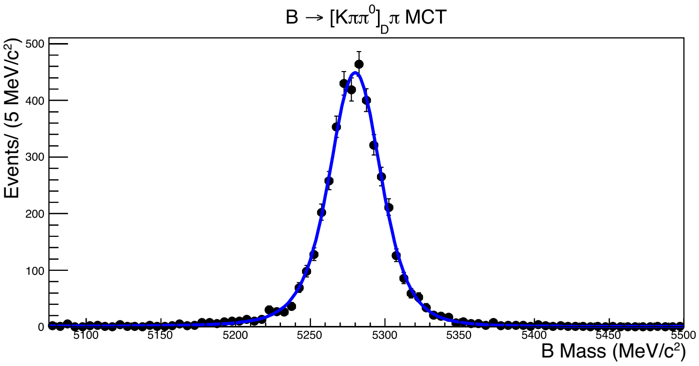

(e) MC B mass distribution for $B^{\mp} \to [K^{\mp}\pi^{\pm}\pi^0]_D\pi^{\mp}$. The peak has a width of 15.2 MeV/c^2.

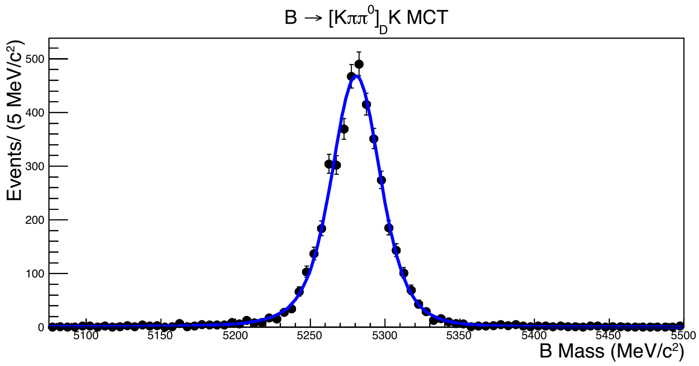

(f) MC B mass distribution for $B^{\mp} \to [K^{\mp}\pi^{\pm}\pi^0]_D K^{\mp}$. The peak has a width of 14.4 MeV/c^2.

Figure 3.15: MC B mass distribution for $B^{\mp} \to [K^{\mp}\pi^{\pm}\pi^0]_D\pi^{\mp}$ and $B^{\mp} \to [K^{\mp}\pi^{\pm}\pi^0]_D K^{\mp}$ using a simultaneous fit.

that rely on the ratio of $B^{\mp} \to DK^{\mp}$ versus $B^{\mp} \to D\pi^{\mp}$ candidates.

To study these differences in efficiency for the $K\pi\pi^0$ decay modes, we use $B^{\mp} \to [K^{\mp}\pi^{\pm}\pi^0]_D K^{\mp}$ and $B^{\mp} \to [K^{\mp}\pi^{\pm}\pi^0]_D \pi^{\mp}$ MC events without any bachelor PID requirements (these PID efficiencies are discussed separately in Section 3.9). Let us begin by defining the following quantities:

- N_{Gen}: The total number of MC events generated for a given decay mode.
- N_{Strip}: The total number of N_{Gen} events that pass the stripping selection for the decay mode of interest.
- N_{Sel}: The total number of N_{Strip} events that pass the selection described in Sections 3.6, 3.7 and 3.7.2.
- N_{Trig}: The total number of N_{Sel} events that pass the trigger requirements of Section 3.4.

Using these quantities, we may calculate the following efficiencies:

$$\epsilon_{\text{Trig}} = \frac{N_{\text{Trig}}}{N_{\text{Sel}}};\ \epsilon_{\text{Sel}} = \frac{N_{\text{Sel}}}{N_{\text{Strip}}};\ \epsilon_{\text{Strip}} = \frac{N_{\text{Strip}}}{N_{\text{Gen}}}. \tag{3.6}$$

In addition, we must also consider the geometric acceptance efficiency of the detector, ϵ_{Acc}. The total efficiency is thus given by

$$\epsilon_{\text{Total}} = \frac{N_{\text{Trig}}}{N_{\text{Gen}}} \cdot \epsilon_{\text{Acc}}. \tag{3.7}$$

Using the expressions of Equation 3.6, we may rewrite the total efficiency as

$$\epsilon_{\text{Total}} = \epsilon_{\text{Trig}} \cdot \epsilon_{\text{Sel}} \cdot \epsilon_{\text{Strip}} \cdot \epsilon_{\text{Acc}}. \tag{3.8}$$

Finally, using Equation 3.8, we can calculate ϵ_{Total} for both the $B^{\mp} \to DK^{\mp}$ and $B^{\mp} \to D\pi^{\mp}$ modes in addition to the ratio between them. These efficiencies and ratios are collected in Table 3.4, where the uncertainties are due to MC statistics.

As expected, all of the ratios are near unity. Following a similar procedure, we can

Table 3.4: Efficiencies and the DK to $D\pi$ ratio for $K\pi\pi^0$

Mode	ϵ_{Trig}	ϵ_{Sel}	$\epsilon_{\mathrm{Strip}}$	ϵ_{Acc}	$\epsilon_{\mathrm{Total}}$
Favoured DK	0.9225 ± 0.0046	0.1726 ± 0.0034	0.0080 ± 0.0001	0.1550 ± 0.0007	0.000197 ± 0.000005
Favoured $D\pi$	0.9227 ± 0.0045	0.1797 ± 0.0035	0.0080 ± 0.0001	0.1534 ± 0.0007	0.000202 ± 0.000005
Ratio DK to $D\pi$	1.000 ± 0.007	0.960 ± 0.027	1.005 ± 0.014	1.010 ± 0.006	0.975 ± 0.034

calculate the ratio of $B^{\mp} \to DK^{\mp}$ to $B^{\mp} \to D\pi^{\mp}$ efficiencies for the $\pi\pi\pi^0$ and $KK\pi^0$ modes as well (presented in Tables 3.5 and 3.6).

Table 3.5: Efficiencies and the DK to $D\pi$ ratio for $\pi\pi\pi^0$

Mode	ϵ_{Trig}	ϵ_{Sel}	ϵ_{Strip}	ϵ_{Acc}	ϵ_{Total}
Favoured DK	0.9064 ± 0.0041	0.1533 ± 0.0026	0.0086 ± 0.0001	0.1570 ± 0.0008	0.000188 ± 0.000004
Favoured $D\pi$	0.9190 ± 0.0037	0.1576 ± 0.0025	0.0088 ± 0.0001	0.1540 ± 0.0006	0.000196 ± 0.000004
Ratio DK to $D\pi$	0.986 ± 0.006	0.972 ± 0.023	0.978 ± 0.010	1.019 ± 0.007	0.957 ± 0.028

Table 3.6: Efficiencies and the DK to $D\pi$ ratio for $KK\pi^0$

Mode	ϵ_{Trig}	ϵ_{Sel}	ϵ_{Strip}	ϵ_{Acc}	ϵ_{Total}
Favoured DK	0.9370 ± 0.0032	0.1659 ± 0.0026	0.0087 ± 0.0001	0.1675 ± 0.0009	0.000227 ± 0.000005
Favoured $D\pi$	0.9333 ± 0.0033	0.1665 ± 0.0026	0.0091 ± 0.0001	0.1632 ± 0.0009	0.000230 ± 0.000004
Ratio DK to $D\pi$	1.004 ± 0.005	0.996 ± 0.022	0.963 ± 0.010	1.026 ± 0.008	0.989 ± 0.028

The final ratio for each of the three decay channels is approximately unity. Their values are summarised in Table 3.7 and these numbers are fixed in the final fit and observable extraction.

Table 3.7: $\frac{\epsilon(DK)}{\epsilon(D\pi)}$ ratios for the different decay modes, as determined in MC. These values are fixed in the final fit and do not include differences in bachelor PID efficiency (which are calculated independently).

Channel	$\frac{\epsilon(DK)}{\epsilon(D\pi)}$
$K\pi\pi^0$	0.975 ± 0.034
$\pi\pi\pi^0$	0.957 ± 0.028
$KK\pi^0$	0.989 ± 0.028

3.9 PID Efficiencies

Given that the difference in mass between the kaon and the pion is relatively small compared to the B mass, there is overlap between the B invariant mass distributions of $B^{\mp} \to DK^{\mp}$ and $B^{\mp} \to D\pi^{\mp}$. In order to separate the events that have a bachelor kaon from those with a bachelor pion, information is used from the RICH system and a cut is placed on a value of PIDK. Understanding the efficiency of such a cut is critical as it influences the overall measured signal yields in the different channels of interest. Generally speaking, the efficiency of selection cuts is calculated using MC, as discussed in Section 3.8. However, since PIDK is known to be improperly modelled in MC, a data-driven approach is taken.

RICH performance varies as a function of momentum as well as density of rings. The latter is affected by the number of tracks in the event, in addition to their angular distribution within detector acceptance. As a result, RICH performance, and consequently, PID performance varies as a function of momentum, η and the number of tracks. As a result, we must measure the performance in relation to these variables and then apply the findings to our analysed data. To determine these efficiency and misidentification values, the `PIDCalib` package [93] is used. This software performs a calibration by using a $D^{*\pm} \to [K^-\pi^+]_{D^0}\pi^\pm$ data sample which can be selected with high purity using topological and kinematic information alone. Consequently, kaon tracks and pion tracks can be distinguished without having to use a PID requirement. The `PIDCalib` package is used to bin the calibration sample in a multidimensional $40 \times 35 \times 50$ efficiency reference histogram of momentum, pseudorapidity and number of tracks. A signal sample is then binned in the same way and its PID performance is compared to the reference; for each bin, the PID performance is mapped to that of the calibration tracks. Thus, the effective performance of the PIDK cut on the signal sample is determined using the weighted sum of the calibration sample's performance in each bin. The signal sample used is $B^\mp \to [K^\mp\pi^\pm\pi^0]_D\pi^\mp$ events that pass all selection criteria (except for the bachelor PID requirements) and that lie in a mass window of ± 50 MeV/c^2 about the nominal B mass. It is possible, due to differences in detector geometry, that PID efficiency will differ between positively and negatively charged particles. To safeguard against such differences, two separate PID efficiency values are calculated for each species of bachelor (*i.e.* positive kaon, negative kaon, positive pion, negative pion); this is achieved using reference histograms and signal samples that deal exclusively with positive or negative bachelor charges.

There are two sources of statistical uncertainty in this efficiency calculation procedure. The first is due to the statistics of the D^* calibration sample and the second has to do with

Table 3.8: Bachelor PID efficiencies of negatively charged kaons for $K\pi\pi^0$ modes.

Year	Magnet Polarity	$\Delta \log \mathcal{L}(K-\pi) > 4$ (%)	Calib. Stat. Err. (±)	Signal Stat. Err. (±)
2011	MagUp	84.8473	0.0047	0.9284
2011	MagDown	84.9019	0.0033	1.1135
2012	MagUp	84.1299	0.0021	0.6927
2012	MagDown	84.3945	0.0017	0.6852

Table 3.9: Bachelor PID efficiencies of positively charged kaons for $K\pi\pi^0$ modes.

Year	Magnet Polarity	$\Delta \log \mathcal{L}(K-\pi) > 4$ (%)	Calib. Stat. Err. (±)	Signal Stat. Err. (±)
2011	MagUp	84.9280	0.0110	1.1217
2011	MagDown	84.7639	0.0032	0.9397
2012	MagUp	83.8999	0.0018	0.6982
2012	MagDown	84.9183	0.0017	0.7017

Table 3.10: Bachelor PID efficiencies of negatively charged pions for $K\pi\pi^0$ modes.

Year	Magnet Polarity	$\Delta \log \mathcal{L}(K-\pi) < 4$ (%)	Calib. Stat. Err. (±)	Signal Stat. Err. (±)
2011	MagUp	96.2815	0.0026	1.0535
2011	MagDown	96.1792	0.0017	1.2614
2012	MagUp	96.1933	0.0010	0.7920
2012	MagDown	96.5927	0.0009	0.7843

Table 3.11: Bachelor PID efficiencies of positively charged pions for $K\pi\pi^0$ modes.

Year	Magnet Polarity	$\Delta \log \mathcal{L}(K-\pi) < 4$ (%)	Calib. Stat. Err. (±)	Signal Stat. Err. (±)
2011	MagUp	96.1042	0.0050	1.2693
2011	MagDown	96.2469	0.0018	1.0670
2012	MagUp	96.1808	0.0011	0.8004
2012	MagDown	96.6347	0.0010	0.7986

Table 3.12: Final bachelor PID efficiencies used in the analysis.

Bachelor Type	Charge	PID Cut Efficiency
K	Negative	$84.47 \pm 0.41\%$
K	Positive	$84.55 \pm 0.41\%$
π	Negative	$96.34 \pm 0.47\%$
π	Positive	$96.34 \pm 0.46\%$

the size and kinematic distribution of the data in the signal sample. The calibration sample has a much larger number of events than the signal sample used, thus the former has a smaller statistical uncertainty. The results of the PID efficiency calculation are illustrated in Tables 3.8 to 3.11 for the PIDK cut of greater than 4 (less than 4) for kaon (pion) identification used in this analysis.

For each set of decay modes, the ultimate PID efficiency value used in the final fits is obtained by taking the average of the set of four values in each of Tables 3.8–3.11, weighted by the integrated luminosity from Table 3.1. The final efficiency values are presented in Table 3.12. The efficiencies of the bachelor particles of the $\pi\pi\pi^0$ and $KK\pi^0$ decay modes are taken to be the same.

Chapter 4

Background Modelling and Additional Selection Requirements

Several sources of background can obscure the signal peaks of the decays of interest. In this Chapter, the most relevant background contributions are discussed, in addition to the fit modelling and selection techniques used to describe or reduce their effects. The following background sources are discussed in detail:

1. Combinatorial backgrounds;
2. Partially reconstructed backgrounds of B hadrons with invariant mass less than the nominal $B^{\mp}$ mass;
3. Misidentified $B^{\mp} \to D\pi^{\mp}$ decays that are reconstructed as $B^{\mp} \to DK^{\mp}$ decays;
4. $B_s^0 \to [K^{\pm}\pi^{\mp}\pi^0]_D K^{*0}$ decays where the K^{*0} decays to $K^{\mp}\pi^{\pm}$, but the pion is lost in the reconstruction;
5. Crossfeed from the favoured ADS $B^{\mp} \to [K^{\mp}\pi^{\pm}\pi^0]_D K^{\mp}$ decay to the suppressed $B^{\mp} \to [\pi^{\mp}K^{\pm}\pi^0]_D K^{\mp}$ decay, where the two charged D daughters from the former are both misidentified;
6. Charmless decays that have the same final-state particles, but do not involve an intermediate D meson decay;

7. Contributions from $B^{\mp} \to [\pi^{+}\pi^{-}\pi^{0}]_{D}h^{\mp}$ and $B^{\mp} \to [K^{+}K^{-}\pi^{0}]_{D}h^{\mp}$ decays where one of the D daughters is misidentified, leading to contamination in the suppressed $B^{\mp} \to [\pi^{\mp}K^{\pm}\pi^{0}]_{D}h^{\mp}$ ADS modes;

8. Decays featuring a wrongly reconstructed D candidate.

We present the PDFs used to represent these backgrounds in the final fits as well as the selection cuts used for further suppression. A full summary of the selection cuts is summarised at the end of the Chapter in Table 4.13.

4.1 Combinatorial Backgrounds

Combinatorial background contributions occur from random combinations of charged tracks and a neutral pion candidate that have the same final-state particles as our decay channels of interest, but are not related to a $B^{\mp} \to Dh^{\mp}$ decay. These candidates are independent of the mass and momentum of the signal modes and thus are distributed across all of the B mass spectrum.

There are two categories of combinatorial background. The first type is where the D candidate is falsely reconstructed, meaning that one or more of the two charged mesons and the neutral pion that are selected as its daughters do not come from a genuine $D \to h'^{\pm}h''^{\mp}\pi^{0}$ decay. The less prominent other category consists of candidates with a genuine $D \to h'^{\pm}h''^{\mp}\pi^{0}$ but with a bachelor particle not related to the B candidate that produced the D meson. In other words, this is a case of a true D but with a random track from the rest of the event.

The combinatorial backgrounds in this analysis are primarily suppressed through the use of the BDT discussed in Section 3.6. However, it should be noted that although the choice of BDT response variable is made to maximise signal significance of the $B^{\mp} \to [\pi^{\mp}K^{\pm}\pi^{0}]_{D}K^{\mp}$ decay, not all of the combinatorial background is eliminated and a residual portion is present in the final fits to the B mass data. This background is modelled by a linear function (as per previous ADS/GLW analyses [83, 88]) with separate slopes for the DK and $D\pi$ modes. The favoured $K\pi\pi^{0}$, suppressed $K\pi\pi^{0}$, $\pi\pi\pi^{0}$ and $KK\pi^{0}$ channels all share these slopes.

In addition, because the favoured and suppressed $K\pi\pi^0$ decays have final states that differ only by charge, they both are expected to have similar levels of combinatorial contamination. This is illustrated in Figure 4.1 where a comparison is made, in data, for the B mass distribution in the upper B sideband for the favoured and suppressed $K\pi\pi^0$ decays. We note that the combinatorial background levels are consistent with each other. As such, in the final mass fits, the yield of combinatorial backgrounds is taken to be the same in the favoured and suppressed $K\pi\pi^0$ decays, with separate yields allocated for the DK and $D\pi$ channels.

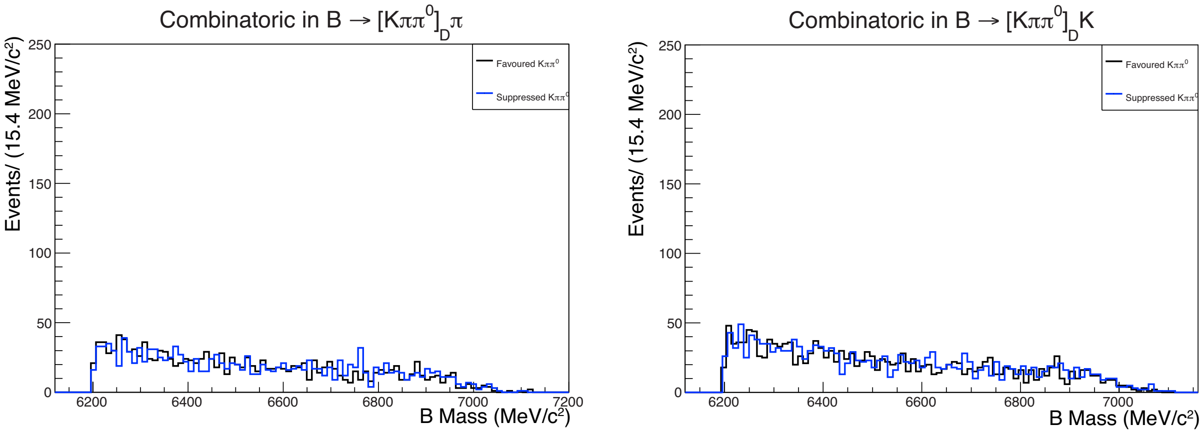

(a) $B^{\mp} \to D\pi^{\mp}$ ADS modes

(b) $B^{\mp} \to DK^{\mp}$ ADS modes

Figure 4.1: B mass distribution, in data, in the upper B sideband for D candidates with masses within ± 50 MeV/c^2 of the nominal D mass. A BDT cut of -0.8 is applied. The black line represents favoured $B^{\mp} \to [K^{\mp}\pi^{\pm}\pi^0]_D h^{\mp}$ candidates while the blue line represents suppressed $B^{\mp} \to [\pi^{\mp}K^{\pm}\pi^0]_D h^{\mp}$ candidates.

4.2 Partially Reconstructed Low-Mass Backgrounds

The low-mass region that lies below the nominal B mass peak has potential background contributions due to partially reconstructed $B^{\mp} \to Dh^{\mp}$ decays. These are decays where the D meson is reconstructed, but one of its final-state decay products is missed, ultimately leading to a set of final state particles that mimic that of a desired signal. An example of a partially reconstructed background contribution is the decay $B^{\pm} \to (D^{*0} \to D^0\pi^0)\pi^{\pm}$, where the π^0 is missed in the reconstruction. If the D^0 meson undergoes a further decay to $K^{\mp}\pi^{\pm}\pi^0$, the final-state particles of the decay are the same as $B^{\mp} \to [K^{\mp}\pi^{\pm}\pi^0]_D\pi^{\mp}$ and the decay will be misidentified as the latter. Since these partially reconstructed decays originate from a genuine $B^{\mp}$ candidate but one of the final-state particles is lost, they appear in the data as having a lower mass than the nominal B mass. Typically, these partially reconstructed decays involve a neutral or a charged D^{*} meson and the missing particle is either a $\pi^{\pm}$, π^{0} or a photon.

The partially reconstructed low-mass background contributions are modelled through the use of an analytic PDF [94]. This shape was originally developed for use in the study of $B^{\mp} \to [h'^{\pm}h''^{\mp}]_{D}h^{\mp}$ decays and has been used in an analysis involving those decays [95] as well as in another with $B^{\mp} \to DK^{\mp}$ decays of the form $B^{\mp} \to [K^{0}_{\mathrm{S}}K^{+}K^{-}]_{D}K^{\mp}$ and $B^{\mp} \to [K^{0}_{\mathrm{S}}\pi^{+}\pi^{-}]_{D}K^{\mp}$ [89]. Effectively, the shape of the distributions that compose the PDF are determined by two factors: the kinematic endpoints (wholly constrained by the invariant masses of the particles in the decay) and the angular distribution of the missing particle. The distribution's shift from the nominal B mass is directly affected by the momentum of the missing particle, which, in turn, is related to the particle's relative angle with respect to the bachelor track. In fact, there is a one-to-one relationship between the angular distribution of the missing particle and the missing momentum of the system and thus, the reconstructed B mass. An example of this relationship is presented in Figure 4.2, which demonstrates the momentum distribution for a π^{0} with respect to helicity angle θ, measured with respect to the boosted momentum direction of the bachelor in the D^{*0} rest frame, and that of the reconstructed invariant B mass for the decay $B^{\pm} \to (D^{*0} \to D^{0}\pi^{0})\pi^{\pm}$, as studied in MC. As can be seen, there is a direct correspondence between the angular distribution of the missing particle and that of the reconstructed B mass of the decay.

With respect to the spin-parity of the missing particles, photons have spin-parity 1^{-} while neutral and charged pions have a value of 0^{-}. As a consequence, two types of PDFs are used, corresponding to each of these spin-parity states.

4.2.1 HORNSdini PDF for Missing Neutral or Charged Pion

The HORNSdini PDF, so-named because of its dual, horn-like, peaking structure (as seen in Figure 4.3(a)), is the PDF used to describe vector to pseudoscalar-pseudoscalar decays

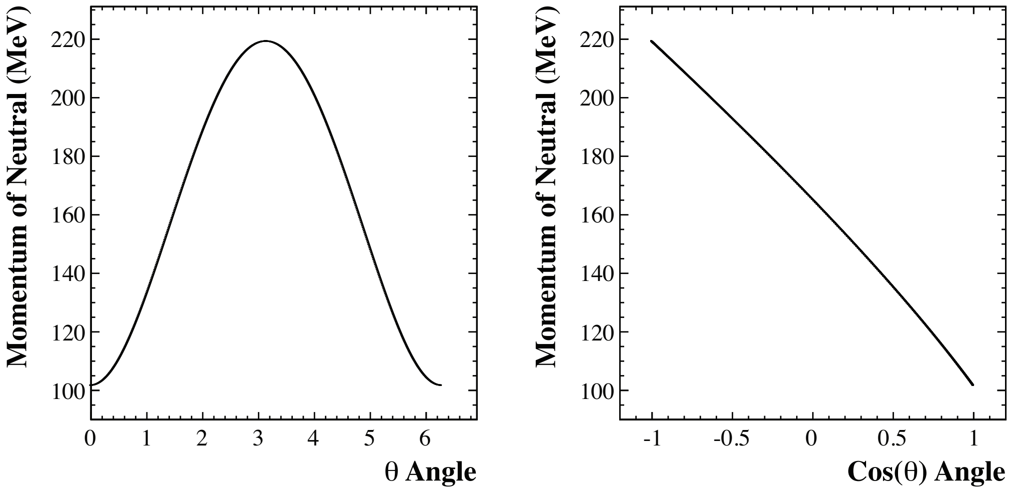

(a) Momentum distribution of missing π^0 meson

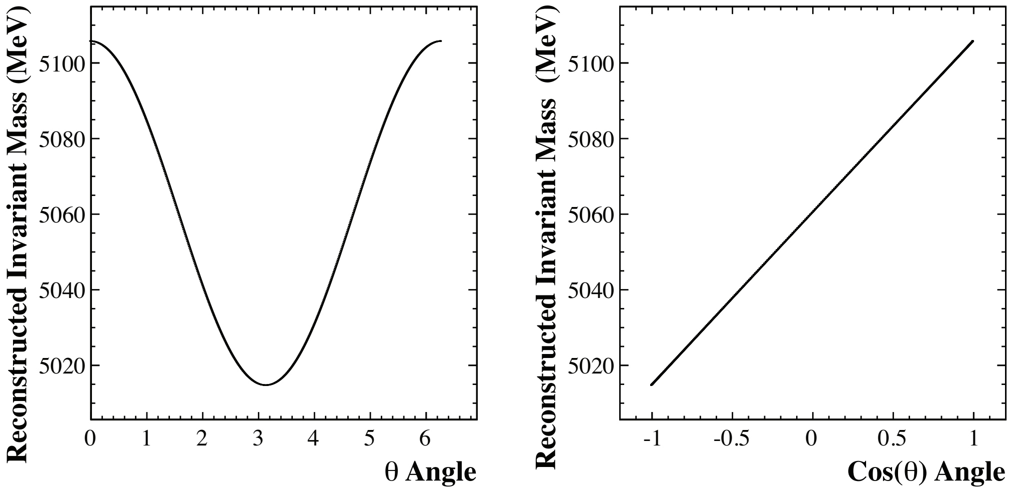

(b) Invariant mass of reconstructed B candidate

Figure 4.2: Momentum distribution of missing π^0 and invariant mass distribution of the reconstructed B candidate. In both cases, the variables are plotted against helicity angle for decays of $B^{\pm} \rightarrow (D^{*0} \rightarrow D^0\pi^0)\pi^{\pm}$ in MC. The helicity angle θ is measured in radians and is measured with respect to the direction of the bachelor in the D^{*0} rest frame [94].

where a charged or neutral pion is lost from the decay chain. For example, in the case of $B^{\pm} \to (D^{*0} \to D^0\pi^0)\pi^{\pm}$, the $D^{*0} \to D^0\pi^0$ decay represents a vector (1^-) decaying to two pseudoscalars (0^- and 0^-). Overwhelmingly, the π^0 will travel in the direction $\theta = 0$ or $\theta = \pi$. As can be seen in Figure 4.2, the former angle corresponds to a higher reconstructed invariant B mass than that of the latter. Consequently, these two different reconstructed B masses give rise to the double-peaking structure in the PDF.

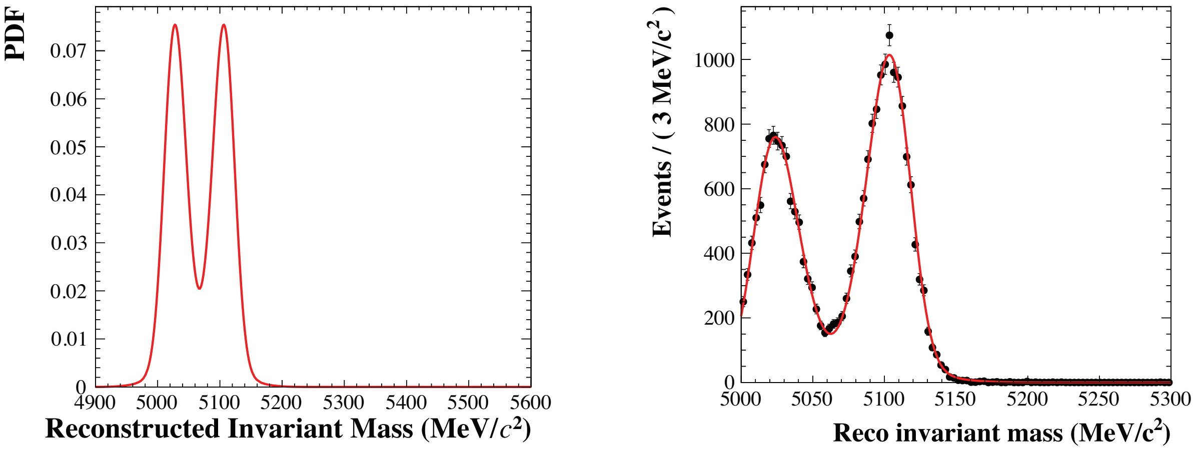

(a) The analytic HORNSdini PDF convolved with a double Gaussian detector resolution function, for $B^{\pm} \to (D^{*0} \to D^0\pi^0)\pi^{\pm}$ decays.

(b) The HORNSdini PDF fit to $B^{\pm} \to (D^{*0} \to D^0\pi^0)\pi^{\pm}$ MC

Figure 4.3: The HORNSdini PDF both in analytical form and as a fit to MC using the ξ factor for different peak heights [94].

The shape of the B mass distribution between the two highest points is parabolic in nature and is described by the expression

$$p(x) = \begin{cases} \left(x - \frac{a+b}{2}\right)^2, & \text{if } a < x < b \\ 0, & \text{otherwise,} \end{cases} \tag{4.1}$$

where x represents the B mass and a and b are the kinematic endpoints of the distribution. However, detector resolution effects require that this function be convolved with an appropriate resolution function. According to studies performed using $B^{\mp} \to [h'^{\pm}h''^{\mp}]_D h^{\mp}$ MC [94], the sum of two Gaussian functions provides an adequate description of the resolution. A Gaussian shape $G(x|\mu,\sigma)$, where μ and σ represent the mean and the width of the shape, respectively, is thus used to define a double Gaussian $D(x)$ function, where

$$D(x) = G(x|\mu, \sigma) + f_g G(x|\mu, R_\sigma \sigma). \tag{4.2}$$

In this expression, f_g is the relative fraction between the two Gaussian functions and R_σ is their relative width; both Gaussian functions share the same mean.

It has also been observed that the impact parameter and lifetime cuts on the B candidate can modify the shape of the double-peaking structure [94]. Most notably, the shape of the distribution can be distorted such that one of the peaks is higher than the other. This is accounted for in the PDF through the use of a linear polynomial with a slope parameter ξ. As this parameter approaches zero, the left-hand peak decreases in height relative to that of the right-hand peak. Including this polynomial, the HORNSdini PDF is analytically defined as

$$\text{HORNSdini}(\mu) = \int_a^b \left(x - \frac{a+b}{2}\right)^2 D(x|\mu, \sigma, f_g, R_\sigma) \left(\frac{1-\xi}{b-a}x + \frac{b\xi - a}{b-a}\right) \mathrm{d}x. \tag{4.3}$$

Additionally, an optional offset of δm can be added to the expression to allow for a translation of the full shape. A fit to $B^\pm \to (D^{*0} \to D^0\pi^0)\pi^\pm$ MC using the HORNSdini shape with ξ parameter is presented in Figure 4.3(b). The double-peaking structure is clearly visible, as is the difference in height between the two peaks.

4.2.2 HILLdini PDF for Missing Photon

Similar to the HORNSdini PDF, the HILLdini PDF is so-named because its shape resembles that of a hill. This shape is used to describe decays in which a photon is missed in the reconstruction. An example of such a decay is $B^\pm \to (D^{*0} \to D^0\gamma)\pi^\pm$. The decays in question are of the vector to pseudoscalar-vector variety, such as $D^{*0} \to D^0\gamma$, where the γ has spin-parity of 1^-. This means that the photon will travel preferentially in the directions of $\theta = \frac{\pi}{2}$ and $\theta = \frac{3\pi}{2}$. Consequently, instead of having a double-peaking structure as the spin-parity 0^- case, these invariant B mass distributions follow an inverted parabolic shape defined by

$$p(x) = \begin{cases} -(x-a)(x-b), & \text{if } a < x < b \\ 0, & \text{otherwise} \end{cases} \tag{4.4}$$

where a and b are the kinematic endpoints.

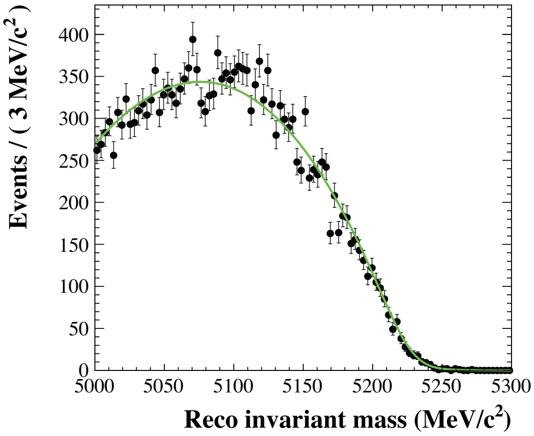

Figure 4.4: The HILLdini PDF fit to $B^{\pm} \to (D^{*0} \to D^{0}\gamma)\pi^{\pm}$ MC [94].

As in Section 4.2.1, this function is convolved with a double Gaussian to account for detector resolution effects. Finally, the selection effects are modelled through the use of the same linear polynomial as in Section 4.2.1, however in this case, as ξ approaches 0, the parabola exhibits a greater tilt to the right. The full HILLdini PDF is expressed as

$$\text{HILLdini}(\mu) = \int_a^b -(x-a)(x-b)D(x|\mu,\sigma,f_g,R_\sigma)\left(\frac{1-\xi}{b-a}x + \frac{b\xi - a}{b-a}\right)\mathrm{d}x. \tag{4.5}$$

A fit using this PDF to MC of the decay $B^{\pm} \to (D^{*0} \to D^{0}\gamma)\pi^{\pm}$ is presented in Figure 4.4.

4.2.3 Decay Modes Incorporated into the PDF Shapes

As noted earlier, these partially reconstructed low-mass PDF shapes were originally designed for use in studies involving $B^{\mp} \to [h'^{\pm}h''^{\mp}]_D h^{\mp}$ decays. As such, the decay modes that were studied to generate the shapes were chosen particularly for that analysis. However, these shapes can largely be used by this $B^{\mp} \to [h'^{\pm}h''^{\mp}\pi^0]_D h^{\mp}$ analysis due to the similarity in the final state decay products; in essence, the missed particle remains the same, but the difference is that the D meson, rather than decaying to a two-body final state, decays into a three-body one. Since the shape of these low mass backgrounds is primarily influenced by the angular distribution of the missing particle, it is reasonable that these shapes will be similar for decay modes where the same particle is lost. For the $B^{\mp} \to D\pi^{\mp}$ decay channels, five background decays are considered; they are listed in Table 4.1 along with the PDF used to model them. The modes that contribute to the partially reconstructed background for the $B^{\mp} \to DK^{\mp}$ selection are listed in Table 4.2.

Table 4.1: $B^{\mp} \to D\pi^{\mp}$ decay channels incorporated into the partially reconstructed low-mass shape.

Decay Channel	PDF for Modelling
$B^{\pm} \to (D^{*0} \to D^0\pi^0)\pi^{\pm}$	HORNSdini
$B^{\pm} \to D^0(\rho^{\pm} \to \pi^{\pm}\pi^0)$	HORNSdini
$B^0 \to (D^{*\mp} \to D^0\pi^{\mp})\pi^{\pm}$	HORNSdini
$B^0 \to D^0(\rho^0 \to \pi^+\pi^-)$	HORNSdini
$B^{\pm} \to (D^{*0} \to D^0\gamma)\pi^{\pm}$	HILLdini

Table 4.2: $B^{\mp} \to DK^{\mp}$ channels incorporated in the partially reconstructed low-mass shape.

Decay Channel	PDF for Modelling
$B^{\pm} \to (D^{*0} \to D^0\pi^0)K^{\pm}$	HORNSdini
$B^{\pm} \to D^0(K^{*\pm} \to K^{\pm}\pi^0)$	HORNSdini
$B^0 \to (D^{*\mp} \to D^0\pi^{\mp})K^{+}$	HORNSdini
$B^0 \to D^0(K^{*0} \to K^{\pm}\pi^{\mp})$	HORNSdini
$B^{\pm} \to (D^{*0} \to D^0\gamma)K^{\pm}$	HILLdini

Using MC from the decays in Tables 4.1 and 4.2, separate HORNSdini and HILLdini shapes are created for the DK and $D\pi$ modes. In each case, the analytic function attributed to the decay mode is convolved with the same double Gaussian resolution function. All of the shapes that use a HORNSdini PDF share a common ξ value, ξ_{HORNS}, as determined from MC, while all of the HILLdini constituents share a common ξ_{HILL} [89].

Although it is assumed that misidentified $B^{\mp} \to DK^{\mp}$ decays have a negligible effect on the low-mass partially reconstructed $B^{\mp} \to D\pi^{\mp}$ shapes, the same is not true for $B^{\mp} \to D\pi^{\mp}$ decays misidentified as $B^{\mp} \to DK^{\mp}$ because the former mode has a branching fraction an order of magnitude higher than the latter decay. For each of the decays that contribute to the $B^{\mp} \to DK^{\mp}$ low-mass shape, there is an additional contribution from misidentified $B^{\mp} \to D\pi^{\mp}$ decays. The HORNSdini and HILLdini PDFs for the DK modes each include contributions from partially reconstructed, misreconstructed $B^{\mp} \to D\pi^{\mp}$ decays; these misidentified decays are distinct from the misidentified signal shapes discussed in Section 4.3, and are modelled fully within the partially reconstructed low-mass PDF. These $B^{\mp} \to D\pi^{\mp}$ misidentified contributions in the low-mass region are studied in MC and are fit using shapes constructed from the sums of Gaussian distributions and error functions [89, 94, 96]. From these MC studies, the widths and means of these Gaussians are fixed as part of the low-mass PDF.

The sum of the respective HORNSdini and HILLdini PDFs for the different contributing decay channels is performed independently for the $B^{\mp} \to D\pi^{\mp}$ and $B^{\mp} \to DK^{\mp}$ (including misidentified $B^{\mp} \to D\pi^{\mp}$ contributions) modes and constitutes the partially reconstructed low-mass PDF used in the final fits.

4.2.4 Modifications for Use in Studying $B^{\mp} \to [h'^{\pm}h''^{\mp}\pi^0]_D h^{\mp}$ Decays

The HORNSdini and HILLSdini PDFs, for the most part, are used in this analysis as they were devised for the $B^{\mp} \to [h'^{\pm}h''^{\mp}]_D h^{\mp}$ analysis. However, several parameters related to the PDFs are allowed to float in the fit so that the shapes may better represent the kinematic differences of the decay modes of interest. These are:

- δm: Overall translation of the low-mass shape. It is possible that the B mass measured in the final fits is offset from the nominal B mass. If this is the case, the kinematic endpoints of the component PDFs of the low-mass shape will be offset as well, resulting in a shift.

- σ: width of the double Gaussian resolution function. From the MC studies performed in Section 3.7.3, it is known that the D mass distribution is wider in the $B^{\mp} \to [h'^{\pm}h''^{\mp}\pi^0]_D h^{\mp}$ decays than it is for the $B^{\mp} \to [h'^{\pm}h''^{\mp}]_D h^{\mp}$ decays. This width difference may be reflected in the low-mass distributions as well.

- The ratio of $D^{*0} \to D^0\gamma$ to $D^{*0} \to D^0\pi^0$ decays. Since the signal final states of interest involve a π^0 meson, this may affect the number of π^0 daughters from D^{*0} decays that are missed.

The yields of the partially reconstructed low-mass backgrounds are independent for each of the eight decay modes of this analysis. Furthermore, they are also independent for the positively and negatively charged B hadron samples in the final fits so as to allow for *CP* violation.

4.3 Misidentified $B^{\mp} \to D\pi^{\mp}$ Decays as $B^{\mp} \to DK^{\mp}$

Given that the discrimination between bachelor pions and kaons provided by the RICH system is not fully efficient, a certain proportion of $B^{\mp} \to D\pi^{\mp}$ candidates will be misidentified as $B^{\mp} \to DK^{\mp}$ decays and vice-versa. As seen in Section 3.9, the PID efficiency for kaon identification at the chosen value of PIDK > 4 is approximately 85% (compared to 97% for pions). As such, misidentified $B^{\mp} \to D\pi^{\mp}$ candidates constitute an important source of background for the $B^{\mp} \to DK^{\mp}$ signal modes. Unless specified otherwise, the term *misidentified* will mean a charged kaon mistakenly reconstructed as a charged pion or vice-versa.

In the case of bachelor misidentifications, the wrongly reconstructed decays will not lie directly on top of the nominal B mass. For instance, if a pion is misidentified as a kaon, when the larger mass is used in 4-momentum calculations, the ensuing B candidate will have a higher mass than expected. Similarly, a kaon misidentified as a pion will lead to a lower B mass measurement.

4.3.1 Double Crystal Ball PDF

In similar ADS/GLW analyses [83, 88], the double Crystal Ball function was used to model such background contributions to the $B^{\mp} \to DK^{\mp}$ signal events. The Crystal Ball function [97], named after the Crystal Ball Collaboration, is a Gaussian-like PDF commonly used in particle physics analyses. It is characterised by a Gaussian core and a power-law tail. Mathematically, the function is defined as

$$f(x;\alpha,n,\mu,\sigma) = N \cdot \begin{cases} \exp\left(-\frac{(x-\mu)^2}{2\sigma^2}\right), & \text{for } \frac{x-\mu}{\sigma} > -\alpha \\ A \cdot \left(B - \frac{x-\mu}{\sigma}\right)^{-n}, & \text{for } \frac{x-\mu}{\sigma} \leq -\alpha \end{cases} \tag{4.6}$$

where

$$A = \left(\frac{n}{|\alpha|}\right)^{n} \cdot \exp\left(-\frac{|\alpha|^2}{2}\right), \tag{4.7}$$

$$B = \frac{n}{|\alpha|} - |\alpha|, \tag{4.8}$$

$$N = \frac{1}{\sigma(C+D)}, \tag{4.9}$$

$$C = \frac{n}{|\alpha|} \cdot \frac{1}{n-1} \cdot \exp\left(-\frac{|\alpha|^2}{2}\right), \tag{4.10}$$

$$D = \sqrt{\frac{\pi}{2}}\left(1 + \mathrm{erf}\left(\frac{|\alpha|}{\sqrt{2}}\right)\right), \tag{4.11}$$

for mean μ, width σ, and tail parameters α and n (erf is the error function).

A double Crystal Ball function is the sum of two Crystal Balls that share a mean. Asymmetric left and right widths, σ_L and σ_R, are present and have the associated tail parameters of α_L, n_L, α_R and n_R.

4.3.2 Misidentified $B^{\mp} \to D\pi^{\mp}$ Decays

In order to verify that the double Crystal Ball is an appropriate shape to describe misidentified $B^{\mp} \to D\pi^{\mp}$ decays, a study is performed in MC. Starting with a $B^{\mp} \to [K^{\mp}\pi^{\pm}\pi^0]_D\pi^{\mp}$ MC sample, the candidates are reconstructed under the hypothesis that they are $B^{\mp} \to [K^{\mp}\pi^{\pm}\pi^0]_D K^{\mp}$ decays. After this reconstruction, the candidates are then weighted for PID performance using the `PIDCalib` reference histograms discussed in Section 3.9. Finally, these candidates are then fit with a double Crystal Ball function, as seen in Figure 4.5. From this plot, it can be seen that the shape fits the distribution well and, as expected, the distribution's mean is greater than the nominal B mass.

In the final fits, the yield of the double Crystal Ball PDF is fixed based on the number of candidates that pass the PID requirement for kaons. For example, if the PID efficiency for bachelor kaons is 85%, this means that 1 minus 85% (or 15%) of candidates that pass the PID requirement are misidentified bachelor pions. As a result, from the number of favoured candidates that pass the PID requirement for kaons and by knowing the PID efficiency of this requirement, the number of $B^{\mp} \to D\pi^{\mp}$ candidates that are misidentified as $B^{\mp} \to DK^{\mp}$

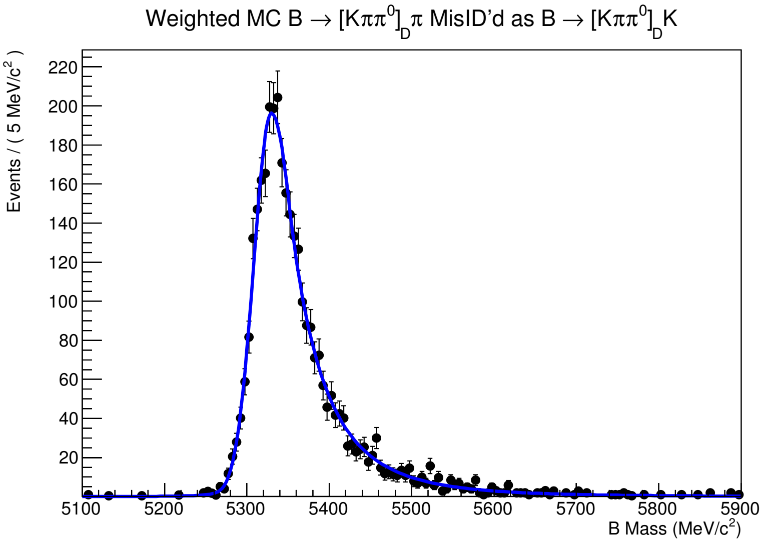

Figure 4.5: $B^{\mp} \to [K^{\mp}\pi^{\pm}\pi^0]_D\pi^{\mp}$ MC that has been misidentified as $B^{\mp} \to [K^{\mp}\pi^{\pm}\pi^0]_D K^{\mp}$ after PID re-weighting. The fit is performed using a double Crystal Ball.

events can be calculated. For each of the $B^{\mp} \to DK^{\mp}$ modes of interest, this calculated value is fixed as they yield of the misidentified events. However, all of the other Crystal Ball parameters are permitted to float, with the exception of the three presented in Table 4.3; fixing these parameters helps with fit convergence.

Table 4.3: Fixed tail parameters in the misidentified $B^{\mp} \to D\pi^{\mp}$ as $B^{\mp} \to DK^{\mp}$ double Crystal Ball shape.

Parameter Name	Value
α_L	$3.0^{+1.0}_{-0.5}$
n_L	3.0 ± 1.0
n_R	$10.0^{+1.0}_{-5.0}$

4.3.3 Misidentified $B^{\mp} \to DK^{\mp}$ Decays

In the final fits, the $B^{\mp} \to DK^{\mp}$ candidates misidentified as $B^{\mp} \to D\pi^{\mp}$ decays are modelled using a double Crystal Ball. A fit to $B^{\mp} \to [K^{\mp}\pi^{\pm}\pi^0]_D K^{\mp}$ MC that has been reconstructed as $B^{\mp} \to [K^{\mp}\pi^{\pm}\pi^0]_D\pi^{\mp}$ and PID reweighted is presented in Figure 4.6. In the final fits, the yields for this shape are fixed based on the PID efficiency of the identification of a bachelor pion. However, since the PID efficiency for the bachelor pion is rather high, the number of expected background contributions from this source is small. In addition, considering that $B^{\mp} \to D\pi^{\mp}$ decays have a branching fraction an order of magnitude greater than $B^{\mp} \to DK^{\mp}$

decays, these misidentified contributions are likely to be dwarfed by the $B^{\mp} \to D\pi^{\mp}$ signal peak. As a result, the shape is fully fixed to the parameters found in a fit to MC. These parameters are presented in Table 4.4.

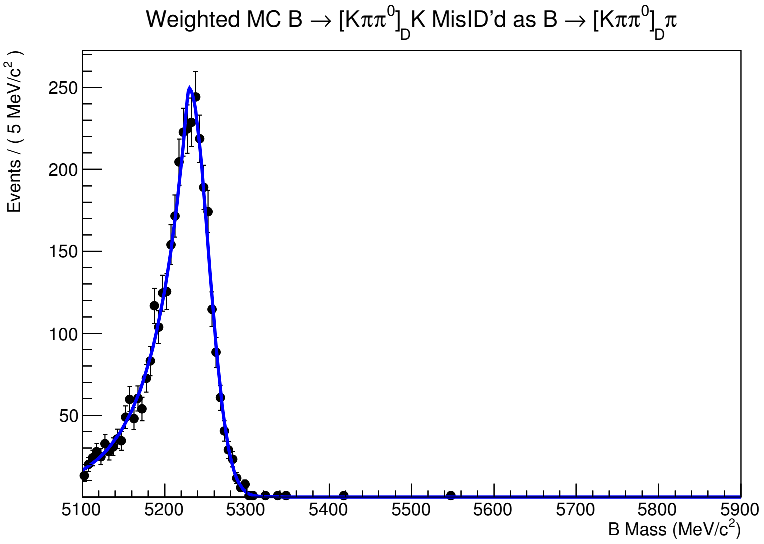

Figure 4.6: $B^{\mp} \to [K^{\mp}\pi^{\pm}\pi^0]_D K^{\mp}$ MC that has been misidentified as $B^{\mp} \to [K^{\mp}\pi^{\pm}\pi^0]_D \pi^{\mp}$ after PID re-weighting. The fit is performed using a double Crystal Ball.

Table 4.4: Fixed double Crystal Ball parameters for the misidentified $B^{\mp} \to DK^{\mp}$ as $B^{\mp} \to D\pi^{\mp}$ shape.

Parameter Name	Value
μ	5230 ± 5 MeV/c^2
σ_L	10 ± 5 MeV/c^2
σ_R	24 ± 1 MeV/c^2
α_L	0.30 ± 0.05
α_R	-4.0 ± 0.2
n_L	9.0 ± 3
n_R	1.0 ± 0.7

4.4 $B_s^0 \to [K^{\pm}\pi^{\mp}\pi^0]_D K^{*0}$

Decays of the form $B_s^0 \to [K^{\pm}\pi^{\mp}\pi^0]_D K^{*0}$, where $K^{*0} \to K^{\mp}\pi^{\pm}$, are a potential background contribution to the suppressed ADS decays $B^{\mp} \to [\pi^{\mp}K^{\pm}\pi^0]_D K^{\mp}$. If the charged pion from the K^{*0} decay is missed during reconstruction, the final state particles (complete with kaons of opposite charge) are the same as the suppressed ADS DK decay. These background decays will have an invariant mass less than the nominal $B^{\mp}$ mass, however, due to resolution effects, the right tail of the mass distribution may overlap with the signal peak of the $B^{\mp} \to [\pi^{\mp}K^{\pm}\pi^0]_D K^{\mp}$ decays, potentially leading to an over-estimation of the number of suppressed candidates observed.

In order to model this background, a study in MC is performed where $B_s^0 \to [K^{\pm}\pi^{\mp}\pi^0]_D K^{*0}$ decays are reconstructed as $B^{\mp} \to [\pi^{\mp}K^{\pm}\pi^0]_D K^{\mp}$. After selection cuts, the MC events that remain are illustrated in Figure 4.7. A fit is applied to these events using a Cruijff shape with separate left and right width parameters.

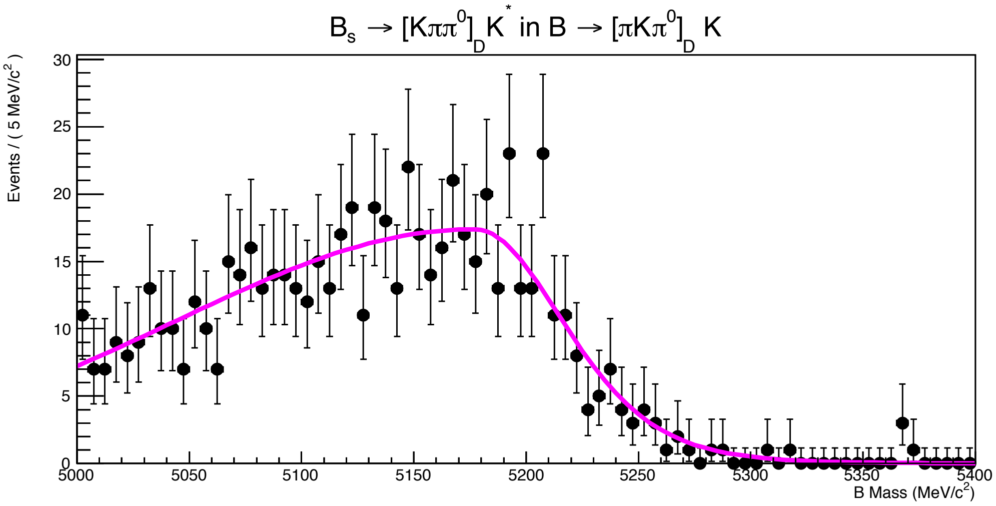

Figure 4.7: MC for $B_s^0 \to [K^{\pm}\pi^{\mp}\pi^0]_D K^*$ that remains after the selection used for $B^{\mp} \to [\pi^{\mp}K^{\pm}\pi^0]_D K^{\mp}$ data events. A Cruijff is used to model the shape.

Table 4.5: Cruijff parameters of the fixed shape modelling the backgrounds of $B_s^0 \to D(K^{\pm}\pi^{\mp}\pi^0)K^{*0}$ in $B^{\mp} \to [\pi^{\mp}K^{\pm}\pi^0]_D K^{\mp}$ decays.

Parameter	Value
μ	5177 ± 7 MeV/c^2
σ_L	133 ± 15 MeV/c^2
σ_R	38 ± 4 MeV/c^2
α_L	0.0100 ± 0.0007
α_R	0.090 ± 0.005

From this fit, it can be seen that the right tail of the distribution does indeed contaminate the vicinity of the nominal $B^{\mp}$ mass of 5279 MeV/c^2. As a result, in the final fit, this background is modelled using a Cruijff with parameters fully fixed from the MC study (these parameters are presented in Table 4.5). The yields, however, are permitted to vary.

4.5 Favoured/Suppressed ADS Crossfeed

A potential source of peaking background in the suppressed ADS decay $B^{\mp} \to [\pi^{\mp}K^{\pm}\pi^0]_D K^{\mp}$ is contributions from the favoured $B^{\mp} \to [K^{\mp}\pi^{\pm}\pi^0]_D K^{\mp}$ decay where the kaon and charged pion D daughters are both misidentified. This background is known as 'favoured/suppressed crossfeed' and its effects are mitigated through the use of PID requirements on the charged D daughters as well as applying a mass veto about the nominal D mass when the daughters are reconstructed under different mass hypotheses.

4.5.1 PID Requirements on D Daughters

The efficiency of PID cuts on the D daughters is evaluated by studying the $B^{\mp} \to [K^{\mp}\pi^{\pm}\pi^0]_D \pi^{\mp}$ data sample directly. This is done by determining the number of D signal candidates that are present without any daughter PID cuts and observing the reduction in the number of candidates as a PID cut is applied (separate PID cuts are placed on the daughter kaon and the charged daughter pion). In order to calculate the signal yields, a fit is performed to the D mass distribution. For the purpose of this study, the signal contribution is represented by a double Crystal Ball function and it is assumed that the background can be represented by a linear function. In Figure 4.8(a), the fit for the case where there are no PID cuts is presented. Figure 4.8(b) shows the same distribution after D daughter PID cuts have been applied.

Prior ADS/GLW analyses [83,88,95] have successfully used PID requirements of PIDK> 2 (kaon) and PIDK< -2 (pion) in order to reduce crossfeed background, so these same cut values are adopted in this analysis. The D mass distribution with these requirements is presented in Figure 4.8(b). In order to prevent the same candidate from appearing in the favoured and suppressed mode samples, the two cut values are mutually exclusive. The efficiency of the simultaneous application of both PID cut values is $(75.93 \pm 0.09)\%$ where the uncertainty is statistical.

In order to ascertain the effect of this D daughter PID requirement on favoured decays misidentified as suppressed decays, the same exercise is repeated for a data sample where the

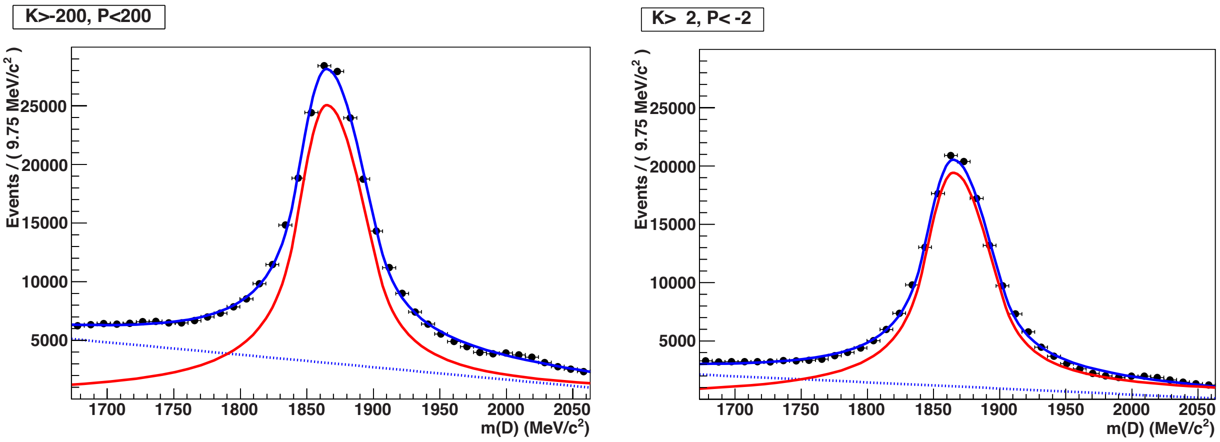

(a) No daughter PID Cuts

(b) Daughter PID cuts used in the final selection

Figure 4.8: Two of the D mass distribution plots used for the determination of the efficiency of PID cuts on the D daughters. The efficiency is measured by calculating how much of the signal (from the case with no cuts) is removed once the cuts are applied. The signal is modelled by the double Crystal Ball in red and the background by the dotted blue line.

D meson has been reconstructed such that its kaon daughter is reconstructed as a charged pion and its charged pion daughter as a kaon. The ratio of events after and before the PID cuts is measured at $(0.19 \pm 0.01)\%$; the low value implies that the chosen PID cut values are quite effective at distinguishing between kaons and pions.

4.5.2 Mass Veto for the D Reconstructed Under Alternate Mass Hypotheses

The mass of the D candidate can be calculated when it is reconstructed in such a way that the charged pion candidate is assumed to be a charged kaon and vice-versa. For the sake of clarity, let the originally reconstructed D mass be known as the *default* D mass and the version reconstructed under different daughter mass hypotheses as the *swapped* D mass. As a means of reducing the favoured/suppressed crossfeed, a mass veto of ± 30 MeV/c^2 about the nominal D mass is applied to the swapped D mass distribution.

The efficiency of such a cut is trivial to calculate for the correctly identified decays; one simply compares the yields of the default D mass distribution before and after the application of the cut on the swapped D mass variable. For doubly-misidentified decays, however, the efficiency of such a cut is calculated by exploiting the fact that the favoured and suppressed

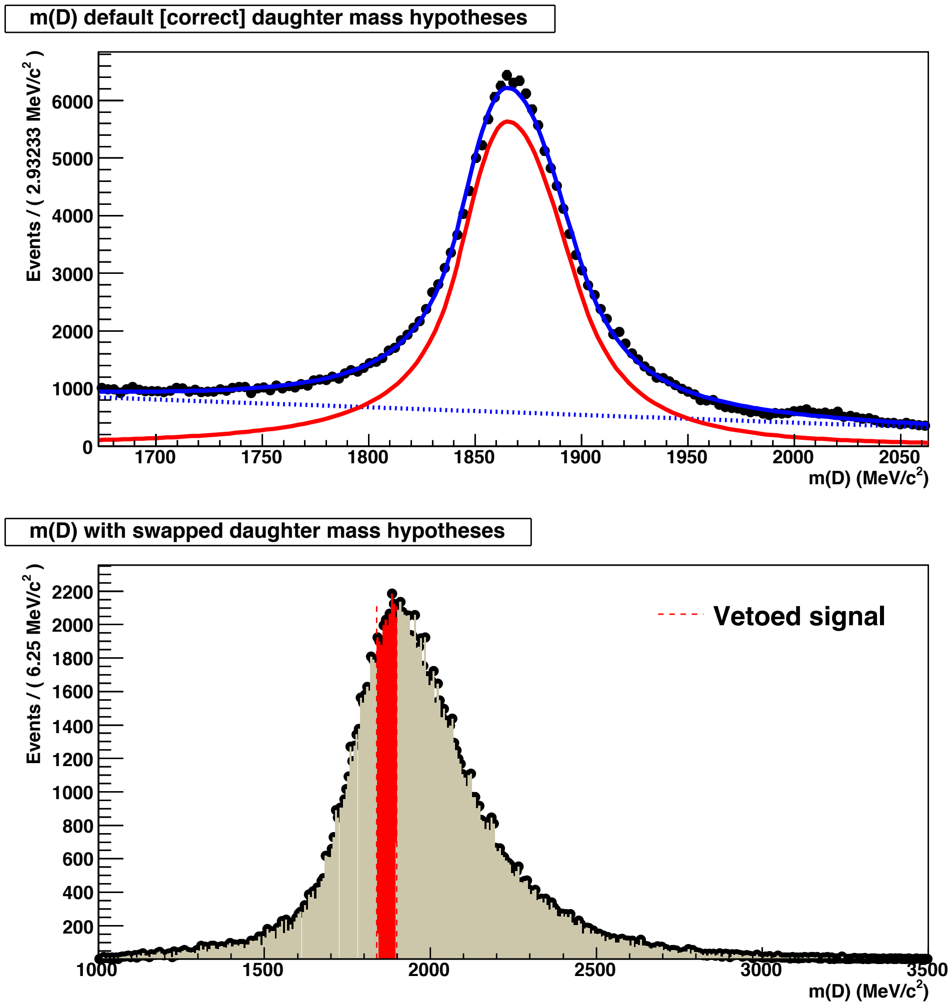

Figure 4.9: In the upper plot, the fitted D mass distribution used for the extraction of weights using the sPlots method is shown. The signal is modelled as a double Crystal Ball (solid red) and the background as a linear function (dotted blue). The weighted signal distribution is presented in the lower plot, after the kaon and charged pion mass have been swapped. The dashed red line in the lower plot shows the region corresponding to the veto on the D mass after the swapped daughter reconstruction.

ADS modes have identical kinematic distributions where only the charges of their final-state particles are different. The upper plot of Figure 4.9 shows the default D mass distribution from the $B^{\mp} \to [K^{\mp}\pi^{\pm}\pi^{0}]_{D}\pi^{\mp}$ data selection after the application of the BDT cut and the bachelor PID cut. We perform a fit with the signal modelled as a double Crystal Ball and the background as a linear function. The signal component of the distribution is extracted using the sPlot technique [98] and these event weights are used to plot the lower distribution of Figure 4.9 which is a D mass distribution with the D daughters' mass hypotheses swapped; this is the distribution of the favoured mode signal when it is misidentified. The effect of the veto can then be ascertained using this weighted, swapped D mass plot. We calculate the proportion of signal events remaining after the veto to be $(87.30 \pm 0.09)\%$ for the correctly identified daughter decays and $(39.05 \pm 0.13)\%$ for the doubly-misidentified decays.

As part of the final selection, there is also a mass window of ± 50 MeV/c^2 applied about the nominal D mass, as discussed in Section 3.7.3. The effect of this cut can be calculated using similar methods as discussed in this section. For correctly identified daughter decays, this mass window retains $(75.65 \pm 0.11)\%$ of events and for doubly-misidentified decays, it retains $(20.73 \pm 0.10)\%$.

4.5.3 The Proportion of Doubly-Misidentified Events

In order to quantify the effect of the favoured/suppressed crossfeed, its yield is expressed as a proportion of the favoured ADS decay. The results of the efficiency studies from Sections 4.5.1 and 4.5.2 are collected in Table 4.6. The first column corresponds to the efficiencies for the properly identified favoured mode and the second gives the efficiencies for a doubly-misidentified favoured mode. The total efficiency is the product of the three efficiencies of the respective column. The ratio of misidentified to favoured efficiencies is the proportion used in the final fit to ascertain the misidentified favoured crossfeed in the suppressed ADS channel. This proportion has a value of $(3.07 \pm 0.15) \times 10^{-4}$ and is fixed as the relative yield for this background in the final fit.

From the branching fractions provided in Section 3.6, the $B^{\mp} \to [\pi^{\mp}K^{\pm}\pi^{0}]_{D}K^{\mp}$ decay has a branching fraction of 1.12×10^{-7}. The favoured mode $B^{\mp} \to [K^{\mp}\pi^{\pm}\pi^{0}]_{D}K^{\mp}$ has a

Table 4.6: The efficiency of D selection window, double-misidentified mass reconstruction veto and PID of D daughter cuts used to reduce favoured/suppressed ADS mode crossfeed. The first column is the efficiency for the properly identified D daughters and the second column for the doubly-misidentified daughters. The subscripts in the mode descriptions indicate what the particle is reconstructed as.

	$[K^{\pm}_{K}\pi^{\mp}_{\pi}\pi^0]_D$	$[K^{\pm}_{\pi}\pi^{\mp}_{K}\pi^0]_D$
Selection: $\lvert m(D) - 1865\rvert < 50$ MeV/c^2	0.7565 ± 0.0011	0.2073 ± 0.0010
Veto on $K \leftrightarrow \pi$: $\lvert m(D) - 1865\rvert > 30$ MeV/c^2	0.8730 ± 0.0009	0.3905 ± 0.0013
PIDK(K) > 2, PIDK(π) < −2	0.7593 ± 0.0009	0.0019 ± 0.0001
Total	0.5015 ± 0.0010	$(1.54 \pm 0.08) \times 10^{-4}$
Proportion	$(3.07 \pm 0.15) \times 10^{-4}$	

branching fraction of 5.1×10^{-5}. If we multiply this value by the proportion calculated in Table 4.6, we expect a residual background from this source an order of magnitude less than the suppressed decay mode. As a result, less than 0.03 $B^{\mp} \to [K^{\mp}\pi^{\pm}\pi^0]_D K^{\mp}$ events are expected to originate from $B^{\mp} \to [\pi^{\mp}K^{\pm}\pi^0]_D K^{\mp}$ crossfeed, so contamination of the favoured ADS decay mode from suppressed ADS candidates is deemed negligible.

4.5.4 Crossfeed Shape

In order to obtain a shape for use in the final fits for the favoured/suppressed crossfeed background component, a study in MC is performed. A sample of $B^{\mp} \to [K^{\mp}\pi^{\pm}\pi^0]_D \pi^{\mp}$ MC is used and the B mass is reconstructed under the hypotheses that the kaon D daughter is a pion and the charged pion D daughter is a kaon. The results of this B mass distribution are presented in Figure 4.10. A fit is performed using a Cruijff PDF that has the same tail parameters as the fit to MC performed in Section 3.7.4, but allowing the width to float. The shape that is obtained has a width of 30 ± 1 MeV/c^2 in contrast to the width of 15.2 ± 0.3 MeV/c^2 measured for $B^{\mp} \to [K^{\mp}\pi^{\pm}\pi^0]_D \pi^{\mp}$ MC in Section 3.7.4. It is thus concluded that the crossfeed component shape is roughly twice the width of the signal peak.

Thus, for the suppressed ADS modes of $B^{\mp} \to [\pi^{\mp}K^{\pm}\pi^0]_D \pi^{\mp}$ and $B^{\mp} \to [\pi^{\mp}K^{\pm}\pi^0]_D K^{\mp}$, the favoured/suppressed crossfeed is modelled in the fit using a Cruijff that shares the same parameters as the signal peaks, with the exception of the width which is fixed to be twice that of the signal peaks. The yields are fixed as a proportion of the signal yields, using the result given in Table 4.6.

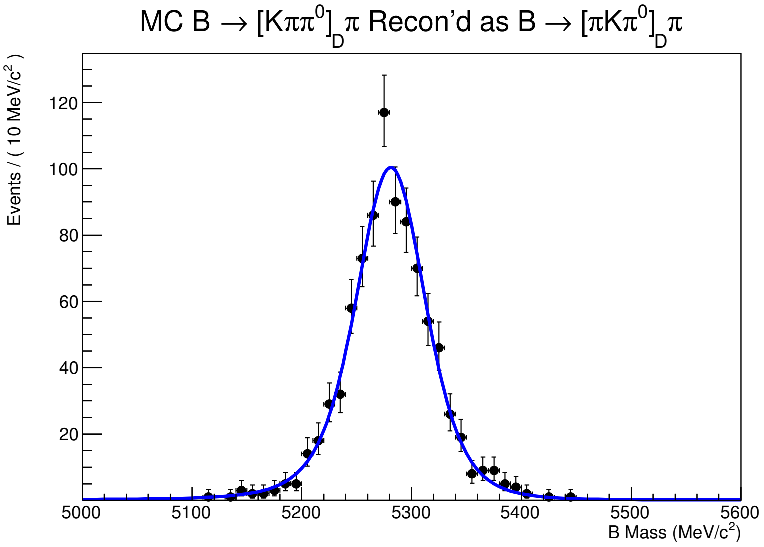

Figure 4.10: The favoured/suppressed crossfeed shape in MC as modelled by a Cruijff function. The width is roughly twice that seen for the B mass in $B^{\mp} \rightarrow [K^{\mp}\pi^{\pm}\pi^0]_D\pi^{\mp}$ MC.

4.6 Charmless Background Contributions

A potential source of peaking backgrounds are charged B decays that do not decay to a D meson, but have the same four-body final state as our modes of interest. An example of such a so-called charmless decay is $B^{\mp} \rightarrow K^{\pm}K^{\mp}\pi^{\mp}\pi^0$; this decay could be a background to the suppressed ADS decay $B^{\mp} \rightarrow [\pi^{\mp}K^{\pm}\pi^0]_D K^{\mp}$ because the final-state particles are the same. We must, therefore, determine a method for suppressing these charmless backgrounds and estimating the residual contamination.

4.6.1 D Flight Distance z-Significance Cut

In the case of a charmless decay, all of the final state particles originate from the $B^{\mp}$ vertex. Thus, if a charmless decay is wrongly reconstructed as a $B^{\mp} \rightarrow Dh^{\mp}$ decay, the wrongly identified D vertex should be relatively close to the B vertex. However, the D meson has a mean lifetime of 4.1×10^{-13} s [2] and therefore flies before it decays, so genuine D vertices are displaced from the B vertices. As such, to suppress charmless contamination, a flight distance z-significance cut on the D meson candidate with respect to the B vertex, as discussed in Section 3.2.7, can be exploited.

A cut of $\text{FD}_D > 2$ has been used in prior ADS/GLW analyses [83, 88] with the effect of reducing charmless contribution by approximately 95% with a signal efficiency of roughly 70% [99]. A cut of the same value is used in this analysis. Figure 4.11 presents the FD$_D$ distribution for the favoured $B^{\mp} \to [K^{\mp}\pi^{\pm}\pi^0]_D h^{\mp}$ modes. In both cases, events to the right of the cut are selected, and thus the peak of the distribution which corresponds to the significance value most commonly attributed to events with a genuine D candidate, is removed.

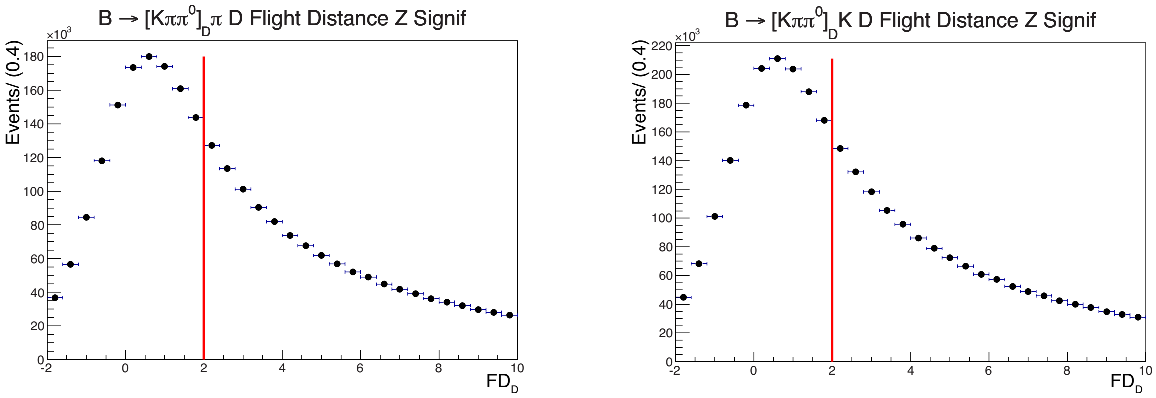

(a) $B^{\mp} \to [K^{\mp}\pi^{\pm}\pi^0]_D \pi^{\mp}$ (b) $B^{\mp} \to [K^{\mp}\pi^{\pm}\pi^0]_D K^{\mp}$

Figure 4.11: FD$_D$ distributions for the favoured $B^{\mp} \to [K^{\mp}\pi^{\pm}\pi^0]_D h^{\mp}$ modes. These distributions are for data in the fitted B mass region after a loose BDT cut of -0.9. The line in red indicates FD$_D = 2$.

The use of this FD$_D$ cut must be characterised and the amount of charmless contributions that remain after its application needs to be ascertained. However, the relevant charmless branching fractions have not been measured. Under these circumstances, it is sometimes possible to study the B mass distribution in the D sidebands; the expectation being that at a D mass sufficiently far away from the nominal D mass, the candidates that remain are less likely to have a genuine D meson and any enhancement in the B mass distribution can be interpreted as a charmless decay. However, this is not practical for the decays of interest in this analysis given that the D mass distribution has long tails (as seen in Figure 4.9), thus meaning that events with a genuine D candidate lie far into the sidebands rendering background studies difficult. Instead, estimates on the level of residual charmless background can be made by considering the results of a study performed in a similar analysis.

4.6.2 Estimating the Charmless Contributions

In the 3 fb^{-1} $B^{\mp} \to [h'^{\pm}h''^{\mp}]_D h^{\mp}$ LHCb analysis [95], an exhaustive study of charmless decays of the form $B^{\mp} \to h'^{\mp}h''^{\pm}h^{\mp}$ contaminating $B^{\mp} \to Dh^{\mp}$ decays where the D decays to two charged daughters was performed. By assuming that the proportion of $B^{\mp} \to h'^{\mp}h''^{\pm}h^{\mp}$ charmless decays (3-body charmless states) that is present in the $B^{\mp} \to [h'^{\pm}h''^{\mp}]_D h^{\mp}$ signal region is comparable to that of the $B^{\mp} \to h'^{\mp}h''^{\pm}h^{\mp}\pi^0$ charmless decays (4-body charmless states) present in the $B^{\mp} \to [h'^{\pm}h''^{\mp}\pi^0]_D h^{\mp}$ signal region, the results from the $B^{\mp} \to [h'^{\pm}h''^{\mp}]_D h^{\mp}$ study can be used to estimate the charmless yields in this analysis.

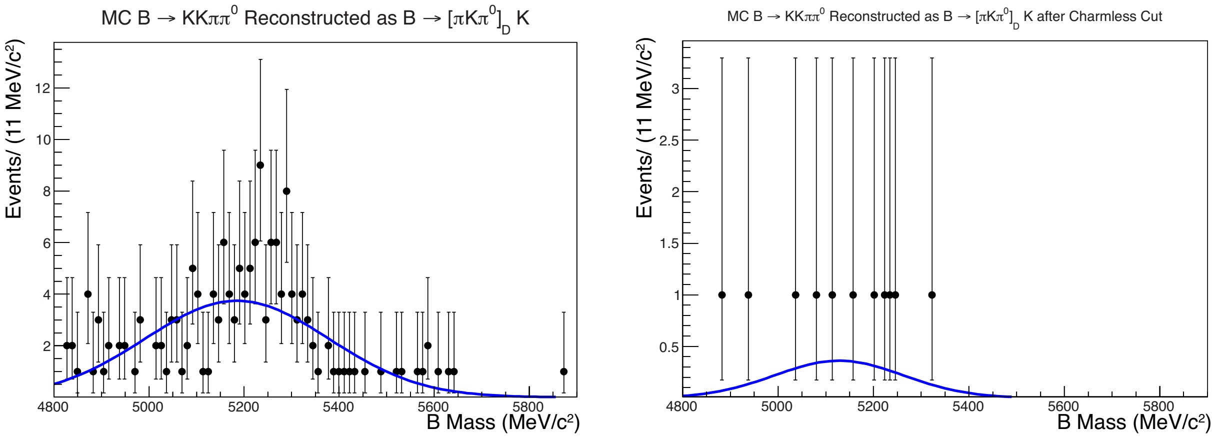

(a) Before the $FD_D > 2$ cut.

(b) After the $FD_D > 2$ cut.

Figure 4.12: B mass distributions for $B^{\mp} \to K^{\pm}K^{\mp}\pi^{\mp}\pi^0$ MC events that pass the stripping selection as $B^{\mp} \to [\pi^{\mp}K^{\pm}\pi^0]_D K^{\mp}$ including a BDT> -0.80 cut.

It is important to ensure that the effect of the FD$_D$ suppression cut also used in the $B^{\mp} \to [h'^{\pm}h''^{\mp}]_D h^{\mp}$ study is similar in 3-body and 4-body final states. This assumption is supported by examining MC events for the decay $B^{\mp} \to K^{\pm}K^{\mp}\pi^{\mp}\pi^0$, as seen in Figure 4.12. These decays are reconstructed under the mass hypotheses and stripping selection for $B^{\mp} \to [\pi^{\mp}K^{\pm}\pi^0]_D K^{\mp}$ decays, a signal mode that this charmless decay is expected to contaminate. Figure 4.12(a) shows the events that remain after the BDT cut and Figure 4.12(b) shows the effect of the application of the FD$_D$ charmless suppression cut. After the cut, approximately 7% of the events of Figure 4.12(a) remain. This proportion is compatible with that seen in the $B^{\mp} \to [h'^{\pm}h''^{\mp}]_D h^{\mp}$ analysis, thus giving confidence that the FD$_D$ cut behaves similarly

Table 4.7: The charmless contributions for the different signal channels. $B^{\mp} \to [h'^{\pm}h''^{\mp}\pi^0]_D h^{\mp}$ decays are referred to as *three-body* modes while the $B^{\mp} \to [h'^{\pm}h''^{\mp}]_D h^{\mp}$ decays are termed *two-body* decays. The scaling factors relate the yields from the relevant $B^{\mp} \to [h'^{\pm}h''^{\mp}]_D h^{\mp}$ (two-body) modes and the comparable $B^{\mp} \to [h'^{\pm}h''^{\mp}\pi^0]_D h^{\mp}$ (three-body) mode. "Cut" and "no cut" refer to the amount of charmless events that remain before and after the FD$_D$ cut. The anticipated number of charmless events, after the use of the FD$_D > 2$ cut, is summarised in the final column.

Decay Mode	Potential Charmless Contribution	Relevant 2-body Charmless Mode	Description	Scale Factor	Ratio of Branching Fractions	Two-Body (no cut $\mid$ cut)	Three-Body (no cut $\mid$ cut)
$B^{\mp} \to [\pi^{\mp}K^{\pm}\pi^0]_D\pi^{\mp}$	$B^{\pm} \to K^{\mp}\pi^{\pm}\pi^0\pi^{\pm}$	$B^{\pm} \to K^{\mp}\pi^{\pm}\pi^{\pm}$	The charmless decay was not seen in the upper sideband of $B^{\mp} \to [\pi^{\pm}\pi^{\mp}]_D K^{\mp}$. An upper limit is assumed.	N/A	N/A	N/A	$1 \pm 1 \mid 1 \pm 1$
$B^{\mp} \to [\pi^{\mp}K^{\pm}\pi^0]_D K^{\mp}$ $B^{\mp} \to [K^+K^-\pi^0]_D\pi^{\mp}$	$B^{\pm} \to K^{\mp}\pi^{\pm}\pi^0 K^{\pm}$	$B^{\pm} \to K^{\mp}K^{\pm}\pi^{\pm}$	The charmless decay was searched for in the upper and lower sidebands of $B^{\mp} \to [\pi^{\pm}K^{\mp}]_D K^{\mp}$.	$\frac{37736 \pm 283}{382902 \pm 676}$	$\frac{0.039 \pm 0.001}{0.139 \pm 0.005}$	$211 \pm 29 \mid 12 \pm 8$	$27 \pm 18 \mid 1 \pm 1$
$B^{\mp} \to [K^{\mp}\pi^{\pm}\pi^0]_D\pi^{\mp}$ $B^{\mp} \to [\pi^+\pi^-\pi^0]_D K^{\mp}$	$B^{\pm} \to K^{\pm}\pi^{\mp}\pi^0\pi^{\pm}$	$B^{\pm} \to K^{\pm}\pi^{\mp}\pi^{\pm}$	Studied in the upper sideband of $B^{\mp} \to [\pi^{\pm}\pi^{\mp}]_D K^{\mp}$.	$\frac{3488 \pm 84}{14667 \pm 124}$	$\frac{0.001 \pm 0.000}{0.014 \pm 0.001}$	$1746 \pm 49 \mid 83 \pm 11$	$178 \pm 25 \mid 4 \pm 1$
$B^{\mp} \to [K^{\mp}\pi^{\pm}\pi^0]_D K^{\mp}$	$B^{\pm} \to K^{\pm}\pi^{\mp}\pi^0 K^{\pm}$	$B^{\pm} \to K^{\pm}K^{\pm}\pi^{\mp}$	Not seen in 2-body sideband studies. An upper limit is assumed.	N/A	N/A	N/A	$1 \pm 1 \mid 1 \pm 1$
$B^{\mp} \to [\pi^+\pi^-\pi^0]_D\pi^{\mp}$	$B^{\pm} \to \pi^{\pm}\pi^{\mp}\pi^0\pi^{\pm}$	$B^{\pm} \to \pi^{\pm}\pi^{\mp}\pi^{\pm}$	Studied in the upper sideband of $B^{\mp} \to [\pi^{\pm}\pi^{\mp}]_D\pi^{\mp}$.	$\frac{3488 \pm 84}{14667 \pm 124}$	$\frac{0.001 \pm 0.000}{0.014 \pm 0.001}$	$1159 \pm 60 \mid 66 \pm 18$	$118 \pm 33 \mid 3 \pm 1$
$B^{\mp} \to [K^+K^-\pi^0]_D K^{\mp}$	$B^{\pm} \to K^{\pm}K^{\mp}\pi^0 K^{\pm}$	$B^{\pm} \to K^{\pm}K^{\mp}K^{\pm}$	Studied in the lower sideband of $B^{\mp} \to [K^{\pm}K^{\mp}]_D K^{\mp}$.	$\frac{1050 \pm 53}{50659 \pm 279}$	$\frac{0.004 \pm 0.000}{0.003 \pm 0.000}$	$1144 \pm 41 \mid 49 \pm 14$	$131 \pm 38 \mid 1 \pm 1$

in the reduction of 4-body charmless with a π^0 as it does on 3-body charmless states.

In order to scale between $n^{\mathrm{no}D}_{h'h''}$, the charmless yield contributions of the $B^{\mp} \to [h'^{\pm}h''^{\mp}]_D h^{\mp}$ analysis, and $n^{\mathrm{no}D}_{h'h''\pi^0}$, the charmless yield in the current analysis, Equation 4.12 is used:

$$n^{\mathrm{no}D}_{h'h''\pi^0} = n^{\mathrm{no}D}_{h'h''} \times 2 \times \frac{\epsilon_{h'h''\pi^0}}{\epsilon_{h'h''}}, \tag{4.12}$$

where the factor of 2 relates the size of the D mass windows used in the final selection of the two analyses and efficiency, ϵ_x, relates the observed signal yield of the $B^{\mp} \to [x]_D h^{\mp}$ decay where the charmless contamination is being considered to the branching fraction of $D \to x$. Specifically,

$$\epsilon_{h'h''\pi^0} = \frac{\mathrm{yield}_{h'h''\pi^0}}{\mathcal{B}(D \to h'h''\pi^0)} \quad \text{and} \quad \epsilon_{h'h''} = \frac{\mathrm{yield}_{h'h''}}{\mathcal{B}(D \to h'h'')} \tag{4.13}$$

are the efficiencies. We may thus rewrite Equation 4.12 as:

$$n^{\mathrm{no}D}_{h'h''\pi^0} = n^{\mathrm{no}D}_{h'h''} \times \frac{\mathrm{yield}_{h'h''\pi^0}}{\mathrm{yield}_{h'h''}} \times \frac{\mathcal{B}(D \to h'h'')}{\mathcal{B}(D \to h'h''\pi^0)} \times 2. \tag{4.14}$$

The first ratio in this expression is a scaling factor using the signal yields of the desired $B^{\mp} \to [h'^{\pm}h''^{\mp}\pi^0]_D h^{\mp}$ mode and its similar corresponding $B^{\mp} \to [h'^{\pm}h''^{\mp}]_D h^{\mp}$ decay. The second ratio is the branching fractions of the relevant 2-body and 3-body D decays modes. The $B^{\mp} \to [h'^{\pm}h''^{\mp}\pi^0]_D h^{\mp}$ analysis uses a 50 MeV/c^2 window (± 25 MeV/c^2 about the nominal D mass), whereas the $B^{\mp} \to [h'^{\pm}h''^{\mp}\pi^0]_D h^{\mp}$ analysis uses a 100 MeV/c^2 window (± 50 MeV/c^2 about the nominal D mass). The charmless studies in the $B^{\mp} \to [h'^{\pm}h''^{\mp}]_D h^{\mp}$ analysis demonstrate that the charmless background is effectively constantly distributed about the D mass space [95], thus the increase in D mass window size is accounted for in Equation 4.14 through the use of a factor of 2.

Table 4.7 summarises the different signal modes in the current analysis, the anticipated contaminating charmless modes, the relevant $B^{\mp} \to [h'^{\pm}h''^{\mp}]_D h^{\mp}$ modes for comparison and the appropriate scaling factors and branching ratios. The yield numbers for the $B^{\mp} \to [h'^{\pm}h''^{\mp}\pi^0]_D h^{\mp}$ modes come from Section 6.1.1 and the branching fractions from the Particle Data Group [2]. These contributions, after the FD$_D$ requirement, are all very small, contributing at most a few events. The Belle Collaboration measured charmless contributions of $B^{\mp} \to K^{\pm}K^{\mp}\pi^{\pm}\pi^{0}$ in their study of $B^{\mp} \to [\pi^{\mp}K^{\pm}\pi^{0}]_{D}K^{\mp}$ decays [36]; the effect was deemed to be negligible. From the estimations in Table 4.7, that charmless decay mode has a yield consistent with 0, thus giving confidence in the estimates.

A summary of the charmless events that remain after the FD_D requirement is presented in Table 4.8. In the final fits, we account for the charmless decay contributions, by employing a fixed shape that has the same parameters as the signal peak with yields fixed to the values of Table 4.8.

Table 4.8: Final charmless yields fixed in the final fits.

Decay Mode	Charmless Contribution	Charmless Event Yield
$B^{\mp} \to [\pi^{\mp}K^{\pm}\pi^{0}]_{D}\pi^{\mp}$	$B^{\pm} \to K^{\mp}\pi^{\pm}\pi^{0}\pi^{\pm}$	1 ± 1
$B^{\mp} \to [\pi^{\mp}K^{\pm}\pi^{0}]_{D}K^{\mp}$	$B^{\pm} \to K^{\mp}\pi^{\pm}\pi^{0}K^{\pm}$	1 ± 1
$B^{\mp} \to [K^{+}K^{-}\pi^{0}]_{D}\pi^{\mp}$	$B^{\pm} \to K^{\mp}\pi^{\pm}\pi^{0}K^{\pm}$	1 ± 1
$B^{\mp} \to [K^{\mp}\pi^{\pm}\pi^{0}]_{D}\pi^{\mp}$	$B^{\pm} \to K^{\pm}\pi^{\mp}\pi^{0}\pi^{\pm}$	4 ± 1
$B^{\mp} \to [\pi^{+}\pi^{-}\pi^{0}]_{D}K^{\mp}$	$B^{\pm} \to K^{\pm}\pi^{\mp}\pi^{0}\pi^{\pm}$	4 ± 1
$B^{\mp} \to [K^{\mp}\pi^{\pm}\pi^{0}]_{D}K^{\mp}$	$B^{\pm} \to K^{\pm}\pi^{\mp}\pi^{0}K^{\pm}$	1 ± 1
$B^{\mp} \to [\pi^{+}\pi^{-}\pi^{0}]_{D}\pi^{\mp}$	$B^{\pm} \to \pi^{\pm}\pi^{\mp}\pi^{0}\pi^{\pm}$	3 ± 1
$B^{\mp} \to [K^{+}K^{-}\pi^{0}]_{D}K^{\mp}$	$B^{\pm} \to K^{\pm}K^{\mp}\pi^{0}K^{\pm}$	1 ± 1

4.7 Quasi-GLW Contamination in the Suppressed ADS Modes

Decays from the quasi-GLW $B^{\mp} \to [\pi^{+}\pi^{-}\pi^{0}]_{D}h^{\mp}$ and $B^{\mp} \to [K^{+}K^{-}\pi^{0}]_{D}h^{\mp}$ modes may be mistaken for suppressed ADS decays of $B^{\mp} \to [\pi^{\mp}K^{\pm}\pi^{0}]_{D}h^{\mp}$ if one of the charged D daughters is misidentified. In principle, such contamination is also possible in the favoured ADS modes, however, given the relative branching fractions of the quasi-GLW modes, the effects are deemed negligible.

To evaluate the contributions of such contamination in the suppressed ADS modes, we perform a study using MC for each of the four quasi-GLW decay modes, but where one of the charged D daughters is misidentified, leading to the same final-state particles as in a suppressed ADS decay. In such a study, particular attention is paid to the charge of the D

daughter that is misidentified, as only cases where the D daughter kaon and the bachelor having opposite charge can be mistaken as suppressed ADS decays.

When examining MC events, it is necessary to scale the yield in MC to the expected number of candidates in the full data set in order to ascertain whether the background will be significant or not in the real data. The scaling is performed through the use of Equation 4.15,

$$N_{\text{expected}} = \sigma f \left(\textstyle\int \mathcal{L}\right) \mathcal{B} \epsilon_{\text{Acc}} \epsilon_{\text{Offline}}. \tag{4.15}$$

The elements of the expression are defined as follows:

- σ: The production cross section of B hadrons from pp interactions. In particular, the interest is in $\sigma(pp \to B^{\pm} + X)$, where X represents any particle or combination of particles, since the channels of interest in the analysis have a charged B parent particle decay. A value of $(38.9 \pm 2.8) \times 10^9$ fb is used [100].

- f: The hadronisation fraction, f_u in the case of $B^{\mp}$ decays. The fraction f_u is defined as the proportion of b quarks produced from LHC pp collisions that hadronise with a u quark to form a B^- or B^+ hadron. Here, $f_u \approxeq f_d$ is taken as 0.373 ± 0.017 [101].

- $\int \mathcal{L}$: The integrated luminosity of the data set. A value of 3.0 fb^{-1} is used.

- $\mathcal{B}$: the branching fraction of the decay in question.

- ϵ_{Acc}: The geometric acceptance efficiency. This value is obtained from the MC generation statistics.

- $\epsilon_{\text{Offline}}$: The offline selection efficiency. This includes efficiencies from triggering, stripping and analysis selection. This value is obtained by dividing the total number of candidates that pass the full selection by the total number of generated MC events.

Figure 4.13, presents the D mass distribution, in MC, that has been PID reweighted, for the four quasi-GLW modes reconstructed as suppressed ADS modes. These distributions have the stripping and BDT selections applied, in addition to the π^0 mass cut. The vertical

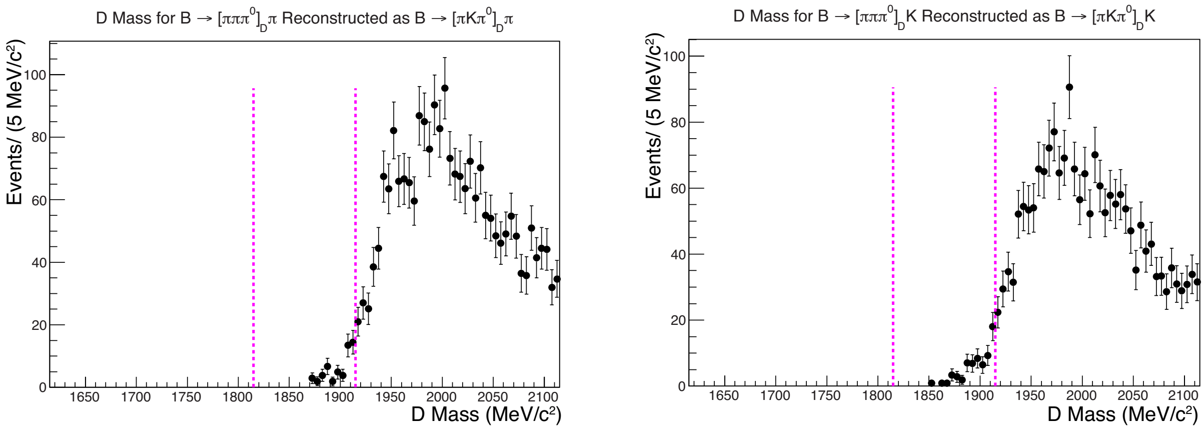

(a) $B^{\mp} \to [\pi^+\pi^-\pi^0]_D\pi^{\mp}$ reconstructed as $B^{\mp} \to [\pi^{\mp}K^{\pm}\pi^0]_D\pi^{\mp}$

(b) $B^{\mp} \to [\pi^+\pi^-\pi^0]_D K^{\mp}$ reconstructed as $B^{\mp} \to [\pi^{\mp}K^{\pm}\pi^0]_D K^{\mp}$

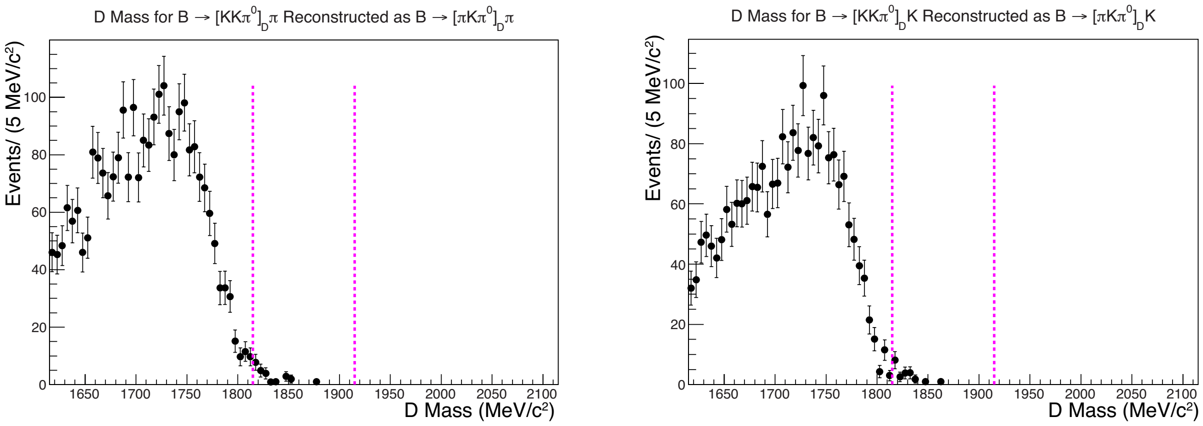

(c) $B^{\mp} \to [K^+K^-\pi^0]_D\pi^{\mp}$ reconstructed as $B^{\mp} \to [\pi^{\mp}K^{\pm}\pi^0]_D\pi^{\mp}$

(d) $B^{\mp} \to [K^+K^-\pi^0]_D K^{\mp}$ reconstructed as $B^{\mp} \to [\pi^{\mp}K^{\pm}\pi^0]_D K^{\mp}$

Figure 4.13: D mass distributions in PID reweighted MC for quasi-GLW modes reconstructed as suppressed ADS modes using only a BDT cut and a π^0 mass window cut. The dashed lines represent the D mass window cut used in the final selection.

dashed lines represent the D mass window used in the final selection. It is seen that in all cases only a small fraction of the misreconstructed decays leak into the signal region.

The B mass distributions of the background candidates that lie within the D mass window of Figure 4.13 are subject to the further requirement that the candidates pass the PID selection criteria for D daughters discussed in Section 4.5.1. As a result of this additional cut, there are fewer candidates remaining in the distributions; the number of remaining candidates is presented in the penultimate column of Table 4.9. Most notably, the $B^{\mp} \to [K^+K^-\pi^0]_D h^{\mp}$ distributions have no candidates remaining after the use of the D daughter PID cuts.

In order to obtain the estimate of the number of misidentified quasi-GLW candidates in the suppressed ADS modes in data, the number of remaining MC candidates are scaled using Equation 4.15. If one assumes that the number of MC candidates that pass the selection is one, ϵ_{Acc} is 1 divided by the total number of generated MC events, thus meaning that the N_{expected} that is calculated is a scaling factor between data and MC events. The results of this scaling are presented in Table 4.9; all of the scaling factors have values less than unity.

Table 4.9: The expected number of $B^{\mp} \to [\pi^{\mp}K^{\pm}\pi^0]_D h^{\mp}$ events in data that are due to misidentified $B^{\mp} \to [\pi^+\pi^-\pi^0]_D h^{\mp}$ and $B^{\mp} \to [K^+K^-\pi^0]_D h^{\mp}$ candidates. Poisson uncertainties are assumed in the penultimate column.

Source Channel	Potentially Contaminated ADS Mode	Scaling Factor	Number of MC Events	Expected Number of Data Events
$B^{\mp} \to [\pi^+\pi^-\pi^0]_D \pi^{\mp}$	$B^{\mp} \to [\pi^{\mp}K^{\pm}\pi^0]_D \pi^{\mp}$	0.22 ± 0.02	1 ± 1	0.22 ± 0.23
$B^{\mp} \to [\pi^+\pi^-\pi^0]_D K^{\mp}$	$B^{\mp} \to [\pi^{\mp}K^{\pm}\pi^0]_D K^{\mp}$	0.017 ± 0.001	8 ± 3	0.14 ± 0.05
$B^{\mp} \to [K^+K^-\pi^0]_D \pi^{\mp}$	$B^{\mp} \to [\pi^{\mp}K^{\pm}\pi^0]_D \pi^{\mp}$	0.038 ± 0.003	0 (assume 1 ± 1)	0.038 ± 0.038
$B^{\mp} \to [K^+K^-\pi^0]_D K^{\mp}$	$B^{\mp} \to [\pi^{\mp}K^{\pm}\pi^0]_D K^{\mp}$	0.0040 ± 0.0004	0 (assume 1 ± 1)	0.0040 ± 0.0040

Despite the fact that 0 candidates are found for the $B^{\mp} \to [K^+K^-\pi^0]_D h^{\mp}$ modes, the corresponding contamination in the data is calculated assuming 1 event for each. After scaling, the conclusion is that there is less than 1 event expected in each of $B^{\mp} \to [\pi^{\mp}K^{\pm}\pi^0]_D \pi^{\mp}$ and $B^{\mp} \to [\pi^{\mp}K^{\pm}\pi^0]_D K^{\mp}$ modes due to quasi-GLW contamination. To be conservative, a fixed yield of 1 ± 1 event is used in the final fit to account for this background source.

4.8 Wrongly Reconstructed D Backgrounds

One of the difficulties in studying $B^{\mp} \to Dh^{\mp}$ decays with a π^0 in the final state is the rather wide D mass distribution, as discussed in Section 3.7.3. However, in data, there is a high level of backgrounds in the D mass distribution underneath the signal peak, as can be seen in Figure 4.14(a). These background events that lie within the D mass window of the full selection must be modelled in the final fits. In order to extract a shape for use in the modelling, a data-driven approach is used.

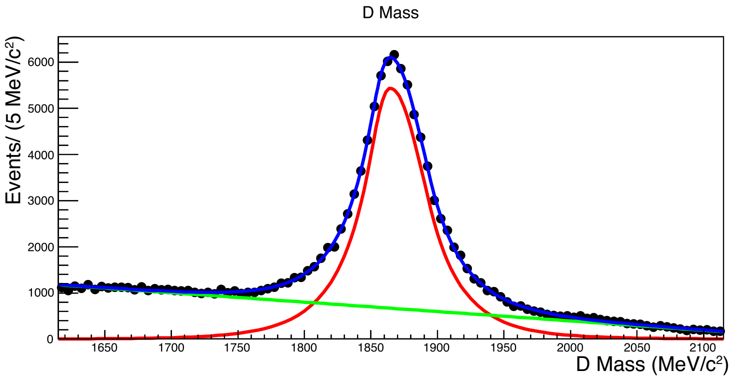

(a) Full range available in stripping

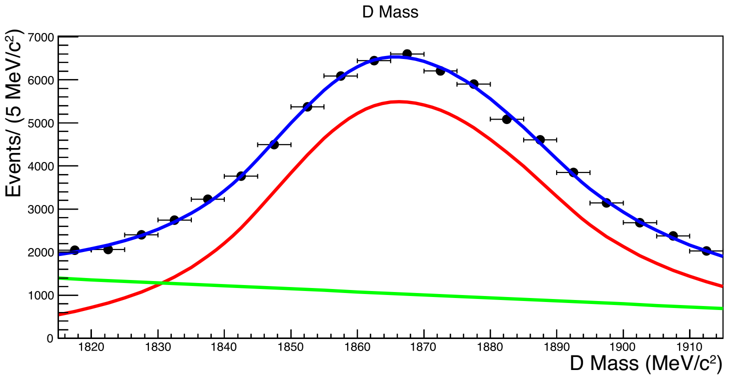

(b) Range used in the final selection

Figure 4.14: Fits to the D mass in $B^{\mp} \to [K^{\mp}\pi^{\pm}\pi^{0}]_{D}\pi^{\mp}$ data, after the application of the full selection. The signal is represented by a double Crystal Ball (red) and the background by a linear function (green).

Figure 4.14(a) shows the D mass distribution in $B^{\mp} \to [K^{\mp}\pi^{\pm}\pi^{0}]_{D}\pi^{\mp}$ data with all selection requirements imposed apart from the cut around the D mass. The full D mass window of ± 250 MeV/c^2 about the nominal D mass available in the stripping is used. A fit is performed using a double Crystal Ball for the signal (red) and a linear function for the background (green). Similar to the procedure described in Section 4.5.2, the sPlots method [98] is applied in order to extract event weights based on the signal and background PDFs. Figure 4.14(b) shows the same fit when applied to the ± 50 MeV/c^2 D mass window used in the final selection.

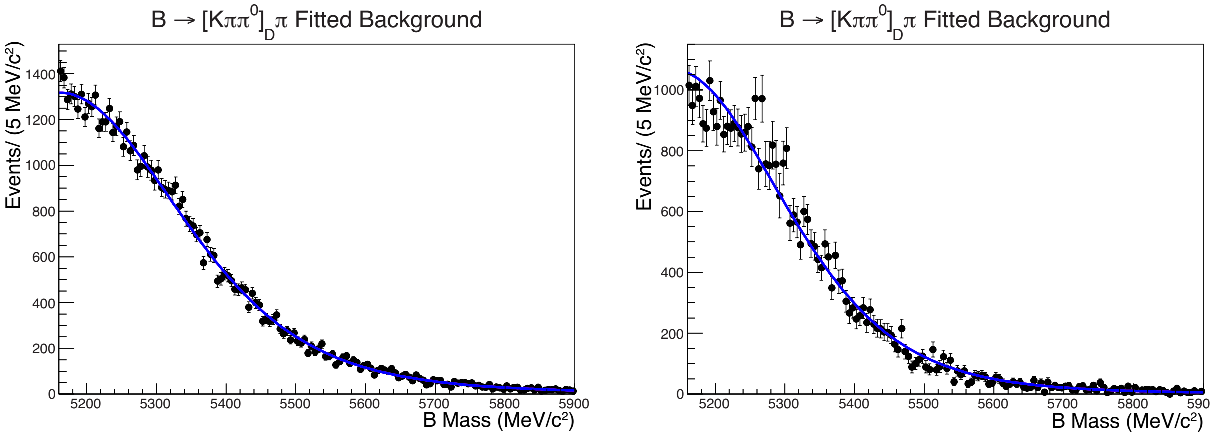

(a) Using the weights obtained from the full D mass range available in the stripping

(b) Using the weights obtained from the restricted D mass range available in the full selection

Figure 4.15: Fits to the B mass of $B^{\mp} \to [K^{\mp}\pi^{\pm}\pi^{0}]_D\pi^{\mp}$ data using the background weights obtained by applying the sPlots method to the D mass distribution. The fitted shape is a Cruijff with a single width and tail parameter.

The B mass distribution, using the *background* weights from the sPlots procedure, is presented in Figure 4.15(a). This distribution is fitted using a Cruijff with a single tail parameter. This shape is representative of the background contributions due to wrongly reconstructed D mesons that will be present in the final fits to B mass data. However, this shape is obtained using a larger D mass window than in the final selection. As an exercise to verify the effect of reducing the D mass window, background sPlot weights extracted from Figure 4.14(b) are used to produce the distribution in Figure 4.15(b). The widths of the two shapes to describe the background are summarised in Table 4.10. The effect of reducing the D mass window is a change in the width of the background shape. Consequently, it is decided to model this background in the final fits as a Cruijff with a single tail parameter, with the mean of the Cruijff fixed from the data-driven study and the fit performed in Figure 4.15(a). The width of the shape is permitted to float as is the tail parameter.

Table 4.10: Cruijff width parameters for wrongly reconstructed D background in $B^{\mp} \to [K^{\mp}\pi^{\pm}\pi^{0}]_D\pi^{\mp}$.

D Mass Window (MeV/c^2)	Width (MeV/c^2)
±250	166 ± 3
±50	122 ± 2

It is possible that the wrongly reconstructed D backgrounds will vary between the DK

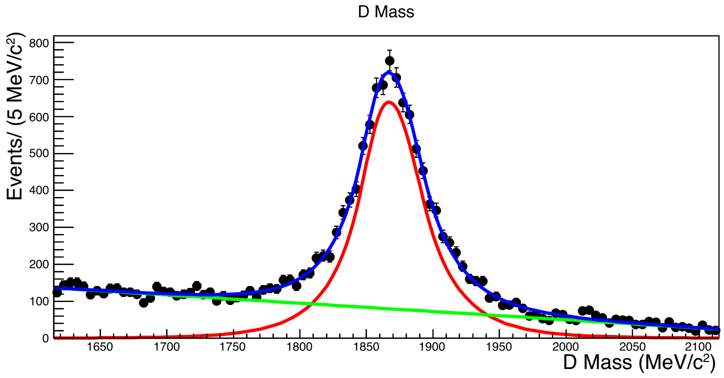

(a) Full range available in stripping

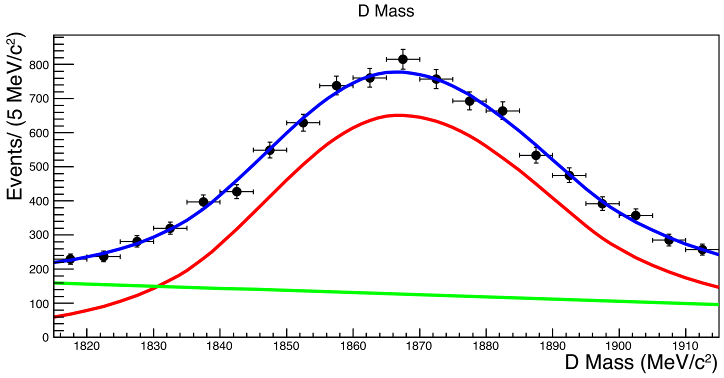

(b) Range used in the final selection

Figure 4.16: Fits to the D mass in $B^{\mp} \to [K^{\mp}\pi^{\pm}\pi^{0}]_{D}K^{\mp}$ data, after application of the full selection. The signal is represented by a double Crystal Ball (red) and the background by a linear function (green).

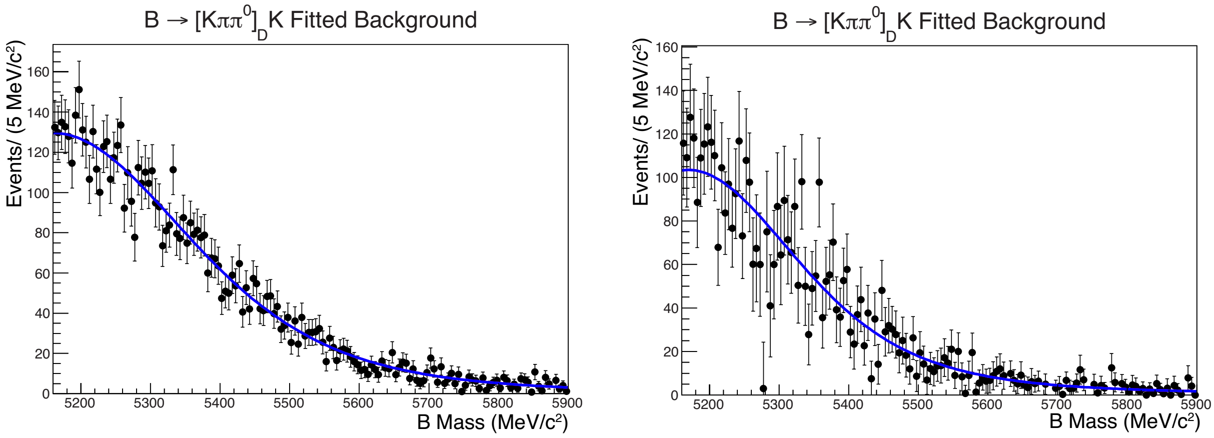

(a) Using the weights obtained from the full D mass range available in the stripping

(b) Using the weights obtained from the restricted D mass range available in the full selection

Figure 4.17: Fits to the B mass of $B^{\mp} \to [K^{\mp}\pi^{\pm}\pi^{0}]_{D}K^{\mp}$ data using the background weights obtained by applying the sPlot method. The fitted shape is a Cruijff with a single width and tail parameter.

and $D\pi$ modes. Therefore, the same study is repeated to obtain a background shape for the DK modes by studying the D mass distribution in $B^{\mp} \to [K^{\mp}\pi^{\pm}\pi^{0}]_{D}K^{\mp}$ data. Figure 4.16 shows the fits to the D mass distribution for this decay, while Figure 4.17 presents the B mass distributions using the background weights from the fits to the D mass. Using a Cruijff function to fit this background shape, it is again observed that the shape widths change with the reduction of the D mass window. The fit results are given in Table 4.11. Therefore, in the $B^{\mp} \to DK^{\mp}$ fits, this background contribution is modelled using a Cruijff function with the mean fixed, but floating width and tail parameters.

Table 4.11: Cruijff width parameters for wrongly reconstructed D background in $B^{\mp} \to [K^{\mp}\pi^{\pm}\pi^{0}]_{D}K^{\mp}$.

D Mass Window (MeV/c^2)	Width (MeV/c^2)
± 250	187 ± 11
± 50	150 ± 4

To summarise, the wrongly reconstructed D background in the final B mass distribution fits are modelled using a Cruijff shape, based upon a data-driven study of these background contributions. The means of the shape are fixed to the values of Table 4.12. A single shape with shared parameters is used for all $B^{\mp} \to D\pi^{\mp}$ channels of study and another shape with shared parameters is used for all of the $B^{\mp} \to DK^{\mp}$ channels. The yields of the background are permitted to float separately for each of the eight decay modes.

Table 4.12: Means of the Cruijff shapes used to model the wrongly reconstructed D backgrounds.

Bachelor Type	Mean (MeV/c^2)
$\pi^{\pm}$	5139 ± 9
$K^{\pm}$	5154 ± 9

4.9 Selection Summary

The various selection requirements used in this analysis are motivated by the arguments provided in Chapters 3 and 4. For completeness, these requirements are summarised in Table 4.13.

Table 4.13: Listing of the final selection cuts that are applied prior to the signal fitting.

Description	Selection
The range of the B invariant mass used in the fit is chosen to be large enough to contain the PDFs of the background components. The B mass used has a `DecayTreeFitter` constraint on the nominal D mass.	$5080 < \mathrm{m}(B) < 5900\ \mathrm{MeV}/c^2$
The D candidate must have a mass within 50 MeV/c^2 of the nominal D mass.	$\lvert\mathrm{m}(D) - 1865\rvert < 50\ \mathrm{MeV}/c^2$
The π^0 candidate must have a mass within 20 MeV/c^2 of the nominal π^0 mass.	$\lvert\mathrm{m}(\pi^0) - 135\rvert < 20\ \mathrm{MeV}/c^2$
Charged D daughters have PID cuts applied so as to restrict the favoured/suppressed crossfeed and eliminate $\pi\pi\pi^0$ and $KK\pi^0$ contamination in the suppressed ADS modes.	$\mathrm{PIDK}(K_D) > 2$ $\mathrm{PIDK}(\pi_D) < -2$
The bachelor particle is designated to either the kaon or pion mass-hypothesis based upon whether it passes or fails a PID cut.	$\mathrm{PIDK}(h) > (<)4$ for $K(\pi)$
Bachelor momentum is restricted to the range over which the RICH can distinguish betwen kaons and pions.	$5 < p(h) < 100\ \mathrm{GeV}/c$
Bachelor transverse momentum is also restricted to the range over which the RICH can distinguish between kaons and pions.	$0.5 < p_{\mathrm{T}}(h) < 10\ \mathrm{GeV}/c$
The BDT variable is chosen so as to reduce the level of combinatoric background while retaining large amounts of signal events.	$\mathrm{BDT} > -0.80$
The crossfeed between the favoured and suppressed $K\pi\pi^0$ modes is reduced through the use of a veto on the D mass with the charged daughter mass hypotheses swapped.	$\lvert\mathrm{m}(D_{K\leftrightarrow\pi}) - 1865\rvert > 30\ \mathrm{MeV}/c^2$
A signed D flight distance z-significance cut is used so as to favour candidates that have flown in the forward direction. This cut suppresses charmless decay contamination.	$\mathrm{FD}_D > 2$
The event, at L0, must have been triggered by the candidate passing the hadron trigger or by some reason independent of the candidate.	`L0HadronTOS||L0GlobalTIS`
The event, at HLT1, must have been triggered by a candidate passing the "track" trigger decision associated to hadrons with a b or c quark.	`HLT1TrackAllL0_TOS`
The event, at HLT2, must have been triggered by the candidate passing one of the "topo" trigger decisions where the D decays to 2, 3 or 4 daughters.	`HLT2Topo*TOS`

Chapter 5

The Simultaneous Fit

This Chapter presents the maximum likelihood fit which is performed simultaneously to the invariant B mass distributions of the eight $B^{\mp} \to [h'^{\pm}h''^{\mp}\pi^0]_D h^{\mp}$ decay modes relevant to this analysis. This fit allows for the extraction of the B^+/B^- production asymmetry at LHCb as well as the relevant *CP* observables discussed in Section 1.5.2. The fit is performed simultaneously as many parameters are shared between the different decay modes and doing so allows for the channels with lower yields to benefit from the influence of the more abundant modes. This Chapter summarises the fit components and the floating fit parameters. The production asymmetry measurement and its role in yield calculations is then discussed. After an analysis of fit stability, the Chapter concludes with a discussion of the systematic uncertainties associated with the parameters that are fixed in the baseline fit.

5.1 Data Subsamples for Fitting

The subsamples of data that are used for fitting are separate for the eight decay modes of interest: $B^{\mp} \to [K^{\mp}\pi^{\pm}\pi^0]_D\pi^{\mp}$, $B^{\mp} \to [K^{\mp}\pi^{\pm}\pi^0]_D K^{\mp}$, $B^{\mp} \to [\pi^{\mp}K^{\pm}\pi^0]_D\pi^{\mp}$, $B^{\mp} \to [\pi^{\mp}K^{\pm}\pi^0]_D K^{\mp}$, $B^{\mp} \to [\pi^+\pi^-\pi^0]_D\pi^{\mp}$, $B^{\mp} \to [\pi^+\pi^-\pi^0]_D K^{\mp}$, $B^{\mp} \to [K^+K^-\pi^0]_D\pi^{\mp}$ and $B^{\mp} \to [K^+K^-\pi^0]_D K^{\mp}$. Separate samples are available for data collected in 2011 and 2012. These subsamples can be further split by charge of the parent B hadron for the study of *CP* asymmetries.

The final selection, as summarised in Table 4.13, is applied to these subsamples before the fitting process. After the selection is applied, a search and treatment of multiple candidates is performed. If a given event has two $B^{\mp}$ candidates and if they are separated by a distance of more than 2 mm along the axis of beam trajectory, both candidates are retained. If not, it is the candidate with the lowest vertex χ^2 that is kept. Approximately 3.8% of events in the final fitted subsamples have multiple candidates.

5.2 Fit Description and Components

The fit used in this analysis is a binned fit of the invariant mass of B candidates. The fit, using the RooFit package [102], maximises the likelihood of an extended probability density function to this distribution. It is performed simultaneously for the eight decay channels of interest. Certain key terms of the fit nomenclature are described below:

- $PASS \,||\, FAIL$

  Candidates with a bachelor kaon are separated from those with a bachelor pion through the use of a cut on the PID variable of the bachelor particle, namely PIDK > 4 for kaons. Samples that share the same D decay mode are combined and then further separated using this cut. Candidates that satisfy the cut (and are selected as $B^{\mp} \to DK^{\mp}$ decays) are classified under the $PASS$ category while those that do not are selected as $B^{\mp} \to D\pi^{\mp}$ and are classified as $FAIL$.

- $PLUS \,||\, MINUS$

  In order to measure charge asymmetries, the fitted subsamples are separated by the charge of the parent B hadron.

- $FAV \,||\, SUP$

  The favoured ADS decays $B^{\mp} \to [K^{\mp}\pi^{\pm}\pi^0]_D h^{\mp}$ are referred to as FAV, while the suppressed ADS modes, $B^{\mp} \to [\pi^{\mp}K^{\pm}\pi^0]_D h^{\mp}$ are referred to as SUP.

5.2.1 Fit Components

The fit is composed of several PDFs used to model the signal and background contributions. The signal peaks for the $B^{\mp} \to D\pi^{\mp}$ candidates in the $FAIL$ subsample are modelled using a Cruijff function. The mean and width of this shape are permitted to float. A total of two means are present in the fit: one shared between all $PLUS$ subsamples and another shared between all the $MINUS$ subsamples. Similarly, three widths are used: one shared between FAV and SUP, one for $\pi\pi\pi^0$ modes and another for $KK\pi^0$ modes.

The $B^{\mp} \to DK^{\mp}$ signal peaks in the $PASS$ subsamples are also modelled as Cruijff functions with all parameters shared from the corresponding $B^{\mp} \to D\pi^{\mp}$ signal decays. However, as discussed in Section 3.7.5, widths are fixed at 95% that of the $B^{\mp} \to D\pi^{\mp}$ modes.

The background PDFs are thoroughly described in Chapter 4. For convenience, we summarise all of the PDFs of the fit in Table 5.1.

Table 5.1: PDF components of the simultaneous fit.

Component	PDF Type
$B^{\mp} \to D\pi^{\mp}$ and $B^{\mp} \to DK^{\mp}$ Signal	Cruijff function
Combinatorial background	Linear function
Partly reconstructed background	Low mass PDF composed of HORNSdini and HILLdini PDFs as well as corresponding $B^{\mp} \to D\pi^{\mp}$ backgrounds misidentified as $B^{\mp} \to DK^{\mp}$
Misidentified $B^{\mp} \to D\pi^{\mp}$ signal as $B^{\mp} \to DK^{\mp}$ and vice-versa	Double Crystal Ball function
$B_s^0 \to [K^{\pm}\pi^{\mp}\pi^0]_D K^{*0}$	Cruijff function with left and right width parameters. Only used in SUP modes.
Favoured/Suppressed cross-feed	Cruijff function with double the width of the signal peaks. Only used in SUP modes.
Charmless backgrounds	Cruijff function sharing signal parameters
Quasi-GLW contamination of SUP	Cruijff function sharing signal parameters. Only used in SUP modes.
Wrongly Reconstructed D	Cruijff function

Table 5.2: A description of all of the floating variables in the fit. The second column lists the variable name as per the fit printout from Section 6.1.2, while the third column provides additional details. For the sake of simplicity, several keywords are used in the variable names: `CHG` $\in$ {plus, minus}, `PID` $\in$ {pass, fail} and `MODE` $\in$ {kpipi0, pikpi0, pipipi0, kkpi0}.

B^+/B^- production asymmetry		
A_{Prod}	`A_Prod`	Floating parameter for measuring B^+/B^- asymmetry
$D\pi$ signal		
μ	`mean_B_CHG_both_d2kpipi0_PID`	Mean shared amongst all modes of the same charge
σ	`sigma_dpi_MODE`	Sigma for all $D\pi$ signal peaks of the respective modes
yield	`n_b2dpi_MODE_both`	Number of events in signal peak
asymmetry	`A_CPP_b2dpi_MODE`	B^- and B^+ asymmetry for $KK\pi^0$ and $\pi\pi\pi^0$
DK signal		
Floating parameters shared with $D\pi$ shape, except for:		
yield	`R_FP_d2MODE`	R_{qGLW} for $KK\pi^0$ and $\pi\pi\pi^0$
asymmetry	`A_FAV_b2dk_d2kpipi0`	B^- and B^+ asymmetry for favoured $K\pi\pi^0$
asymmetry	`A_CPP_b2dk_MODE`	B^- and B^+ asymmetry for $KK\pi^0$ and $\pi\pi\pi^0$
Misidentified $D\pi$ in the DK sample		
σ_{CB_L}	`CB_sigmaL_d2kpi`	Crystal Ball left sigma
σ_{CB_R}	`CB_sigmaR_d2kpi`	Crystal Ball right sigma
α_{CB_R}	`CB_alphaR_d2kpi`	Crystal Ball right tail parameter
Suppressed $D\pi$ peak for $\pi K\pi^0$		
Same shape as the favoured $D\pi$ signal peaks		
yield	`R_ADS_b2dpi_d2pikpi0`	Multiplicative factor for use with $D\pi$ yield
asymmetry	`A_ADS_b2dpi_d2pikpi0`	B^- and B^+ asymmetry for $B^\mp \to [\pi^\mp K^\pm \pi^0]_D \pi^\mp$
Suppressed DK peak for $\pi K\pi^0$		
Same shape as the favoured DK signal peaks		
yield	`R_ADS_b2dk_d2pikpi0`	Multiplicative factor for use with DK yield
yield	`A_ADS_b2dk_d2pikpi0`	B^- and B^+ asymmetry for $B^\mp \to [\pi^\mp K^\pm \pi^0]_D K^\mp$
Combinatorial background		
slope	`comb_coeff_PID`	Slope parameter for linear shape
yield	`n_com_MODE_PID_both`	Separate DK and $D\pi$ yields
$B_s^0 \to D^0 K^*$ background		
yield	`R_d0kst_pass`	Multiplicative factor to be used with $D\pi$ yield
Partially reconstructed low mass background		
$DK/D\pi$ ratio	`low_DK_vs_Dpi_d2kpipi0`	Shared between all modes
$D\gamma/D\pi^0$ ratio	`low_P_GAM_vs_PI0_D2kpipi0`	Shared between all modes
mean	`low_shift_d2kpipi0`	Shared between all modes
width	`low_sigma_d2kpipi0`	Shared between all modes
yield	`n_low_MODE_PID_CHG_both`	Separate yields for all mode/charge/PID combinations
Wrongly reconstructed D background		
σ	`sigma_kppz_PID`	Shared width between all similar bachelor subsamples
α	`alpha_kppz_PID`	Shared tail parameter
yield	`n_dco_MODE_PID`	Separate yields for all mode/PID combinations

5.2.2 Floating Fit Variables

In the fit, a selection of variables are fixed and the remainder are left to float to the value best determined by the fit. These floating variables are presented in Table 5.2, where, in addition to a description of the variable, is the name as it appears in the printout of the fit result presented later in Section 6.1.2.

In this table, we can see that the B^+/B^- production asymmetry, A_{Prod}, and the eleven *CP* observables of interest are all floating variables. A conversion between the fit variable name and the name from Section 1.5.2 is presented in Table 5.3.

Table 5.3: Conversion between floating fit parameter names and standard observable names from Section 1.5.2. The B^+/B^- production asymmetry variable, A_{Prod}, is also listed.

Floating Parameter	Observable Name
`A_Prod`	A_{Prod}
`R_ADS_b2dk_d2pikpi0`	$R_{\text{ADS}(K)}$
`R_ADS_b2dpi_d2pikpi0`	$R_{\text{ADS}(\pi)}$
`A_ADS_b2dk_d2pikpi0`	$A_{\text{ADS}(K)}$
`A_ADS_b2dpi_d2pikpi0`	$A_{\text{ADS}(\pi)}$
`A_FAV_b2dk_d2kpipi0`	$A_K^{K\pi\pi^0}$
`A_CPP_b2dk_d2kkpi0`	$A_{\text{qGLW}(K)}^{KK\pi^0}$
`A_CPP_b2dk_d2pipipi0`	$A_{\text{qGLW}(K)}^{\pi\pi\pi^0}$
`A_CPP_b2dpi_d2kkpi0`	$A_{\text{qGLW}(\pi)}^{KK\pi^0}$
`A_CPP_b2dpi_d2pipipi0`	$A_{\text{qGLW}(\pi)}^{\pi\pi\pi^0}$
`R_FP_d2kkpi0`	$R_{\text{qGLW}}^{KK\pi^0}$
`R_FP_d2pipipi0`	$R_{\text{qGLW}}^{\pi\pi\pi^0}$

5.3 Signal Yields and the B^+/B^- Production Asymmetry

As introduced in Section 1.6, the $B^\mp \to [K^\mp\pi^\pm\pi^0]_D\pi^\mp$ mode can be used for a measurement of A_{Prod}. In this decay mode, *CP* violation is expected to be negligible, as can be seen in Equation 1.56 where the *CP* violating term is subdominant by four orders of magnitude. Essentially, by assuming that there is no *CP* violation in this mode, after accounting for differences in kaon and pion detection asymmetries, the relative difference between the signal yields of the B^- and B^+ candidates of the decay is a measurement of A_{Prod}.

5.3.1 Kaon and Pion Detection Asymmetries

Because this analysis has final states with charged kaons and pions, any asymmetry in the detection of K^+ versus K^- or π^+ versus π^- will have an effect on the observed asymmetry between B^+ and B^-. In the case of the charged pions, this asymmetry, A_π, is defined as

$$A_\pi \equiv \frac{\epsilon_{\pi^-} - \epsilon_{\pi^+}}{\epsilon_{\pi^-} + \epsilon_{\pi^+}}, \tag{5.1}$$

where ϵ_π refers to the detection efficiency of positive or negative pions. A_π has been measured and is consistent with zero; this analysis uses a value of $(0.0 \pm 0.3)\%$ [32]. For charged kaons, a similar quantity, A_K, is defined where

$$A_K \equiv \frac{\epsilon_{K^-} - \epsilon_{K^+}}{\epsilon_{K^-} + \epsilon_{K^+}}. \tag{5.2}$$

Due to different interaction lengths of K^+ and K^- in nuclear matter, a slight excess of K^+ is expected. The most precise relevant measurement that is available at LHCb is not of the kaon detection asymmetry, but rather the difference between the kaon and pion detection asymmetries, $A_{K\pi}$, where $A_{K\pi} = A_K - A_\pi$. The latest measured value of $A_{K\pi}$ is $(-1.1 \pm 0.4)\%$, measured in decays of $D^\pm \to K^\mp\pi^\pm\pi^\pm$ and $D^\pm \to K^0_S\pi^\pm$ [33].

Table 5.4: Detection asymmetry expressions for the different decay channels of interest in this analysis. The final column shows the quantity expressed in terms of the $A_{K\pi}$ asymmetry variable in use at LHCb.

Decay Mode	Detection Asymmetry	Detection Asymmetry Using $A_{K\pi}$
$B^\mp \to [K^\mp\pi^\pm\pi^0]_D\pi^\mp$	$A_K - A_\pi + A_\pi$	$A_{K\pi} + A_\pi$
$B^\mp \to [K^\mp\pi^\pm\pi^0]_D K^\mp$	$A_K - A_\pi + A_K$	$2A_{K\pi} + A_\pi$
$B^\mp \to [\pi^\mp K^\pm\pi^0]_D\pi^\mp$	$A_\pi - A_K + A_\pi$	$A_\pi - A_{K\pi}$
$B^\mp \to [\pi^\mp K^\pm\pi^0]_D K^\mp$	$A_\pi - A_K + A_K$	A_π
$B^\mp \to [\pi^+\pi^-\pi^0]_D\pi^\mp$	$A_\pi - A_\pi + A_\pi$	A_π
$B^\mp \to [\pi^+\pi^-\pi^0]_D K^\mp$	$A_\pi - A_\pi + A_K$	$A_{K\pi} + A_\pi$
$B^\mp \to [K^+K^-\pi^0]_D\pi^\mp$	$A_K - A_K + A_\pi$	A_π
$B^\mp \to [K^+K^-\pi^0]_D K^\mp$	$A_K - A_K + A_K$	$A_{K\pi} + A_\pi$

Depending on the number of charged kaons and pions in the final state of the decay modes, the overall detection asymmetry expressions will be different. Furthermore, the appropriate substitutions of A_K for $A_{K\pi}$ also need to be made. These detection asymmetry expressions are listed in Table 5.4 for the different decay channels of interest.

5.3.2 Yield Expressions

It is necessary to correct the measured yields for production and detection efficiencies and relate these corrected quantities to the physical observables.

Several terms and simplifications are defined below:

- $n_{\mathrm{raw}}{}^{D\pi}_{\mathrm{channel}}$: This is the yield of $D\pi$ events for a given channel, summed over charge, without considering PID efficiency effects.

- $\epsilon_{PIDh^{\pm}}$: The PID efficiency of the bachelor h, dependent on the charge of the bachelor, as described in Section 3.9

- $R^{K\pi\pi^0}_{K/\pi}$: The $B^{\mp} \to DK^{\mp}$ to $B^{\mp} \to D\pi^{\mp}$ ratio, as described in Section 1.5.2 and fixed in the fit (see Section 5.5 for details)

- R_{qGLW}: The partial-width ratio for $KK\pi^0$ and $\pi\pi\pi^0$, as described in Section 1.5.2, where $R^{hh\pi^0}_{\mathrm{qGLW}} \cdot R^{K\pi\pi^0}_{K/\pi} \approx R^{hh\pi^0}_{K/\pi}$.

- $\epsilon_{K/\pi}$: The ratio of selection efficiencies between DK and $D\pi$ modes, defined as $\epsilon_{DK}/\epsilon_{D\pi}$ in Section 3.8

- $A_{\mathrm{ADS}(h)}$: The ADS asymmetry variable for the different h bachelors, as described in Section 1.5.2

- $A^{K\pi\pi^0}_{K}$, $A^{\pi\pi\pi^0}_{\mathrm{qGLW}(h)}$, $A^{KK\pi^0}_{\mathrm{qGLW}(h)}$: The asymmetry variables for the different decay channels, for different bachelors h, as described in Section 1.5.2.

It is mathematically convenient to work with the following set of transformed variables:

$$a_{\mathrm{Prod}} \equiv \frac{1 + A_{\mathrm{Prod}}}{1 - A_{\mathrm{Prod}}};\ a_{K\pi} \equiv \frac{1 + A_{K\pi}}{1 - A_{K\pi}};\ a_{\pi} \equiv \frac{1 + A_{\pi}}{1 - A_{\pi}}; \tag{5.3}$$

$$a_{\mathrm{ADS}(\pi)} \equiv \frac{1 + A_{\mathrm{ADS}(\pi)}}{1 - A_{\mathrm{ADS}(\pi)}};\ a_{\mathrm{ADS}(K)} \equiv \frac{1 + A_{\mathrm{ADS}(K)}}{1 - A_{\mathrm{ADS}(K)}}. \tag{5.4}$$

This allows for the yields of positively and negatively charged particles to be calculated using almost identical expressions. Another useful transformation is

$$a_K^{K\pi\pi^0} \equiv \frac{1 + A_K^{K\pi\pi^0}}{1 - A_K^{K\pi\pi^0}} \tag{5.5}$$

with similar transformations defining $a_{\text{qGLW}(K)}^{\pi\pi\pi^0}$, $a_{\text{qGLW}(\pi)}^{\pi\pi\pi^0}$, $a_{\text{qGLW}(K)}^{KK\pi^0}$ and $a_{\text{qGLW}(\pi)}^{KK\pi^0}$ in terms of the physics asymmetry variables $A_{\text{qGLW}(K)}^{\pi\pi\pi^0}$, $A_{\text{qGLW}(\pi)}^{\pi\pi\pi^0}$, $A_{\text{qGLW}(K)}^{KK\pi^0}$, $A_{\text{qGLW}(\pi)}^{KK\pi^0}$, respectively.

Using the transformed variables, we can create a series of expressions that relate $n_{\text{raw}\ \text{channel}}^{D\pi}$ to the measured signal yields after correction for efficiency and detection effects. We denote these latter yields n_{channel}^{Dh}, which are defined separately for positively and negatively charged bachelors: n_{channel}^{Dh+} and n_{channel}^{Dh-}. These expressions are presented in Equations 5.6 to 5.13.

$$n_{K\pi\pi^0}^{D\pi\pm} = \frac{n_{\text{raw}\ \text{K}\pi\pi^0}^{D\pi} \cdot \epsilon_{PID\pi\pm}}{1 + \left[a_{\text{Prod}} \cdot a_{K\pi} \cdot a_{\pi}\right]^{\pm 1}} \tag{5.6}$$

$$n_{K\pi\pi^0}^{DK\pm} = \frac{n_{\text{raw}\ \text{K}\pi\pi^0}^{D\pi} \cdot R_{K/\pi}^{K\pi\pi^0} \cdot \epsilon_{K/\pi} \cdot \epsilon_{PIDK\pm}}{1 + \left[a_{\text{Prod}} \cdot a_{K\pi} \cdot a_{K\pi} \cdot a_{\pi} \cdot a_K^{K\pi\pi^0}\right]^{\pm 1}} \tag{5.7}$$

$$n_{\pi K\pi^0}^{D\pi\pm} = \frac{n_{\text{raw}\ \text{K}\pi\pi^0}^{D\pi} \cdot R_{\text{ADS}(\pi)} \cdot \epsilon_{PID\pi\pm}}{1 + \left[a_{\text{Prod}} \cdot a_{\pi}/a_{K\pi} \cdot a_{\text{ADS}(\pi)}\right]^{\pm 1}} \tag{5.8}$$

$$n_{\pi K\pi^0}^{DK\pm} = \frac{n_{\text{raw}\ \text{K}\pi\pi^0}^{D\pi} \cdot R_{K/\pi}^{K\pi\pi^0} \cdot R_{\text{ADS}(K)} \cdot \epsilon_{K/\pi} \cdot \epsilon_{PIDK\pm}}{1 + \left[a_{\text{Prod}} \cdot a_{\pi} \cdot a_{\text{ADS}(K)}\right]^{\pm 1}} \tag{5.9}$$

$$n_{\pi\pi\pi^0}^{D\pi\pm} = \frac{n_{\text{raw}\ \pi\pi\pi^0}^{D\pi} \cdot \epsilon_{PID\pi\pm}}{1 + \left[a_{\text{Prod}} \cdot a_{\pi} \cdot a_{\text{qGLW}(\pi)}^{\pi\pi\pi^0}\right]^{\pm 1}} \tag{5.10}$$

$$n_{\pi\pi\pi^0}^{DK\pm} = \frac{n_{\text{raw}\ \pi\pi\pi^0}^{D\pi} \cdot R_{\text{qGLW}}^{\pi\pi\pi^0} \cdot R_{K/\pi}^{K\pi\pi^0} \cdot \epsilon_{K/\pi} \cdot \epsilon_{PIDK\pm}}{1 + \left[a_{\text{Prod}} \cdot a_{K\pi} \cdot a_{\pi} \cdot a_{\text{qGLW}(K)}^{\pi\pi\pi^0}\right]^{\pm 1}} \tag{5.11}$$

$$n_{KK\pi^0}^{D\pi\pm} = \frac{n_{\text{raw}\ \text{KK}\pi^0}^{D\pi} \cdot \epsilon_{PID\pi\pm}}{1 + \left[a_{\text{Prod}} \cdot a_{\pi} \cdot a_{\text{qGLW}(\pi)}^{KK\pi^0}\right]^{\pm 1}} \tag{5.12}$$

$$n^{DK\pm}_{KK\pi^0} = \frac{n_{\text{raw}}{}^{D\pi}_{\text{KK}\pi^0} \cdot R^{KK\pi^0}_{\text{qGLW}} \cdot R^{K\pi\pi^0}_{K/\pi} \cdot \epsilon_{K/\pi} \cdot \epsilon_{PIDK\pm}}{1 + \left[a_{\text{Prod}} \cdot a_{K\pi} \cdot a_{\pi} \cdot a^{KK\pi^0}_{\text{qGLW}(K)}\right]^{\pm 1}} \tag{5.13}$$

The fit reports the total post-efficiency yields summed over charge, $n_{\text{fit}}{}^{Dh}_{\text{channel}}$, where

$$n_{\text{fit}}{}^{Dh}_{\text{channel}} = n^{Dh+}_{\text{channel}} + n^{Dh-}_{\text{channel}}. \tag{5.14}$$

However, the fit result only reports the explicit yields of three $D\pi$ modes: $n_{\text{fit}}{}^{D\pi}_{\text{K}\pi\pi^0}$, $n_{\text{fit}}{}^{D\pi}_{\pi\pi\pi^0}$ and $n^{D\pi}_{KK\pi^0}$; all other final signal yields can be determined by multiplying one of these modes by the relevant ratio or *CP* observable. For completeness, Equations 5.15 to 5.22 present the final summed-by-charge signal yields to their corresponding fit output variable, and appropriate multipliers, if necessary:

$$n_{\text{fit}}{}^{D\pi}_{\text{K}\pi\pi^0} = \texttt{n\_b2dpi\_d2kpipi0} \tag{5.15}$$

$$n_{\text{fit}}{}^{DK}_{\text{K}\pi\pi^0} = n_{\text{fit}}{}^{D\pi}_{\text{K}\pi\pi^0} \cdot R^{K\pi\pi^0}_{K/\pi} \tag{5.16}$$

$$n_{\text{fit}}{}^{D\pi}_{\pi\text{K}\pi^0} = n_{\text{fit}}{}^{D\pi}_{\text{K}\pi\pi^0} \cdot R_{\text{ADS}(\pi)} \tag{5.17}$$

$$n_{\text{fit}}{}^{DK}_{\pi\text{K}\pi^0} = n_{\text{fit}}{}^{D\pi}_{\text{K}\pi\pi^0} \cdot R^{K\pi\pi^0}_{K/\pi} \cdot R_{\text{ADS}(K)} \tag{5.18}$$

$$n_{\text{fit}}{}^{D\pi}_{\pi\pi\pi^0} = \texttt{n\_b2dpi\_d2pipipi0} \tag{5.19}$$

$$n_{\text{fit}}{}^{DK}_{\pi\pi\pi^0} = n_{\text{fit}}{}^{D\pi}_{\pi\pi\pi^0} \cdot R^{\pi\pi\pi^0}_{\text{qGLW}} \cdot R^{K\pi\pi^0}_{K/\pi} \tag{5.20}$$

$$n_{\text{fit}}{}^{D\pi}_{\text{KK}\pi^0} = \texttt{n\_b2dpi\_d2kkpi0} \tag{5.21}$$

$$n_{\text{fit}}{}^{DK}_{\text{KK}\pi^0} = n_{\text{fit}}{}^{D\pi}_{\text{KK}\pi^0} \cdot R^{KK\pi^0}_{\text{qGLW}} \cdot R^{K\pi\pi^0}_{K/\pi}. \tag{5.22}$$

5.4 Fit Stability

In order to test the stability of the fit, ‘toy’ experiments are conducted. These are MC simulated experiments, where starting from an initial set of parameters, a simulated data set is generated and then fitted using the same fitting procedure as data. The primary objective of this process is to ensure that the floating fit variables of the *CP* observables are not biased and that the uncertainties reported by the fit are correctly estimated.

In order to perform these evaluations, a pull distribution is used. The pull for a floating observable θ is defined as

$$P(\theta) \equiv \frac{\theta_{\text{fit}} - \theta_{\text{generated}}}{\sigma_{\text{fit}}}. \tag{5.23}$$

This pull value is calculated for every toy experiment and the distribution is plotted for each of the CP observables and A_{Prod}. The expectation is that the distributions are Gaussian with a mean of 0 and width of 1. A mean significantly different to 0 indicates a bias in the central value of the fit parameter that must be corrected. Correspondingly, a width significantly different than 1 indicates that uncertainties are incorrectly estimated. The pull plots are presented in Figure 5.1 and their means and sigmas from the fitted Gaussians are summarised in Table 5.5.

Table 5.5: Pull distribution sigma and means from the toy studies.

Observable	Pull Mean	Pull Sigma
$A_{\text{ADS}(K)}$	0.065 ± 0.016	0.938 ± 0.011
$A_{\text{ADS}(\pi)}$	-0.016 ± 0.016	0.952 ± 0.011
$A^{KK\pi^0}_{\text{qGLW}(K)}$	-0.054 ± 0.016	0.936 ± 0.011
$A^{\pi\pi\pi^0}_{\text{qGLW}(K)}$	-0.013 ± 0.017	1.026 ± 0.012
$A^{KK\pi^0}_{\text{qGLW}(\pi)}$	0.019 ± 0.016	0.962 ± 0.011
$A^{\pi\pi\pi^0}_{\text{qGLW}(\pi)}$	0.016 ± 0.016	0.972 ± 0.012
$A^{K\pi\pi^0}_{K}$	0.078 ± 0.016	0.978 ± 0.012
A_{Prod}	0.032 ± 0.017	1.014 ± 0.012
$R_{\text{ADS}(K)}$	-0.060 ± 0.015	0.889 ± 0.011
$R_{\text{ADS}(\pi)}$	-0.050 ± 0.016	0.940 ± 0.011
$R^{KK\pi^0}_{\text{qGLW}}$	-0.063 ± 0.016	0.960 ± 0.011
$R^{\pi\pi\pi^0}_{\text{qGLW}}$	0.013 ± 0.017	1.031 ± 0.012

As expected, all of the distributions are Gaussian-like in appearance. However, several of the observables have pull-distribution means that differ by more than 2 sigma from the expected value of 0. This may be indicative of a slight bias for these observables and thus we apply a correction to the central values ultimately reported by the fit. For example, the $A_{\text{ADS}(K)}$ variable shows a pull mean of 0.065 and thus represent a positive bias on the central value from the fit. Consequently, the reported final value should be lower than the fit's central value by 6.5% of the 1σ error returned by the fit. The widths of the pulls are

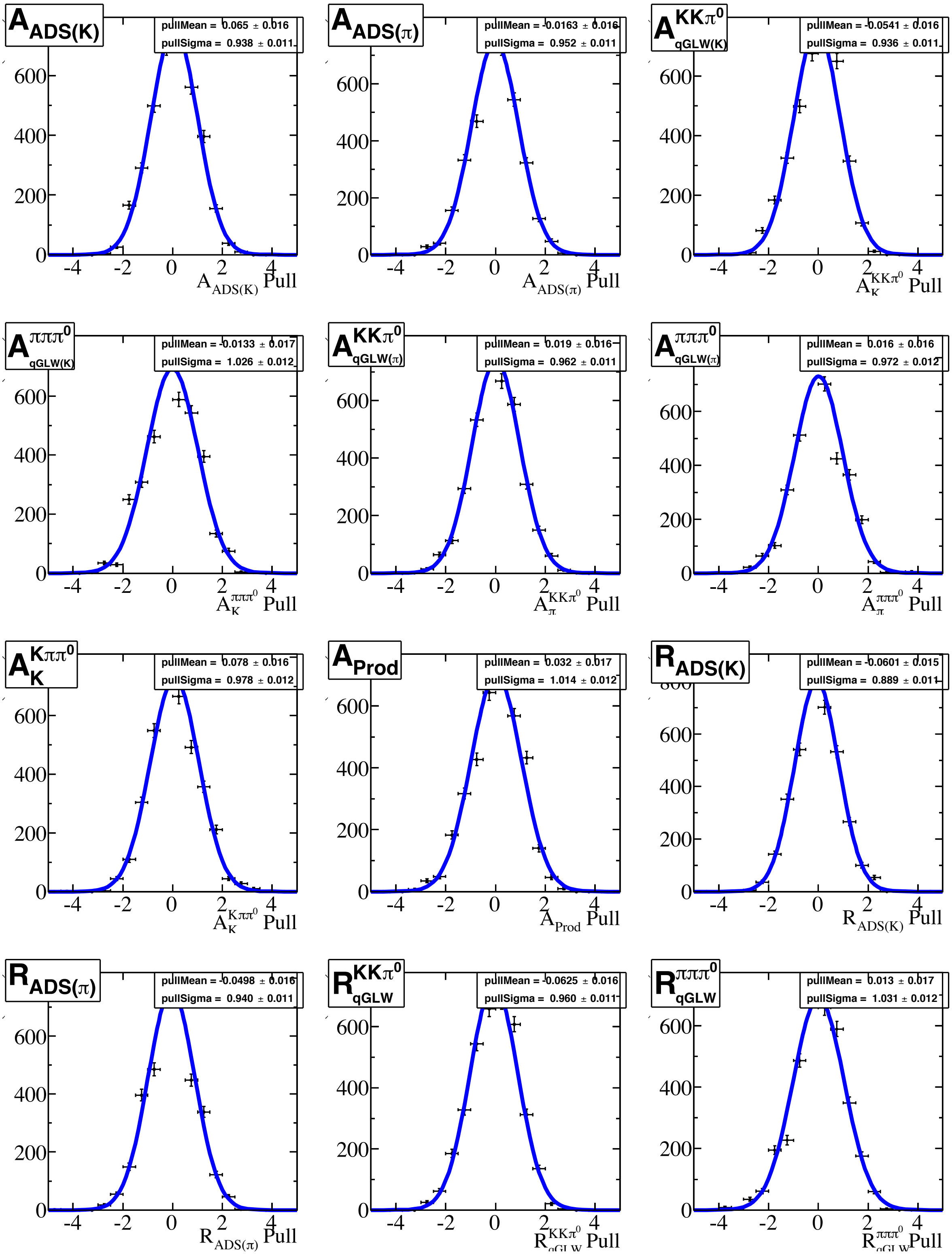

Figure 5.1: Toy study pull distribution on analysis observables. A Gaussian is fitted to each of the distributions.

deemed acceptable and no corrections are made to the uncertainties of the observables.

The correction offsets are summarised in Table 5.6 for the observables that require them. These offsets are each less than 0.1σ and do not represent major biases.

Table 5.6: Applied correction offsets for *CP* observables.

Observable	Correction Offset
$A_{\mathrm{ADS}(K)}$	-0.065σ
$A^{KK\pi^0}_{\mathrm{qGLW}(K)}$	$+0.054\sigma$
$A^{K\pi\pi^0}_{K}$	-0.078σ
$R_{\mathrm{ADS}(K)}$	$+0.060\sigma$
$R_{\mathrm{ADS}(\pi)}$	$+0.050\sigma$
$R^{KK\pi^0}_{\mathrm{qGLW}}$	$+0.063\sigma$

5.5 Systematic Uncertainties

The sources of systematic uncertainty are assumptions made in the fitting procedure. These assumptions are expressed by applying fixed values in the fitting process. In order to determine the effect of these systematic uncertainties, the fit is re-run many times, varying the value of the previously fixed parameter. Each of these assumptions, represented by a systematic constant, has an uncertainty associated to it. When the fit is re-run, the systematic constant is varied according to a Gaussian distribution of width equal to its uncertainty. The values of the floating analysis observables are also recorded. For each of these observables, a histogram is then constructed for each of the sources of systematic uncertainty, showing the distribution of the observable under the systematic variations. An example of such histograms for the $R_{\mathrm{ADS}(\pi)}$ observable is presented in Figure B.5. For each of these histograms, the root mean square (RMS) is taken as the systematic uncertainty contribution due to that particular systematics source and the sum in quadrature of these RMS values is taken as the total systematic uncertainty on the $R_{\mathrm{ADS}(\pi)}$ observable. For completeness, histograms for all of the analysis observables are presented in Appendix B.

The systematic uncertainties for each of the analysis observables are listed in Table 5.7. A full description of the fifteen different sources of systematic uncertainties, in addition to the uncertainties of these fixed values used as variations, is presented in the remainder of

Table 5.7: Systematic uncertainty contributions for each analysis observable. The total is the sum in quadrature of the column's contributions.

	$A_{\text{ADS}(K)}$	$A_{\text{ADS}(\pi)}$	$A^{KK\pi^0}_{\text{qGLW}(K)}$	$A^{\pi\pi\pi^0}_{\text{qGLW}(K)}$	$A^{KK\pi^0}_{\text{qGLW}(\pi)}$	$A^{\pi\pi\pi^0}_{\text{qGLW}(\pi)}$	$A^{K\pi\pi^0}_{K}$	A_{Prod}	$R_{\text{ADS}(K)}$	$R_{\text{ADS}(\pi)}$	$R^{KK\pi^0}_{\text{qGLW}}$	$R^{\pi\pi\pi^0}_{\text{qGLW}}$
ϵ_{PIDK}	0.003	0.0005	0.001	0.0007	0.0001	0.0000	0.0001	0.0000	0.0002	0.000007	0.004	0.001
$\epsilon_{PID\pi}$	0.002	0.0015	0.005	0.0004	0.0007	0.0003	0.0004	0.0003	0.0002	0.000009	0.023	0.008
$\sigma_{DK}/\sigma_{D\pi}$	0.002	0.0010	0.005	0.0003	0.0006	0.0003	0.0007	0.0001	0.0002	0.000008	0.006	0.006
$D\pi$ Fixed Mis-ID Tail	0.004	0.0007	0.001	0.0012	0.0010	0.0006	0.0003	0.0001	0.0002	0.000002	0.005	0.010
Fav/Sup Crossfeed	0.002	0.0020	0.001	0.0002	0.0004	0.0001	0.0002	0.0001	0.0001	0.000011	0.004	0.001
A_{int}	0.006	0.0069	0.002	0.0009	0.0044	0.0042	0.0042	0.0050	0.0001	0.000006	0.008	0.005
DK Mis-ID Shape	0.004	0.0034	0.007	0.0009	0.0006	0.0001	0.0005	0.0001	0.0002	0.000014	0.010	0.007
Eff. Corrections	0.005	0.0006	0.007	0.0036	0.0008	0.0005	0.0012	0.0005	0.0005	0.000011	0.032	0.041
B_S Shape	0.037	0.0037	0.002	0.0074	0.0014	0.0003	0.0004	0.0002	0.0019	0.000028	0.004	0.012
Low-Mass Shape	0.002	0.0026	0.003	0.0009	0.0008	0.0002	0.0003	0.0001	0.0001	0.000016	0.008	0.009
Wrongly Recon'd D Shape	0.003	0.0016	0.001	0.0003	0.0001	0.0000	0.0002	0.0000	0.0002	0.000011	0.006	0.003
$R_{K/\pi}$ for $K\pi\pi^0$	0.003	0.0005	0.006	0.0014	0.0002	0.0001	0.0003	0.0001	0.0003	0.000005	0.010	0.005
Charmless Yields	0.006	0.0043	0.016	0.0062	0.0007	0.0004	0.0003	0.0001	0.0001	0.000005	0.011	0.008
Fixed Signal Tails	0.001	0.0021	0.001	0.0003	0.0009	0.0005	0.0002	0.0001	0.0001	0.000012	0.009	0.002
Comb Yields	0.011	0.0037	0.006	0.0023	0.0003	0.0003	0.0004	0.0001	0.0006	0.000026	0.017	0.006
Total	0.041	0.0113	0.022	0.0108	0.0051	0.0044	0.0046	0.0050	0.0021	0.000056	0.051	0.048

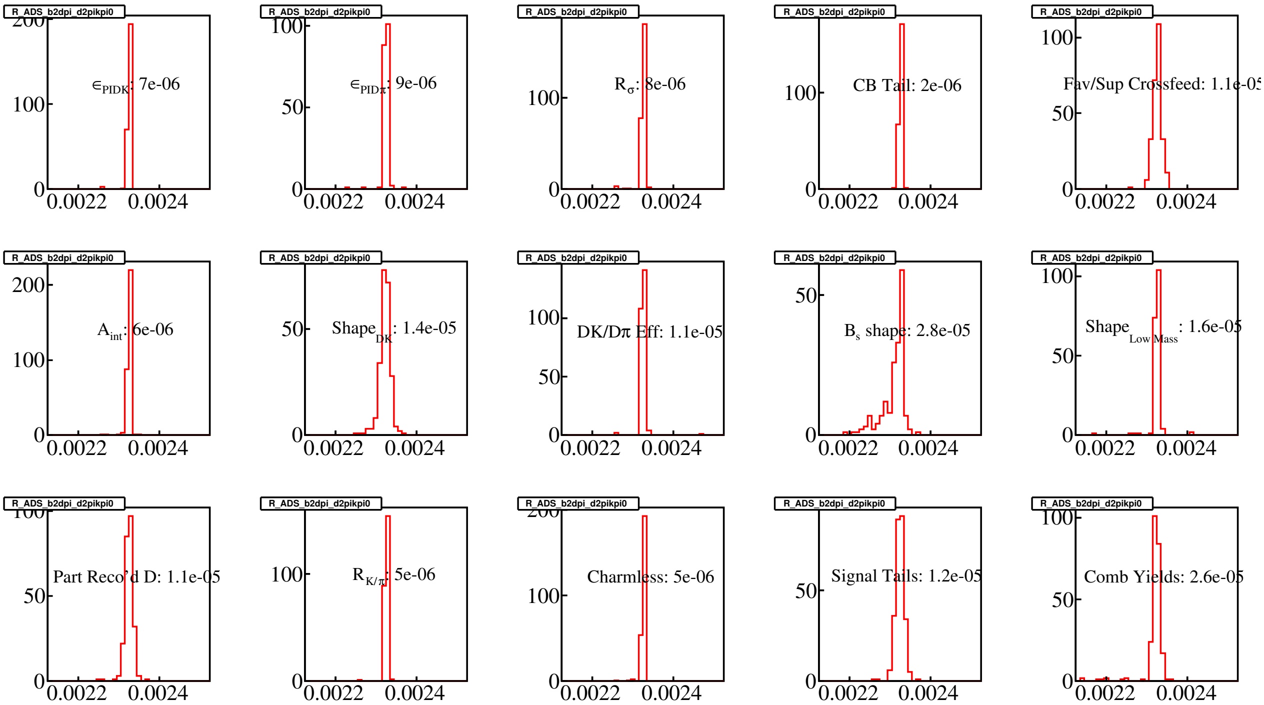

Figure 5.2: Changes in the fit result of $R_{\text{ADS}(\pi)}$ due to the Gaussian variation of the fixed fit parameters related to systematic uncertainties. Each histogram corresponds to a different systematic uncertainty source. The RMS of each histogram is the systematic uncertainty contribution from that particular source.

this Section.

1. The bachelor PID calibration is performed using the `PIDCalib` tool, as discussed in Section 3.9. For the DK modes, an additional uncertainty of 0.8% is added in quadrature to the values reported in Table 3.12 to account for the fact that the signal sample used in the calibration process is $B^{\mp} \to D\pi^{\mp}$ candidates. For bachelor kaons and a PID cut of PIDK > 4, the identification efficiency is $(84.5 \pm 0.9)\%$ for negative kaons and $(84.6 \pm 0.9)\%$ for positive kaons. In the systematics table, this source of uncertainty is depicted as ϵ_{PIDK}.

2. The bachelor PID calibration uncertainty for pion identification is considered as a separate source of systematic uncertainty. The identification efficiency is $(96.3 \pm 0.5)\%$ for both negative and positive pions. The source of systematic uncertainty is represented as $\epsilon_{PID\pi}$ in the systematics table.

3. In the fits, the width of the DK Cruijff signal shape is fixed to be a fraction of that

of the $D\pi$ shape, as discussed in Section 3.7.5. This source of systematic uncertainty is represented in the systematics table as $\sigma_{DK}/\sigma_{D\pi}$.

4. The double Crystal Ball function used to model the misidentified $D\pi$ candidates as DK, as discussed in Section 4.3, has three fixed parameters specified in Table 4.3. These parameters are a source of systematic uncertainty and are represented in the table as "$D\pi$ Fixed Mis-Id Tail".

5. The yields of the favoured/suppressed ADS crossfeed are determined by a ratio calculated in Section 4.5. This ratio is fixed at the value specified in Table 4.6, varied according to its calculated uncertainty and is listed in the systematics table as "Fav/-Sup Crossfeed".

6. Although the B^+/B^- production asymmetry is a floating value of the fit, the kaon and pion detection asymmetries are fixed to the values mentioned in Section 5.3. Furthermore, the level of *CP* violation in $B^\mp \to [K^\mp\pi^\pm\pi^0]_D\pi^\mp$ is taken to be $(0.00 \pm 0.05)\%$. These systematic sources, in the table, are listed as A_{int}.

7. The DK events that are misidentified as $D\pi$ events are modelled as a double Crystal Ball function, as described in Section 4.3.3, with fully fixed parameters. These values are fixed as specified in Table 4.4 and varied according to their uncertainties reported in this Table. In the systematics table, this source is referred to as "DK Mis-ID Shape".

8. The efficiency due to trigger, reconstruction, stripping and offline selection is discussed in Section 3.8, and it is determined that such efficiencies are slightly different for the DK decay modes compared to the $D\pi$ modes. The ratio of these efficiencies, $\epsilon(DK)/\epsilon(D\pi)$, is fixed to the values specified in Table 3.7 and varied according to their reported uncertainties. This source of systematic uncertainty is represented in the table as "Eff. Corrections".

9. The background contributions from partially reconstructed B_s^0 decays, discussed in Section 4.4, are modelled using a Cruijff shape with the fixed parameters from Table 4.5

and varied according to their reported uncertainties. In the systematics table, this uncertainty source is labelled "B_s Shape".

10. The partially reconstructed low-mass background is modelled using the HILLdini and HORNSdini PDFs, described in Section 4.2. There is a systematic uncertainty contribution from the shift of the mean of the DK shape, relative to the $D\pi$ shape, of 0.7 ± 2.0 MeV/c^2 and another from the fixed width of the DK contributions relative to the $D\pi$ contributions, set at 0.95 ± 0.10. In the table, the systematic source due to the assumptions of the low-mass background shape are labelled as "Low-Mass Shape".

11. The wrongly reconstructed D backgrounds are modelled as a Cruijff function with a single tail parameter, as described in Section 4.8. The means are fixed to the values specified in Table 4.12. This systematic uncertainty source is marked as "Wrongly Recon'd D Shape" in the table.

12. The DK to $D\pi$ yield ratio is fixed for the favoured $B^{\mp} \to [K^{\mp}\pi^{\pm}\pi^{0}]_{D}h^{\mp}$ decays at a value of 0.0774 ± 0.0022 [83]. In the table, this systematic uncertainty source is classified as "$R_{K/\pi}$ for $K\pi\pi^0$ ".

13. The yields from charmless background contributions are fixed using the values depicted in Table 4.8. The asymmetry due to CP violation in the charmless modes is assigned a value of 0 with an uncertainty of 50%. Furthermore, the potential misidentification of $\pi\pi\pi^0$ and $KK\pi^0$ modes in the $B^{\mp} \to [\pi^{\mp}K^{\pm}\pi^{0}]_{D}h^{\mp}$ decays has a fixed yield as per Section 4.7. These sources of systematic uncertainties are collected under the label of "Charmless Yields" in the table.

14. The tails of the signal Cruijff shapes are fixed to the values of $\alpha_L = 0.15 \pm 0.03$ and $\alpha_R = 0.12 \pm 0.02$ based on studies in MC performed in Section 3.7.4. In the systematics table, this source is depicted as "Fixed Signal Tails".

15. The yields of the combinatorial backgrounds in the $B^{\mp} \to [\pi^{\mp}K^{\pm}\pi^{0}]_{D}K^{\mp}$ and $B^{\mp} \to [\pi^{\mp}K^{\pm}\pi^{0}]_{D}\pi^{\mp}$ modes are fixed to the same levels of the $B^{\mp} \to [K^{\mp}\pi^{\pm}\pi^{0}]_{D}K^{\mp}$ and

$B^{\mp} \to [K^{\mp}\pi^{\pm}\pi^{0}]_{D}\pi^{\mp}$ decays, respectively. A systematic uncertainty of 50% is assigned. This systematics source is labelled as "Comb Yields" in the table.

The dominant source of systematic uncertainty for each observable is as expected. For example, for the R_{qGLW} observables, which relate to the $DK/D\pi$ ratios, the primary systematic uncertainty contributions come from the $DK/D\pi$ efficiency corrections. For $R_{\text{ADS}(K)}$, the largest systematic uncertainty contribution comes from the B_{s}^{0} background shape; this is expected because of the prominence of this shape in the $B^{\mp} \to [\pi^{\mp}K^{\pm}\pi^{0}]_{D}K^{\mp}$ decays and the fact that it is fully fixed. Also, as expected, the greatest systematic uncertainty to the A_{Prod} measurement is the fixed instrumentation uncertainties.

Chapter 6

Results and Interpretations

In this Chapter, the results of the simultaneous fit to data are presented. The yields of the different decay modes are shown in addition to the extraction of the *CP* observables. These results are then discussed along with a calculation of signal significance for the heretofore unobserved suppressed ADS decays and the $B^{\mp} \to [K^{+}K^{-}\pi^{0}]_{D}h^{\mp}$ decays. The Chapter concludes by interpreting the observables in terms of the underlying physics parameters r_B, δ_B and γ.

6.1 Fit Results

In this Section, the results of the fits are presented for the different data subsamples. First the summed-over-charge results are given, and then the cases where they are split by charge; the latter are used for the extraction of the fit observables. In all cases, the PDF modelling shows good agreement with the data within the range of interest for the invariant $B^{\mp}$ mass.

6.1.1 Fit Results Summed by Charge

The yields from the summed-over-charge fits are given in Table 6.1 and the fits to data are presented in Figures 6.1 to 6.2.

The favoured $B^{\mp} \to [K^{\mp}\pi^{\pm}\pi^{0}]_{D}h^{\mp}$ decays, in addition to the $B^{\mp} \to [\pi^{+}\pi^{-}\pi^{0}]_{D}h^{\mp}$ and $B^{\mp} \to [K^{+}K^{-}\pi^{0}]_{D}h^{\mp}$ modes all display prominent signal peaks. To a lesser extent, signal

Table 6.1: Signal yields and statistical uncertainties from the summed-over-charge fits.

Decay Mode	Yield
$B^{\mp} \to [K^{\mp}\pi^{\pm}\pi^{0}]_{D}\pi^{\mp}$	37736 ± 283
$B^{\mp} \to [K^{\mp}\pi^{\pm}\pi^{0}]_{D}K^{\mp}$	2921 ± 22
$B^{\mp} \to [\pi^{\mp}K^{\pm}\pi^{0}]_{D}\pi^{\mp}$	88 ± 19
$B^{\mp} \to [\pi^{\mp}K^{\pm}\pi^{0}]_{D}K^{\mp}$	40 ± 14
$B^{\mp} \to [\pi^{+}\pi^{-}\pi^{0}]_{D}\pi^{\mp}$	3488 ± 84
$B^{\mp} \to [\pi^{+}\pi^{-}\pi^{0}]_{D}K^{\mp}$	265 ± 30
$B^{\mp} \to [K^{+}K^{-}\pi^{0}]_{D}\pi^{\mp}$	1050 ± 53
$B^{\mp} \to [K^{+}K^{-}\pi^{0}]_{D}K^{\mp}$	76 ± 18

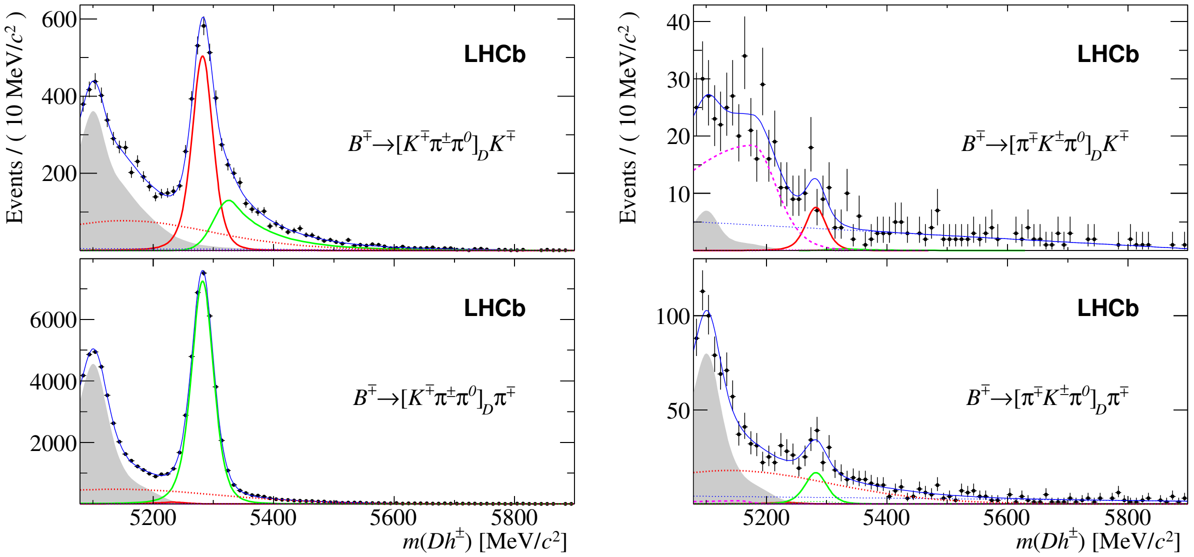

(a) Favoured ADS $K\pi\pi^0$

(b) Suppressed ADS $K\pi\pi^0$

Figure 6.1: The full fit applied to the invariant mass distributions of $B^{\mp} \to [K\pi\pi^0]_D h^{\mp}$ candidates, summed by charge. $B^{\mp} \to DK^{\mp}$ ($B^{\mp} \to D\pi^{\mp}$) signal events are in the upper (lower) plots. The solid red curve represents $B^{\mp} \to DK^{\mp}$ events and the green curve represents $B^{\mp} \to D\pi^{\mp}$ events. The grey shape indicates partially reconstructed $B^{\mp}$ decays and the heavy dotted red curve indicates wrongly reconstructed D decays. The lightly dotted blue line represents the combinatorial component and the magenta line indicates contributions from partially reconstructed $B_s^0 \to [K^{\pm}\pi^{\mp}\pi^0]_D(K^{*0} \to K^{\mp}\pi^{\pm})$ decays where the pion or kaon from the K^{*0} is not reconstructed. The solid blue line represents the total PDF.

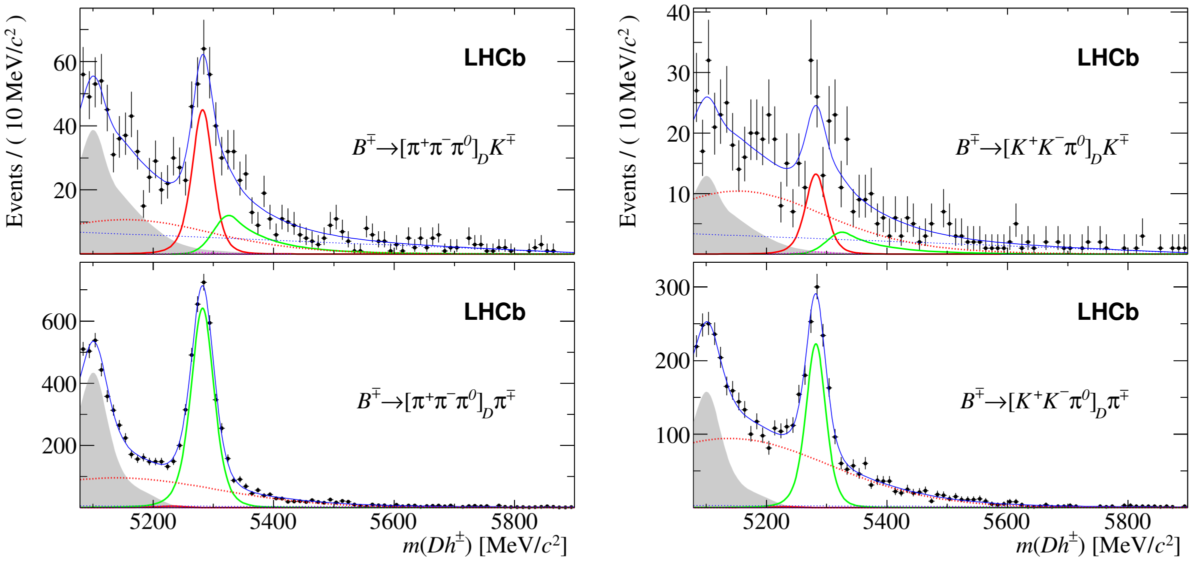

(a) $B^{\mp}\to[\pi^{+}\pi^{-}\pi^{0}]_{D}h^{\mp}$ (b) $B^{\mp}\to[K^{+}K^{-}\pi^{0}]_{D}h^{\mp}$

Figure 6.2: The full fit applied to the invariant mass distributions of $B^{\mp}\to[\pi^{+}\pi^{-}\pi^{0}]_{D}h^{\mp}$ and $B^{\mp}\to[K^{+}K^{-}\pi^{0}]_{D}h^{\mp}$, summed by charge. A full fit description is provided in the caption of Figure 6.1

peaks are also visible in the suppressed $B^{\mp}\to[\pi^{\mp}K^{\pm}\pi^{0}]_{D}h^{\mp}$ decays. The significance of these signals is further discussed in Section 6.3.

6.1.2 Fit Results Split by Charge

The same fitting exercise is performed for each of the different decay modes after they have been split according to the parent B hadron charge. The signal yields are summarised in Table 6.2 and the fits are presented in Figures 6.3 to 6.6. The values of the floating variables, as determined by the fit, are listed in Table 6.3.

Table 6.2: Signal yields and statistical uncertainties, split by charge type.

$B^{-}\to[K^{-}\pi^{+}\pi^{0}]_{D}\pi^{-}$	18854 ± 176	$B^{+}\to[K^{+}\pi^{-}\pi^{0}]_{D}\pi^{+}$	18882 ± 176
$B^{-}\to[K^{-}\pi^{+}\pi^{0}]_{D}K^{-}$	1478 ± 39	$B^{+}\to[K^{+}\pi^{-}\pi^{0}]_{D}K^{+}$	1442 ± 39
$B^{-}\to[\pi^{-}K^{+}\pi^{0}]_{D}\pi^{-}$	63 ± 13	$B^{+}\to[\pi^{+}K^{-}\pi^{0}]_{D}\pi^{+}$	25 ± 13
$B^{-}\to[\pi^{-}K^{+}\pi^{0}]_{D}K^{-}$	16 ± 9	$B^{+}\to[\pi^{+}K^{-}\pi^{0}]_{D}K^{+}$	24 ± 9
$B^{-}\to[\pi^{+}\pi^{-}\pi^{0}]_{D}\pi^{-}$	1716 ± 55	$B^{+}\to[\pi^{+}\pi^{-}\pi^{0}]_{D}\pi^{+}$	1772 ± 55
$B^{-}\to[\pi^{+}\pi^{-}\pi^{0}]_{D}K^{-}$	139 ± 19	$B^{+}\to[\pi^{+}\pi^{-}\pi^{0}]_{D}K^{+}$	125 ± 19
$B^{-}\to[K^{-}K^{+}\pi^{0}]_{D}\pi^{-}$	509 ± 34	$B^{+}\to[K^{+}K^{-}\pi^{0}]_{D}\pi^{+}$	541 ± 34
$B^{-}\to[K^{-}K^{+}\pi^{0}]_{D}K^{-}$	49 ± 12	$B^{+}\to[K^{+}K^{-}\pi^{0}]_{D}K^{+}$	27 ± 12

The header of the fit result, as provided by the RooFit package, is displayed in the

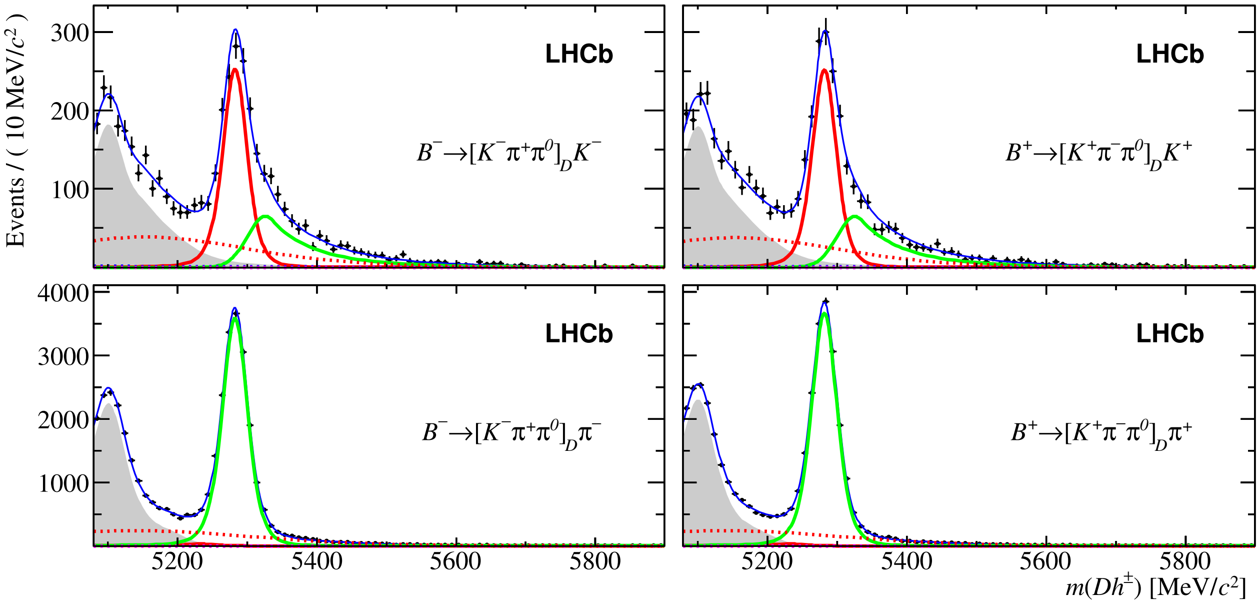

Figure 6.3: The full fit applied to the invariant mass distributions of $B^\mp \to [K^\mp\pi^\pm\pi^0]_D h^\mp$. B^- candidates are on the left and B^+ candidates are on the right. A full fit description is provided in the caption of Figure 6.1.

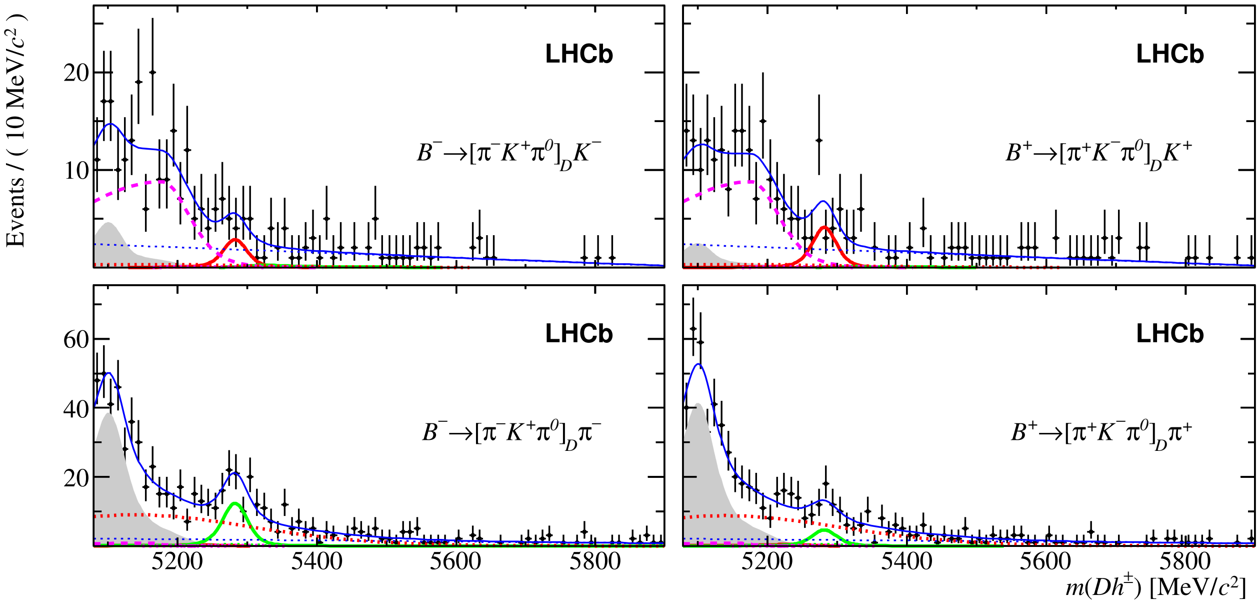

Figure 6.4: The full fit applied to the invariant mass distributions of $B^\mp \to [\pi^\mp K^\pm\pi^0]_D h^\mp$. B^- candidates are on the left and B^+ candidates are on the right. A full fit description is provided in the caption of Figure 6.1.

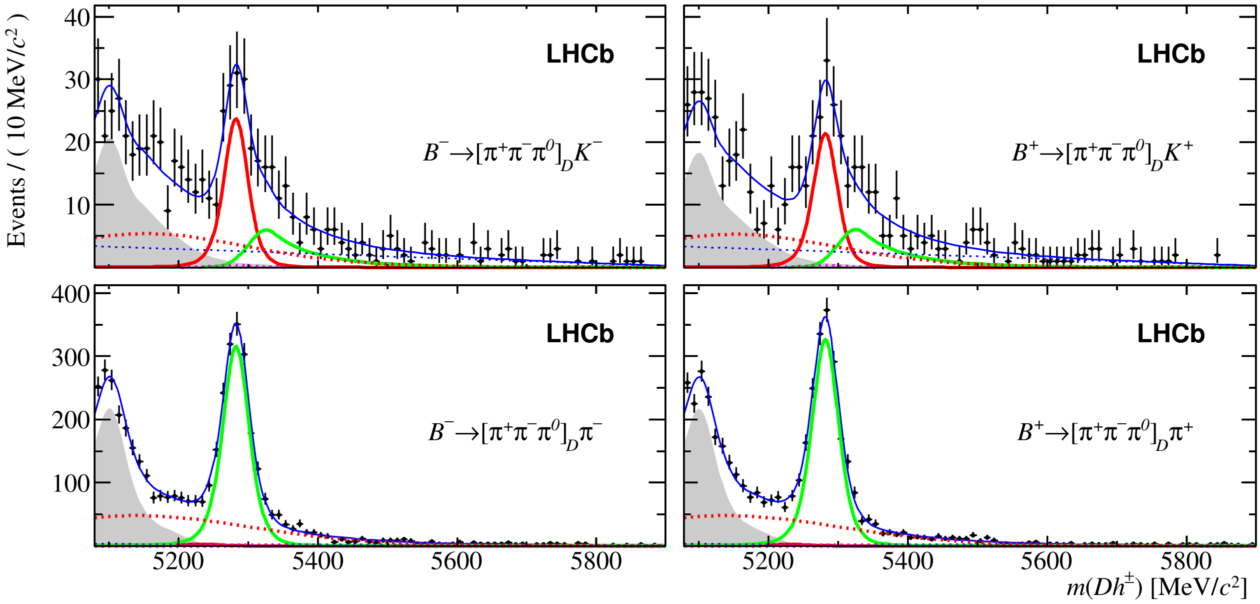

Figure 6.5: The full fit applied to the invariant mass distributions of $B^{\mp} \rightarrow [\pi^+\pi^-\pi^0]_D h^{\mp}$. B^- candidates are on the left and B^+ candidates are on the right. A full fit description is provided in the caption of Figure 6.1.

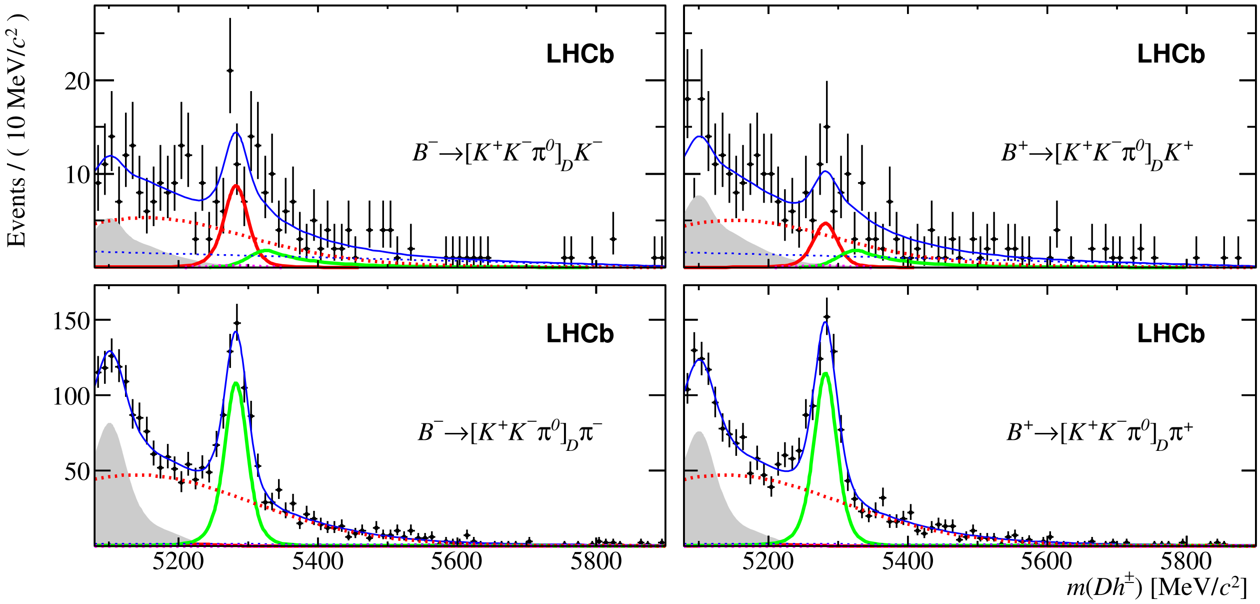

Figure 6.6: The full fit applied to the invariant mass distributions of $B^{\mp} \rightarrow [K^+K^-\pi^0]_D h^{\mp}$. B^- candidates are on the left and B^+ candidates are on the right. A full fit description is provided in the caption of Figure 6.1.

Table 6.3: Output of the final values of the floating parameters, as presented by the fit result to the data split by charge type.

```
RooFitResult:  minimized FCN value:  -55627.9, estimated distance to minimum:  0.00124724
covariance matrix quality:  Full, accurate covariance matrix
Status :  MIGRAD=0 HESSE=0
```

Floating Parameter	Final Value
A_ADS_b2dk_d2pikpi0	-1.8005e-01 +/- 2.72e-01
A_ADS_b2dpi_d2pikpi0	4.3839e-01 +/- 1.90e-01
A_CPP_b2dk_d2kkpi0	2.8797e-01 +/- 2.00e-01
A_CPP_b2dk_d2pipipi0	5.4123e-02 +/- 9.14e-02
A_CPP_b2dpi_d2kkpi0	-2.9794e-02 +/- 4.01e-02
A_CPP_b2dpi_d2pipipi0	-1.6019e-02 +/- 2.01e-02
A_FAV_b2dk_d2kpipi0	1.2402e-02 +/- 2.58e-02
A_Prod	-7.7369e-04 +/- 5.55e-03
CB_alphaR_d2kpi	-4.0285e-01 +/- 6.33e-02
CB_sigmaL_d2kpi	1.4524e+01 +/- 7.54e-01
CB_sigmaR_d2kpi	2.5926e+01 +/- 2.99e+00
R_ADS_b2dk_d2pikpi0	1.3753e-02 +/- 4.67e-03
R_ADS_b2dpi_d2pikpi0	2.3245e-03 +/- 4.96e-04
R_FP_d2kkpi0	9.3322e-01 +/- 2.18e-01
R_FP_d2pipipi0	9.7997e-01 +/- 1.08e-01
R_d0kst_pass	6.6122e-03 +/- 1.02e-03
alpha_kppz_fail	-1.4682e+00 +/- 1.65e-01
alpha_kppz_pass	-1.0774e+00 +/- 2.01e-01
comb_coeff_fail	-4.8162e-01 +/- 1.66e-01
comb_coeff_pass	-8.6764e-01 +/- 6.58e-02
low_DK_vs_Dpi_d2kpipi0	5.5787e-01 +/- 6.01e-02
low_P_GAM_vs_PI0_d2kpipi0	6.0888e-01 +/- 2.74e-02
low_shift_d2kpipi0	4.1650e+00 +/- 3.70e-01
low_sigma_d2kpipi0	1.6552e+01 +/- 5.98e-01
mean_B_minus_both_d2kpipi0_fail	5.2823e+03 +/- 1.72e-01
mean_B_plus_both_d2kpipi0_fail	5.2818e+03 +/- 1.69e-01
n_b2dpi_d2kkpi0_both	1.0500e+03 +/- 5.34e+01
n_b2dpi_d2kpipi0_both	3.7736e+04 +/- 2.83e+02
n_b2dpi_d2pipipi0_both	3.4882e+03 +/- 8.41e+01
n_com_d2kkpi0_fail_both	8.0041e+01 +/- 2.27e+01
n_com_d2kkpi0_pass_both	7.1784e+01 +/- 1.58e+01
n_com_d2kpipi0_fail_both	1.1515e+02 +/- 2.23e+01
n_com_d2kpipi0_pass_both	1.0452e+02 +/- 1.62e+01
n_com_d2pipipi0_fail_both	1.6040e+02 +/- 3.42e+01
n_com_d2pipipi0_pass_both	1.4708e+02 +/- 2.19e+01
n_dco_d2kkpi0_fail	1.2867e+03 +/- 5.29e+01
n_dco_d2kkpi0_pass	1.3793e+02 +/- 2.56e+01
n_dco_d2kpipi0_fail	6.5448e+03 +/- 2.70e+02
n_dco_d2kpipi0_pass	1.0227e+03 +/- 1.33e+02
n_dco_d2pikpi0_fail	2.4243e+02 +/- 3.15e+01
n_dco_d2pikpi0_pass	7.6434e+00 +/- 2.73e+01
n_dco_d2pipipi0_fail	1.3103e+03 +/- 7.37e+01
n_dco_d2pipipi0_pass	1.4201e+02 +/- 3.78e+01
n_low_d2kkpi0_fail_minus_both	4.9602e+02 +/- 3.78e+01
n_low_d2kkpi0_fail_plus_both	4.6316e+02 +/- 3.69e+01
n_low_d2kkpi0_pass_minus_both	4.3426e+01 +/- 1.78e+01
n_low_d2kkpi0_pass_plus_both	6.6434e+01 +/- 1.86e+01
n_low_d2kpipi0_fail_minus_both	1.3646e+04 +/- 2.18e+02
n_low_d2kpipi0_fail_plus_both	1.4016e+04 +/- 2.18e+02
n_low_d2kpipi0_pass_minus_both	1.5185e+03 +/- 1.31e+02
n_low_d2kpipi0_pass_plus_both	1.5346e+03 +/- 1.32e+02
n_low_d2pikpi0_fail_minus_both	2.3179e+02 +/- 2.11e+01
n_low_d2pikpi0_fail_plus_both	2.5495e+02 +/- 2.15e+01
n_low_d2pikpi0_pass_minus_both	2.6929e+01 +/- 1.36e+01
n_low_d2pikpi0_pass_plus_both	1.4462e+01 +/- 1.29e+01
n_low_d2pipipi0_fail_minus_both	1.3235e+03 +/- 5.32e+01
n_low_d2pipipi0_fail_plus_both	1.3151e+03 +/- 5.34e+01
n_low_d2pipipi0_pass_minus_both	1.7188e+02 +/- 2.83e+01
n_low_d2pipipi0_pass_plus_both	1.5544e+02 +/- 2.58e+01
sigma_dpi_d2kkpi0	1.5660e+01 +/- 8.73e-01
sigma_dpi_d2kpipi0	1.7324e+01 +/- 1.33e-01
sigma_dpi_d2pipipi0	1.8091e+01 +/- 4.78e-01
sigma_kppz_fail	1.6683e+02 +/- 4.72e+00
sigma_kppz_pass	1.4555e+02 +/- 1.69e+01

caption to Table 6.3. The fit converges and has an accurate correlation matrix. The values and statistical uncertainties of the analysis observables are extracted from these fit results, where the nomenclature of the floating variables is given in Table 5.2.

As noted in Section 5.4, the fit procedure is slightly biased for several *CP* observables. Based upon the statistical uncertainties reported by the fit, these central values are corrected, as displayed in Table 6.4.

Table 6.4: The corrected central values for observables deemed in Section 5.4 to be biased. The first two columns are values reported directly from the fit, while the correction offset is as specified in Table 5.6.

Observable	Central Value	1σ Fit Uncertainty	Correction Offset	Corrected Central Value
$A_{\mathrm{ADS}(K)}$	-0.18	0.27	-0.065σ	-0.20
$A^{KK\pi^0}_{\mathrm{qGLW}(K)}$	0.29	0.20	$+0.054\sigma$	0.30
$A^{K\pi\pi^0}_{K}$	0.012	0.026	-0.078σ	0.0103
$R_{\mathrm{ADS}(K)}$	0.0138	0.0047	$+0.060\sigma$	0.0140
$R_{\mathrm{ADS}(\pi)}$	0.00232	0.00050	$+0.050\sigma$	0.00235
$R^{KK\pi^0}_{\mathrm{qGLW}}$	0.93	0.22	$+0.063\sigma$	0.95

6.2 *CP* Observables

The final results for the *CP* observables are listed in Table 6.5 alongside their statistical uncertainties from the fit and the systematic uncertainties, assigned as described in Section 5.5. It is apparent that the measurements are statistically limited; in certain cases the systematic uncertainties are an order of magnitude less than that of the statistical uncertainties.

The B^+/B^- production asymmetry variable, A_{Prod}, is consistent with 0. However, the total uncertainty on this measurement is 0.0074 which is the same order of magnitude as the 0.009 uncertainty from a previous study using B^+ and B^- candidates [34] and the 0.0024 measured in a more general plus/minus charge asymmetry analysis using D_s^+ and D_s^- candidates [103]. The result of the A_{Prod} measurement demonstrates the feasibility of measuring the B^+/B^- asymmetry using $B^{\mp} \to D\pi^{\mp}$ decays with high statistics. Consequently, it encourages the use of this method with $B^{\mp} \to D\pi^{\mp}$ decays of larger expected signal yields than $B^{\mp} \to [K^{\mp}\pi^{\pm}\pi^0]_D\pi^{\mp}$ to obtain a more precise measurement of A_{Prod} than that currently available.

Table 6.5: The *CP* observables of the analysis, complete with statistical (fit) uncertainties and systematic uncertainties.

Observable	Value	Statistical Uncertainty	Systematic Uncertainty
$A_{\mathrm{ADS}(K)}$	-0.20	0.27	0.04
$A_{\mathrm{ADS}(\pi)}$	0.44	0.19	0.01
$A^{KK\pi^0}_{\mathrm{qGLW}(K)}$	0.30	0.20	0.02
$A^{\pi\pi\pi^0}_{\mathrm{qGLW}(K)}$	0.054	0.091	0.011
$A^{KK\pi^0}_{\mathrm{qGLW}(\pi)}$	-0.030	0.040	0.005
$A^{\pi\pi\pi^0}_{\mathrm{qGLW}(\pi)}$	-0.016	0.020	0.004
$A^{K\pi\pi^0}_{K}$	0.010	0.026	0.005
A_{Prod}	-0.0008	0.0055	0.0050
$R_{\mathrm{ADS}(K)}$	0.0140	0.0047	0.0021
$R_{\mathrm{ADS}(\pi)}$	0.00235	0.00049	0.00006
$R^{KK\pi^0}_{\mathrm{qGLW}}$	0.95	0.22	0.05
$R^{\pi\pi\pi^0}_{\mathrm{qGLW}}$	0.98	0.11	0.05

Of particular interest are the A_{ADS} and R_{ADS} *CP* observables that are related to the suppressed $K\pi\pi^0$ decays. As expected, the central value of $R_{\mathrm{ADS}(K)}$ is an order of magnitude greater than that of $R_{\mathrm{ADS}(\pi)}$, largely due to the difference in magnitude between r_B and r_B^π. Furthermore, the measured values of the $D \to K^\pm\pi^\mp\pi^0$ ADS observables are similar to the $D \to K^\pm\pi^\mp$ and $D \to K^\pm\pi^\mp\pi^+\pi^-$ ADS observables previously measured at LHCb [83, 88], although due to differences in coherence factor and average strong phase differences, the ADS observables from these analyses are not expected to be identical.

When comparing specifically to $K\pi\pi^0$ analyses, all of the A_{ADS} and R_{ADS} observables from this analysis are in agreement with those measured by BaBar and Belle [35, 36] (discussed in Sections 1.7.2 and 1.7.3). Comparison plots of the ADS observables are presented in Figure 6.7. For $R_{\mathrm{ADS}(K)}$, the measured value has a central value that is lower than that measured by Belle and higher than that measured by BaBar, but is compatible with both. Of these two other experiments, only Belle reports a measurement of $A_{\mathrm{ADS}(K)}$; their central value is positive, reporting an excess of B^- events while the central value from this analysis is negative, seeing an excess of B^+. If one uses Equation 1.66 with an assumed γ value of 73° and the world's best measurements [2] for the other inputs, a negative central value is expected. Nevertheless, both the value of $A_{\mathrm{ADS}(K)}$ from this analysis and from Belle are compatible with each other and zero asymmetry. The $A_{\mathrm{ADS}(\pi)}$ measurement is compatible with

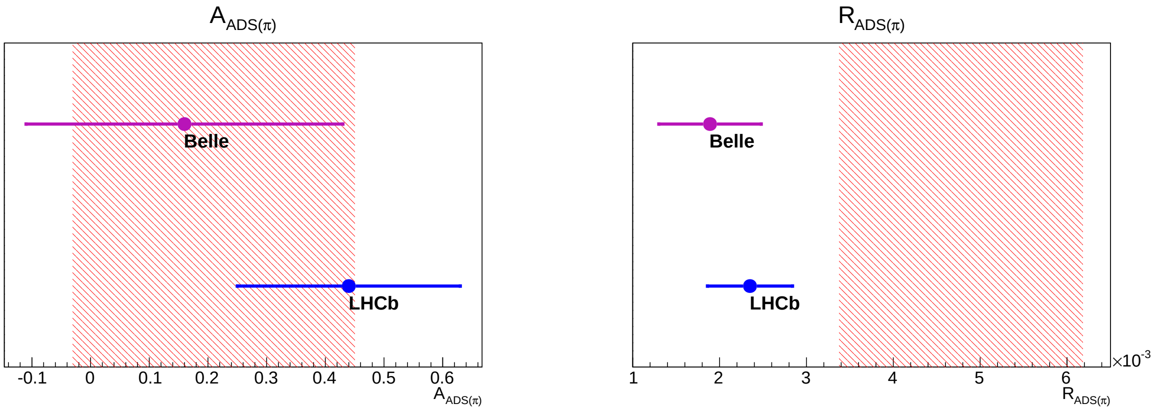

(a) $A_{\mathrm{ADS}(\pi)}$ measurements (b) $R_{\mathrm{ADS}(\pi)}$ measurements

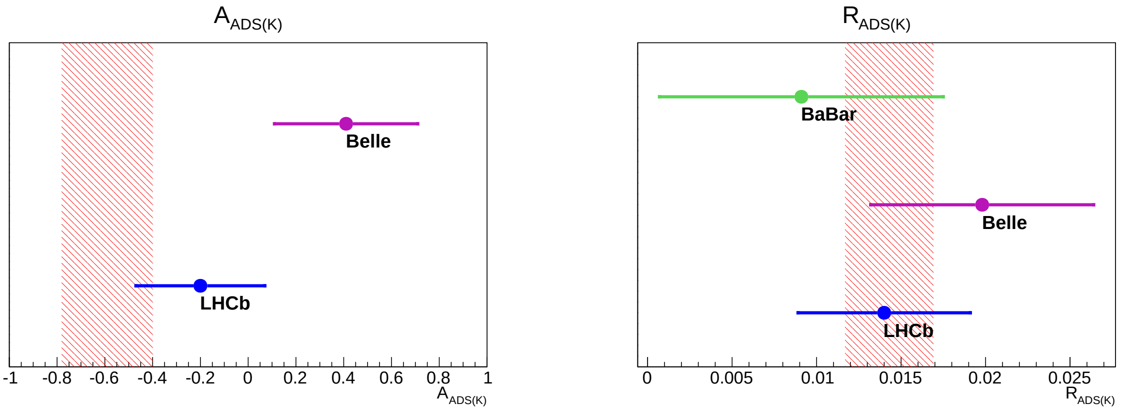

(c) $A_{\mathrm{ADS}(K)}$ measurements (d) $R_{\mathrm{ADS}(K)}$ measurements

Figure 6.7: Comparison of measured ADS observables for $K\pi\pi^0$ decays. The results from this analysis, using LHCb data, are presented in blue, while those from Belle are in purple and, when applicable, results from BaBar in green. The red region represents expected value of the observable calculated using the world's best measurements for the parameters and a value of $\gamma = 73°$. The width of the red region corresponds to the 1σ band, as determined from the experimental inputs used in the expected observable central value calculation.

Belle's, although both have large uncertainties. Interestingly, the $R_{\mathrm{ADS}(\pi)}$ value measured, like the one from Belle, is less than the central value expected from the known value of the physics parameters. However, the uncertainties on the expected value are rather large, in part due to large uncertainties on r_B^π.

With regards to the quasi-GLW decays, all of the measured asymmetries are compatible with zero. The only one of the quasi-GLW *CP* observables to have been previously measured is $A^{\pi\pi\pi^0}_{\mathrm{qGLW}(K)}$ in an analysis by BaBar where it was found to be $-0.02 \pm 0.15(\mathrm{stat.}) \pm 0.03(\mathrm{syst.})$ [37]. The value measured in this analysis is compatible. In addition, the measured values of $R^{\pi\pi\pi^0}_{\mathrm{qGLW}}$ and $R^{KK\pi^0}_{\mathrm{qGLW}}$ are consistent with expectations that they be approximately 1, as per Equations 1.88 and 1.87.

This analysis marks the first time the *CP* observables $A^{\pi\pi\pi^0}_{\mathrm{qGLW}(\pi)}$, $A^{KK\pi^0}_{\mathrm{qGLW}(\pi)}$, $A^{KK\pi^0}_{\mathrm{qGLW}(K)}$, $R^{\pi\pi\pi^0}_{\mathrm{qGLW}}$ and $R^{KK\pi^0}_{\mathrm{qGLW}}$ have been measured. Furthermore, the results for $A^{K\pi\pi^0}_{K}$, $A^{\pi\pi\pi^0}_{\mathrm{qGLW}(K)}$, $A^{K\pi\pi^0}_{\mathrm{ADS}(\pi)}$, $R^{K\pi\pi^0}_{\mathrm{ADS}(\pi)}$, $A^{K\pi\pi^0}_{\mathrm{ADS}(K)}$ and $R^{K\pi\pi^0}_{\mathrm{ADS}(K)}$ are more precise than any previous measurement of these *CP* observables.

6.3 Signal Significance

Of the decay modes studied in this analysis, four of them, $B^\mp \to [\pi^\mp K^\pm \pi^0]_D K^\mp$, $B^\mp \to [\pi^\mp K^\pm \pi^0]_D \pi^\mp$, $B^\mp \to [K^+ K^- \pi^0]_D K^\mp$ and $B^\mp \to [K^+ K^- \pi^0]_D \pi^\mp$ have been heretofore unobserved. The statistical significance of the signal yields of these decays is evaluated through the use of Wilks' Theorem [104],

$$\sigma = \sqrt{-2 \ln \left(\frac{\mathcal{L}_0}{\mathcal{L}} \right)}. \tag{6.1}$$

In this expression, $\mathcal{L}$ represents the likelihood of the default fit whereas $\mathcal{L}_0$ is that of the null result corresponding to no signal contributions.

In this analysis, rather than evaluate significances using candidate yields, we can instead employ the R_{ADS} and $R^{KK\pi^0}_{\mathrm{qGLW}}$ *CP* observables. As in Equations 5.17, 5.18 and 5.22, these particular observables are multipliers that influence yield quantities. If R_{ADS} or $R^{KK\pi^0}_{\mathrm{qGLW}}$ are equal to zero, the corresponding decay channels will have zero entries.

To evaluate the significance, the fit is performed for a variety of fixed values of the relevant *CP* observables. For each fixed value, the negative log likelihood returned by the fit is recorded. The difference in negative log likelihoods between that of the varied value of the parameter and its base value from the fit (reported in Section 6.1.2) is plotted. In order to obtain a smoother shape, an interpolation is performed on this $\Delta(\log(L))$ distribution between the values measured by the fit. Using this interpolated $\Delta(\log(L))$ distribution, the corresponding likelihood distribution is plotted. This likelihood is then convolved with a Gaussian function of width corresponding to the systematic uncertainty of the parameter. This convolved likelihood is then used to re-calculate the $\Delta(\log(L))$ distribution and the value of the difference in negative log likelihoods is extracted for a *CP* observable value of zero, corresponding to the null hypothesis. This difference is then used in Wilks' Theorem to calculate the significance of the result.

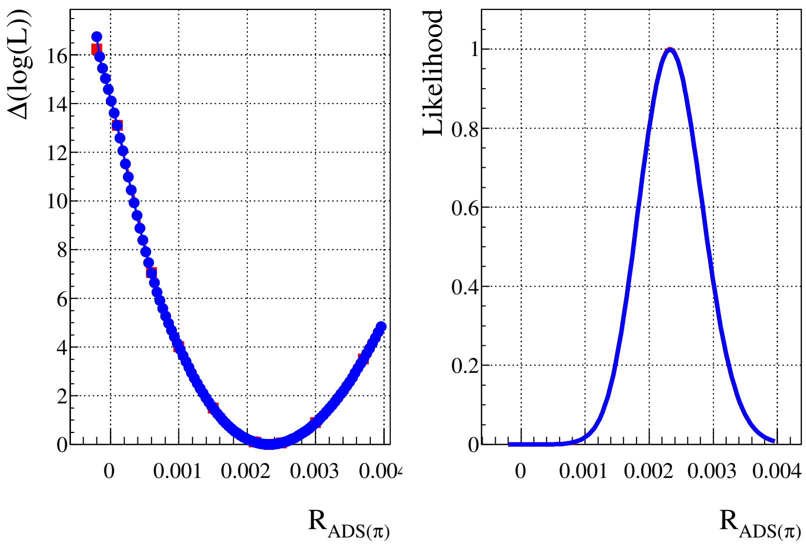

Figure 6.8: Evaluation of the signal significance of $B^{\mp} \to [\pi^{\mp} K^{\pm} \pi^{0}]_{D} \pi^{\mp}$ decays by performing a likelihood scan of $R_{\mathrm{ADS}(\pi)}$. The red curve (largely obscured behind the blue curve) represents the results of the likelihood scan, while the blue curve includes the systematic uncertainties. The null hypothesis corresponds to an $R_{\mathrm{ADS}(\pi)}$ value of zero. The plot on the left shows the difference in log likelihood values for a variety of $R_{\mathrm{ADS}(\pi)}$ values and the plot on the right, for reference, shows the corresponding likelihood.

For the case of $B^{\mp} \to [\pi^{\mp} K^{\pm} \pi^{0}]_{D} \pi^{\mp}$, the significance is evaluated through the study of the $R_{\mathrm{ADS}(\pi)}$ observable. The plot representing the difference in log likelihoods is presented in

Figure 6.8. In this plot, the red line (which is largely obscured by the blue curve) corresponds to the difference in log likelihoods as evaluated from the full binned fit for a variety of different $R_{\mathrm{ADS}(\pi)}$ values, while the blue line shows the results after accounting for the systematic uncertainty on $R_{\mathrm{ADS}(\pi)}$. From Figure 6.8, at the null hypothesis value of $R_{\mathrm{ADS}(\pi)} = 0$, a difference of log likelihoods corresponding to 14 is seen, which translates to a significance of 5.3σ. The signal yields of the $B^{\mp} \to [\pi^{\mp}K^{\pm}\pi^0]_D\pi^{\mp}$ channel thus allow for a claim of the first observation of this decay mode.

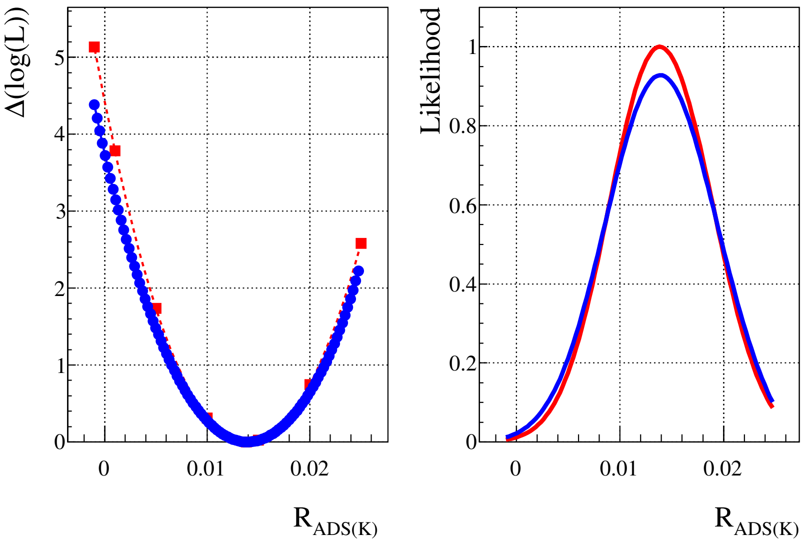

Figure 6.9: Evaluation of the signal significance of $B^{\mp} \to [\pi^{\mp}K^{\pm}\pi^0]_DK^{\mp}$ decays by performing a likelihood scan of $R_{\mathrm{ADS}(K)}$. The red curve represents the results of the likelihood scan, while the blue curve includes the systematic uncertainties. The null hypothesis corresponds to an $R_{\mathrm{ADS}(K)}$ value of zero. The plot on the left shows the difference in log likelihood values for a variety of $R_{\mathrm{ADS}(K)}$ values and the plot on the right, for reference, shows the corresponding likelihood.

For the $B^{\mp} \to [\pi^{\mp}K^{\pm}\pi^0]_DK^{\mp}$ decay, a similar exercise is performed using the $R_{\mathrm{ADS}(K)}$ observable. Once again, a value of 0 for this parameter corresponds to the null hypothesis. The parameter scan is presented in Figure 6.9, where a significance of 2.8σ is obtained.

With regards to the $KK\pi^0$ decay modes, the signal yield of the $B^{\mp} \to [K^+K^-\pi^0]_D\pi^{\mp}$ channel is sufficient to make an unambiguous first observation with a statistical significance of greater than 10σ. For the $B^{\mp} \to [K^+K^-\pi^0]_DK^{\mp}$ decay, a likelihood scan is performed using the $R^{KK\pi^0}_{\mathrm{qGLW}}$ observable with a value of 0 representing the null hypothesis. The results are presented in Figure 6.10. The significance is found to be 4.5σ, and thus we claim first evidence of this decay mode.

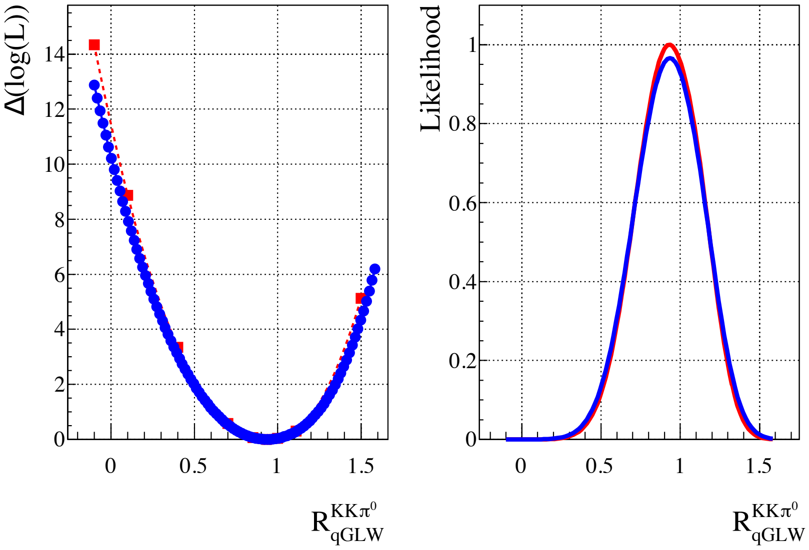

Figure 6.10: Evaluation of the signal significance of $B^{\mp} \to [K^+K^-\pi^0]_D K^{\mp}$ decays by performing a likelihood scan of $R_{\mathrm{qGLW}}^{KK\pi^0}$. The red curve represents the results of the likelihood scans, while the blue curve includes the systematic uncertainties. The null hypothesis corresponds to a value of zero. The plot on the left shows the difference in log likelihood values for a variety of $R_{\mathrm{qGLW}}^{KK\pi^0}$ values and the plot on the right, for reference, shows the corresponding likelihood.

6.4 Use of External Inputs

In order to extract the *CP* observables of r_B, δ_B and γ, the equations of Section 1.5.2 are used. However, these expressions also include the parameters $\kappa_D^{K\pi\pi^0}$, $\delta_D^{K\pi\pi^0}$, $F_+^{KK\pi^0}$ and $F_+^{\pi\pi\pi^0}$ that have been measured at CLEO-c. The product of the coherence factor and an exponential with the strong-phased difference can be expressed as [105]

$$\kappa_D^{K\pi\pi^0} e^{-i\delta_D^{K\pi\pi^0}} = \frac{\int \mathcal{A}_{K^-\pi^+\pi^0}(\mathbf{x})\mathcal{A}_{K^+\pi^-\pi^0}(\mathbf{x})\,\mathrm{d}\mathbf{x}}{\sqrt{\int |\mathcal{A}_{K^-\pi^+\pi^0}(\mathbf{x})|^2\,\mathrm{d}\mathbf{x}}\sqrt{\int |\mathcal{A}_{K^+\pi^-\pi^0}(\mathbf{x})|^2\,\mathrm{d}\mathbf{x}}} \tag{6.2}$$

where $\mathcal{A}_{K^\pm\pi^\mp\pi^0}(\mathbf{x})$ is the amplitude of the decay of $D^0 \to K^\pm\pi^\mp\pi^0$ at a point $\mathbf{x}$ in phase space. The integrals of Equation 6.2 are evaluated over all of phase space. Experimentally, a selection efficiency, $\varepsilon(\mathbf{x})$, is also present. Thus, Equation 6.2 is modified as

$$\kappa_D^{K\pi\pi^0}\, e^{-i\delta_D^{K\pi\pi^0}} = \frac{\int \varepsilon(\mathbf{x})^2 \mathcal{A}_{K^-\pi^+\pi^0}(\mathbf{x})\mathcal{A}_{K^+\pi^-\pi^0}(\mathbf{x})\,\mathrm{d}\mathbf{x}}{\sqrt{\int \varepsilon(\mathbf{x})^2|\mathcal{A}_{K^-\pi^+\pi^0}(\mathbf{x})|^2\,\mathrm{d}\mathbf{x}}\sqrt{\int \varepsilon(\mathbf{x})^2|\mathcal{A}_{K^+\pi^-\pi^0}(\mathbf{x})|^2\,\mathrm{d}\mathbf{x}}}. \tag{6.3}$$

This expression, makes the assumption that the selection efficiency is identical regardless of the charge of the D daughters. At CLEO-c, there is a uniform selection efficiency across the Dalitz plot. However, this may not be the case at LHCb, resulting in the introduction of a systematic bias if the external values from CLEO-c are used. We must thus determine the impact, if any, of this bias.

6.4.1 Efficiency Effects

For D meson decays in which there are more than two final state particles, multiple intermediate resonances are possible, with varying amplitudes. The MINT software package [106] is commonly used for amplitude analyses at CLEO-c and LHCb and is thus used in this study to assess the possible bias in the effective coherence factor and mean strong-phase difference with a variety of Dalitz plot efficiencies. MINT is used to generate the decays using amplitude models for the CF and DCS decays of $D^0 \to K^-\pi^+\pi^0$ and $\overline{D}^0 \to K^-\pi^+\pi^0$. These models originate from studies at CLEO-c [107] and BaBar [108] for the CF and DCS decays, respectively.

To determine the effect of the selection across the Dalitz plot, a MC sample of $B^\mp \to [K^\mp\pi^\pm\pi^0]_D h^\mp$ decays is used. After the application of the selection and MC truth association, approximately 1500 candidates remain. The Dalitz distribution of this sample is presented in Figure 6.11(a). Since the MC was generated uniformly across the D decay phase space, we can assume that the selection efficiency is proportional to the yield of events at a particular point on the Dalitz plot.

The MINT package requires the use of an efficiency histogram. However, given the low statistics of Figure 6.11, a coarse binning would be required in order to avoid large statistical fluctuations in adjacent bins. As a result, a kernel estimation PDF [110] is applied to the MC candidates to interpolate a 100×100 bin efficiency histogram, as presented in Figure 6.11(b).

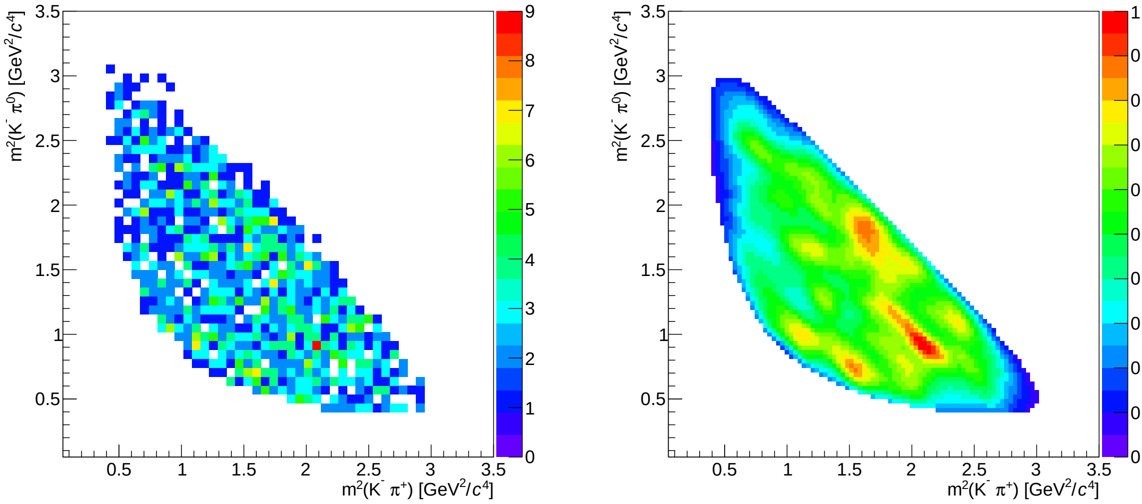

(a) Original MC distribution

(b) Extrapolated distribution

Figure 6.11: Dalitz plot distribution of MC events. The x axis represents the Dalitz variable of the products of the masses of the kaon and charged pion (from the D candidate). Similarly, the y axis is the product of the masses of the kaon and π^0 candidate. The units of the z scale are number of events. The original distributions from MC as well as the extrapolated distribution from the kernel estimation PDFs are presented [109].

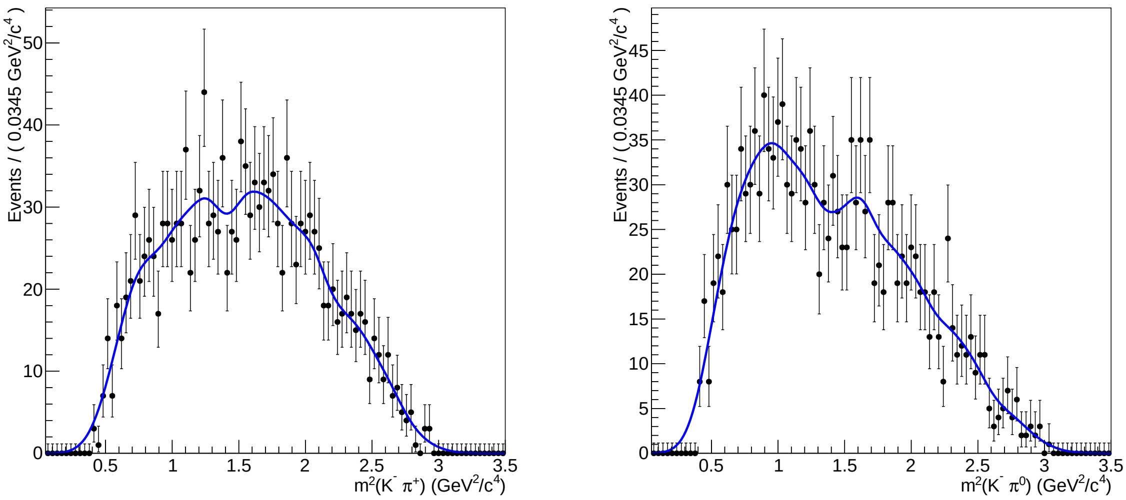

(a) PDF for the $m^2(K^-\pi^+)$ Dalitz variable

(b) PDF for the $m^2(K^-\pi^0)$ Dalitz variable

Figure 6.12: The kernel estimation PDFs (in blue) fit to the MC events. These are projections of the two Dalitz variables [109].

The kernel estimation PDF fit to MC is displayed in Figure 6.12. The efficiency histogram is normalised such that the bin with the largest number of entries corresponds to 100%. Using this efficiency profile, the effective coherence factor and average strong-phase difference are measured to be 0.879 and 163.6°, respectively. If one assumes a perfect efficiency profile of 100% across the Dalitz plane, these values differ by 0.003 and 0.3°, respectively, implying that the efficiency profile has a minimal effect on these two parameters.

There are two potential sources of uncertainty associated to this procedure. The first is the interpolation used. Studies using a coarse 20×20 histogram of MC events were performed and $\kappa_D^{K\pi\pi^0}$ and $\delta_D^{K\pi\pi^0}$ measured. The second potential source relates to the small sample size of MC used. In order to measure this effect, the bootstrap method is used where 1000 new samples are generated and the spread in the central value of the observables is taken as their uncertainty. For both of these sources of uncertainty, the measured effects on $\kappa_D^{K\pi\pi^0}$ and $\delta_D^{K\pi\pi^0}$ are much less than the uncertainties reported [44] and are thus deemed negligible.

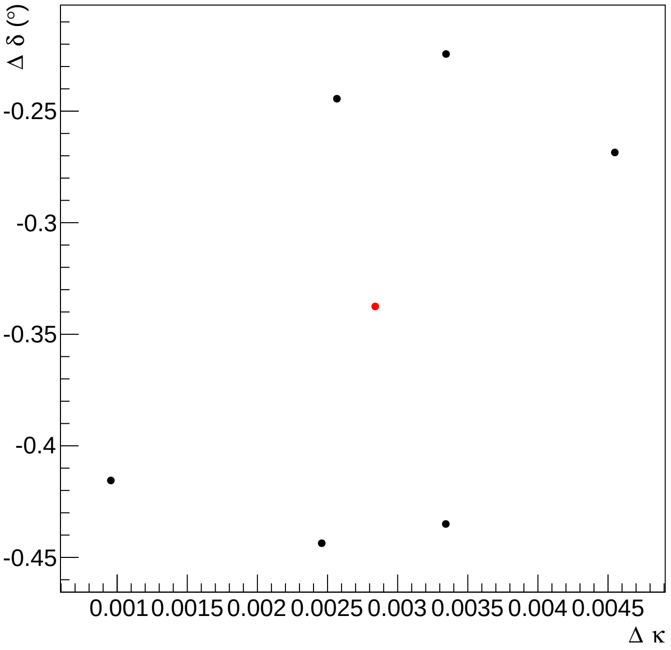

Figure 6.13: Difference between coherence factor and strong-phase difference with and without LHCb efficiency effects for variations in the DCS model. The red point indicates the default model and the black points represent models where components have been varied. All points have uncertainties smaller than the chosen scale [109].

It is also possible that the components of the decay model used may contribute an uncertainty. These components in the DCS model are varied by ±5% and the effect on $\kappa_D^{K\pi\pi^0}$ and $\delta_D^{K\pi\pi^0}$ are measured with and without the effects of selection efficiency. The results of these variations are presented in Figure 6.13. The red point represents the base model and the black points represent model instances where the components of the DCS model are varied. The $\Delta\delta$ and $\Delta\kappa$ values reported relate to the measured differences between the case of the LHCb efficiency profile and that of a 100% efficiency profile. The largest change in $\kappa_D^{K\pi\pi^0}$ is an increase of approximately 0.0045 and the largest noted change in $\delta_D^{K\pi\pi^0}$ is a decrease of approximately 0.45°. These differences are significantly less than the reported experimental uncertainties of ±0.07 for $\kappa_D^{K\pi\pi^0}$ and $^{+20^\circ}_{-14^\circ}$ for $\delta_D^{K\pi\pi^0}$ [44].

We thus conclude that any potential bias due to differences in selection efficiency are much less than the experimental uncertainties on $\kappa_D^{K\pi\pi^0}$ and $\delta_D^{K\pi\pi^0}$ and can be neglected. A similar study for the $F_+^{\pi\pi\pi^0}$ and $F_+^{KK\pi^0}$ parameters is performed using decay models developed at BaBar [37, 111]. The effects of selection efficiency are also found to be negligible compared to the experimental uncertainty [109]. As a result, $\kappa_D^{K\pi\pi^0}$, $\delta_D^{K\pi\pi^0}$, $F_+^{KK\pi^0}$ and $F_+^{\pi\pi\pi^0}$ are all used as external inputs with their experimental uncertainties as depicted in the CLEO-c analyses [31, 105] without any additional corrections or uncertainties assigned.

6.5 Constraints on r_B, δ_B and γ

Using the equations from Section 1.5.2, the extracted *CP* observables from this analysis are used to gain insight into the parameters of interest (POI) r_B, δ_B and γ. This is done through the use of the gammadini framework [112], a software package designed to perform a combined measurement of γ by incorporating experimental results from a multitude of analyses with observables sensitive to γ.

In this exercise, only the DK observables of $A_K^{K\pi\pi^0}$, $A_{\text{ADS}(K)}^{K\pi\pi^0}$, $R_{\text{ADS}(K)}^{K\pi\pi^0}$, $A_{\text{qGLW}(K)}^{\pi\pi\pi^0}$, $A_{\text{qGLW}(K)}^{KK\pi^0}$, $R_{\text{qGLW}}^{\pi\pi\pi^0}$ and $R_{\text{qGLW}}^{KK\pi^0}$ are used. This is because the $D\pi$ modes have reduced interference effects compared to the DK modes and thus it is expected that they will not be sensitive to the relevant parameters of interest at the current level of experimental precision. Furthermore, in this analysis, the full effects of $D^0-\overline{D}^0$ mixing are ignored. While this is a reasonable assumption with negligible effects in the DK sector, it has been demonstrated to have a significant effect in the $D\pi$ sector [38,39].

Explicitly, the expressions from Section 1.5.2 that are used in this calculation are:

$$R^{K\pi\pi^0}_{\mathrm{ADS}(K)} = \frac{(r_B)^2 + (r_D^{K\pi\pi^0})^2 + 2\kappa_D^{K\pi\pi^0} r_B r_D^{K\pi\pi^0}\cos(\delta_B + \delta_D^{K\pi\pi^0})\cos\gamma}{1 + (r_B r_D^{K\pi\pi^0})^2 + 2\kappa_D^{K\pi\pi^0} r_B r_D^{K\pi\pi^0}\cos(\delta_B - \delta_D^{K\pi\pi^0})\cos\gamma}, \tag{6.4}$$

$$A^{K\pi\pi^0}_{\mathrm{ADS}(K)} = \frac{2\kappa_D^{K\pi\pi^0} r_B r_D^{K\pi\pi^0}\sin(\delta_B + \delta_D^{K\pi\pi^0})\sin\gamma}{(r_B)^2 + (r_D^{K\pi\pi^0})^2 + 2\kappa_D^{K\pi\pi^0} r_B r_D^{K\pi\pi^0}\cos(\delta_B + \delta_D^{K\pi\pi^0})\cos\gamma}, \tag{6.5}$$

$$A^{K\pi\pi^0}_{K} = \frac{2\kappa_D^{K\pi\pi^0} r_B r_D^{K\pi\pi^0}\sin(\delta_B - \delta_D^{K\pi\pi^0})\sin\gamma}{1 + (r_B r_D^{K\pi\pi^0})^2 + 2\kappa_D^{K\pi\pi^0} r_B r_D^{K\pi\pi^0}\cos(\delta_B - \delta_D^{K\pi\pi^0})\cos\gamma}, \tag{6.6}$$

$$A^{KK\pi^0}_{\mathrm{qGLW}(K)} = \frac{2\left(2F_+^{KK\pi^0} - 1\right) r_B \sin\delta_B \sin\gamma}{1 + (r_B)^2 + 2\left(2F_+^{KK\pi^0} - 1\right) r_B \cos\delta_B \cos\gamma}, \tag{6.7}$$

$$A^{\pi\pi\pi^0}_{\mathrm{qGLW}(K)} = \frac{2\left(2F_+^{\pi\pi\pi^0} - 1\right) r_B \sin\delta_B \sin\gamma}{1 + (r_B)^2 + 2\left(2F_+^{\pi\pi\pi^0} - 1\right) r_B \cos\delta_B \cos\gamma}, \tag{6.8}$$

$$R^{KK\pi^0}_{\mathrm{qGLW}} = 1 + (r_B)^2 + 2\left(2F_+^{KK\pi^0} - 1\right) r_B \cos\delta_B \cos\gamma, \tag{6.9}$$

$$R^{\pi\pi\pi^0}_{\mathrm{qGLW}} = 1 + (r_B)^2 + 2\left(2F_+^{\pi\pi\pi^0} - 1\right) r_B \cos\delta_B \cos\gamma, \tag{6.10}$$

where $\kappa_D^{K\pi\pi^0}$ is the coherence factor, $\delta_D^{K\pi\pi^0}$ is the average strong-phase difference and F_+ are the CP fractions; all of these values have been measured using CLEO-c data. The parameter $r_D^{K\pi\pi^0}$ is the absolute ratio of suppressed to favoured $D \to K\pi\pi^0$ decays. In order to obtain a constraint on $r_D^{K\pi\pi^0}$, we invoke the use of the ratio of suppressed to favoured time integrated branching fractions,

$$\begin{aligned} \frac{\mathcal{B}(D^0 \to K^+\pi^-\pi^0)}{\mathcal{B}(D^0 \to K^-\pi^+\pi^0)} = \left(r_D^{K\pi\pi^0}\right)^2 \Big[1 - \left(y/r_D^{K\pi\pi^0}\right)\kappa_D^{K\pi\pi^0}\cos\delta_D^{K\pi\pi^0} \\ + \left(x/r_D^{K\pi\pi^0}\right)\kappa_D^{K\pi\pi^0}\sin\delta_D^{K\pi\pi^0} + \left(x^2 + y^2\right)/2\left(r_D^{K\pi\pi^0}\right)^2 \Big], \end{aligned} \tag{6.11}$$

where x and y are D^0–$\overline{D}^0$ mixing parameters [23] and the $D \to K\pi\pi^0$ branching fractions are taken from the Particle Data Group [2].

Using Equations 6.4 to 6.11, the results from the analysis and the relevant external inputs, we perform a χ^2 minimisation fit. This fit result corresponds to the global χ^2 minimum. Once the global minimum has been identified, one can then explore the sensitivity to the POIs, r_B, δ_B and γ, by calculating the χ^2 as a function of POI. The difference between this χ^2 value and that of the global minimum, $\Delta\chi^2$, quantifies the confidence in the global minimum. This relationship is expressed in Equation 6.12.

$$\Delta\chi^2(r_B, \delta_B, \gamma) = -2\ln L(r_B, \delta_B, \gamma) = [\vec{x}_{\text{meas}} - \vec{x}_{\text{away}}]^T \mathbf{V^{-1}} [\vec{x}_{\text{meas}} - \vec{x}_{\text{away}}] \tag{6.12}$$

Here, $\vec{x}_{\text{meas}}$ is a vector of the measured observables while $\vec{x}_{\text{away}}(r_B, \delta_B, \gamma)$ is a vector of the corresponding values when calculated using the parameters of interest at a location away from the global minimum. The matrix $\mathbf{V}$ is the covariance matrix between the observables.

In practice, $\Delta\chi^2$ is calculated for a variety of values of the three POIs by performing a scan across the parameters. In this analysis, 2D likelihood ($\Delta\chi^2$) scans are performed with 200 steps for each POI. In Figure 6.14, such a plot is presented for r_B vs γ with the 1σ and 2σ contours illustrated in light blue and dark blue, respectively. The current best measurement of these values from LHCb [38] is represented by a point on the plot and it lies completely within the 1σ contour. Given the shape of this 1σ contour, from this distribution, there are no useful constraints placed on the preferred value of γ. However, r_B is constrained to 0.11 ± 0.03 at the 1σ level.

Figure 6.15 presents the 2D likelihood scan of δ_B vs γ. Once again, the best LHCb measurement of these values is indicated by the marker. This point, which lies just outside the the 1σ band, is compatible with the likelihood scan from the analysis. No useful bounds are placed on δ_B.

Overall, other than the limits placed on r_B, no useful additional information on the observables δ_B and γ are obtained using the decay modes from this analysis. However, this is the first time the decay modes in question have ever been used for the extraction of γ or either of the other POIs.

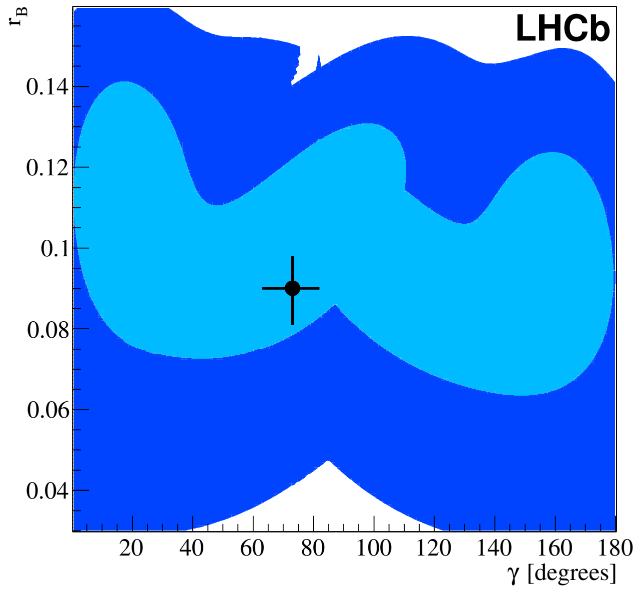

Figure 6.14: A 2D likelihood scan of r_B vs γ using the DK observables from this analysis and experimental inputs from CLEO-c. The light blue and dark blue areas correspond to the 1σ and 2σ bands, respectively. The marker corresponds to the current best LHCb measurement of these parameters.

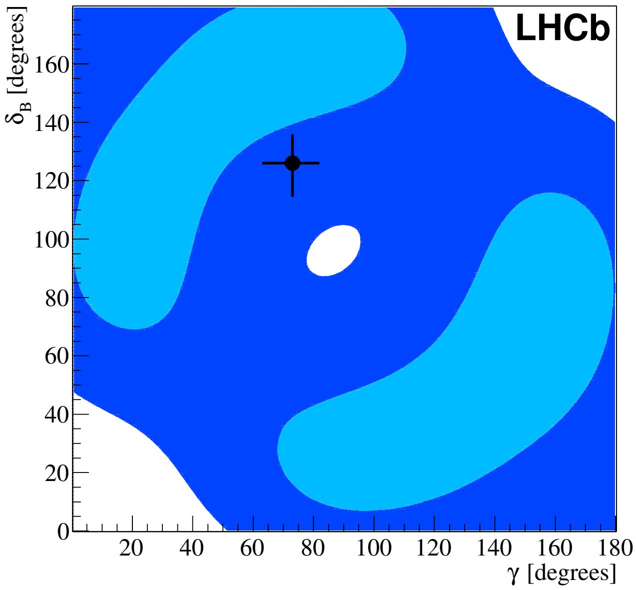

Figure 6.15: A 2D likelihood scan of δ_B vs γ using the DK observables from this analysis and experimental inputs from CLEO-c. The light blue and dark blue areas correspond to the 1σ and 2σ bands, respectively. The marker corresponds to the current best LHCb measurement of these parameters.

Chapter 7

Conclusions and Future Outlook

Improving the precision of the CKM angle γ is one of the core physics objectives of LHCb. In this thesis, an analysis of *CP* violation in $B^{\mp} \to DK^{\mp}$ and $B^{\mp} \to D\pi^{\mp}$ decays is presented, where the D meson is reconstructed in the final states of $K^{\mp}\pi^{\pm}\pi^{0}$, $\pi^{\mp}K^{\pm}\pi^{0}$, $\pi^{+}\pi^{-}\pi^{0}$ and $K^{+}K^{-}\pi^{0}$. The analysis was performed using 3.0 fb^{-1} of LHCb data collected in 2011 and 2012. From the decay modes of interest, through the use of a simultaneous fit to the data, *CP* observables are extracted. This is the first time that these decay modes have been analysed at LHCb and the first time at this experiment that D decay modes which include a π^{0} meson in the final state have been used in a b-physics measurement.

The *CP* observables of this analysis are measured to be

$$
\begin{aligned}
A^{K\pi\pi^0}_{\mathrm{ADS}(K)} &= -0.20 \pm 0.27 \pm 0.04 \\
A^{K\pi\pi^0}_{\mathrm{ADS}(\pi)} &= 0.44 \pm 0.19 \pm 0.01 \\
A^{KK\pi^0}_{\mathrm{qGLW}(K)} &= 0.30 \pm 0.20 \pm 0.02 \\
A^{\pi\pi\pi^0}_{\mathrm{qGLW}(K)} &= 0.054 \pm 0.091 \pm 0.011 \\
A^{KK\pi^0}_{\mathrm{qGLW}(\pi)} &= -0.030 \pm 0.040 \pm 0.005 \\
A^{\pi\pi\pi^0}_{\mathrm{qGLW}(\pi)} &= -0.016 \pm 0.020 \pm 0.004 \\
A^{K\pi\pi^0}_{K} &= 0.010 \pm 0.026 \pm 0.005 \\
R^{K\pi\pi^0}_{\mathrm{ADS}(K)} &= 0.0140 \pm 0.0047 \pm 0.0021 \\
R^{K\pi\pi^0}_{\mathrm{ADS}(\pi)} &= 0.00235 \pm 0.00049 \pm 0.00006 \\
R^{KK\pi^0}_{\mathrm{qGLW}} &= 0.95 \pm 0.22 \pm 0.05 \\
R^{\pi\pi\pi^0}_{\mathrm{qGLW}} &= 0.98 \pm 0.11 \pm 0.05 \\
A_{\mathrm{Prod}} &= -0.0008 \pm 0.0055 \pm 0.0050,
\end{aligned}
$$

where the first uncertainty is statistical and the second is systematic. The results for $A^{K\pi\pi^0}_{\mathrm{ADS}(K)}$, $A^{K\pi\pi^0}_{\mathrm{ADS}(\pi)}$, $A^{\pi\pi\pi^0}_{\mathrm{qGLW}(K)}$, $A^{K\pi\pi^0}_{K}$, $R^{K\pi\pi^0}_{\mathrm{ADS}(K)}$, $R^{K\pi\pi^0}_{\mathrm{ADS}(\pi)}$ are all compatible with previous measurements [35–37] but are more precise. Furthermore, this analysis marks the first time that the observables $A^{KK\pi^0}_{\mathrm{qGLW}(K)}$, $A^{KK\pi^0}_{\mathrm{qGLW}(\pi)}$, $A^{\pi\pi\pi^0}_{\mathrm{qGLW}(\pi)}$, $R^{KK\pi^0}_{\mathrm{qGLW}}$ and $R^{\pi\pi\pi^0}_{\mathrm{qGLW}}$ have been measured. When analysed in the context of underlying physics, these results display consistency with prior LHCb measurements. The measurement of A_{Prod} is also consistent with similar LHCb measurements [34, 103]; its value is in agreement with zero asymmetry and has larger uncertainties than prior measurements, but demonstrates the viability of performing B^+/B^- production asymmetry measurements using high-yield decay modes with low rates of *CP* violation.

Within the current experimental precision, no evidence of *CP* violation is obtained. However, this analysis obtains a first observation of the decays $B^{\mp} \to [\pi^{\mp}K^{\pm}\pi^0]_D\pi^{\mp}$ and

$B^{\mp} \to [K^+K^-\pi^0]_D\pi^{\mp}$ at the 5.3σ and greater than 10σ levels, respectively, and first evidence of the decay $B^{\mp} \to [K^+K^-\pi^0]_D K^{\mp}$ at a significance of 4.5σ. These results have been published in Reference [113].

The analysis is statistically limited and, thus, the precision of the measurements will increase when more data are collected and analysed. For the LHC's Run II, it is estimated that an additional 6 fb^{-1} of data will be collected by LHCb at a centre-of-mass energy of 13 TeV. Furthermore, during this period, it is expected that the BES III experiment [114] will make improvements to the measurements of $\kappa_D^{K\pi\pi^0}$, $\delta_D^{K\pi\pi^0}$, $F_+^{\pi\pi\pi^0}$ and $F_+^{KK\pi^0}$. If we assume that the $B^{\pm}$ production cross-section scales linearly with the increase in collision energy and that the new BES III measurements will improve the precision on the external inputs by a factor of two, we can perform the same 2D scans for the parameters r_B, δ_B and γ, as done in Section 6.5. In all cases, the systematic uncertainties are, conservatively, assumed to be unchanged. These scans are presented in Figure 7.1, where the central values of the experimental inputs are idealised based on the world's best measurements of their constituent parameters.

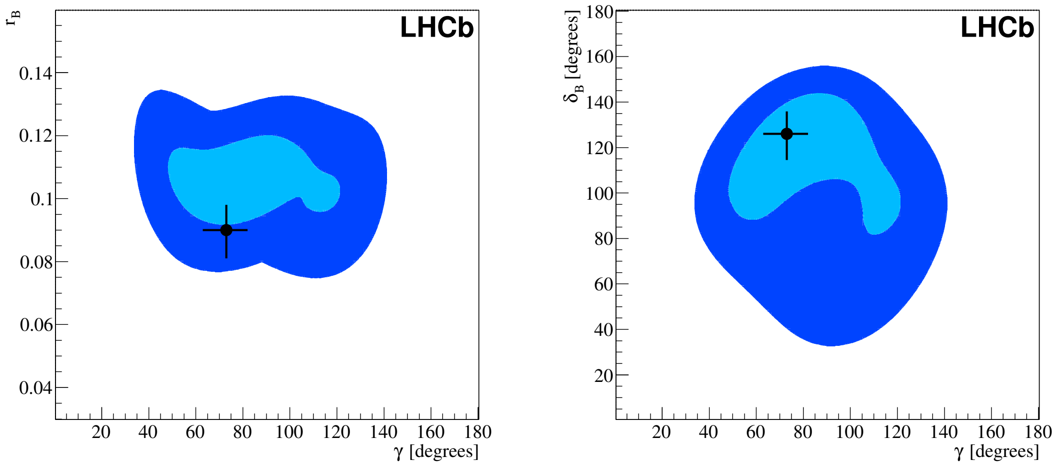

(a) r_B vs γ

(b) δ_B vs γ

Figure 7.1: A 2D likelihood scan of r_B vs γ and δ_B vs γ using the DK observables with uncertainties estimated from the LHC Run II. The light blue and dark blue areas correspond to the 1σ and 2σ bands, respectively. The marker corresponds to the current best LHCb measurement of these parameters.

Compared to Figures 6.14 and 6.15, the improvement these new 2D plots show with respect to the three parameters of interest is particularly striking. The angle γ, under these assumptions for LHCb Run II, using the decay modes of interest of this thesis, can be measured to within an uncertainty of 30°. Furthermore, using these same assumptions, we may also estimate whether the decays of $B^{\mp} \to [K^+K^-\pi^0]_D K^{\mp}$ and $B^{\mp} \to [\pi^{\mp}K^{\pm}\pi^0]_D K^{\mp}$ will be observed after the completion of Run II. The reduced statistical uncertainties imply that the $B^{\mp} \to [K^+K^-\pi^0]_D K^{\mp}$ decay will be observed at the 7.3σ level, while the $B^{\mp} \to [\pi^{\mp}K^{\pm}\pi^0]_D K^{\mp}$ decay will be observed at approximately the 6.2σ significance level.

After the LHC's Run II, the LHCb detector will be upgraded, including a change to a full software trigger. If we assume that 50 fb^{-1} of data will be collected at $\sqrt{s} = 14$ TeV and the new trigger will have double the efficiency of the current one, the 2D scans of Figure 7.2 are obtained. These figures assume the same systematic uncertainties on the observables as the current analysis.

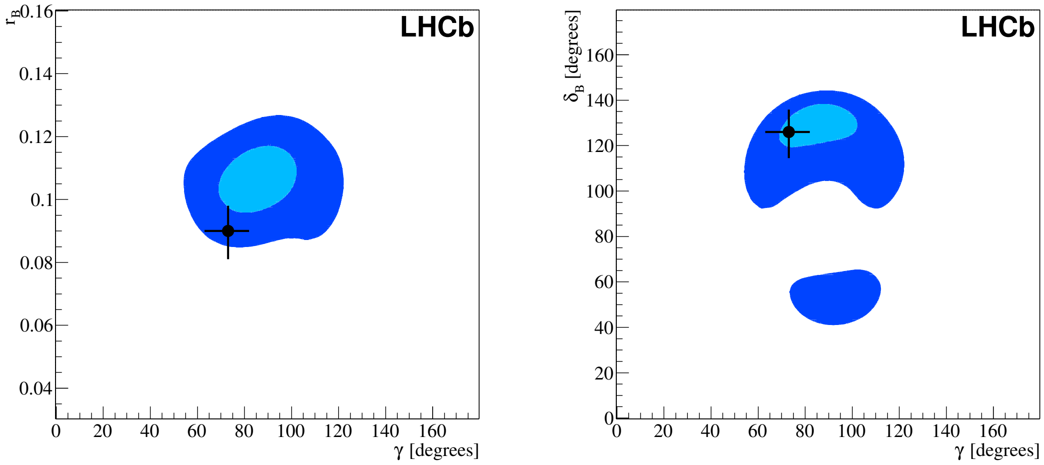

(a) r_B vs γ

(b) δ_B vs γ

Figure 7.2: A 2D likelihood scan of r_B vs γ and δ_B vs γ using the DK observables with uncertainties estimated from the LHCb upgrade. The light blue and dark blue areas correspond to the 1σ and 2σ bands, respectively. The marker corresponds to the current best LHCb measurement of these parameters.

As expected, the 1σ and 2σ contours are further reduced with the uncertainty on γ reduced to approximately 16°.

Overall, the decay modes of this analysis have been successfully used for the determination of CP observables. However, the greatest contribution of these decay modes will come when they are added to the LHCb γ combination. The $K\pi\pi^0$ modes are another ADS mode in the suite of decays for LHCb's study of *CP* violation, but no quasi-GLW modes are currently used as part of the combination, hence the $\pi\pi\pi^0$ and $KK\pi^0$ decays should be a welcome addition.

Undoubtedly, as more data is collected by LHCb and new decay modes are added to its γ combination, the precision on γ will improve. Perhaps, such improvements will ultimately answer the question of whether the CKM Unitarity Triangle is described solely by the SM or if some New Physics is present.

Appendix A

BDT Training Variables

The signal and background distributions of the BDT variables from the training input samples are presented in this Appendix. In all cases, the signal distributions are in blue and the background distributions are in red. The y-axis is in arbitrary units.

The variable names in Figures A.1 to A.5 use a different nomenclature than that of Table 3.2. A conversion between the two sets of names is provided in Table A.1.

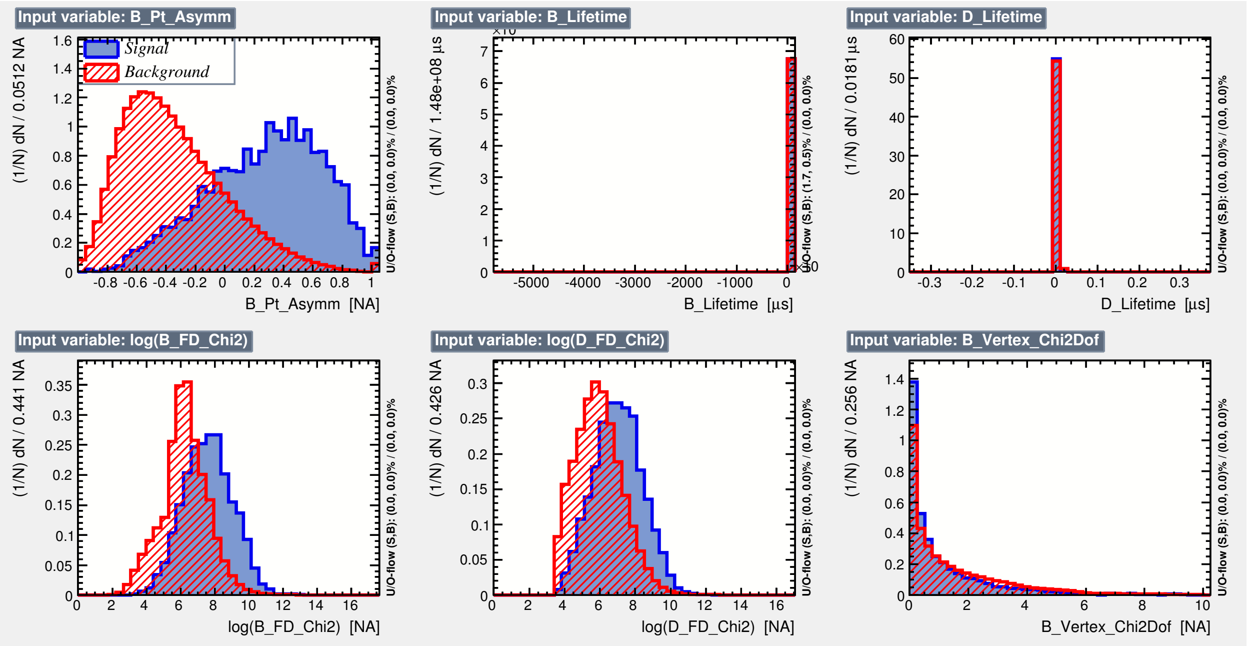

Figure A.1: Signal and background distributions for several BDT training variable inputs. Signal distributions are in blue and the background distributions are in red.

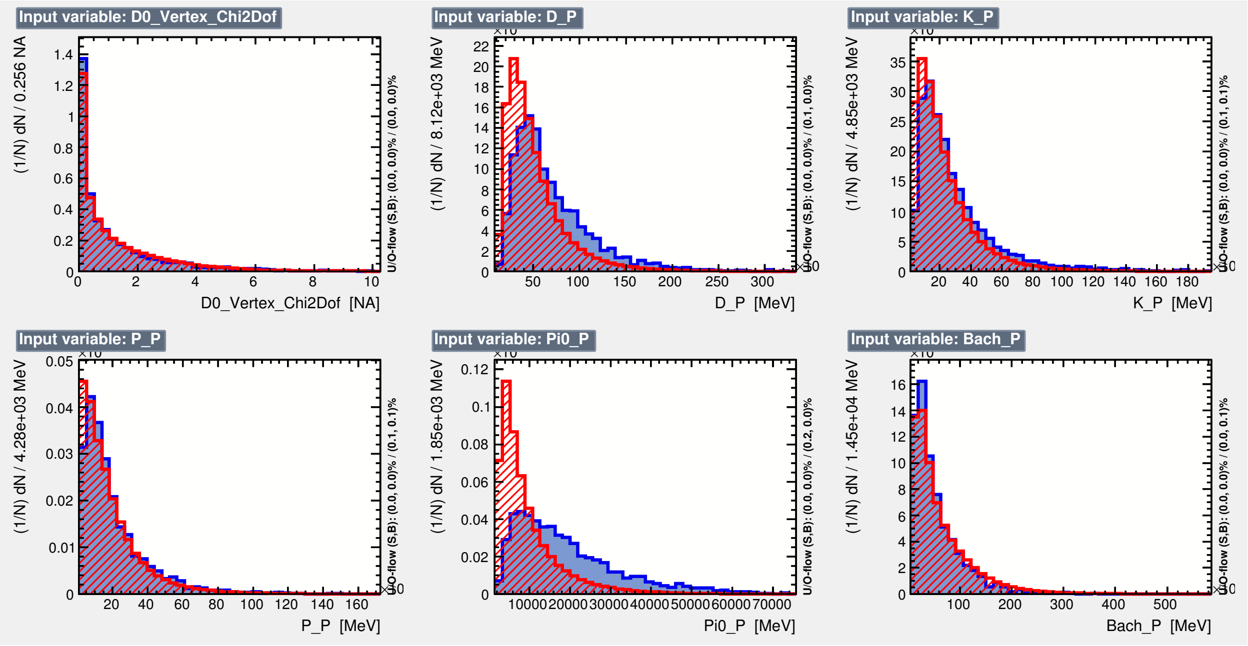

Figure A.2: Signal and background distributions for several BDT training variable inputs. Signal distributions are in blue and the background distributions are in red.

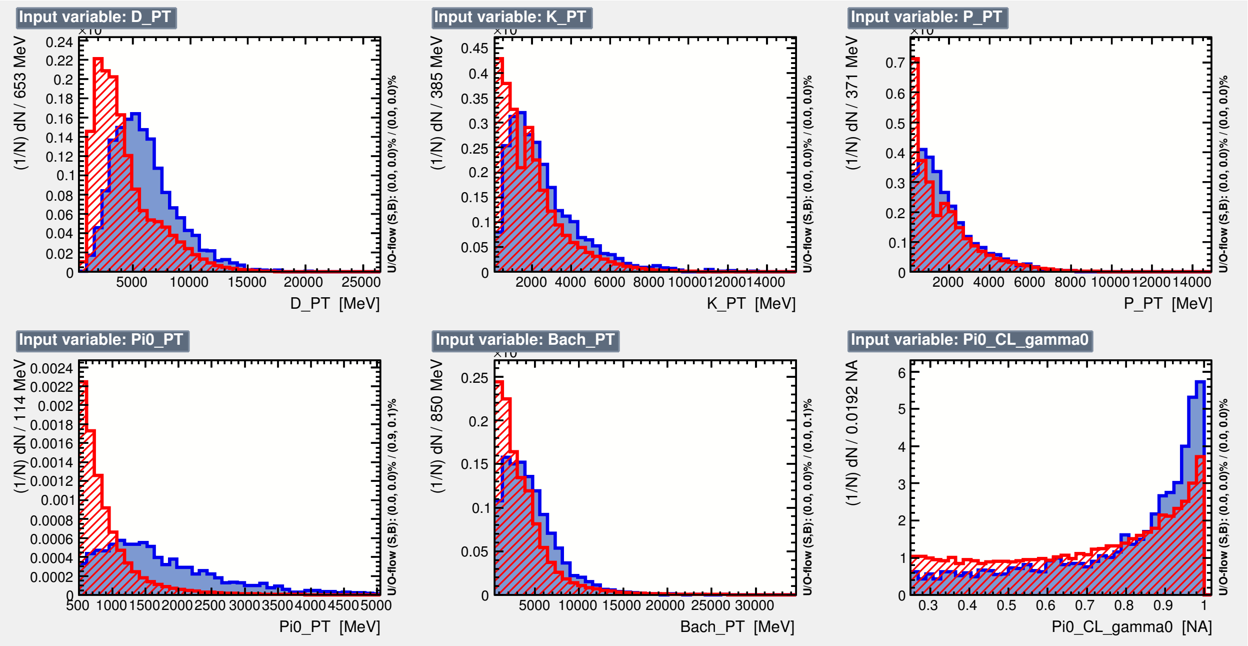

Figure A.3: Signal and background distributions for several BDT training variable inputs. Signal distributions are in blue and the background distributions are in red.

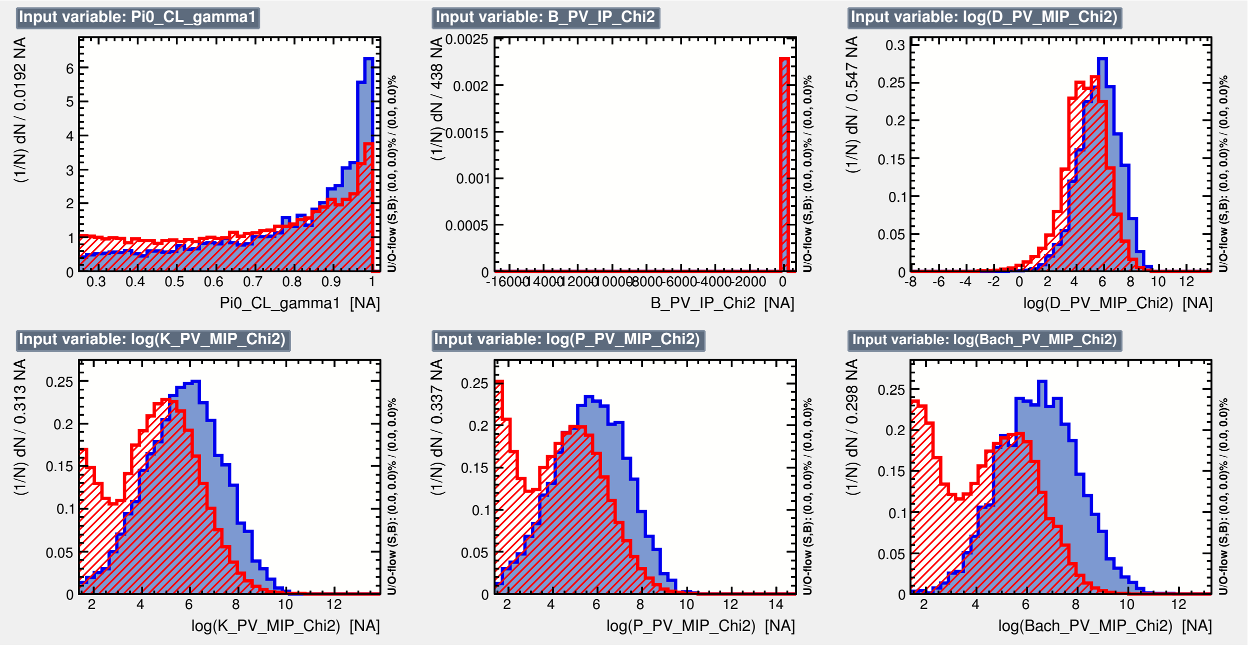

Figure A.4: Signal and background distributions for several BDT training variable inputs. Signal distributions are in blue and the background distributions are in red.

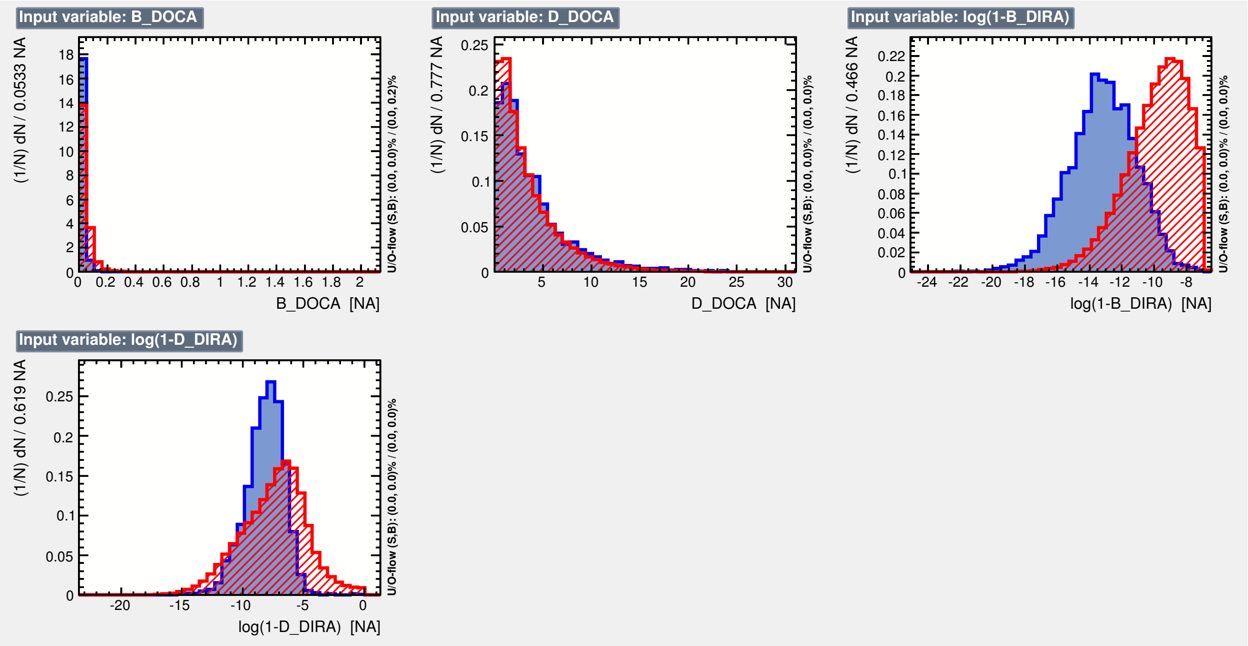

Figure A.5: Signal and background distributions for several BDT training variable inputs. Signal distributions are in blue and the background distributions are in red.

Table A.1: Conversion between the variable names used in Table 3.2 and Figures A.1 to A.5.

Variable Name in Main Text	Variable Name in Appendix Plots
B p_{T} asymmetry	B_Pt_Asymm
π^0 p_{T}	Pi0_PT
$\log(1 - B$ DIRA)	log(1-B_DIRA)
log(Bachelor Min χ^2_{IP})	log(Bach_PV_MIP_Chi2)
π^0 p	Pi0_P
Bachelor p	Bach_P
$\log(B\ \chi^2_{\mathrm{FD}})$	log(B_FD_Chi2)
$\log(D$ Min $\chi^2_{\mathrm{IP}})$	log(D_PV_MIP_Chi2)
D p	D_P
D p_{T}	D_PT
Bachelor p_{T}	Bach_PT
$\log(1 - D$ DIRA)	log(1-B_DIRA)
$\log(\pi^{\pm}$ Min $\chi^2_{\mathrm{IP}})$	log(P_PV_MIP_Chi2)
$\log(K^{\pm}$ Min $\chi^2_{\mathrm{IP}})$	log(K_PV_MIP_Chi2)
$K^{\pm}$ p_{T}	K_PT
$\log(D\ \chi^2_{\mathrm{FD}})$	log(D_FD_Chi2)
D τ	D_Lifetime
Photon CL 1	Pi0_CL_gamma0
B vertex χ^2	B_Vertex_Chi2Dof
Photon CL 2	Pi0_CL_gamma1
$K^{\pm}$ p	K_P
B τ	B_Lifetime
$\pi^{\pm}$ p	P_P
D Max DOCA	D_DOCA
D vertex χ^2	D0_Vertex_Chi2Dof
B Min χ^2_{IP}	B_PV_IP_Chi2
$\pi^{\pm}$ p_{T}	P_PT
B Max DOCA	B_DOCA

Appendix B

Systematic Uncertainty Contributions

A full presentation of the systematic uncertainty contributions for each of the analysis observables is given in this Appendix. For each observable, the histograms representing the measured value of the observable under the variations for the 15 different sources of systematic uncertainty are presented. The RMS values of these histograms are the systematic uncertainty contributions for each systematics source that have been collected in Table 5.7. The nomenclature used in the plots is defined in Section 5.5.

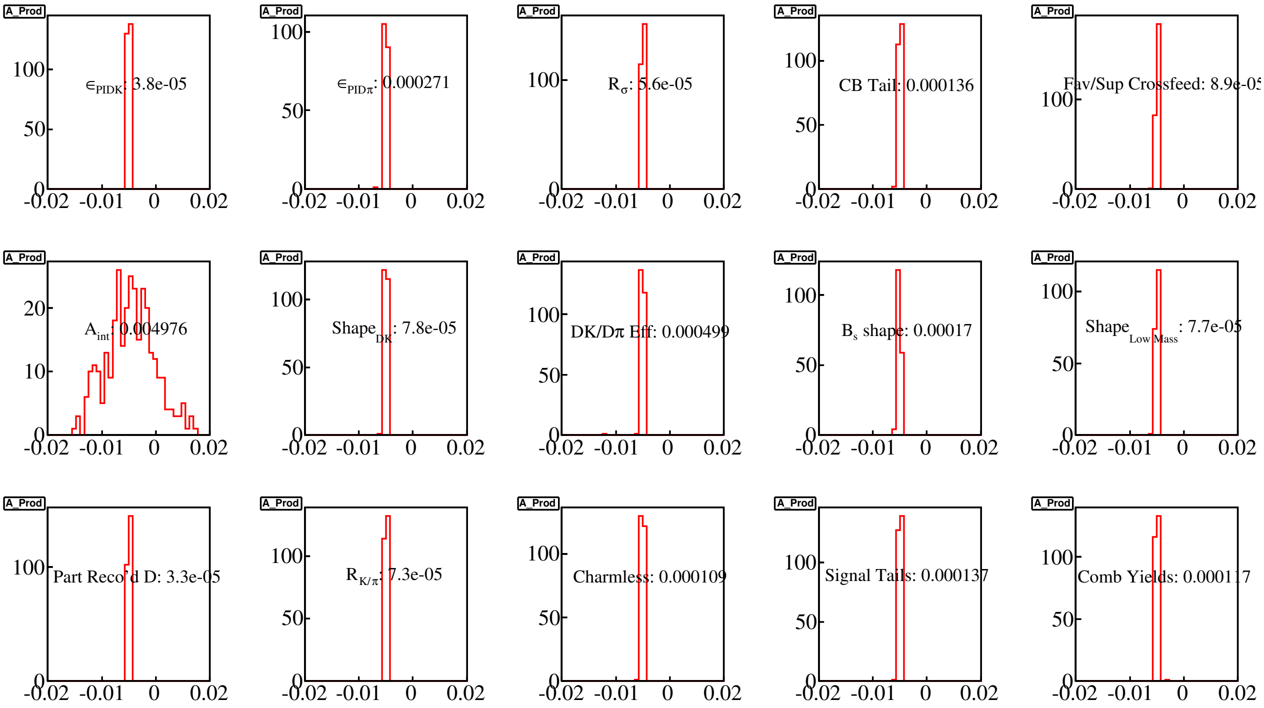

Figure B.1: Variation in the fit result of A_{Prod} due to the Gaussian variation of the systematic errors.

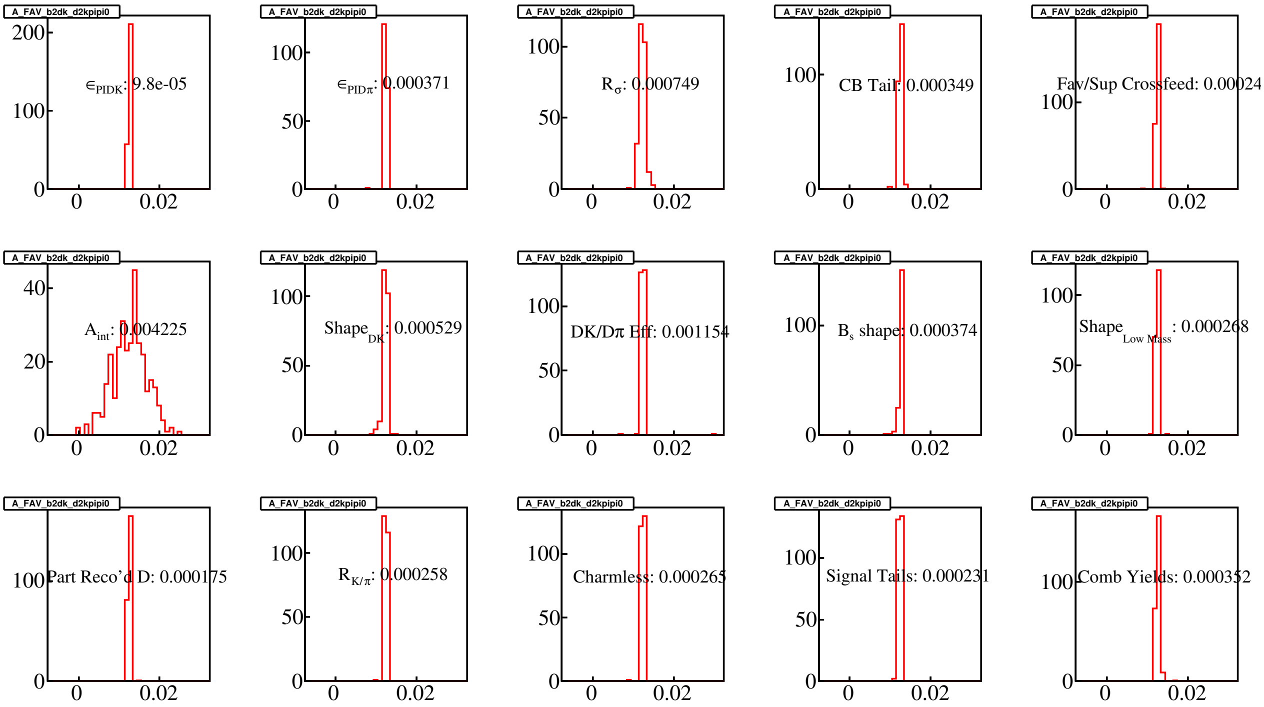

Figure B.2: Variation in the fit result of $A_K^{K\pi\pi^0}$ due to the Gaussian variation of the systematic errors.

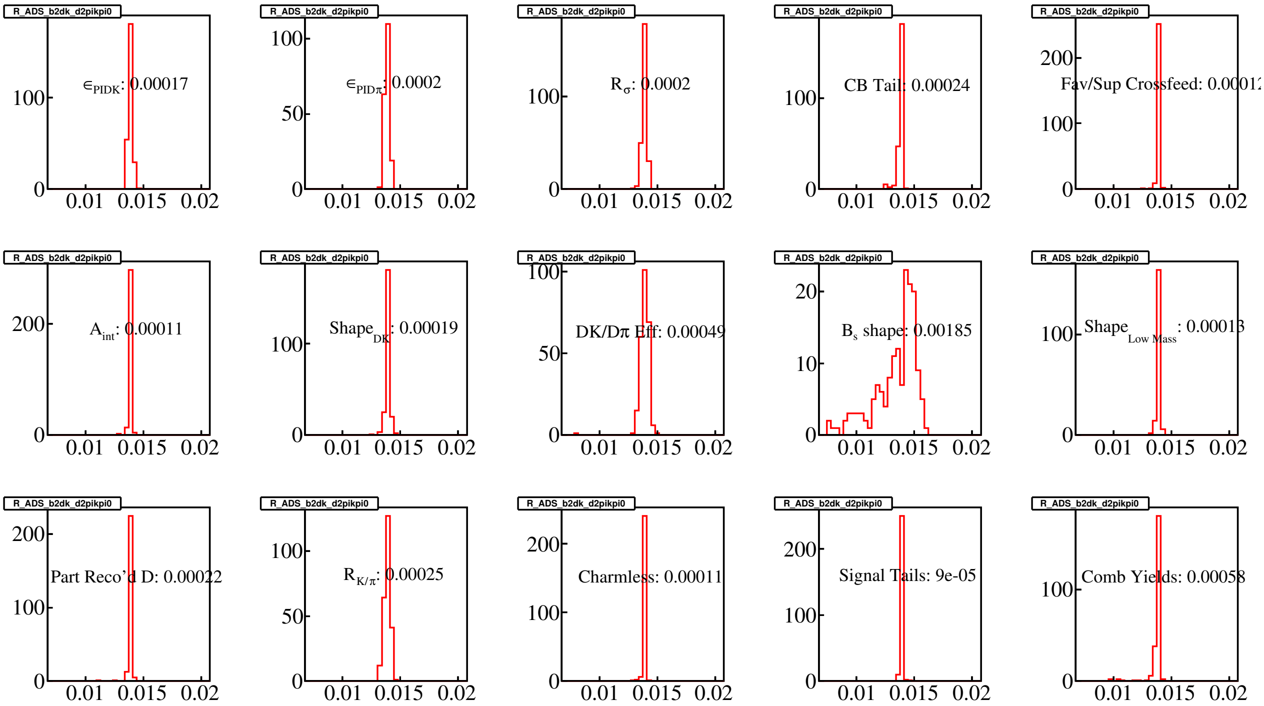

Figure B.3: Variation in the fit result of $R_{\mathrm{ADS}(K)}$ due to the Gaussian variation of the systematic errors.

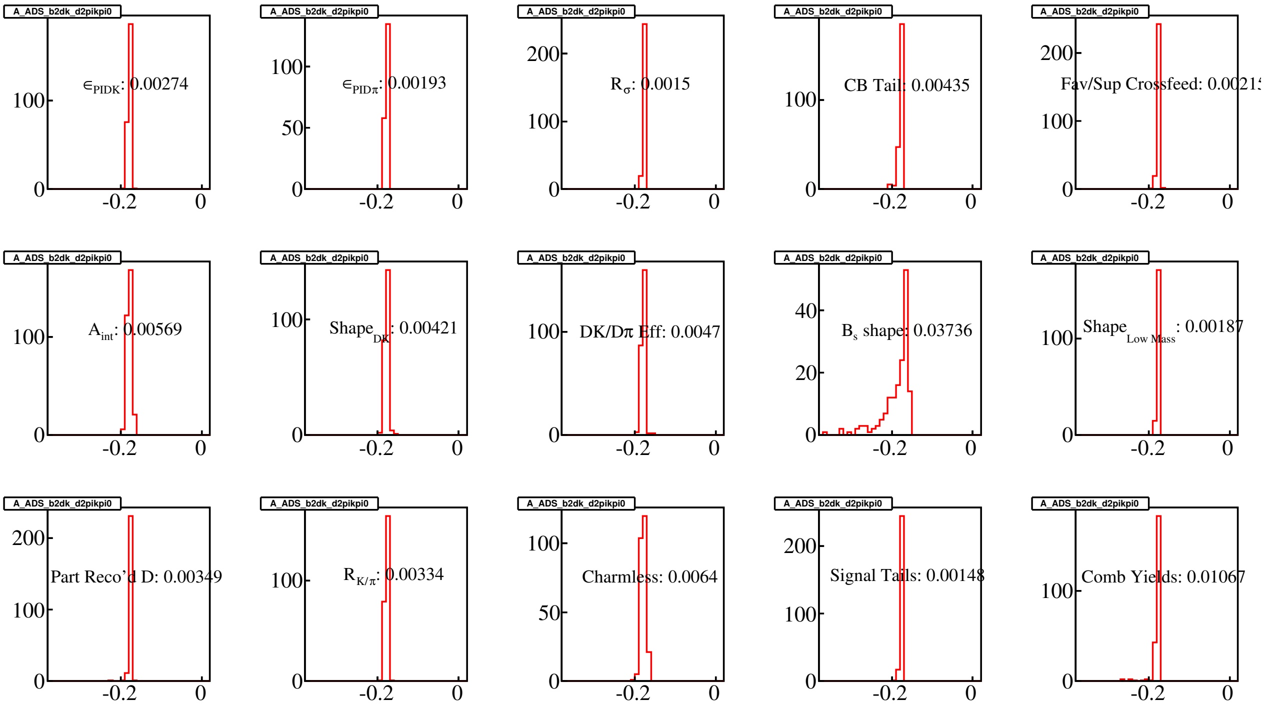

Figure B.4: Variation in the fit result of $A_{\mathrm{ADS}(K)}$ due to the Gaussian variation of the systematic errors.

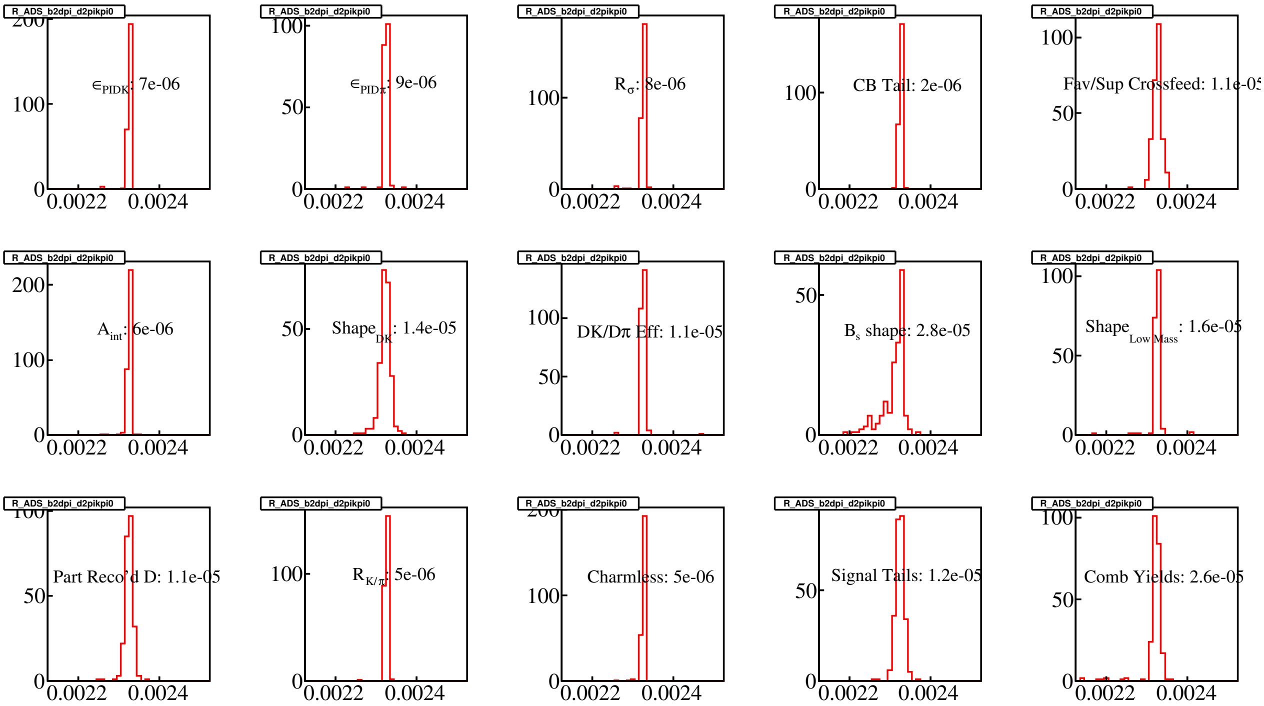

Figure B.5: Variation in the fit result of $R_{\mathrm{ADS}(\pi)}$ due to the Gaussian variation of the systematic errors.

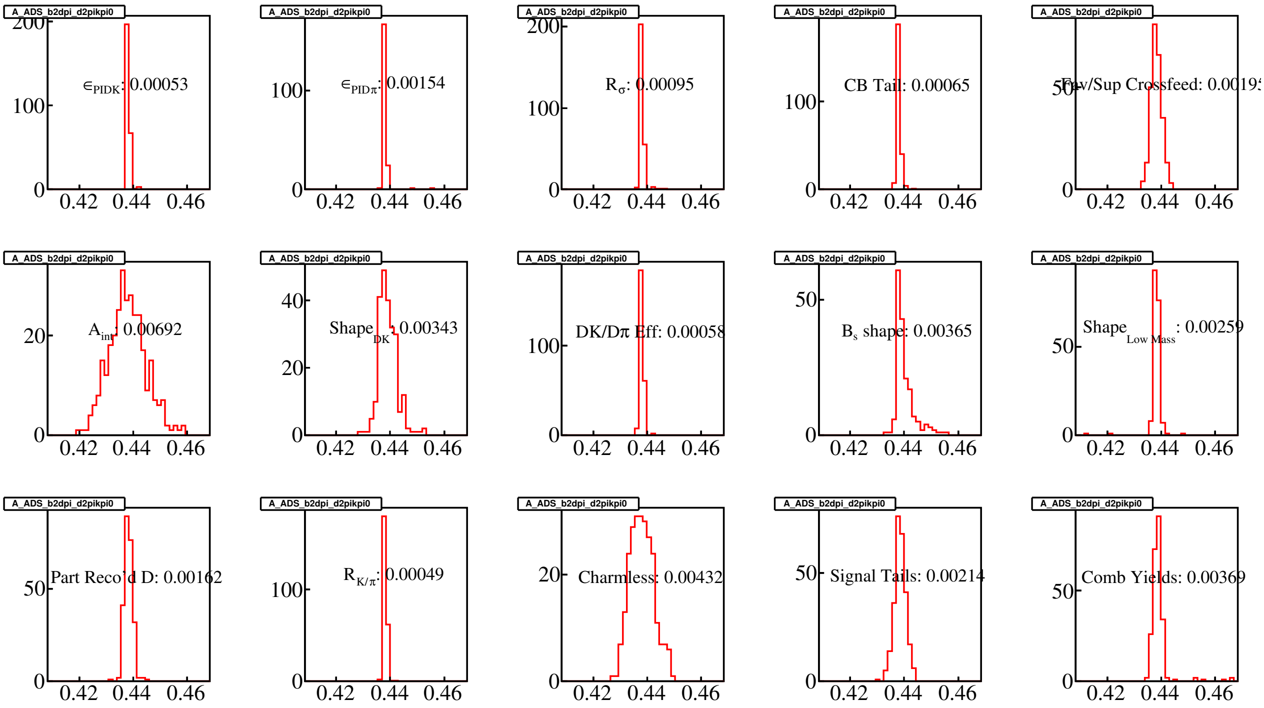

Figure B.6: Variation in the fit result of $A_{\mathrm{ADS}(\pi)}$ due to the Gaussian variation of the systematic errors.

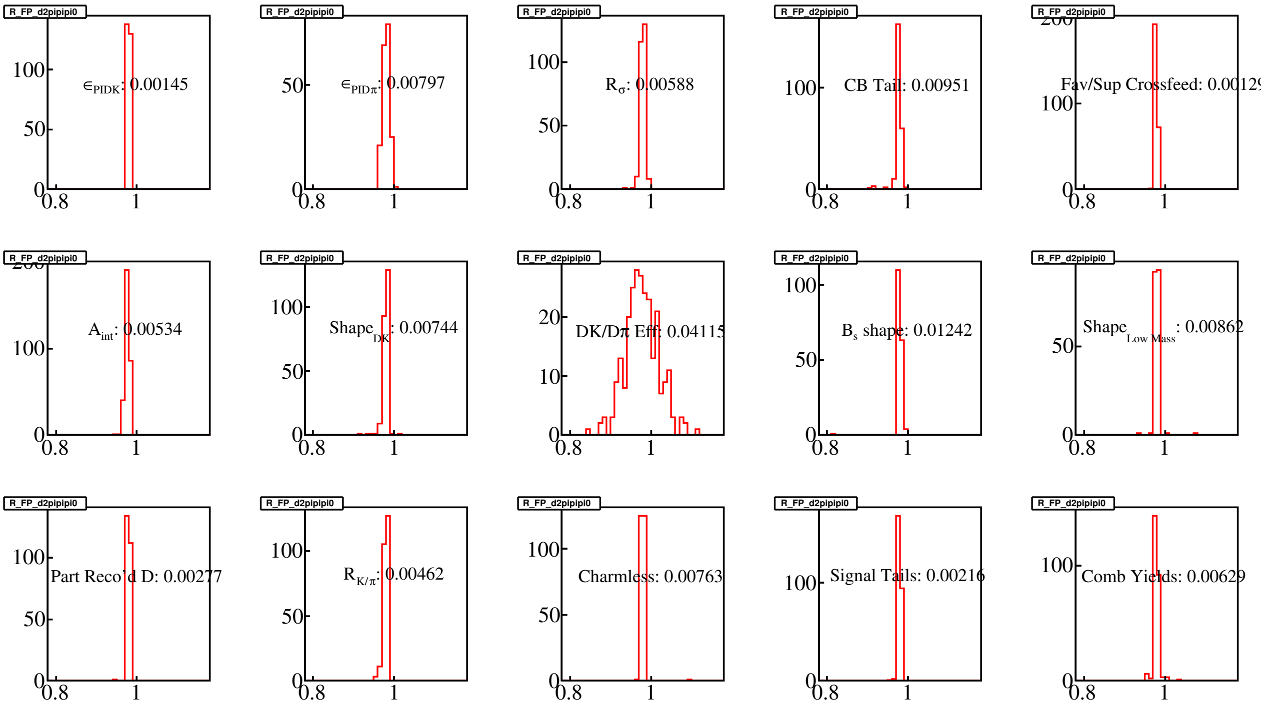

Figure B.7: Variation in the fit result of $R^{\pi\pi\pi^0}_{\mathrm{qGLW}}$ due to the Gaussian variation of the systematic errors.

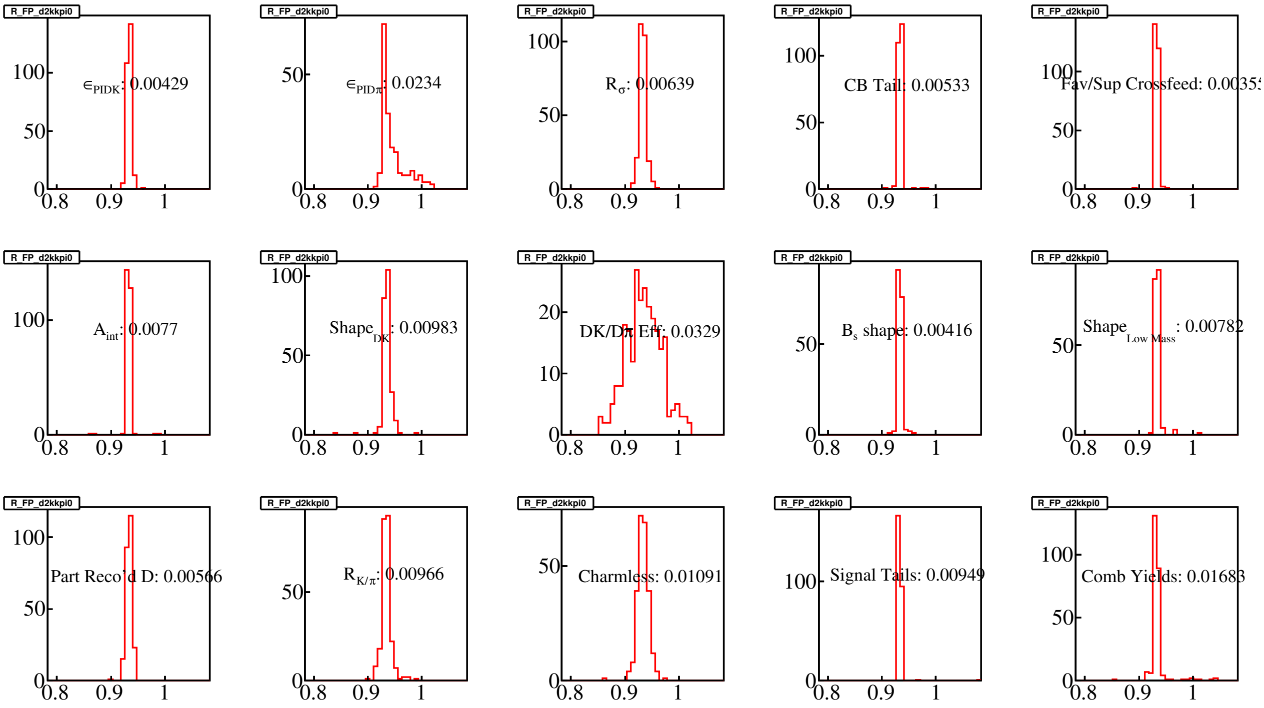

Figure B.8: Variation in the fit result of $R^{KK\pi^0}_{\mathrm{qGLW}}$ due to the Gaussian variation of the systematic errors.

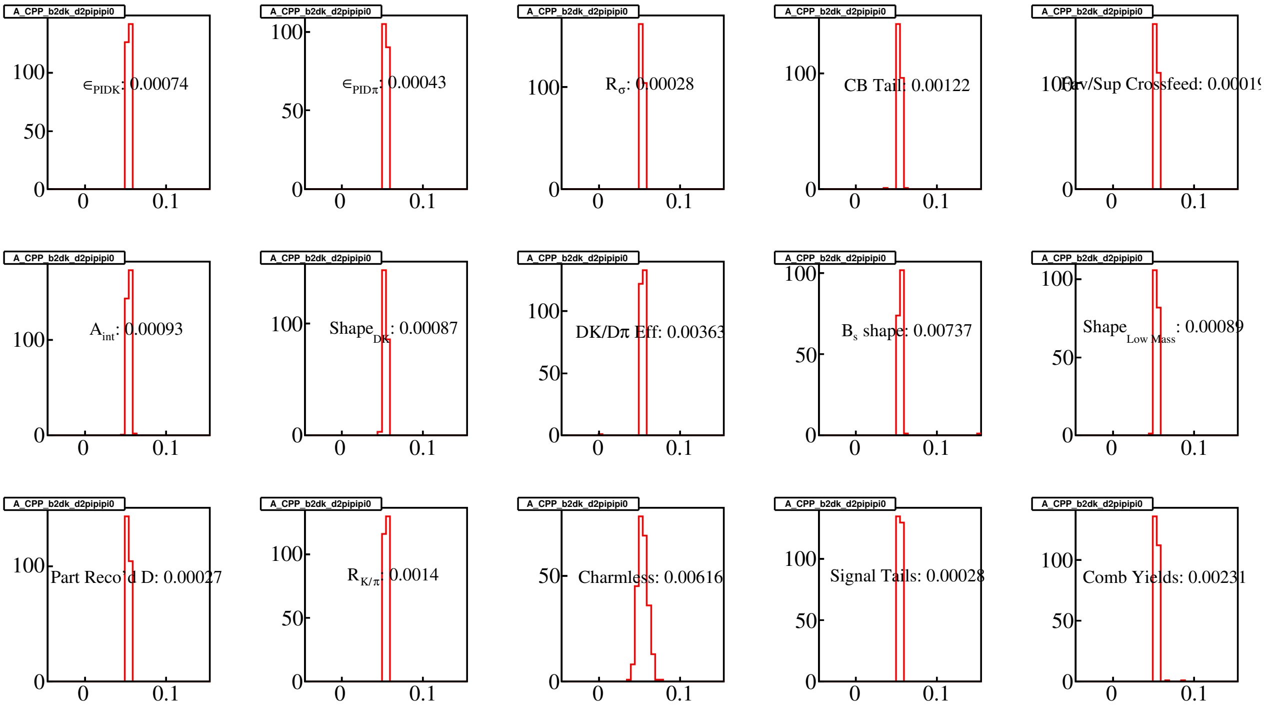

Figure B.9: Variation in the fit result of $A^{\pi\pi\pi^0}_{\mathrm{qGLW}(K)}$ due to the Gaussian variation of the systematic errors.

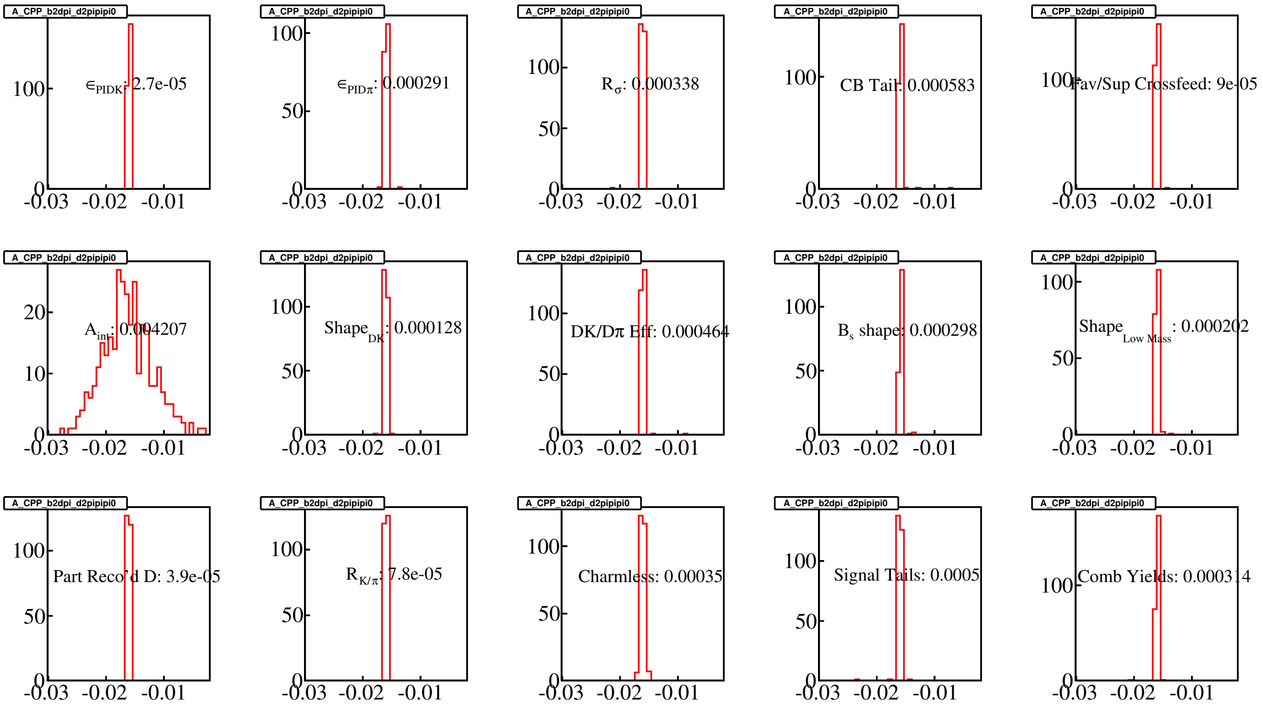

Figure B.10: Variation in the fit result of $A^{\pi\pi\pi^0}_{\mathrm{qGLW}(\pi)}$ due to the Gaussian variation of the systematic errors.

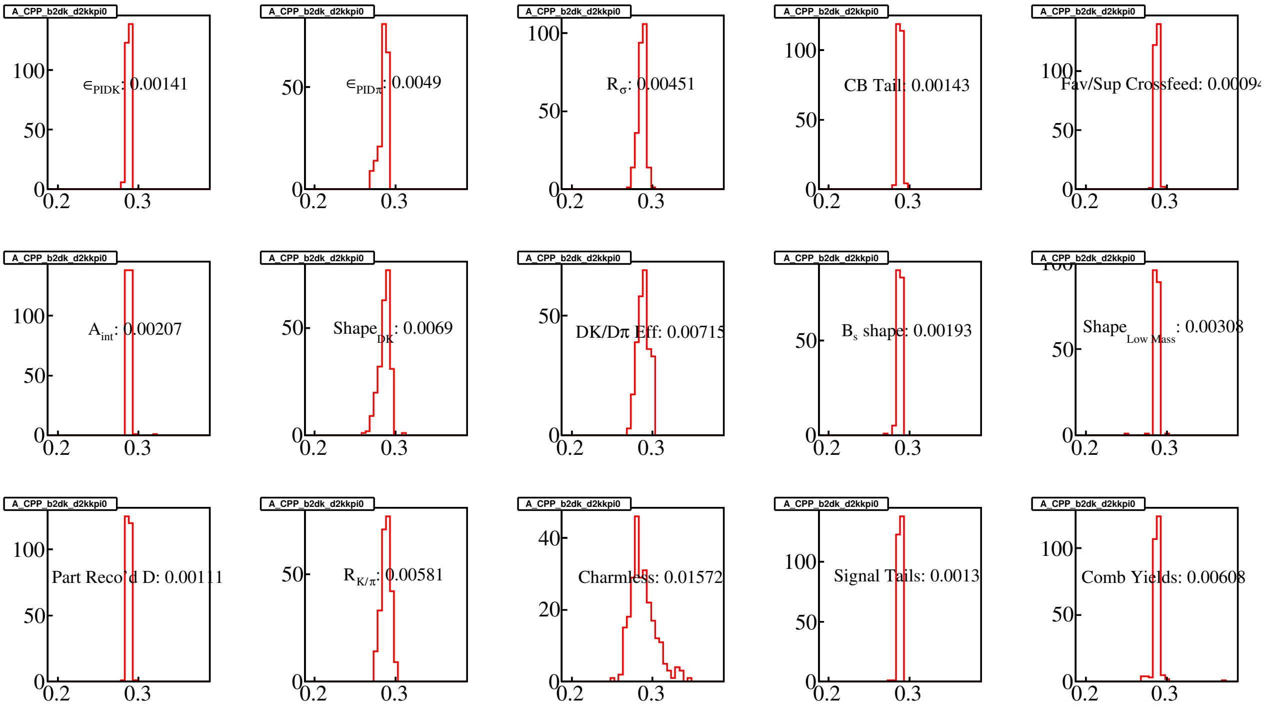

Figure B.11: Variation in the fit result of $A^{KK\pi^0}_{\mathrm{qGLW}(K)}$ due to the Gaussian variation of the systematic errors.

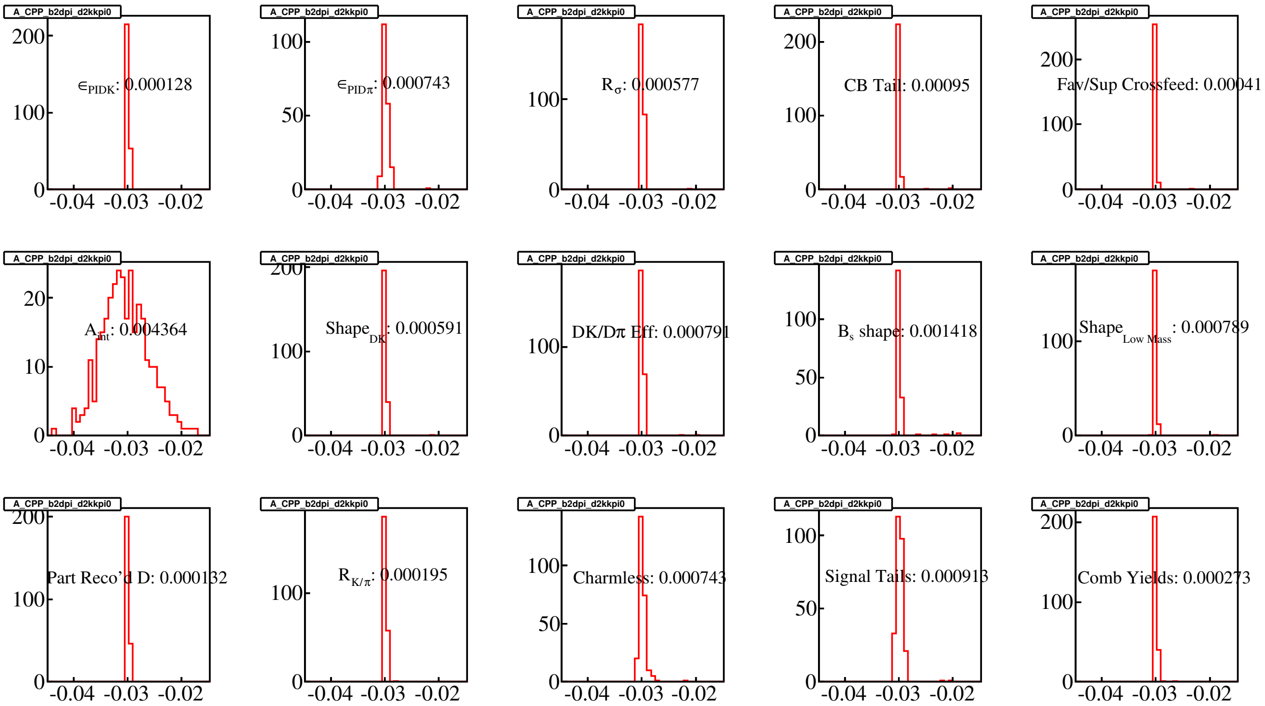

Figure B.12: Variation in the fit result of $A_{\mathrm{qGLW}(\pi)}^{KK\pi^0}$ due to the Gaussian variation of the systematic errors.

Bibliography

[1] D. J. Griffiths, Introduction to Elementary Particles, Wiley, Hoboken, 1987.

[2] Particle Data Group, K. Olive et al., *Review of particle physics*, Chin. Phys. C **38** (2014) 090001.

[3] C. Burgess and G. Moore, The Standard Model: A Primer, Cambridge University Press, Cambridge, 2007.

[4] M. E. Peskin and D. V. Schroeder, An Introduction to Quantum Field Theory, Westview, 1995.

[5] B. Martin and G. Shaw, Particle Physics, Wiley, Toronto, 3rd ed., 2008.

[6] Belle Collaboration, S. K. Choi et al., *Observation of a resonance-like structure in the $\pi^{\pm}\psi'$ mass distribution in exclusive $B \to K\pi^{\pm}\psi'$ decays*, Phys. Rev. Lett. **100** (2008) 142001, `arXiv:0708.1790`.

[7] LHCb Collaboration, R. Aaij et al., *Observation of the resonant character of the $Z(4430)^{-}$ state*, Phys. Rev. Lett. **112** (2014) 222002, `arXiv:1404.1903`.

[8] LHCb Collaboration, R. Aaij et al., *Observation of $J/\psi p$ resonances consistent with pentaquark states in $\Lambda\_b^0 \to J/\psi K^{-}p$ decays*, `arXiv:1507.03414`.

[9] P. Higgs, *Broken Symmetries and the Masses of Gauge Bosons*, Phys. Rev. Lett. **13** (1964) 508.

[10] F. Englert and R. Brout, *Broken Symmetry and the Mass of Gauge Vector Mesons*, Phys. Rev. Lett **13** (1964) 321.

[11] C. S. Wu et al., *Experimental Test of Parity Conservation in Beta Decay*, Phys. Rev. **105** (1957) 1413.

[12] J. Christenson, J. Cronin, V. Fitch, and R. Turlay, *Evidence for the 2 π Decay of the K_2^0 Meson*, Phys. Rev. Lett. **13** (1964) 138.

[13] Belle, K. Abe et al., *Observation of large CP violation in the neutral B meson system*, Phys. Rev. Lett. **87** (2001) 091802, `arXiv:hep-ex/0107061`.

[14] LHCb, R. Aaij et al., *First observation of CP violation in the decays of B_s^0 mesons*, Phys. Rev. Lett. **110** (2013) 221601, `arXiv:1304.6173`.

[15] Belle Collaboration, A. Garmash et al., *Evidence for Large Direct CP Violation in* $B^{\pm} \to \rho(770)^0 K^{\pm}$ *from Analysis of Three-Body Charmless* $B^{\pm} \to K^{\pm}\pi^{\pm}\pi^{\pm}$ *Decays*, Phys. Rev. Lett. **96** (2006) 251803.

[16] N. Cabibbo, *Unitary Symmetry and Leptonic Decays*, Phys. Rev. Lett. **10** (1963) 531.

[17] M. Kobayashi and T. Maskawa, *CP-Violation in the Renormalizable Theory of Weak Interaction*, Prog. Theor. Phys. **49** (1973) 652.

[18] L.-L. Chau and W.-Y. Keung, *Comments on the Parameterization of the Kobayashi-Maskawa Matrix*, Phys. Rev. Lett. **53** (1984) 1802.

[19] L. Wolfenstein, *Parametrization of the Kobayashi-Maskawa Matrix*, Phys. Rev. Lett. **51** (1983) 1945.

[20] UT Fit Collaboration, A. Bevan et al., *UTFit Standard Model Fit*, `http://www.utfit.org/UTfit/ResultsSummer2014PostMoriondSM`, 2014.

[21] CKMfitter Group, J. Charles et al., *CP Violation and the CKM Matrix: Assessing the Impact of the Asymmetric B Factories*, Eur. Phys. J. **C41** (2005) 1.

[22] P. Gandini, Observation of CP violation in $B^{\mp} \to DK^{\mp}$ decays, PhD thesis, University of Oxford, 2012.

[23] Heavy Flavor Averaging Group (HFAG), Y. Amhis et al., *Averages of b-hadron, c-hadron, and* τ*-lepton properties as of summer 2014*, `arXiv:1412.7515`.

[24] M. Rama, *Effect of* $D - \overline{D}$ *mixing in the extraction of* γ *with* $B^- \to D^0 K^-$ *and* $B^- \to D^0 \pi^-$ *decays*, Phys. Rev. **D89** (2014) 014021, `arXiv:1307.4384`.

[25] UT fit Collaboration, A. Bevan et al., *UTFit gamma from trees*, `http://www.utfit.org/UTfit/GammaFromTreesPostMoriond2014`, 2014.

[26] M. Gronau and D. London, *How to determine all the angles of the unitarity triangle from* $B_d^0 \to DK_S^0$ *and* $B_s^0 \to D\phi$, Phys. Lett. **B253** (1991) 483.

[27] M. Gronau and D. Wyler, *On determining a weak phase from CP asymmetries in charged B decays*, Phys. Lett. **B265** (1991) 172.

[28] D. Atwood, I. Dunietz, and A. Soni, *Enhanced CP violation with* $B \to KD^0(\overline{D}^0)$ *modes and extraction of the CKM angle* γ, Phys. Rev. Lett. **78** (1997) 3257, `arXiv:hep-ph/9612433`.

[29] D. Atwood, I. Dunietz, and A. Soni, *Improved methods for observing CP violation in* $B^{\pm} \to KD$ *and measuring the CKM phase* γ, Phys. Rev. **D63** (2001) 036005, `arXiv:hep-ph/0008090`.

[30] A. Powell, Measuring the CKM Angle γ with $B^{\pm} \to DK^{\pm}$ Decays at LHCb and a Determination of the $D \to K\pi\pi\pi$ Coherence Factor at CLEO-c, PhD thesis, University of Oxford, 2009.

[31] M. Nayak et al., *First determination of the CP content of $D \to \pi^+\pi^-\pi^0$ and $D \to K^+K^-\pi^0$*, Phys. Lett. **B740** (2015) 1, `arXiv:1410.3964`.

[32] LHCb Collaboration, R. Aaij et al., *Search for CP violation in $D^+ \to \phi\pi^+$ and $D_s^+ \to K_S^0\pi^+$ decays*, JHEP **06** (2013) 112, `arXiv:1303.4906`.

[33] H. Gordon, R. Lambert, J. van Tilburg, and M. Vesterinen, *A Measurement of the $K\pi$ Detection Asymmetry*, LHCb-INT-2012-027, 2012.

[34] LHCb Collaboration, R. Aaij et al., *Measurements of the branching fractions and CP asymmetries of $B^\pm \to J/\psi\pi^\pm$ and $B^\pm \to \psi(2S)\pi^\pm$ decays*, Phys. Rev. **D85** (2012) 091105(R), `arXiv:1203.3592`.

[35] BaBar Collaboration, J. Lees et al., *Search for $b \to u$ transitions in $B^\pm \to [K^\mp\pi^\pm\pi^0]_D K^\pm$ decays*, Phys. Rev. **D84** (2011) 012002, `arXiv:1104.4472`.

[36] Belle Collaboration, M. Nayak et al., *Evidence for the suppressed decay $B^- \to DK^-$, $D \to K^+\pi^-\pi^0$*, Phys. Rev. **D88** (2013) 091104, `arXiv:1310.1741`.

[37] BaBar Collaboration, B. Aubert et al., *Measurement of CP violation parameters with a Dalitz plot analysis of $B^\pm \to D(\pi^+\pi^-\pi^0)\ K^\pm$*, Phys. Rev. Lett. **99** (2007) 251801, `arXiv:hep-ex/0703037`.

[38] LHCb Collaboration, *Improved constraints on γ: CKM2014 update*, LHCB-CONF-2014-004, 2014.

[39] LHCb Collaboration, R. Aaij et al., *A measurement of the CKM angle γ from a combination of $B^\pm \to Dh^\pm$ analyses*, Phys. Lett. **B726** (2013) 151, `arXiv:1305.2050`.

[40] BaBar Collaboration, J. Lees et al., *Observation of direct CP violation in the measurement of the Cabibbo-Kobayashi-Maskawa angle gamma with $B^\pm \to D^{(*)}K^{(*)\pm}$ decays*, Phys. Rev. **D87** (2013) 052015, `arXiv:1301.1029`.

[41] Belle Collaboration, K. Trabelsi, *Study of direct CP in charmed B decays and measurement of the CKM angle gamma at Belle*, `arXiv:1301.2033`.

[42] R. H. Dalitz, *Decay of τ mesons of known charge*, Phys. Rev. **94** (1954) 1046.

[43] R. Dalitz, *On the analysis of τ-meson data and the nature of the τ-meson*, The London, Edinburgh, and Dublin Philosophical Magazine and Journal of Science **44** (1953) 1068.

[44] J. Libby et al., *New determination of the $D^0 \to K^-\pi^+\pi^0$ and $D^0 \to K^-\pi^+\pi^+\pi^-$ coherence factors and average strong-phase differences*, Phys. Lett. **B731** (2014) 197, `arXiv:1401.1904`.

[45] S. Malde et al., *First determination of the CP content of $D \to \pi^+\pi^-\pi^+\pi^-$ and updated determination of the CP contents of $D \to \pi^+\pi^-\pi^0$ and $D \to K^+K^-\pi^0$*, Phys. Lett. **B747** (2015) 9, `arXiv:1504.05878`.

[46] CLEO Collaboration, N. Lowrey et al., *Determination of the* $D^0 \to K^-\pi^+\pi^0$ *and* $D^0 \to K^-\pi^+\pi^+\pi^-$ *coherence factors and average strong-phase differences using quantum-correlated measurements*, Phys. Rev. **D80** (2009) 031105, `arXiv:0903.4853`.

[47] L. Evans and P. Bryant, *LHC Machine*, JINST **3** (2008) S08001.

[48] P. Mouche. OPEN-PHO-ACCEL-2014-001-2, 2014.

[49] M. Lamont, *Status of the LHC*, J. Phys. Conf. Ser. **455** (2013) 012001.

[50] F. Follin and D. Jacquet, *Implementation and experience with luminosity levelling with offset beam*, CERN Yellow Report CERN-2014-004, 2014.

[51] R. Lindner. LHCb-PHO-GENE-2008-002-1, 2008.

[52] LHCb Collaboration, A. A. Alves Jr. et al., *The LHCb detector at the LHC*, JINST **3** (2008) S08005.

[53] P. Collins. `https://lhcb.web.cern.ch/lhcb/speakersbureau/html/Schematics/Luminosities_Run1.gif`, 2012.

[54] LHCb Collaboration, P. R. Barbosa-Marinho et al., LHCb VELO (VErtex LOcator): Technical Design Report, CERN, Geneva, 2001.

[55] R. Aaij et al., *Performance of the LHCb Vertex Locator*, JINST **9** (2014) 09007, `arXiv:1405.7808`.

[56] LHCb Collaboration, R. Aaij et al., *LHCb detector performance*, Int. J. Mod. Phys. **A30** (2015) 1530022, `arXiv:1412.6352`.

[57] LHCb Collaboration, S. Amato et al., LHCb magnet: Technical Design Report, CERN, Geneva, 2000.

[58] LHCb Collaboration, P. R. Barbosa-Marinho et al., LHCb Inner Tracker: Technical Design Report, CERN, Geneva, 2002.

[59] P. A. Cherenkov, *Visible emission of clean liquids by action of* γ *radiation*, Doklady Akademii Nauk SSSR **2** (1934) 451.

[60] M. Adinolfi et al., *Performance of the LHCb RICH detector at the LHC*, Eur. Phys. J. **C73** (2013) 2431, `arXiv:1211.6759`.

[61] LHCb Collaboration, S. Amato et al., LHCb Calorimeters: Technical Design Report, CERN, Geneva, 2000.

[62] LHCb Collaboration, P. R. Barbosa-Marinho et al., LHCb Muon System: Technical Design Report, CERN, Geneva, 2001.

[63] LHCb HLT Project, J. Albrecht, V. Gligorov, G. Raven, and S. Tolk, *Performance of the LHCb High Level Trigger in 2012*, J. Phys. Conf. Ser. **513** (2014) 012001, `arXiv:1310.8544`.

[64] R. Aaij et al., *The LHCb trigger and its performance in 2011*, JINST **8** (2013) P04022, `arXiv:1211.3055`.

[65] V. V. Gligorov, C. Thomas, and M. Williams, *The HLT inclusive B triggers*, LHCb-PUB-2011-016, 2011.

[66] V. V. Gligorov and M. Williams, *Efficient, reliable and fast high-level triggering using a bonsai boosted decision tree*, JINST **8** (2013) P02013.

[67] F. Alessio et al., *The LHCb Data Acquisition during LHC Run I*, J. Phys. Conf. Ser. **513** (2014) 012033.

[68] G. Barrand et al., *GAUDI – A software architecture and framework for building HEP data processing applications*, Computer Physics Communications **140** (2001) 45.

[69] M. Clemencic et al., *The LHCb simulation application, Gauss: Design, evolution and experience*, J. Phys. Conf. Ser. **331** (2011) 032023.

[70] T. Sjöstrand, S. Mrenna, and P. Skands, *A brief introduction to PYTHIA 8.1*, Comput. Phys. Commun. **178** (2008) 852, `arXiv:0710.3820`.

[71] I. Belyaev et al., *Handling of the generation of primary events in Gauss, the LHCb simulation framework*, J. Phys. Conf. Ser. **331** (2011) 032047.

[72] J. Pumplin et al., *New generation of parton distributions with uncertainties from global QCD analysis*, JHEP **07** (2002) 012, `arXiv:hep-ph/0201195`.

[73] D. J. Lange, *The EvtGen particle decay simulation package*, Nucl. Instrum. Meth. **A462** (2001) 152.

[74] Geant4 Collaboration, S. Agostinelli et al., *Geant4: A simulation toolkit*, Nucl. Instrum. Meth. **A506** (2003) 250.

[75] Geant4 Collaboration, J. Allison et al., *Geant4 developments and applications*, IEEE Trans. Nucl. Sci. **53** (2006) 270.

[76] LHCb Collaboration, *The Boole Project*, `http://lhcb-release-area.web.cern.ch/LHCb-release-area/DOC/boole/`.

[77] LHCb Collaboration, *The Moore Project*, `http://lhcb-release-area.web.cern.ch/LHCb-release-area/DOC/moore/`.

[78] LHCb Collaboration, *The Brunel Project*, `http://lhcb-release-area.web.cern.ch/LHCb-release-area/DOC/brunel/`.

[79] LHCb Collaboration, *The DaVinci Project*, `http://lhcb-release-area.web.cern.ch/LHCb-release-area/DOC/davinci/`.

[80] W. D. Hulsbergen, *Decay chain fitting with a Kalman filter*, Nucl. Instrum. Meth. **A552** (2005) 566, `arXiv:physics/0503191`.

[81] M. Kucharczyk, P. Morawski, and M. Witek, *Primary Vertex Reconstruction at LHCb*, LHCb-PUB-2014-044, 2014.

[82] F. Hampel et al., Robust Statistics: The Approach Based on Influence Functions, John Wiley & Sons, New York, 1986.

[83] LHCb Collaboration, R. Aaij et al., *Observation of CP violation in* $B^{\pm} \to DK^{\pm}$ *decays*, Phys. Lett. **B712** (2012) 203, `arXiv:1203.3662`.

[84] LHCb Collaboration, R. Aaij et al., *First observation and amplitude analysis of the* $B^{-} \to D^{+}K^{-}\pi^{-}$ *decay*, Phys. Rev. **D91** (2015) 092002, `arXiv:1503.02995`.

[85] LHCb Collaboration, *Stripping Stream Defnitions*, `https://twiki.cern.ch/twiki/bin/view/LHCb/StreamDefinitionStripping20`.

[86] L. Breiman, J. H. Friedman, R. A. Olshen, and C. J. Stone, Classification and regression trees, Wadsworth, Belmont, 1984.

[87] B. P. Roe et al., *Boosted decision trees as an alternative to artificial neural networks for particle identification*, Nucl. Instrum. Meth. **A543** (2005) 577, `arXiv:physics/0408124`.

[88] LHCb Collaboration, R. Aaij et al., *Observation of the suppressed ADS modes* $B^{\pm} \to [\pi^{\pm}K^{\mp}\pi^{+}\pi^{-}]_{D}K^{\pm}$ *and* $B^{\pm} \to [\pi^{\pm}K^{\mp}\pi^{+}\pi^{-}]_{D}\pi^{\pm}$, Phys. Lett. **B723** (2013) 44, `arXiv:1303.4646`.

[89] LHCb Collaboration, R. Aaij et al., *Measurement of the CKM angle* γ *using* $B^{\pm} \to DK^{\pm}$ *with* $D \to K^{0}_{S}\pi^{+}\pi^{-}$, $K^{0}_{S}K^{+}K^{-}$ *decays*, JHEP **10** (2014) 097, `arXiv:1408.2748`.

[90] A. Hoecker et al., *TMVA: toolkit for multivariate data analysis*, PoS **ACAT** (2007) 040, `arXiv:physics/0703039`.

[91] J. H. Friedman, *Stochastic gradient boosting*, Computational Statistics & Data Analysis **38** (2002) 367.

[92] W. Hulsbergen, *Cruijff PDF Class*, `https://www.slac.stanford.edu/BFROOT/www/doc/workbook_backup_010108/examples/ex1/workdir/PARENT/RooFitBabar/RooCruijff.cc`.

[93] P. Hunt, *PIDCalib: packages for extracting PID performance results from both collision data and MC*, `https://twiki.cern.ch/twiki/bin/view/LHCb/PIDCalibPackage`.

[94] P. Gandini, *New PDFs for partially reconstructed backgrounds in* $B \to DX$ *decays*, Personal documentation, 2013.

[95] D. Hill, M. John, N. Hussain, and G. Wilkinson, *Analysis of* $B^{\pm} \to Dh^{\pm}$ *with* $D \to K\pi, KK, \pi\pi, K\pi\pi\pi, \pi\pi\pi\pi$ *final states 3* fb^{-1} *update*, LHCb-ANA-2014-071, 2015.

[96] S. Cheung, S. Malde, C. Thomas, and G. Wilkinson, *The measurement of the CKM angle* γ *using the decays* $B^{\pm} \to D[K^{0}_{S}\pi\pi]K^{\pm}$ *and* $B^{\pm} \to D[K^{0}_{S}KK]K^{\pm}$, LHCb-ANA-2014-040, 2014.

[97] T. Skwarnicki, A study of the radiative cascade transitions between the Upsilon-prime and Upsilon resonances, PhD thesis, Institute of Nuclear Physics, Krakow, 1986.

[98] M. Pivk and F. R. Le Diberder, *sPlot: A statistical tool to unfold data distributions*, Nucl. Instrum. Meth. **A555** (2005) 356, `arXiv:physics/0402083`.

[99] N. Hussain, A. Powell, M. John, and G. Wilkinson, *Search for the suppressed ADS modes* $B^{\pm} \to (\pi^{\pm}K^{\mp}\pi^{\pm}\pi^{\mp})_D h^{\pm}$, LHCb-ANA-2012-069, 2013.

[100] LHCb Collaboration, R. Aaij et al., *Measurement of B meson production cross-sections in proton-proton collisions at* $\sqrt{s} = 7$ *TeV*, JHEP **08** (2013) 117, `arXiv:1306.3663`.

[101] LHCb Collaboration, R. Aaij et al., *Measurement of b hadron production fractions in 7 TeV pp collisions*, Phys. Rev. **D85** (2012) 032008, `arXiv:1111.2357`.

[102] W. Verkerke and D. P. Kirkby, *The RooFit toolkit for data modeling*, eConf **C0303241** (2003) MOLT007, `arXiv:physics/0306116`.

[103] LHCb Collaboration, R. Aaij et al., *Measurement of the* D_s^+–D_s^- *production asymmetry in 7 TeV pp collisions*, Phys. Lett. **B713** (2012) 186, `arXiv:1205.0897`.

[104] S. S. Wilks, *The large-sample distribution of the likelihood ratio for testing composite hypotheses*, Annals Math. Statist. **9** (1938) 60.

[105] D. Atwood and A. Soni, *Role of charm factory in extracting CKM phase information via* $B \to DK$, Phys. Rev. **D68** (2003) 033003, `arXiv:hep-ph/0304085`.

[106] J. Rademacker, *MINT: Minuit Interface package for Dalitz plot studies*, `http://www.phy.bris.ac.uk/people/rademacker_j/index.html`.

[107] CLEO Collaboration, S. Kopp et al., *Dalitz analysis of the decay* $D^0 \to K^-\pi^+\pi^0$, Phys. Rev. **D63** (2001) 092001, `arXiv:hep-ex/0011065`.

[108] BaBar Collaboration, B. Aubert et al., *Measurement of* $D^0 - \bar{D}^0$ *mixing from a time-dependent amplitude analysis of* $D^0 \to K^+\pi^-\pi^0$ *decays*, Phys. Rev. Lett. **103** (2009) 211801, `arXiv:0807.4544`.

[109] N. Hussain, M. John, C. Thomas, and G. Wilkinson, *Search for the suppressed ADS modes* $B^{\pm} \to (\pi^{\pm}K^{\mp}\pi^0)_D h^{\pm}$, LHCb-ANA-2013-075, 2015.

[110] K. S. Cranmer, *Kernel estimation in high-energy physics*, Comput. Phys. Commun. **136** (2001) 198, `arXiv:hep-ex/0011057`.

[111] BaBar Collaboration, B. Aubert et al., *Amplitude analysis of the decay* $D^0 \to K^-K^+\pi^0$, Phys. Rev. **D76** (2007) 011102, `arXiv:0704.3593`.

[112] M. John, *Gammadini: Combination Framework*, 2014.

[113] LHCb Collaboration, R. Aaij et al., *Study of CP violation in* $B^{\mp} \to Dh^{\mp}$ $(h = K, \pi)$ *with the modes* $D \to K^{\mp}\pi^{\pm}\pi^0$, $D \to \pi^+\pi^-\pi^0$ *and* $D \to K^+K^-\pi^0$, Phys. Rev. **D91** (2015) 112014, `arXiv:1504.05442`.

[114] D. Asner et al., *Physics at BES-III*, Int. J. Mod. Phys. **A24** (2009) S1, `arXiv:0809.1869`.